PERIODIC MESOPOROUS ORGANOSILICA: PREPARATION CHARACTERIZATION AND APPLICATIONS OF NOVEL MATERIALS

by

Steven Edward Dickson

A thesis submitted to the Department of Chemistry
In conformity with the requirements for
the degree of Doctor of Philosophy

Queen's University
Kingston, Ontario, Canada
(March, 2011)

Abstract

There is currently a great interest in the field of porous organosilica materials because of the high surface areas (> 1000 m^2/g) and narrow pore size distributions which are beneficial for applications such as chromatography, chiral catalysis, sensing or selective adsorption. Periodic mesoporous organosilicas (PMOs) represent an interesting class of hybrid silica materials because of the wide variety of bridging organic groups which can be incorporated within the precursors $[(OR)_3Si\text{-}\boldsymbol{R}\text{-}Si(OR)_3]$ giving rise to materials with exceptional properties.

We have synthesized and characterized various aromatic PMOs composed of supporting structural monomers (phenylene- or biphenylene-bridged) and functional stilbene monomers (*cis* and *trans*) (**1**, **2**). The effect of the different synthetic procedures and varying amounts of functional stilbene monomer on the properties of the materials was examined. The functional *trans*-stilbene component was determined to be well distributed in a phenylene-bridged PMO using P123 as a pore template from TEM techniques with Os staining. The *trans*-stilbene linkers were completely transformed to aryl aldehydes through ozonolysis with dimethylsulfide workup. Further transformation of the carbonyl functionality to an aryl imine showed a moderate level of success.

Enantiomeric forms of a novel, chiral PMO precursor (**CM**) were synthesized and incorporated into biphenylene-bridged PMOs. Under basic pH conditions templated with $C_{18}TMACl$, although very low levels of **CM** are

incorporated, enantiomeric forms of chiral, porous materials are obtained as was verified by distinct mirror-image circular dichroism spectra. Powder XRD patterns suggest that a tightly packed asymmetric biphenylene arrangement may be necessary for the optical activity. Preliminary results using these materials as a chiral chromatographic phase are promising.

Finally, a thin film morphology of an ethane-bridged PMO incorporating a thiol ligand, (3-mercaptopropyl)trimethoxysilane, was prepared on a fibre optic cable and used as a component in a heavy-metal sensing application.

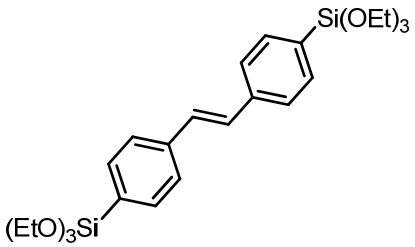

1

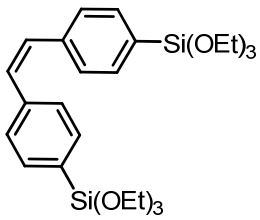

2

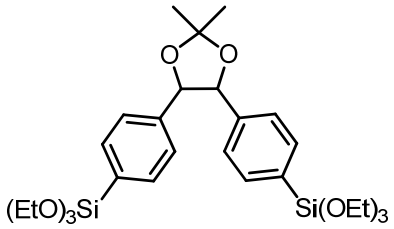

CM

Acknowledgements

In these acknowledgements, I would like to express my gratitude to many people for their help and encouragement throughout my doctoral program and thesis writing process. Firstly, to my supervisor Dr. Cathy Crudden- you have been an exceptional mentor and your devotion to science and chemistry is truly inspiring. Thank-you Cathy for having patience and motivating words when I needed them.

A special thank-you to those who have helped with the characterizations necessary for this work including Dr. Françoise Sauriol and Dr. Aris Docoslis and other support staff of Queen's University, Louise Weaver of University of New Brunswick and Srebri Petrov of University of Toronto. Informative discussions with many are appreciated, including Dr. Jean-Michel Nunzi, Dr. Bob Lemieux and Dr. Peter Loock.

To my former and current lab mates, who have graciously offered their time and patience in helping to better the work of a fellow student- you have made my experience here at Queen's University an enriching and enjoyable one. I owe a great big thank you to those who were here when I arrived, including Daryl Allen, Yonek Hleba, and Kevin McEleney, with a special mention to Dave Edwards, who on day one, hosted me in his fumehood, gave me constant direction and who always had time to discuss chemistry. Thanks for all the bumps and bruises on the bike trails as well. Thanks to Jeremy Praetorius, Jon Webb and Ben Glasspoole and for all of the good times in the lab and at the bars

and golf courses. Some of my fondest memories of my years in Kingston will be with you guys. To Jenny Du, your dedication and drive in all you do is unbelievable. I have learned so much from you and thank-you for making the Crudden lab a great place to be. To all other Crudden lab members, as well as many from other labs who have shared a drink, or a lunch, or a discussion (chemistry related or not), thank you. You have made the day to day work much more enjoyable.

I owe my deepest gratitude to my friends and family, especially my parents. Your constant support along my educational path has been strong and unwavering. I simply wouldn't be where I am today without you. I hope you understand how much I appreciate all you have done for me over the years and especially in this, my final stretch.

Statement of Originality

I hereby certify that all of the work described within this thesis is the original work of the author. Any published (or unpublished) ideas and/or techniques from the work of others are fully acknowledged in accordance with the standard referencing practices.

Steven Edward Dickson

(March, 2011)

Table of Contents

List of Figures

List of Schemes

List of Equations

List of Tables

List of Abbreviations

ºC	degrees Celsius
Å	angstrom
Ac	acetyl
Ar	aryl
BET	Brunauer-Emmett-Teller
BJH	Barrett-Joyner-Halenda
BP or BTEBP	4,4'-bis(triethoxysilyl)biphenyl
BTEB	4,4'-bis(triethoxysilyl)benzene
BTEBP or BP	4,4'-bis(triethoxysilyl)biphenyl
BTECS	4,4'-bis(triethoxysilyl)*cis*-stilbene
BTEE	1,2-bis(triethoxysilyl)ethane
BTETS	4,4'-bis(triethoxysilyl)*trans*-stilbene
BTME	1,2-bis(trimethoxysilyl)ethane
C_{16}TMACl	cetyltrimethylammonium chloride
C_{18}TMACl	octadecyltrimethylammonium chloride
CD	circular dichroism
CM	chiral monomer, 4-[2,2-dimethyl-5-[4-(triethoxysilyl)phenyl]-1,3-dioxolan-4-yl]phenyl)(triethoxy)silane
cmc	critical micelle assembly
CP	cross-polarization
COD	1,5-cyclooctadiene
CTAB	cetyltrimethylammonium bromide
CTACl	cetyltrimethylammonium chloride
d	day
DCM	dichloromethane
DMF	*N,N*-dimethylformamide
DMSO	dimethylsulfoxide
EDX	energy dispersive X-ray
ee	enantiomeric excess
EISA	evaporation induced self-assembly
EO	ethylene oxide
Et	ethyl
EtOAc	ethyl acetate
EtOH	ethanol
F127	Pluronic F127 ($EO_{106}PO_{70}EO_{106}$)
GC	gas chromatography
h	hour
HCl	hydrochloric acid
hex	hexanes
HMDS	hexamethyldisilazane
HRMS	high-resolution mass spectrometry
Hz	hertz
^{i}Pr	isopropyl
IR	infrared
IUPAC	International Union of Pure and Applied Chemists
M41S	MCM-41 family of materials

MAS	magic angle spin
J	coupling constant
K	Kelvin
min	minute
MCM	Mobil composition of matter
Me	methyl
MeOH	methanol
MPTES	3-mercaptopropyltriethoxysilane
MPTMS	3-mercaptopropyltrimethoxysilane
n	refractive index
nm	nanometer
NMO	*N*-methyl morpholine-*N*-oxide
NMR	nuclear magnetic resonance
OTAC	octadecyltrimethylammonium chloride
P123	Pluronic P123 ($EO_{20}PO_{70}EO_{20}$)
Ph	phenyl
PO	propylene oxide
PMO	periodic mesoporous organosilica
ppm	parts per million
Pr	propyl
$Q^{\#}$	quaternary silicon sites ($^{\#}$ indicates siloxane bonds)
R_f	retention factor
RI	refractive index
s	second
S/N	signal to noise ratio
SBA	Santa Barbara Material
SEM	scanning electron microscope
$T^{\#}$	trifunctional silicon sites ($^{\#}$ indicates siloxane bonds)
T	temperature
TEM	transmission electron microscope
TEOS	tetraethyl orthosilicate or tetraethoxysilane
THF	tetrahydrofuran
TLC	thin-layer chromatography
TMOS	tetramethyl orthosilicate or tetramethoxysilane
Tol	toluene
Ts	p-toluenesulfonate
UV	ultraviolet
XRD	X-ray diffraction

Chapter 1

Introduction to mesoporous silica and characterization

1.1 Introduction

Zeolites are by far the best known and most widely used porous inorganic materials.[1-3] These “molecular sieves” have pore diameters less than 2 nm, which classifies them as *microporous* materials, according to IUPAC.[4] There are natural and synthetic variants of these aluminosilicates which have high catalytic activity and exceptional stability because of their crystalline nature. It is because of these pores and a number of other features that these materials have had such widespread use in areas such as catalysis.[5] They have high surface areas, controllable adsorption properties, and are able to preactivate substrates confined in their micropores.[6] With the possibility to incorporate various heteroatoms into their structures, it is easy to see why they are prominent in a variety of processes such as ion exchange applications, molecular sieving, and catalysis in cracking for gasoline production, xylene and butene isomerization among others. It is because of the industrial relevance of these materials that some of the more exciting synthetic discoveries have been made in the labs of Mobil, Union Carbide, British Petroleum and Chevron.[1] In light of their desirable properties, there was interest in designing zeolites with larger pores which would be better able to accommodate bigger, more complex organic molecules in the void space.

The first report of mesoporous silica with a controllable pore size was in 1990 by Yanagisawa[7] *et al*. who used a layered polysilicate, kanemite ($NaHSi_2O_5 \cdot 3H_2O$), as a silica source and found that in the presence of alkyltrimethylammonium chloride solutions ($C_nH_{2n+1}(CH_3)_3N^+Cl^-$), n = 12, 14, 16 and 18) at pH 8-9, a porous material resulted from a "swelling" of the layered structure. The pores (2- 4 nm) were labeled as "micro pores", but were in fact, in the accepted IUPAC range for mesopores (2-50 nm).[4] These structures however, retained much of the layered or lamellar nature of the silica precursor.

The report often cited as that leading to the vast amount of current research on mesoporous silica was that of the Kresge[8] *et al*. of Mobil Research and Development Corporation. Here, the authors were able to produce mesoporous silica with regular (periodic) arrays of uniform pore channels in the range of 1.6 to 10 nm, beginning with molecular forms of silica such as sodium silicate or tetraethylorthosilicate (TEOS). Like microporous crystalline zeolites, this class of materials is characterized by very high surface areas and narrow pore radius distributions. However, unlike the zeolites, these materials possess amorphous silica in the walls. This family of materials was designated as M41S with the best known and most widely studied initial member being MCM-41, for Mobil composition of matter[9] (sometimes referred to as Mobil crystalline material[10]). This material has a hexagonally arrayed pore structure, while other architectures in this family possess cubic (MCM-48) or lamellar pores (MCM-50) which are described later. Following this report, researchers began exploring

novel compositions and architectures of mesoporous silica for applications in areas such as catalysis, gas storage, drug delivery, sensing, and optics.

1.2 Mesoporous silica templating pathways

Although synthetic zeolites are often templated by the use of quaternary ammonium hydroxides, key to the discovery of mesoporous silica was the use of a templating molecule that underwent self assembly into larger supramolecular arrays. In its broadest sense, a template can be thought of as a structure around which a network is formed, and when removing the template, a cavity or void is created which bears some morphological and/or stereochemical resemblance to the template.[11,12] There are *exotemplate* methods known as “noncasting” or “hard-matter templating”, where a porous solid is eventually removed from a system, for example by dissolution, to give a porous network resembling the removed solid.[13] The methods used here are *endotemplate* methods or “soft-matter templating” through the use of surfactant molecules.

There are two main mechanisms that are involved for the templated formation of mesoporous silica, originally outlined by Beck *et al.*[14] The first is through a true liquid-crystal templating process. In this mechanism, the concentration of the surfactant is such that at an appropriate temperature and pH, a lyotropic liquid-crystalline phase is present in the medium before the addition of the silica precursor(s). When the silica is added, it hydrolyses and condenses around the preformed template. In the second mechanism, a co-operative self-assembly process takes place between the surfactant and inorganic silica to form the liquid-crystalline phase at even lower concentrations

of surfactant than in the first case. The mesophase produced is a result of the combined effects of the constituents (Figure 1.1).

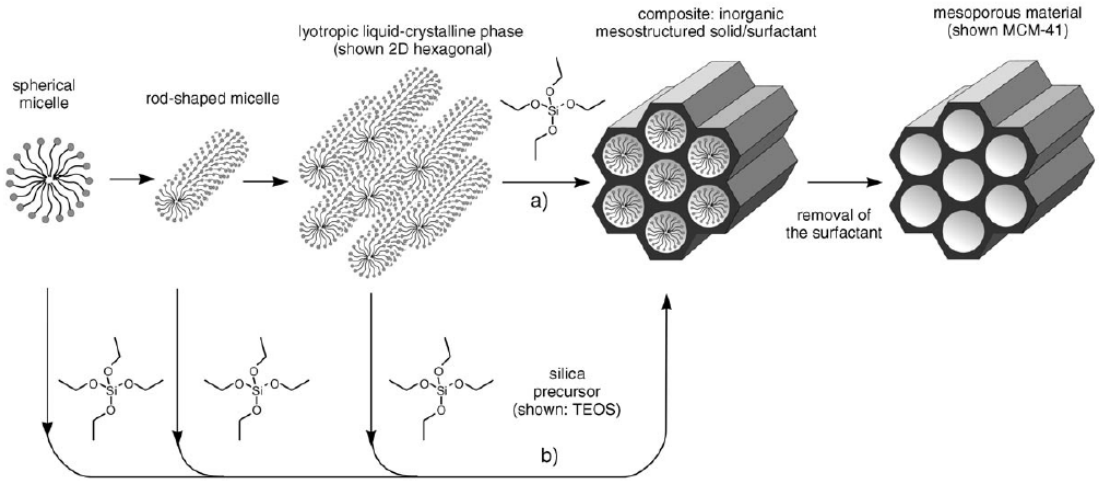

Figure 1.1 Two main templating mechanisms: a) true liquid-crystal b) cooperative liquid-crystal. Reproduced from Hoffmann *et al.*[15]

Fundamental to these soft templating methods is an attractive interaction between the surfactant and the silica precursors so that the template is included in the organization and not phase separated. Stucky and co-workers[16] have classified these interactions according to the charges on the surfactant head group, the inorganic precursors and any salts or counterions. These interactions are depicted in Figure 1.2. Here, the charges must balance at the interface between the inorganic silica source (I) and the surfactant head group (S), sometimes mediated by a counterion (M) or a halide (X). The charges are indicated by the superscript. For example, MCM-41 which is made under basic conditions and in the presence of cationic surfactants would fall under the electrostatic pathway and use the notation of S^+I^-. Other materials are templated from attractive interactions mediated by hydrogen bonds, for example with

nonionic surfactants (S^0 for a long-chained amine, or N^0 for polyethylene oxide) and uncharged silica species. This is the case for SBA-15, which utilizes a nonionic surfactant in acidic conditions and would fall under the hydrogen bonding pathway using notation $N^0(XI)^0$.

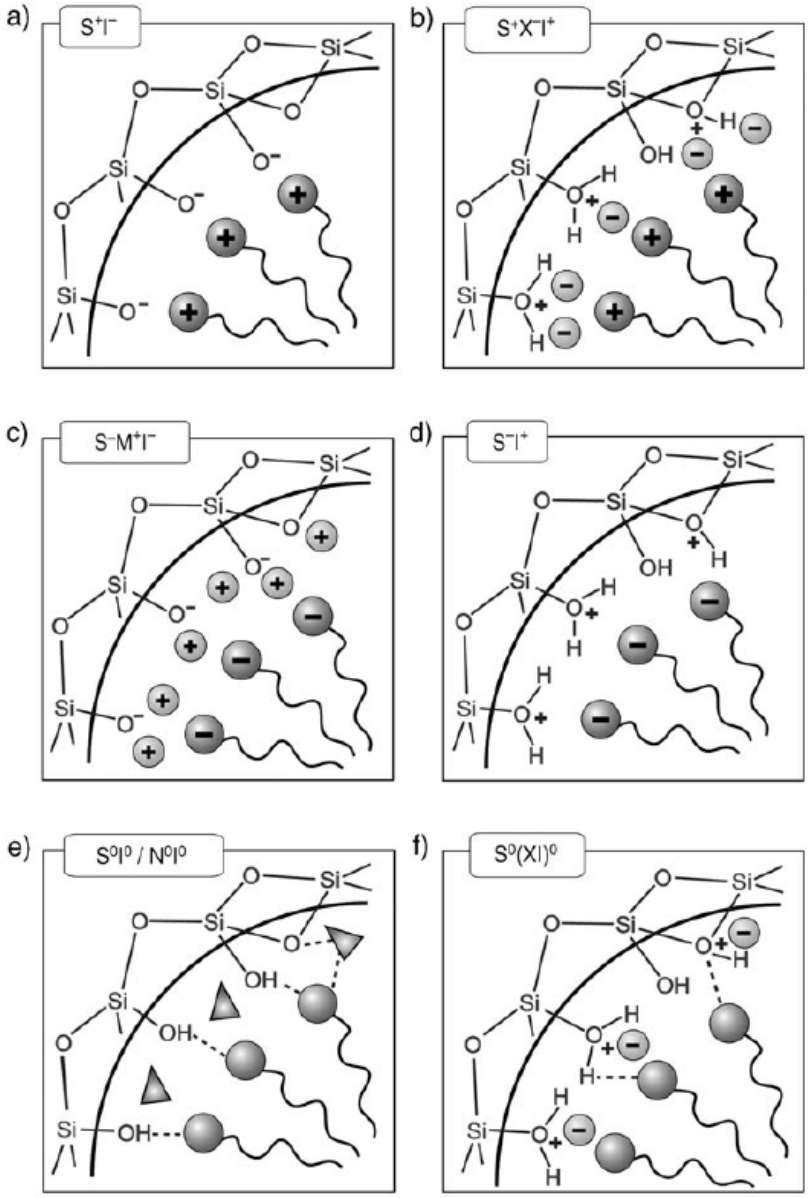

Figure 1.2 Interactions between inorganic species (I) and the surfactant head group (S) with consideration to possible synthetic pathways in acidic, basic, or neutral media. Electrostatic: S^+I^-, $S^+X^-I^+$, $S^-M^+I^-$, S^-I^+; through hydrogen bonds: S^oI^o/N^oI^o, $S^o(XI)^o$. Reproduced from Hoffmann *et al.*[15]

1.2.1 Surfactants

As mentioned above, surfactant molecules and their self assembled supramolecular structures are key components to the templation process. The surfactants employed can be divided into a number of groups (Figure 1.3). Ionic alkyl ammonium surfactants generally include C_{12}-C_{18} alkyl chains with trimethylammonium head groups. Examples from the literature include cetyltrimethylammonium bromide (CTAB) and octadecyltrimethylammonium chloride (OTAC or C_{18}TMACl). Nonionic surfactants include alkyl polyether type molecules such the Brij surfactants and the triblock copolymers such as Pluronic P123 and F127.

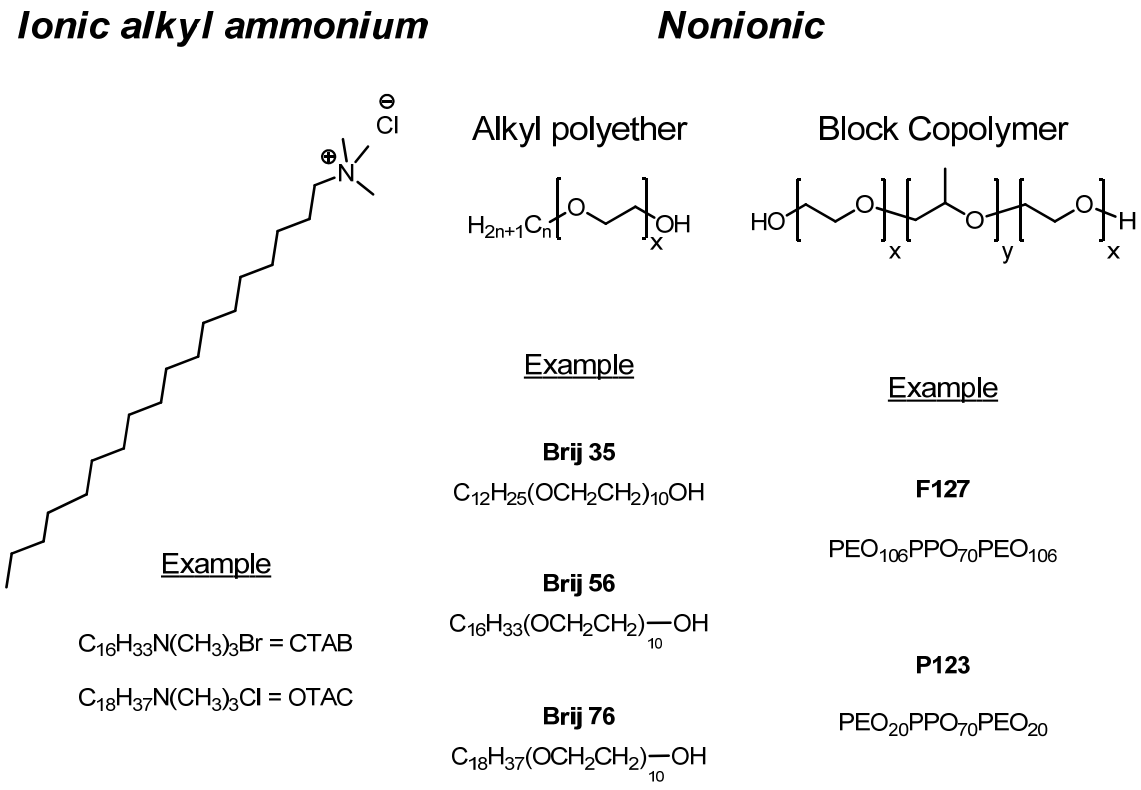

Figure 1.3 Common surfactant types and representative examples.

After the synthesis of the material, in order to obtain a porous structure the surfactant template needs to be removed from the pores. The most common method of doing this is by calcination, which is a high temperature (usually up to 550 ºC) treatment in the presence of air or oxygen to completely oxidize and decompose the surfactant. There are advantages to this method, namely the completeness with which the surfactant is removed and the relative efficiency of the process. However, the heating rate needs to be controlled (usually at less than 2 ºC/min) in order to maintain mesophase order; moreover calcination is generally unsuitable for removing surfactant from organically modified silica.[17]

An alternative to calcination for surfactant removal is solvent extraction. This is a milder approach which usually involves an organic solvent such as ethanol or THF with a small amount of acid such as HCl which promotes cross-linking as the surfactant is removed. The acid helps stabilize the mesophase and avoid pore-collapse.[18] Unlike calcination, more than 95 % of P123 surfactant can be recovered and reused with this procedure.[19] Also, more surface hydroxyl groups can be kept with extraction, enhancing the hydrophilic character and modifying the reactivity of the materials towards functionalization. However, the complete removal of the surfactant is difficult to accomplish with extraction.[17] Other more exotic methods of surfactant removal have been studied such as microwave[20] or ultraviolet irradiation.[21]

1.2.2 *g* parameter

The formation of mesoporous silica can be partly explained by the effective surfactant ion pair packing parameter, '*g*'. This is a useful parameter for predicting the geometry of a product mesophase (Equation 1.1).

$$g = V / a_0 l \qquad \text{(Equation 1.1)}$$

In this equation, *V* is the total volume of the surfactant chain plus any cosolvent between the chains, a_0 is equal to the area of the head group at the micelle surface, and *l* is equal to the kinetic length of the surfactant chain.[22,23] With the organic micelles and inorganic species meeting at an interface surface, the curvature here is determined by the energetics, so as to optimize the charge repulsions and van der Waals interactions. Any changes of the liquid crystalline micellar mesophase are a result of the changes of the curvature at this surface. There is a competition between the elastic energy of bending the interfaces and the energies resulting from separating charges and interfaces. Therefore, the size, charges, and shapes of surfactant molecules are important parameters for structure determination. The expected mesophases corresponding to various *g* parameters are shown in Table 1.1.[22] Space-filling images of some common mesophases are found in Figure 1.4.

Table 1.1 *g* parameter and mesophases

***g* parameter**	**mesophase**
⅓	Cubic (*Pm*3*n*)
½	Hexagonal (p6m)
½-⅔	Cubic (*Ia*3*d*)
1	Lamellar

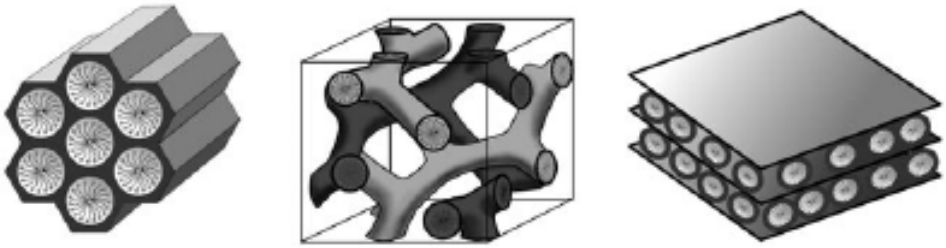

Figure 1.4 Common silica mesophases. From left to right: 2D-hexagonal, bicontinuous cubic and lamellar. Reproduced from Hoffmann *et al.*[15]

1.3 Characterization of mesoporous organosilica

With the silica materials prepared, the next step is to characterize them. With smaller molecules, techniques such as NMR, infrared (IR) and mass spectrometry (MS) are generally sufficient for characterization, however with silica materials, depending on the property under study, one will choose appropriate techniques. The methods commonly employed are solid state NMR, scanning electron microscopy (SEM), transmission electron microscopy TEM, powder X-ray diffraction (PXRD) and nitrogen porosimetry. Solid state NMR gives critical insight into the chemical environment of common nuclei such as ^{13}C and ^{29}Si. The ^{29}Si NMR can also give information regarding the degree of condensation of the material. This point is discussed later in the text. Unfortunately, solid state NMR suffers from much lower resolution than solution phase NMR due to anisotropic nuclear interactions, which can be somewhat averaged out by spinning the rotor at a magic angle (MAS) of 54.74 º. Cross-polarization (CP) is often used in the MAS NMR experiment where a more abundant nucleus (ex, ^{1}H) is irradiated so that the energy is transferred to the less sensitive nucleus of interest (ex, ^{13}C). SEM is used to determine particle

morphology, which can range from spheres, to rods or helices. TEM has a much higher spatial resolution than SEM and can be used to image pore dimensions of only a few nanometers. Powder X-ray diffraction (PXRD) is perhaps the most common method of characterizing materials. X-rays are diffracted from the atoms in a powdered sample and if the atoms are arranged in a periodic fashion as in a crystal, there will be a regular interference pattern detected. The peaks in the pattern are directly related to the distance between the repeating groups through Bragg's law: $n\lambda = 2d\sin\theta$, where n is an integer, λ is the wavelength of the incident X-ray radiation, d is the distance between repeating groups and θ is the angle of incidence. The patterns (positions and intensities of the peaks) are used to characterize the crystalline nature and the long-range order of the materials. Gas porosimetry analysis is an important technique for porous material characterization as it is used to collect such data as surface area, and pore dimensions (volume, diameter).[24] Importantly, unlike microscopy, this is a bulk technique, characterizing the entire sample at once. Typically, the analyte is outgassed in a glass vessel under elevated temperature (>100 °C) and high vacuum (<0.004 mm Hg) to remove any trace water or solvents. A calibrated volume of gas (usually nitrogen due to availability, but sometimes argon for microporous analysis) is added to a vessel containing the porous analyte which is kept at the boiling point of the gas (-195.79 °C, 77.35 K for nitrogen). The added gas is allowed to equilibrate with the surface of the analyte, where some is physically adsorbed (physisorbed). The pressure is then monitored and once stable, the volume and pressure are recorded before repeating the process. The

most energetic surface atoms will adsorb the gas molecules first, until a complete monolayer of gas is formed, after which subsequent multilayers are deposited. After the complete adsorption branch of the experiment is finished, data for the reverse process is taken by gradually applying a vacuum to the vessel. The resulting data consists of an adsorption and desorption isotherm as shown in Figure 1.5.

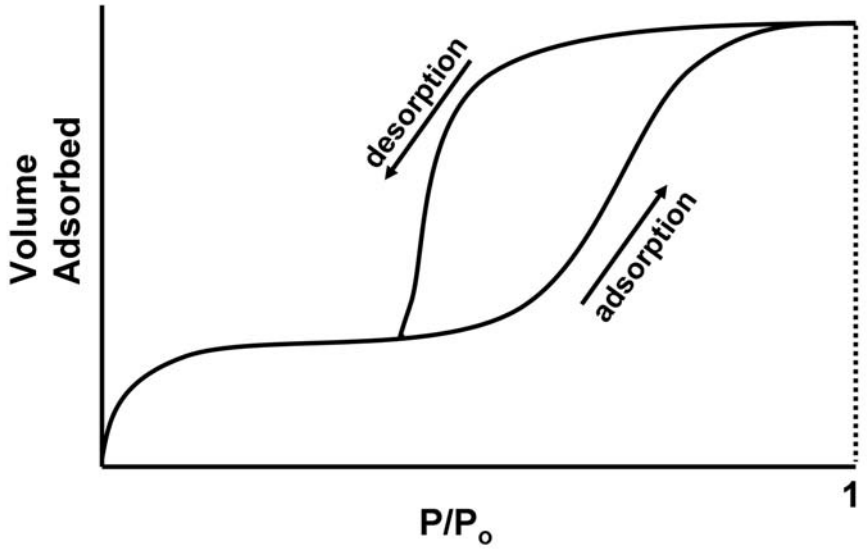

Figure 1.5. Example adsorption-desorption isotherm.

Isotherms are usually classified depending on their basic shape, as IUPAC Type I to Type VI (Figure 1.6).[25] Type I isotherms have prominent gas adsorption at low relative pressures and are indicative of microporous materials having relatively low external surface areas and pore diameters less than 2 nm. Examples of materials exhibiting this Type I isotherm are activated carbons and zeolites. Type IV isotherms are characterized by a hysteresis loop which is associated with capillary condensation taking place in mesopores as well as a

limiting uptake over a range of high relative pressures. The lower relative pressures of Type IV represent a monolayer-multilayer gas adsorption and this type is seen for mesoporous materials of pore diameters in the range of 2 to 50 nm.

Although the exact origins of the hysteresis loop are still under debate, it is believed to be a result of a combination of thermodynamic and pore-network effects. In the past, certain hysteresis types were assigned to certain pore shapes, including non-connected, cylindrical pores open at both ends, and disordered interconnected pores.[25,26] Thermodynamically, the hysteresis is usually explained by the different shape of the adsorbate/vapour interface (the meniscus of the liquid) during adsorption and desorption in pores open at both ends. This simplified view has recently been challenged, with support for the notion that pore connectivity leads to interdependent emptying of the pores.[27] Even pores that are not interconnected (for example, through micropores) are nonetheless dependent on one another, whereby the emptying or filling of one pore can lead to changes in a neighbouring pore, through elastic deformation of the pore walls.[27-29]

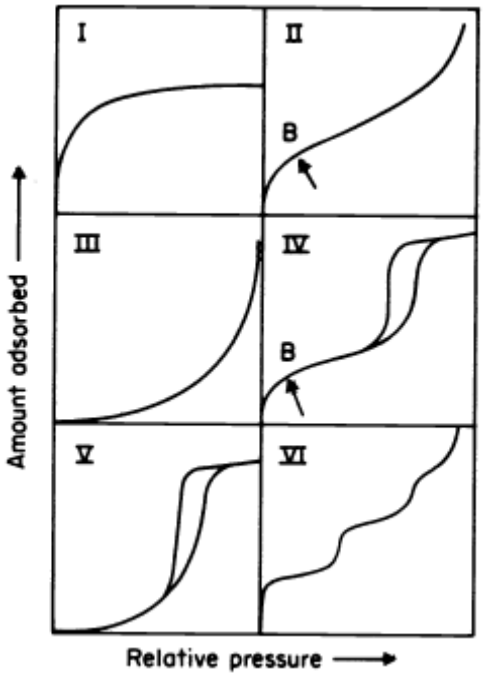

Figure 1.6 Types of physisorption isotherms. Reproduced from Sing *et al*.[25]

From the isotherm data, surface areas and pore dimensions are calculated. The surface area is generally calculated with the BET method (Brunauer, Emmet and Teller), which is an extension of the Langmuir theory used to determine specific surface area based on a monolayer of adsorptive gas.[30] BET theory extends the Langmuir theory to incorporate multilayer formation. By equating the rate of condensation to evaporation of gas molecules onto an already condensed layer and summing for an infinite number of layers, the BET expression is obtained, [24]

$$V_a = \frac{V_m C P}{(P_o - P)\left[1 + (C-1)\frac{P}{P_o}\right]} \qquad \text{(Equation 1.2)}$$

where V_a is the volume adsorbed at pressure P, P_o is the saturation pressure, V_m is the volume of a monolayer of adsorbate, and C is a constant. The value of C in simplest terms is

$$C \propto e^{\frac{q_1 - q_L}{RT}} \qquad \text{(Equation 1.3)}$$

where q_1 and q_L are the heat of adsorption of the first layer and the heat of liquefaction of the adsorptive respectively. The gas constant and absolute temperature are given as R and T respectively.[24] Care must be taken with the BET method due to the number of assumptions the calculation makes, including a flat surface and adsorbed molecules having no lateral interactions with one another.[30,31] The BET method can also be used to gain an estimation of the gas-surface interaction energy from the C parameter. This can be useful when comparing hydrophobic versus hydrophilic surfaces. Again, care is necessary as the results are dependent on the validity of the BET treatment of the isotherm data. The total volume of the pores can be calculated by converting the amount of gas adsorbed near the saturation vapour pressure to a volume at STP (standard temperature and pressure) conditions.[30]

The pore size distributions can be determined from a number of models. Most commonly they are determined from the BJH model (Barrett, Joyner and Holenda) which is based on the Kelvin model (Equation 1.4) of pore filling. Here, P and P_o are the vapour pressure and the saturated pressure respectively, λ is the surface tension, V_m is the molar volume, R is the gas constant, r is the radius of the droplet and T is the absolute temperature. This model uses the same basic concepts for adsorption and desorption, where adsorption in the mesopores is

pictured as a multilayer formation, followed by a capillary condensation within the core of the pore. The reverse is pictured for the desorption process, where the cores of the mesopores are emptied in a capillary evaporation process, followed by multilayer evaporation. Studies on mesoporous MCM-41 with approximately cylindrical pores show this general picture adequately represents the nature of the adsorption process.[32] It should be noted that this theory is valid for mesoporous to small macroporous ranges only and for nitrogen at 77 K the *upper limit* for which the model holds is 200-400 nm, which is well above the upper range of mesopore diameters (50 nm).[30]

$$\frac{\ln P}{P_0} = \frac{2\lambda V_m}{rRT} \qquad \text{(Equation 1.4)}$$

When there is a hysteresis present in the isotherm, there is the question as to which branch to use for proper pore size determination. It has been recommended by Kruk and Jaroniec[30] to avoid use of the desorption branch as it is often delayed due to network effects and artifacts may be present. They recommend the use of the adsorption branch to improve the accuracy of pore size determinations.

1.4 Organically-modified silica

There have been many reports and reviews on the organic functionalization of pure silica and other metallic oxide phases, as well as some which have focused on mesoporous silica.[12,33-35] A schematic of the possible routes to incorporating organic functionality to create hybrid organic-inorganic

materials is shown in Figure 1.7. As can be seen in method 1 known as grafting, the pure silica mesophase is generated first with the templation process, after which a condensable organosilane, usually of type $(R'O)_3SiR$, is added to the surface. This can be done through a solution or vapour phase condensation process. The advantage of this process is that the mesophase of the silica is usually retained, however there is often a reduction in the resulting porosity depending on the size of the organic and the degree of loading. If there is a preference for condensation at the pore openings, this can impair further diffusion to the center of the pore channels and result in inhomogeneous organic loadings or complete pore blockage.[36] An alternative method is to incorporate the organosilane of the same $(R'O)_3SiR$ type into the mesophase concurrently with the tetraalkoxysilanes such as TEOS [$Si(OEt_4)$] or TMOS [$Si(OMe_4)$] in a co-condensation method (route 2, Figure 1.7).[37,38] Here, the advantage is that there is generally a more homogeneous loading of the organic groups throughout the pores, however this method tends to see limited amounts of organic incorporation into the material. Generally there is about a 20-25 % maximum amount of organosilane that can be accommodated in the templation process before a substantial loss in the mesoscale order is seen[39]. To help alleviate these issues, work began which incorporates the organic fragments into the precursor by flanking the organic segment with two or more condensable trialkoxysilyl groups [$(R'_3O)SiRSi(OR'_3)$]. The gelation of these monomers was reviewed by Shea and Loy[40], and Corriu's group[41,42] who observed anisotropic ordering among the more rigid monomers, but these materials were formed under

nontemplated conditions. The method to the porous organosilica is shown in route 3 of Figure 1.7, with the advantages here being more homogeneous and higher organic loadings with the organic group incorporated throughout the hybrid organic-inorganic skeleton. The resulting surfactant-templated materials from these organically-bridged poly(trialkoxysilyl) monomers make up the family known as *periodic mesoporous organosilicas.*

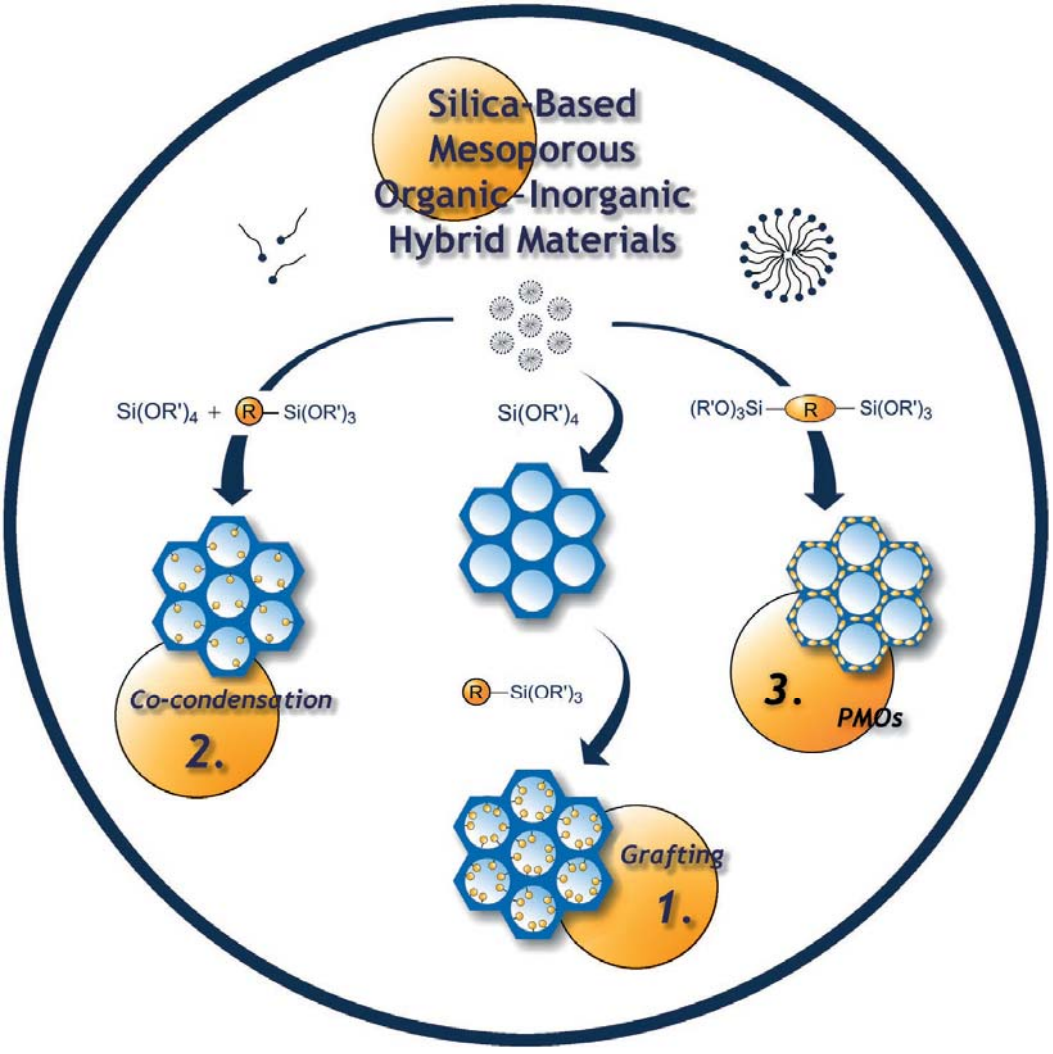

Figure 1.7 Organic modifications of mesoporous silica. Reproduced from Hoffmann *et al.*[15]

1.5 Periodic mesoporous organosilicas (PMOs)

In 1999, three groups independently reported the use of organically-bridged bis(trialkoxysilyl) precursors[43] as monomers for the synthesis of hybrid organic-inorganic mesoporous silica materials. Inagaki's group from Toyota Central R&D Laboratories in Japan[44] used 1,2-bis(trimethoxysilyl)ethane (BTME) to integrate the inorganic and organic moieties into a hybrid material (Figure 1.8). A highly ordered material, using C_{18}TMACl as a template, was produced with hexagonal symmetry and pore diameters of 3.1 nm. The well-ordered porous network, which can be seen in the TEM image below, resulted in a high surface area (750 m^2 g^{-1}) material.

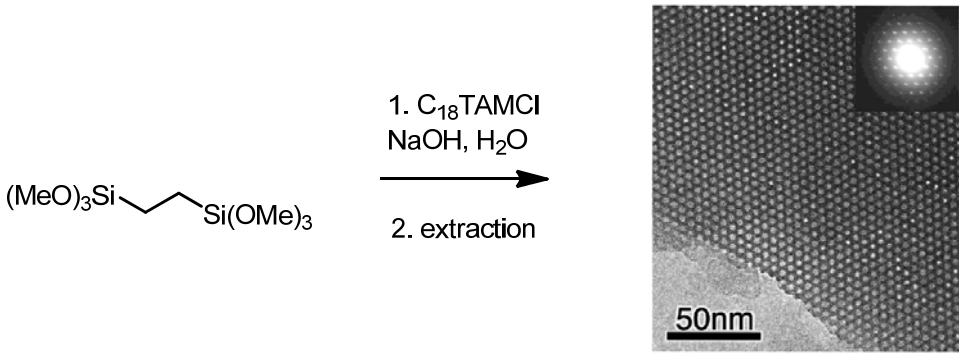

Figure 1.8 BTME forming 2D hexagonal mesoporous silica shown in TEM image. Reproduced from reference [44].

Ozin and coworkers,[45] employed a functional monomer, 1,2-(bistriethoxysilyl)ethene (Figure 1.9), under basic conditions using CTAB as the surfactant, producing an ethene-bridged PMO. They were then able to brominate the material to determine accessibility to the olefin, however despite having consumed all olefin as confirmed by CP MAS ^{13}C NMR, bromine analysis

suggested that only 10 % of the olefin was brominated. It was proposed by the group that the remaining olefin had reacted with the solvent.

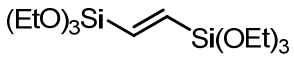

Figure 1.9 Bis(triethoxysilyl)ethene

At nearly the same time as the previous two groups, Stein and co-workers[46] made the ethene-bridged materials described above, which were also treated with bromine to test the olefin accessibility. In this case, bromine vapour was unable to completely react with all olefin groups, but EDX analysis showed the presence of bromine and CP MAS ^{13}C NMR confirmed the presence of carbon bound to bromine. They were then able to test this material as a bromide source by stirring with $AgNO_3$ to make AgBr.

It should be noted that the nomenclature of periodic mesoporous organosilicas has not yet been standardized.[15] For this work, we will employ the most commonly used convention, which is to refer to a PMO by the name of the respective *parent* bridging group of the precursor. For example, Figure 1.8 shows an *ethane*-bridged PMO precursor (as opposed to an IUPAC recommended *ethylene* bridging group). This minimizes confusion in that the parent hydrocarbon of Figure 1.9 is commonly named 'ethylene'. Some exceptions to this would include the *methylene*, *phenylene* or *biphenylene*-bridging groups where the IUPAC recommendations are used for less ambiguous groups. Although the requirements for classifying a material as a "PMO" are not standardized, for this text, we will follow the convention of Fröba and coworkers[15]

that limits the classification of PMOs to those materials that are prepared from bis- or poly-(trialkoxysilyl) organically-bridged precursors as their exclusive silica source. This will exclude materials that incorporate the tetrafunctional TEOS monomer and trialkoxysilyl monomers [$RSi(OR')_3$] in the preparation.

Since the initial reports of periodic mesoporous organosilica, there have been many reports of groups incorporating various organics within PMOs. A number of reviews on PMOs are available[15,47-52] which present many of the different precursors used to date in PMOs as well as their application in areas such as catalysis.

A number of the commonly found precursors that have been used in PMO synthesis are shown in Figure 1.10. As is clear from the monomers employed, researchers have relied heavily on short, rigid organic linkers (such as #1-3) or aromatic linkers, as disordered materials result from flexible linkers over two carbons in length. One benefit from the aromatic precursors is the structural support these organics offer. PMOs based on two aromatic groups (#5 and #9) made by Inagaki's group under basic conditions have been shown to be stable in air or nitrogen up to 500 °C by thermogravimetric analysis.[53,54] An obvious disadvantage to these simple alkyl and aromatic monomers is the lack of chemical handles available for further manipulations. Forcing conditions (25% SO_3/H_2SO_4 over 100 ºC, followed by 6 M HCl) were required by Inagaki's group to sulphonate less than 10% of the phenylene-silica.[54] The mesophase was retained to produce a 0.4 mmol H^+ g^{-1} solid acid catalyst. The catalytic activity was not reported.

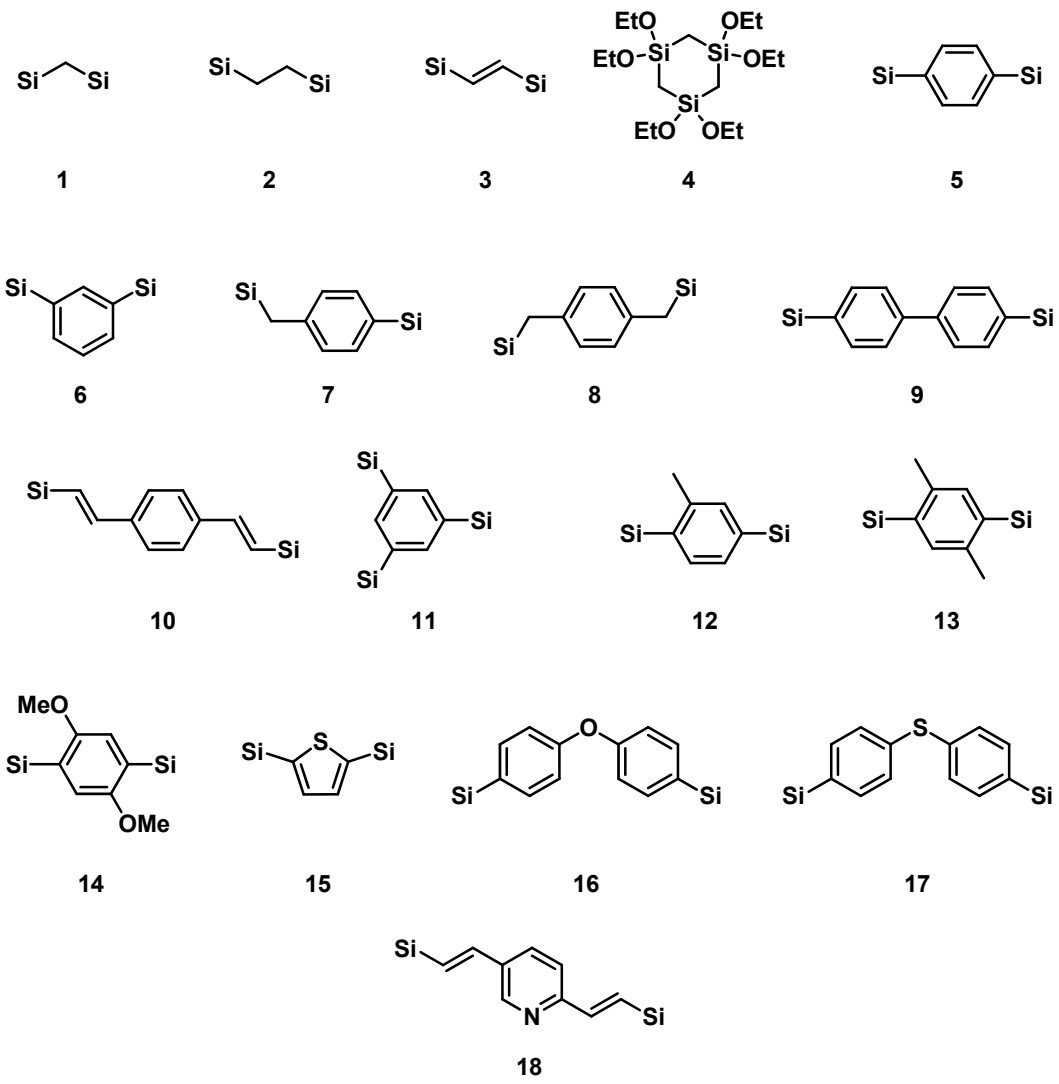

Figure 1.10 Organically-bridged precursor molecules used for the preparation of PMOs. Si = $Si(OR)_3$, R= Me or Et. Adapted from reference [15].

1.5.1 Crystal-like pore walls

One important feature noted by Inagaki and coworkers in the phenylene-bridged PMO material was the appearance of crystallinity in the pore walls.[54] The crystal-like pore walls were evidenced from the powder X-ray diffraction (PXRD) pattern which showed peaks at medium scattering angles representing a structural periodicity of 7.6 Å along the length of the pore channel. These peaks

originated from an alternating hydrophobic benzene and hydrophilic silica layer. This was a breakthrough in organosilica materials, where amorphous walls were normally observed. This is in contrast to zeolites, which are characterized by high crystallinity. Thus these materials could be considered to bridge the gap between highly ordered microporous zeolites and the amorphous, large pore organosilicas. It is interesting to note that in Inagaki's modeling of the phenylene mesoporous silica, the rings were as close as 4.4 Å apart, yet if they were able to pack slightly closer, the π-π stacking could give rise to a conductive material. Inagaki subsequently demonstrated that materials with crystal-like pore walls could also be prepared from a biphenyl-bridged monomer[53] which gave a correspondingly larger *d* spacing of 11.6 Å (#9, Figure 1.10).

Sayari and Wang[55] and nearly concurrent with Fröba and coworkers[56] extended the list of precursors which afforded crystal-like pore walls when they made PMOs from 1,4-bis[(*E)*-2-(triethoxysilyl)vinyl]benzene (#10, Figure 1.10). More recently Inagaki's group prepared a PMO with crystal-like walls from a divinylpyridine-bridged precursor (#18, Figure 1.10).[57] However, in all of these cases, it was imperative to use basic conditions with long-chain trialkylammonium surfactants such as C_{18}TMACl. The alkaline pH conditions are known to promote a higher degree of condensation and likely facilitate a tighter packing of the π-stacking monomers to form the well-organized, crystal-like channel walls.

1.6 Functionality in PMOs

The above methods of incorporating a desired organic functionality into a material include post-synthetic grafting or co-condensation of an organo-trialkoxysilane [$(R'O)_3SiR$] and the use of organically-bridged bis(trialkoxysilyl) monomers [$(R'_3O)SiRSi(OR'_3)$] to produce PMOs. In addition to these methods, one can imagine attaining a desired functionality through the transformation of a currently existing functional group. Although, the obvious disadvantage of this method is that it is an additional step along the synthetic path, the purifications of such products are typically nothing more than a filtration and solvent wash. Nevertheless, the additional step may be necessary. It may be the case that a desirable functional group does not survive under the normally harsh conditions of PMO synthesis (very high/ low pH, high temperature, long duration) or that the bridging group is incompatible with the siloxane groups (for example a strong acid or base which influences hydrolysis and condensation) or perhaps the precursor is not rigid enough to produce a well-ordered, porous material. In these instances, it would be advantageous to work with precursors having functional groups that are inert under the required synthetic conditions and yield the desired porous structures, however are still able to be transformed into a desired functionality. Comparing to a concept from synthetic organic chemistry, the material to be transformed can be considered a “protected” material of the desired functionality. On the other hand, one must be aware that there may be a decrease in the framework strength or stability upon any modifications, which

could have drastic effects on the porosity of the material. Pore collapse may result, which often leads to decreased material function.[58]

There have been several attempts at modifications of the bridging groups of PMOs. Aside from the groups of Ozin[45] and Stein[46] both attempting to brominate the olefin of their ethene-bridged PMOs as mentioned earlier, there have been other modifications of an ethene-bridged PMO by amination,[59,60] hydroxylation,[38] and Diels-Alder chemistry.[61] More recently, Inagaki has nitrated and reduced up to 28 % of the arene rings of phenylene-bridged silica to form an amino-functionalized PMO, which was useful as a solid base catalyst.[62]

Inagaki's group also reported the bromination of ethene-bridged PMOs, where they quantified the amount of reactive olefin in the silicate framework at 30 % by bromination in $CHCl_3$ and subsequent iodometric titration.[63] This is three times as much accessible olefin as was determined by Ozin's group[45] for the same ethene-bridged PMO. This can likely be explained by the higher surface areas and larger pore volumes reported under the Inagaki conditions (1040 m^2/g versus 637 m^2/g and 1.35 cm^3/g versus 0.60 cm^3/g for BET surface areas and pore volumes respectively).

Although a methylene bridging group is not a handle for many further chemical transformations, Ozin's group[64] examined the behaviour of these PMOs under thermal conditions and discovered a bridging organic group in the walls of a PMO being converted to a terminally bound group in the pore space. Bridging methylene groups in the channel walls were converted into terminal methyl

groups in the channel space through a Si-C bond cleavage and neighbouring SiO-H transfer to form a new Si-CH_3 and Si-O-Si bond (Figure 1.11).

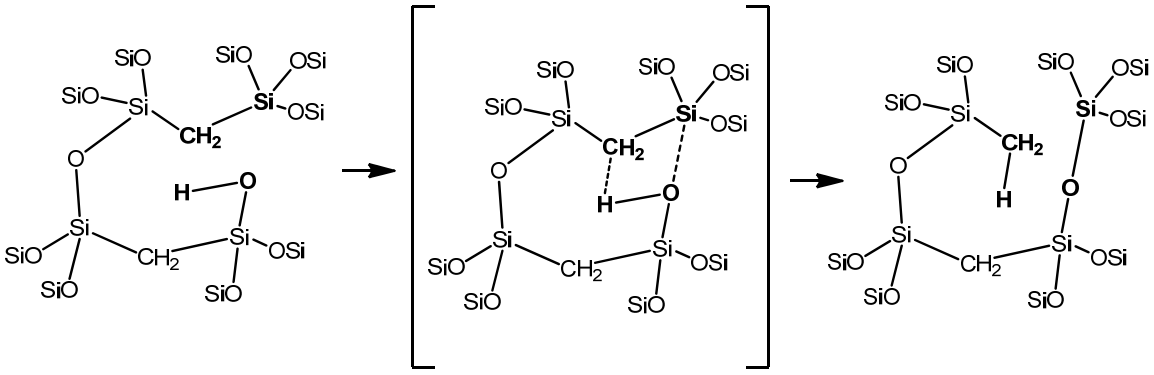

Figure 1.11 Thermal cleavage of Si-CH_2 to form a new bridging Si-O-Si group and a terminal Si-CH_3. Reproduced from reference [15].

In 2001, Ozin with Jaroniec, introduced the concept of adding two or more organics into a PMO when they reported bifunctional PMOs which incorporated bridging and terminal ethylene groups.[65] The PMO was subsequently hydroborated with BH_3·THF and oxidized to the alcohols and although the terminal ethylene groups underwent reaction, the bridging groups of the PMO showed much lower reactivity and were unreacted. It could be interesting if this chemistry is followed by bromination of the internal ethylene groups so that one can attain the benefits of orthogonal reactivity with multicomponent PMOs (Figure 1.12).

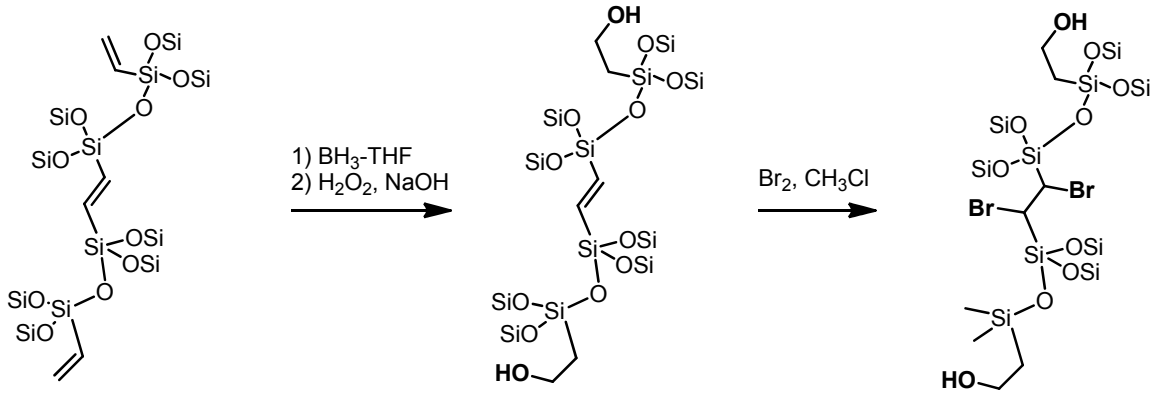

Figure 1.12 Bifunctional PMOs. A proposed hydroboration-oxidation of terminal olefin, followed by bromination of internal olefin.

Sayari's group used octadecyltrimethylammonium chloride (C_{18}TMACl) as the structure directing agent under basic conditions to produce for the first time a PMO using (bis(triethoxysilyl)ethen-2-yl)benzene, a single precursor incorporating aromatic and olefinic groups (#10, Figure 1.10, R = Et).[55] This PMO exhibited the crystal-like pore walls in a similar fashion to other aromatic precursors, with a slightly larger *d* spacing of 11.9 Å attributed to the lamellar stacking of the precursor in the pore walls. They also noted that the long-range molecular order of the monomer was not dependent on the use of a structure directing agent as observed by Corriu's group.[41,66] Sayari and coworkers have also investigated the homogeneity of a two-component PMO incorporating biphenyl- and phenyl-bridged precursors under basic conditions using C_{18}TMACl, and found evidence of phase separation or island formation.[67]

One other notable report by Sayari's group in 2007 was that of the first observation of molecular scale periodicity of PMOs under acidic conditions.[68] Large-pore PMOs were prepared using a biphenyl-bridged precursor, templated with P123 under acidic conditions. Although the mesoscale order of the PMOs was low (wormhole) and PXRD patterns for the molecular scale periodicity were much weaker than those under alkaline pH, this was evidence that molecular scale ordering could be obtained under acidic hydrolysis/ condensation conditions.

An approach taken by Polarz and coworkers was to create a bromo-phenyl bridged PMO precursor which allowed the preparation of PMOs with carboxylic, vinyl and phosphonic ester groups on the surface either with modification of the precursor or from the resulting bromo functionalized PMO (Figure 1.13).[69,70] Interestingly, they found it necessary to use tri-*iso*-propoxy over ethoxy, methoxy and *tert*-butoxy for the alkoxides on silicon to yield a mesoporous material, despite isopropanol being somewhat disruptive in the templating process.

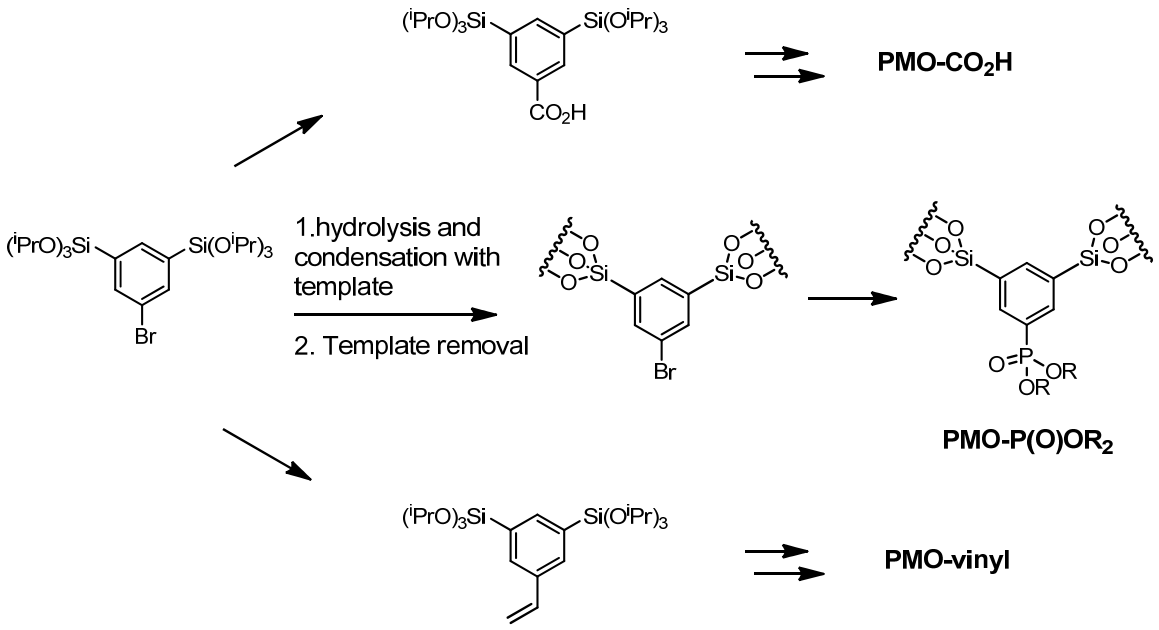

Figure 1.13 PMOs made by Polarz and coworkers from bromophenyl-bridged precursor.

Even more complex structures have been incorporated into porous materials including organometallic complexes, but these functionalities required the addition of a long flexible linker or the addition of another silica source such as TEOS or TMOS and thus will not be discussed further.[71-75] However, an ionic diarylimidazolium structure (Figure 1.14) has been incorporated into a PMO despite the resulting material having a very low surface area of 100 m^2/g.[76]

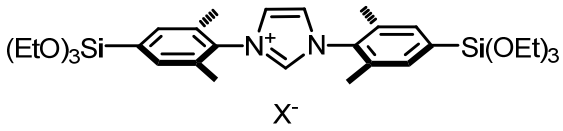

Figure 1.14 Structure of ionic diarylimidazolium PMO precursor.[76]

1.7 Chirality in PMOs

A logical progression in the development of PMOs occurred with the use of *chiral* bridging organic groups. Chiral PMOs have potential applications in areas of enantioselective catalysis and chiral chromatography among others. Again, flexible linkers and other silica sources were needed to incorporate some chiral bridging groups including organometallic complexes,[71] chiral diaminocyclohexane, binaphthyl, and others into organosilica[72,77,78] but here we will focus on materials made exclusively from organically-bridged silica sources.

As mentioned above, Polarz's group prepared PMOs with chiral amino acids at the pore surface which showed differential adsorption of enantiomeric propylene oxide gases.[70] Ozin[60] and Polarz[38] reported chiral PMOs from a precursor prepared from an asymmetric hydroboration of 1,2-bis(triethoxysilyl)ethene. Polarz's hydroboration of ethene bridges led to PMOs with chiral hydroxy and amino functionality. Asymmetric hydrogenation of a silylated aromatic ketone[79] and hydrosilylation[80] of a phenylsilylethene unit have also led to chiral precursors for PMO synthesis (Figure 1.15).

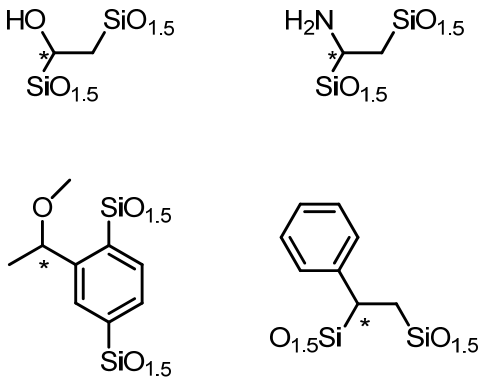

Figure 1.15 Linker units of several chiral PMOs.

Characterizing the enantiomeric purity of the PMOs has been achieved by dissolving the silica in HF followed by HPLC of the organics on a chiral stationary phase.[80] Circular dichroism of chiral PMOs has been performed using isorefractive index solvents[60,79] or dispersions in KBr pellets.[81-83] Ozin's group showed they were able to observe optical activity of an achiral chromophore (benzoic acid) adsorbed onto a chiral amine-functionalized PMO through induced circular dichroism.[60]

Our group has recently demonstrated the transfer of chirality from an axially chiral precursor to a biphenyl-bridged precursor within the pore walls of a PMO (Figure 1.16).[83]

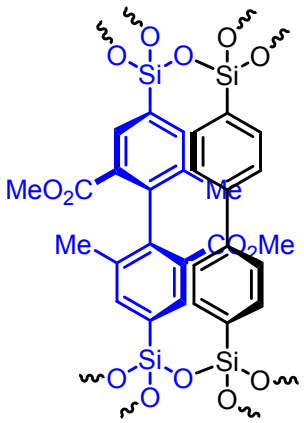

Figure 1.16 Transfer of chirality or induced chirality from a precursor having axial chirality to a biphenyl-bridged precursor within a PMO organosilica matrix.

1.8 PMO morphology

Typical PMO syntheses usually lead to particles with irregular external form or morphology and non-uniform particle size. It is highly desirable to have

control over particle morphology for certain applications. As an example, in HPLC, a solid phase consisting of monodisperse spherical particles with diameters on the order of 10 μm would be necessary for optimal separation results. In areas of sensing or coatings, a uniform film thickness is generally desired.

Inagaki's group prepared PMOs from 1,2-bis(trimethoxysilyl)ethane (BTME) in the presence of C_{18}TMACl with 2 different sets of molar ratios of reagents.[44] One procedure gave a particle of 2D-hexagonal symmetry and the other was indexed to a 3D-hexagonal symmetry. In the 2D-hexagonal particles, they observed rods a few microns in diameter and 10-20 μm in length having a hexagonal cross-section. In the 3D-hexagonal particles, they observed spheres of diameters of 0.1 - 10 μm (Figure 1.18). Inagaki also reported conditions where highly regular particles of decaoctahedron shape were obtained from BTME and cetyltrimethylammonium chloride (C_{16}TMACl) (Figure 1.19).[84]

Sayari's group reported on the growth of ethane-bridged PMOs with C_{16} or C_{18} trimethylammonium chloride as structure directing agent under two different synthetic methods.[85] "Method 1" had molar ratios of reagents given as BTME (or BTEE), 1.0; C_{16}TMACl (or C_{18}TMACl), 0.12; NaOH, 1.0; H_2O, 231, while "Method 2" had a slightly higher surfactant and NaOH concentration with molar ratios of BTME (or BTEE), 1.0; C_{16}TMACl (or C_{18}TMACl), 0.57; NaOH, 2.36; H_2O, 353. While Method 1 was conducted at room temperature with stirring, Method 2 employed an additional static (no stirring) aging stage at 85 ºC to 100 ºC for 20-24 h. They found that under Method 1, the PMOs in the presence of C_{16}TMACl

as structure directing agent formed rough, spherical particles of a broad size distribution which were composed of agglomerations of smaller spherical particles, while under Method 2 at 85 ºC, the materials consisted of isolated or agglomerated particles with truncated rhombic dodecahedral morphology (Figure 1.17). Higher temperatures for Method 2 at first glance appeared spherical but were concluded to be a less ordered form of the lower temperature morphology. With the longer C_{18}TMACl surfactant, again, spherical particles composed of tiny (< 100 nm) spherical particles were grown under Method 1 with BTME whereas Method 2 led to a variety of different shapes at various temperatures including 10 μm faceted rods.

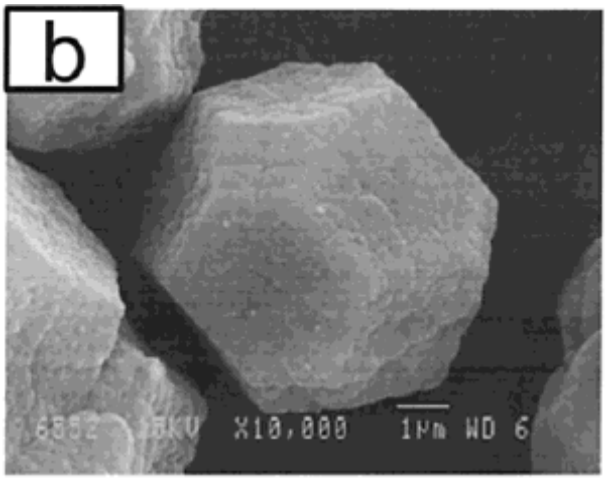

Figure 1.17 Truncated rhombic dodecahedral particles as observed by Sayari and coworkers. Reproduced from reference [85].

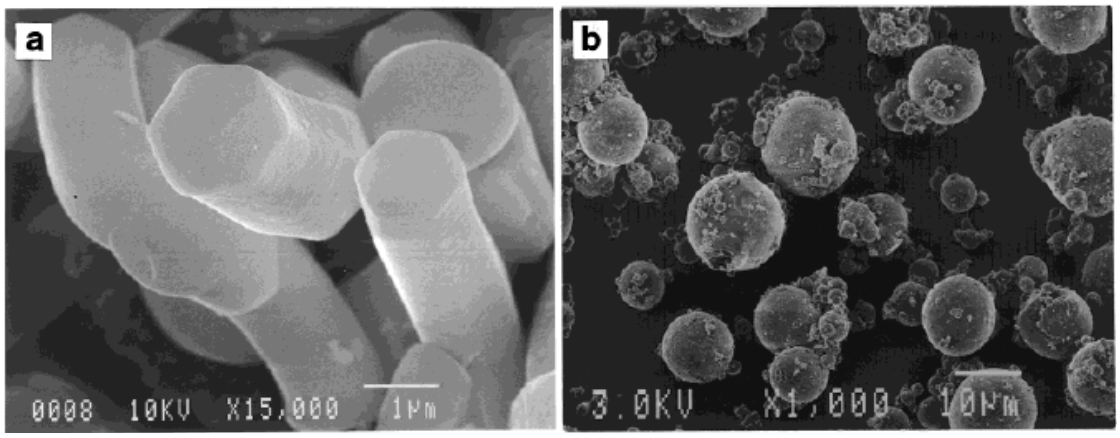

Figure 1.18 SEM images of a) rod-like particles with hexagonal cross section of 2D-hexagonal symmetry b) spherical particles of 3D-hexagonal symmetry. Reproduced from reference [44].

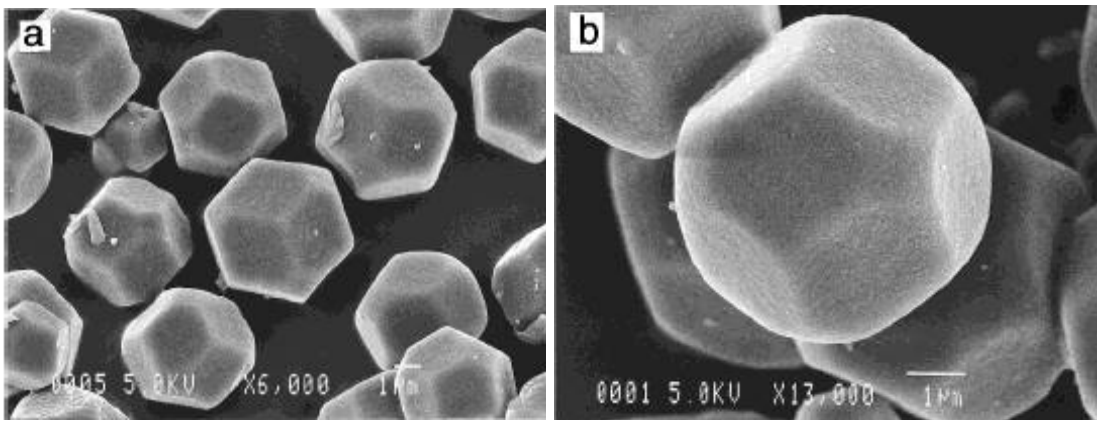

Figure 1.19 SEM images of ethane-silica PMOs displaying decaoctahedral particle morphology. Reproduced from reference [84].

A variety of complex morphologies such as ropes, gyroids, spirals and spheres have been observed by Park's group using 1,2-bis(trimethoxysilyl)ethane (BTME) under basic conditions, templated with octadecyltrimethyl ammonium bromide.[86] Stirring gave a higher curvature to the rope-like particles versus static conditions but all the particles displayed a

hexagonal basal plane. Silica-micellar growth induced by topological defects was identified as a potential explanation for the variety of curvatures and morphologies observed.[87,88] These studies also demonstrated that the symmetry of the micellar arrangement also dictates the external morphology and explains the difficulty in preparing the less common spherical PMO particles.

More recently, Zhao and coworkers reported the synthesis of highly regular, ethane-bridged *single crystal* PMOs of uniform external morphologies, attributed to a kinetically controlled growth of the particles.[89] Notably, in the area of single crystal PMO morphology, the majority of studies focus on ethane-bridged precursors, while there appears to be a lack of literature on any aromatic precursors. This may imply some difficulty in preparing single crystal morphology-type materials with aromatic hybrid precursors.

Most attempts at monodisperse spherical PMOs are based on the Stöber procedure[90] which uses a dilute ethanolic ammonia solution rather than aqueous sodium hydroxide solution. Inagaki and Kapoor reported spherical, phenylene-bridged PMOs with pore diameters of 1.8 – 2.0 nm and particle diameters from 0.6 – 1.0 μm.[91] They noted that dilute, mildly basic and slow condensation conditions were necessary for the simultaneous nucleation, growth and termination of the silica particles in order to achieve monodispersity. Fröba and coworkers prepared much larger spherical phenylene-bridged PMOs (particle diameters of ~10 μm) which were used in an HPLC separation. They used P123 and CTAB in a mixed surfactant system with an acidic water/ethanol solution to achieve spherical particles (Figure 1.20).[92]

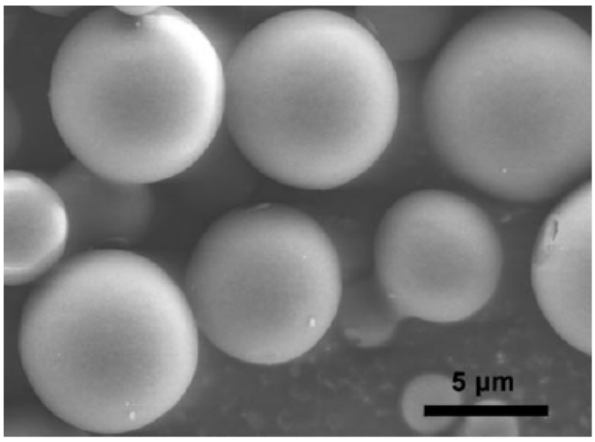

Figure 1.20 SEM image of spherical particles prepared by Fröba and coworkers. Reproduced from reference [92].

Brinker and Loy reported the first PMO thin films that were prepared from bridged silsesquioxanes by applying an evaporation-induced self-assembly process (EISA).[93] Here, precipitation was avoided and the self-assembly process occurred quickly after spin- or dip-coating a substrate. This was accomplished by using dilute ethanolic solutions that suppressed the self-assembly as well as acidic conditions that slowed the condensation process. After coating, preferential ethanol evaporation concentrates the sol in water, surfactant and the PMO precursor. During evaporation, the increasing surfactant concentration leads to a self-assembly process at the critical micelle concentration (cmc).

Ahn's group, prepared 1.5-2.5 µm PMO spheres of ethane-silica (pore diameters 3.2 nm) with C_{16}TMACl and NaOH solution, followed by a microwave treatment. The particles showed larger pore diameters and volumes as well as improved separations in HPLC over particles prepared by conventional means (without microwave).[94]

As PMOs are a relatively new development in the area of porous silica, researchers are still actively pursuing novel architectures, functionalities and applications of such materials. Indeed, the number of research papers on the subject is growing. Although there are a variety of organic functionalities which have already been included in PMOs, there has been less work done on the exploration of materials capable of further chemical manipulation or transformation. Those reports which have been mentioned are typically lacking efficient reactivity, or have poorly characterized products. Here, we pursue the preparation, characterization and transformation of novel PMOs, the studies of which will hold promise for the development and progress of research in related fields.

1.9 References

(1) Cheetham, A. K.; Ferey, G.; Loiseau, T. *Angew. Chem., Int. Ed.* **1999**, *38*, 3268-3292.
(2) Davis, M. E.; Lobo, R. F. *Chem. Mater.* **1992**, *4*, 756-768.
(3) Smith, J. V. *Chem. Rev.* **1988**, *88*, 149-182.
(4) Everett, D. H. *Pure Appl. Chem.* **1972**, *31*, 577-638.
(5) Corma, A. *Chem. Rev.* **1997**, *97*, 2373-2419.
(6) Zicovich-Wilson, C. M.; Corma, A.; Viruela, P. *J. Phys. Chem.* **1994**, *98*, 10863-10870.
(7) Yanagisawa, T.; Shimizu, T.; Kuroda, K.; Kato, C. *Bull. Chem. Soc. Jpn.* **1990**, *63*, 988-992.
(8) Kresge, C. T.; Leonowicz, M. E.; Roth, W. J.; Vartuli, J. C.; Beck, J. S. *Nature* **1992**, *359*, 710-712.
(9) Melero, J. A.; van Grieken, R.; Morales, G. *Chem. Rev.* **2006**, *106*, 3790-3812.
(10) Trewyn, B. G.; Slowing, II; Giri, S.; Chen, H. T.; Lin, V. S. Y. *Acc. Chem. Res.* **2007**, *40*, 846-853.
(11) Beck, J. S.; Vartuli, J. C.; Kennedy, G. J.; Kresge, C. T.; Roth, W. J.; Schramm, S. E. *Chem. Mater.* **1994**, *6*, 1816-1821.
(12) Raman, N. K.; Anderson, M. T.; Brinker, C. J. *Chem. Mater.* **1996**, *8*, 1682-1701.
(13) Ryoo, R.; Joo, S. H.; Jun, S. *J. Phys. Chem. B* **1999**, *103*, 7743-7746.
(14) Beck, J. S.; Vartuli, J. C.; Roth, W. J.; Leonowicz, M. E.; Kresge, C. T.; Schmitt, K. D.; Chu, C. T. W.; Olson, D. H.; Sheppard, E. W.; McCullen, S. B.; Higgins, J. B.; Schlenker, J. L. *J. Am. Chem. Soc.* **1992**, *114*, 10834-10843.
(15) Hoffmann, F.; Cornelius, M.; Morell, J.; Froba, M. *Angew. Chem., Int. Ed.* **2006**, *45*, 3216-3251.
(16) Huo, Q. S.; Margolese, D. I.; Ciesla, U.; Feng, P. Y.; Gier, T. E.; Sieger, P.; Leon, R.; Petroff, P. M.; Schuth, F.; Stucky, G. D. *Nature* **1994**, *368*, 317-321.
(17) Wan, Y.; Zhao, D. *Chem. Rev.* **2007**, *107*, 2821-2860.
(18) Inagaki, S.; Sakamoto, Y.; Fukushima, Y.; Terasaki, O. *Chem. Mater.* **1996**, *8*, 2089-2095.
(19) Zhao, D. Y.; Huo, Q. S.; Feng, J. L.; Chmelka, B. F.; Stucky, G. D. *J. Am. Chem. Soc.* **1998**, *120*, 6024-6036.
(20) Gallis, K. W.; Landry, C. C. *Adv. Mater.* **2001**, *13*, 23-26.
(21) Hozumi, A.; Yokogawa, Y.; Kameyama, T.; Hiraku, K.; Sugimura, H.; Takai, O.; Okido, M. *Adv. Mater.* **2000**, *12*, 985-987.
(22) Huo, Q. S.; Margolese, D. I.; Stucky, G. D. *Chem. Mater.* **1996**, *8*, 1147-1160.
(23) Israelachvili, J. N.; Mitchell, D. J.; Ninham, B. W. *J. Chem. Soc., Faraday Trans. 2* **1976**, *72*, 1525-1568.

(24) Webb, P. A.; Orr, C. *Analytical methods in fine particle technology*; Micromeritics Norcross, GA, 1997; Vol. 229.
(25) Sing, K. S. W.; Everett, D. H.; Haul, R. A. W.; Moscou, L.; Pierotti, R. A.; Rouquerol, J.; Siemieniewska, T. *Pure Appl. Chem.* **1985**, *57*, 603-619.
(26) Cohan, L. *J. Am. Chem. Soc.* **1938**, *60*, 433-435.
(27) Grosman, A.; Ortega, C. *Appl. Surf. Sci.* **2010**, *256*, 5210-5215.
(28) Coasne, B.; Grosman, A.; Ortega, C.; Simon, M. *Phys. Rev. Lett.* **2002**, *88*, 256102.
(29) Grosman, A.; Ortega, C. *Physical Review B* **2008**, *78*, 085433.
(30) Kruk, M.; Jaroniec, M. *Chem. Mater.* **2001**, *13*, 3169-3183.
(31) Rouquerol, J.; Avnir, D.; Fairbridge, C.; Everett, D.; Haynes, J.; Pernicone, N.; Ramsay, J.; Sing, K.; Unger, K. *Pure Appl. Chem.* **1994**, *66*, 1739-1758.
(32) Kruk, M.; Jaroniec, M. *Chem. Mater* **2000**, *12*, 222-230.
(33) Stein, A. *Adv. Mater.* **2003**, *15*, 763-775.
(34) Soler-illia, G. J. D.; Sanchez, C.; Lebeau, B.; Patarin, J. *Chem. Rev.* **2002**, *102*, 4093-4138.
(35) Ying, J. Y.; Mehnert, C. P.; Wong, M. S. *Angew. Chem., Int. Ed.* **1999**, *38*, 56-77.
(36) Lim, M. H.; Stein, A. *Chem. Mater.* **1999**, *11*, 3285-3295.
(37) Burkett, S. L.; Sims, S. D.; Mann, S. *Chem. Commun.* **1996**, 1367-1368.
(38) Polarz, S.; Kuschel, A. *Adv. Mater.* **2006**, *18*, 1206-1209.
(39) Lim, M.; Blanford, C.; Stein, A. *Chem. Mater.* **1998**, *10*, 467-470.
(40) Shea, K.; Loy, D. *Acc. Chem. Res.* **2001**, *34*, 707-716.
(41) Cerveau, G.; Chappellet, S.; Corriu, R. J. P.; Dabiens, B.; Le Bideau, J. *Organometallics* **2002**, *21*, 1560-1564.
(42) Ben, F.; Boury, B.; Corriu, R. J. P.; Le, S. V. *Chem. Mater.* **2000**, *12*, 3249-3252.
(43) Shea, K. J.; Loy, D. A. *Chem. Mater.* **2001**, *13*, 3306-3319.
(44) Inagaki, S.; Guan, S.; Fukushima, Y.; Ohsuna, T.; Terasaki, O. *J. Am. Chem. Soc.* **1999**, *121*, 9611-9614.
(45) Asefa, T.; MacLachlan, M. J.; Coombs, N.; Ozin, G. A. *Nature* **1999**, *402*, 867-871.
(46) Melde, B. J.; Holland, B. T.; Blanford, C. F.; Stein, A. *Chem. Mater.* **1999**, *11*, 3302-3308.
(47) Shylesh, S.; Samuel, P. P.; Sisodiya, S.; Singh, A. P. *Catal. Surv. Asia* **2008**, *12*, 266-282.
(48) Fujita, S.; Inagaki, S. *Chem. Mater.* **2008**, *20*, 891-908.
(49) Yang, Q. H.; Liu, J.; Zhang, L.; Li, C. *J. Mater. Chem.* **2009**, *19*, 1945-1955.
(50) Hunks, W. J.; Ozin, G. A. *J. Mater. Chem.* **2005**, *15*, 3716-3724.
(51) Hatton, B.; Landskron, K.; Whitnall, W.; Perovic, D.; Ozin, G. A. *Acc. Chem. Res.* **2005**, *38*, 305-312.
(52) Asefa, T.; Yoshina-Ishii, C.; MacLachlan, M. J.; Ozin, G. A. *J. Mater. Chem.* **2000**, *10*, 1751-1755.

(53) Kapoor, M. P.; Yang, Q.; Inagaki, S. *J. Am. Chem. Soc.* **2002**, *124*, 15176-15177.
(54) Inagaki, S.; Guan, S.; Ohsuna, T.; Terasaki, O. *Nature* **2002**, *416*, 304-307.
(55) Sayari, A.; Wang, W. *J. Am. Chem. Soc.* **2005**, *127*, 12194-12195.
(56) Cornelius, M.; Hoffmann, F.; Froba, M. *Chem. Mater.* **2005**, *17*, 6674-6678.
(57) Waki, M.; Mizoshita, N.; Ohsuna, T.; Tani, T.; Inagaki, S. *Chem. Commun.* **2010**, *46*, 8163-8165.
(58) Glasspoole, B.; Webb, J.; Crudden, C. *J. Catal.* **2009**, *265*, 148-154.
(59) Voss, R.; Thomas, A.; Antonietti, M.; Ozin, G. A. *J. Mater. Chem.* **2005**, *15*, 4010-4014.
(60) Ide, A.; Voss, R.; Scholz, G.; Ozin, G. A.; Antonietti, M.; Thomas, A. *Chem. Mater.* **2007**, *19*, 2649-2657.
(61) Nakajima, K.; Tomita, I.; Hara, M.; Hayashi, S.; Domen, K.; Kondo, J. N. *Adv. Mater.* **2005**, *17*, 1839-1842.
(62) Ohashi, M.; Kapoor, M. P.; Inagaki, S. *Chem. Commun.* **2008**, 841-843.
(63) Nakajima, K.; Lu, D.; Kondo, J. N.; Tomita, I.; Inagaki, S.; Hara, M.; Hayashi, S.; Domen, K. *Chem. Lett.* **2003**, *32*, 950-951.
(64) Asefa, T.; MacLachlan, M. J.; Grondey, H.; Coombs, N.; Ozin, G. A. *Angew. Chem., Int. Ed.* **2000**, *39*, 1808-1811.
(65) Asefa, T.; Kruk, M.; MacLachlan, M. J.; Coombs, N.; Grondey, H.; Jaroniec, M.; Ozin, G. A. *J. Am. Chem. Soc.* **2001**, *123*, 8520-8530.
(66) Cerveau, G.; Corriu, R. J. P.; Framery, E.; Lerouge, F. *Chem. Mater.* **2004**, *16*, 3794-3799.
(67) Yang, Y.; Sayari, A. *Chem. Mater.* **2008**, *20*, 2980-2984.
(68) Yang, Y.; Sayari, A. *Chem. Mater.* **2007**, *19*, 4117-4119.
(69) Kuschel, A.; Polarz, S. *Adv. Funct. Mater.* **2008**, *18*, 1272-1280.
(70) Kuschel, A.; Sievers, H.; Polarz, S. *Angew. Chem., Int. Ed.* **2008**, *47*, 9513-9517.
(71) Baleizao, C.; Gigante, B.; Das, D.; Alvaro, M.; Garcia, H.; Corma, A. *Chem. Commun.* **2003**, 1860-1861.
(72) Jiang, D. M.; Yang, Q. H.; Wang, H.; Zhu, G. R.; Yang, J.; Li, C. *J. Catal.* **2006**, *239*, 65-73.
(73) Dufaud, V.; Beauchesne, F.; Bonneviot, L. *Angew. Chem., Int. Ed.* **2005**, *44*, 3475-3477.
(74) Corma, A.; Das, D.; Garcia, H.; Leyva, A. *J. Catal.* **2005**, *229*, 322-331.
(75) Baleizao, C.; Gigante, B.; Das, D.; Alvaro, M.; Garcia, H.; Corma, A. *J. Catal.* **2004**, *223*, 106-113.
(76) Nguyen, P.; Hesemann, P.; Gaveau, P.; Moreau, J. J. E. *J. Mater. Chem.* **2009**, *19*, 4164-4171.
(77) Alvaro, M.; Benitez, M.; Das, D.; Ferrer, B.; Garcia, H. *Chem. Mater.* **2004**, *16*, 2222-2228.
(78) Garcia, R. A.; van Grieken, R.; Iglesias, J.; Morales, V.; Gordillo, D. *Chem. Mater.* **2008**, *20*, 2964-2971.

(79) Morell, J.; Chatterjee, S.; Klar, P. J.; Mauder, D.; Shenderovich, I.; Hoffmann, F.; Froba, M. *Chem.-Eur. J.* **2008**, *14*, 5935-5940.
(80) Inagaki, S.; Guan, S. Y.; Yang, Q.; Kapoor, M. P.; Shimada, T. *Chem. Commun.* **2008**, 202-204.
(81) Kuroda, R.; Honma, T. *Chirality* **2000**, *12*, 269-277.
(82) Yang, Y. G.; Suzuki, M.; Fukui, H.; Shirai, H.; Hanabusa, K. *Chem. Mater.* **2006**, *18*, 1324-1329.
(83) MacQuarrie, S.; Thompson, M. P.; Blanc, A.; Mosey, N. J.; Lemieux, R. P.; Crudden, C. M. *J. Am. Chem. Soc.* **2008**, *130*, 14099-14101.
(84) Guan, S.; Inagaki, S.; Ohsuna, T.; Terasaki, O. *J. Am. Chem. Soc.* **2000**, *122*, 5660-5661.
(85) Sayari, A.; Hamoudi, S.; Yang, Y.; Moudrakovski, I. L.; Ripmeester, J. R. *Chem. Mater.* **2000**, *12*, 3857-3863.
(86) Lee, C. H.; Park, S. S.; Choe, S. J.; Park, D. H. *Microporous Mesoporous Mater.* **2001**, *46*, 257-264.
(87) Yang, H.; Coombs, N.; Ozin, G. A. *Nature* **1997**, *386*, 692-695.
(88) Park, S.; Lee, C.; Cheon, J.; Park, D. *J. Mater. Chem.* **2001**, *11*, 3397-3403.
(89) Li, J.; Wei, Y.; Deng, Y. H.; Gu, D.; Yang, X. D.; Zhang, L. J.; Tu, B.; Zhao, D. Y. *J. Mater. Chem.* **2010**, *20*, 6460-6463.
(90) Stöber, W.; Fink, A.; Bohn, E. *J. Colloid Interface Sci.* **1968**, *26*, 62-69.
(91) Kapoor, M. P.; Inagaki, S. *Chem. Lett.* **2004**, *33*, 88-89.
(92) Rebbin, V.; Schmidt, R.; Froba, M. *Angew. Chem., Int. Ed.* **2006**, *45*, 5210-5214.
(93) Lu, Y. F.; Fan, H. Y.; Doke, N.; Loy, D. A.; Assink, R. A.; LaVan, D. A.; Brinker, C. J. *J. Am. Chem. Soc.* **2000**, *122*, 5258-5261.
(94) Kim, D. J.; Chung, J. S.; Ahn, W. S.; Kam, G. W.; Cheong, W. J. *Chem. Lett.* **2004**, *33*, 422-423.

Chapter 2

Stilbene as a functional monomer for transformable PMOs

2.1 Introduction

The use of monomers in PMOs that are capable of further chemical modification have mainly focused on simple ethene-bridged materials, or stable aromatic ring systems which required the use of harsh conditions for functionalization. Here we wish to explore the use of functional monomers, in particular stilbene-bridged monomers, as novel organic architectures in PMOs. The resulting materials will be characterized and assessed for further chemical modifications.

2.2 Results and discussion

2.2.1 Functional monomer preparation

We chose to target stilbene as our functional monomer linker. Stilbenes have both *cis* and *trans* stereoisomers which could lead to interesting morphologies in the resulting materials. Furthermore, high enantioselectivities can result from asymmetric chemical transformations such as dihydroxylations,[1] epoxidations,[2] and cyclopropanations,[3] on this type of organic system. Our initial attempts at PMO functionalization were of a 1,4-divinylbenzene-bridged PMO reported previously by Sayari's group (Figure 2.1). This PMO exhibited pore diameters and surface area of 3.06 nm and 536 m^2/g respectively, as well as crystal-like lamellar-structures within the pore walls observed by PXRD.[4] Our

epoxidation of this PMO, under racemic or enantioselective conditions, was met with little success and resulted in observable amounts of Si-C bond cleavage by CP MAS ^{29}Si NMR. We believed this cleavage could be related to the "beta-silicon effect" where silicon is known to stabilize, through hyperconjugation, beta carbocations, which would also be stabilized here as a benzylic carbocation (Figure 2.2).

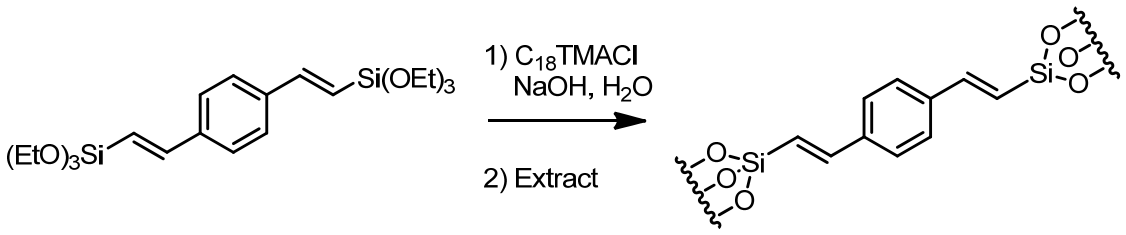

Figure 2.1 1,4-Bis(triethoxysilylethen-2-yl)benzene prepared by Sayari's group.[4]

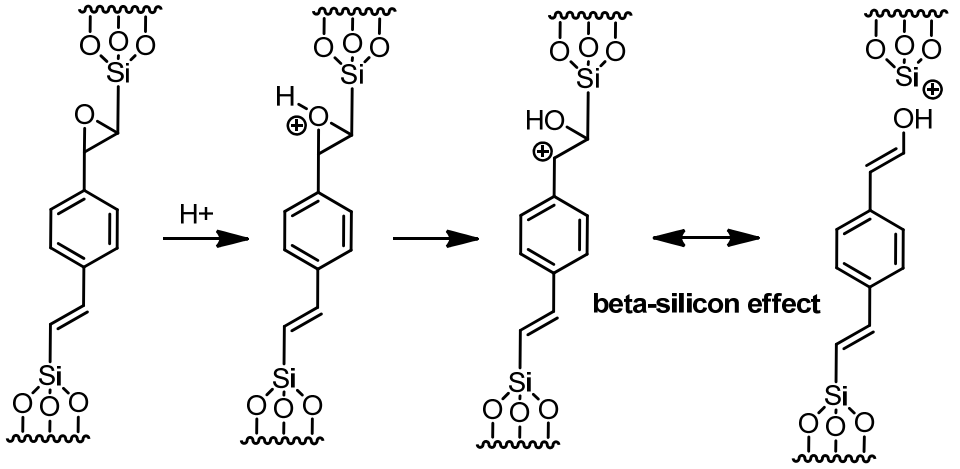

Figure 2.2 Beta-silicon effect leading to C-Si cleavage after epoxidation.

We then sought to prepare a monomer where the functional group was removed from the silicon as in 4,4'-bis(triethoxysilyl)*trans*-stilbene (BTETS) (**1**) (Figure 2.3). To prepare the *trans*-stilbene functional monomer, a Grubbs

olefination reaction was employed which results in the dimerization of 4-bromostyrene with loss of ethylene in near-quantitative yield (99 %).[5] The catalytic loading of this reaction was eventually reduced by two orders of magnitude from 2.5 mol % to a very low loading of 0.02 mol % using the second generation Grubbs' catalyst,[6] while still maintaining the high chemical yield (99 %). The *trans* isomer is made exclusively with no evidence of the *cis* isomer by ^{1}H NMR. Subsequent conversion of the bromo substituents to iodides[7] is necessary for increasing the reactivity in the following C-Si coupling reaction[8] to introduce the polymerizable siloxane units (Scheme 2.1). This precursor molecule was obtained in 58 % overall yield after the three steps.

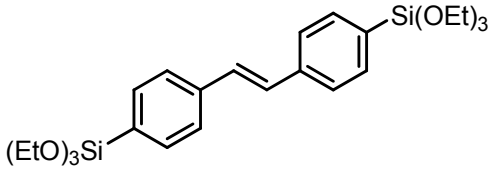

BTETS (1)

Figure 2.3 4,4'-Bis(triethoxysilyl)*trans*-stilbene, BTETS (**1**)

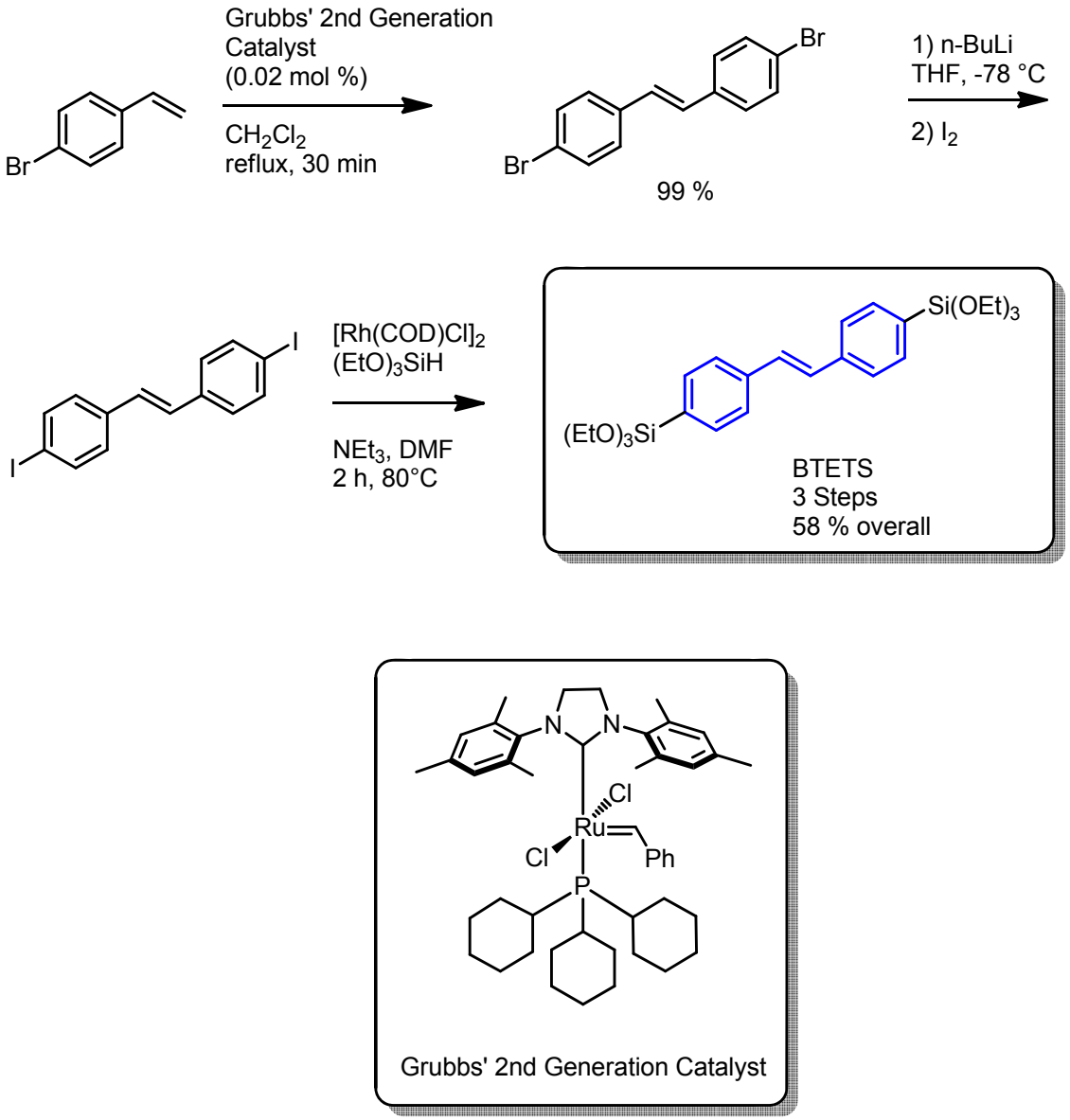

Scheme 2.1 Synthesis of 4,4'-bis(triethoxysilyl)*trans*-stilbene, BTETS (**1**).

For the more synthetically challenging *cis* isomer (**2**), a Wittig-based route was chosen. Thus 4-bromobenzylbromide was reacted with triphenylphosphine to make the phosphonium bromide salt. A lithium-free Wittig reagent was prepared by reaction between by deprotonation of this salt with KOH.[9,10] Treatment with 4-bromobenzaldehyde affords 4,4'-dibromo-*cis*-stilbene in 72%

yield with 80% stereochemical control. Following halogen exchange, the siloxane units were installed using the chemistry of Masuda *et al.* as described above (Scheme 2.2).

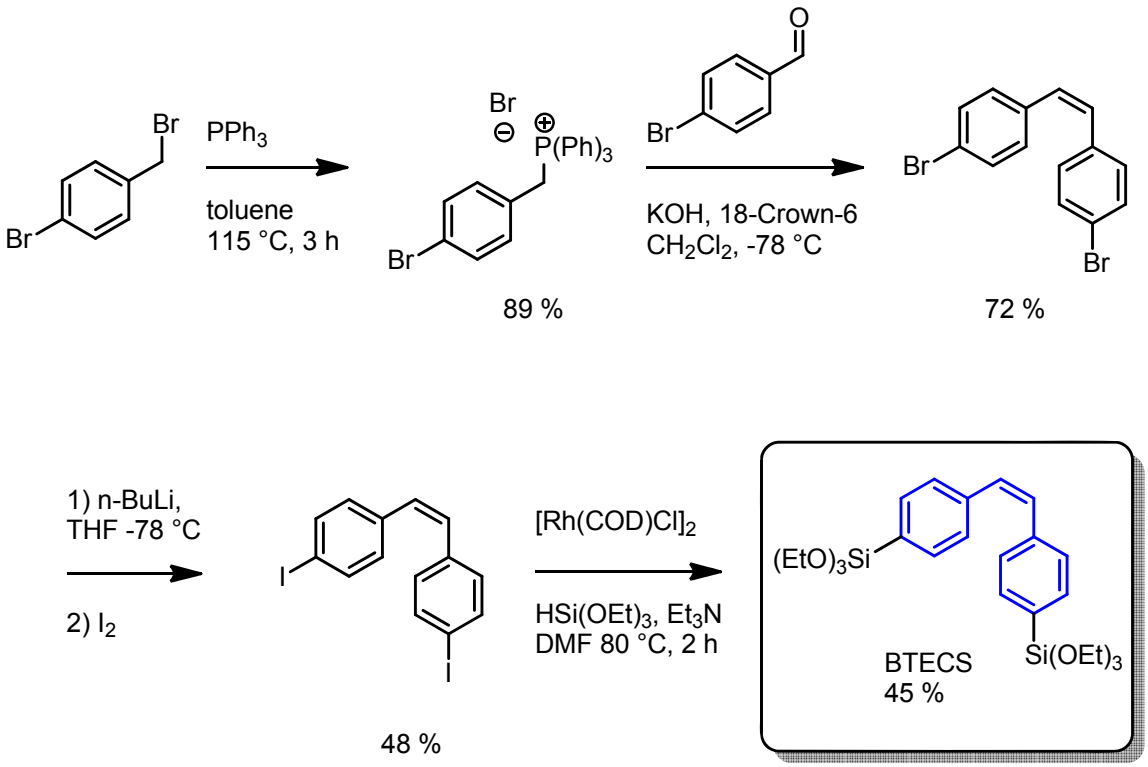

Scheme 2.2 Synthesis of 4,4'-bis(triethoxysilyl)*cis*-stilbene, BTECS (**2**).

It should be noted that these molecules are notoriously problematic when silica gel column chromatography is applied for the purification as significant amounts of product can react with the stationary phase. Distillation is often used when possible. In our case, distillation was not an option due to high molecular weight so we resorted to silica gel chromatography which resulted in decent yields of the final products.

2.2.2 Material preparation and characterization

Following the synthesis of the desired precursors, PMO materials were prepared. Our goal was to prepare a material that contained a functional monomer which could be used in further transformations of the material along with a structural monomer which would impart strength and mesophase retention to the material. We chose to use 15 % of the functional monomer as a starting point, so as to have a large enough quantity of functionality without sacrificing the well-ordered mesoporous character of the material. This was accomplished by mixing the newly synthesized functional monomer (**1** or **2**) with either 1,4-bis(triethoxysilyl)benzene (BTEB) (**3**) or 4,4'-bis(triethoxysilyl)biphenyl (BTEBP) (**4**) as the structural component, in the presence of a structure directing template (small or large pore-producing) under acidic or basic conditions (Figure 2.4). Throughout the chapter, materials are named to indicate the two monomers that were involved in the synthesis and the relative pH that was employed. For example, **"PMO-1/3^{H+}"** is used to denote a PMO made from 15 mol % functional monomer **1** and 85 mol % structural monomer **3**, under acidic conditions. In some cases where we varied the amount of functional monomer used, the mol % will be indicated in brackets after the monomer, for example **PMO-1(30%)/4^{H+}**, contains 30 mol % monomer **1** and 70 mol % monomer **4**. Finally, materials made of pure monomers will include the surfactant in the notation for more description or to avoid ambiguity, for example **PMO-Brij76-4^{H+}**.

In general, PMOs are formed at room or slightly elevated temperatures over extended times (~1 day) in closed vials so as to form a highly condensed,

organosiloxane network around the surfactant template. The precipitated as-synthesized (still containing surfactant) materials are isolated by filtration (or sometimes centrifugation) from the reaction vial and the porous templating agent is extracted with solvent. The detailed experimental procedures for each material can be found in the Experimental chapter.

For our materials, we chose to follow and compare several well-established procedures for producing mesoporous materials.[11-13] The general synthetic conditions for PMOs containing a 15: 85 mole ratio of functional monomer: structural monomer are given in Table 2.1, with all molar ratios of reagents indicated below. The aromatic structural monomers were chosen so that the resulting functional materials would benefit from their desirable properties, namely the thermal stability of the crystal-like walls and their ability to form a well-ordered, mesoporous network.

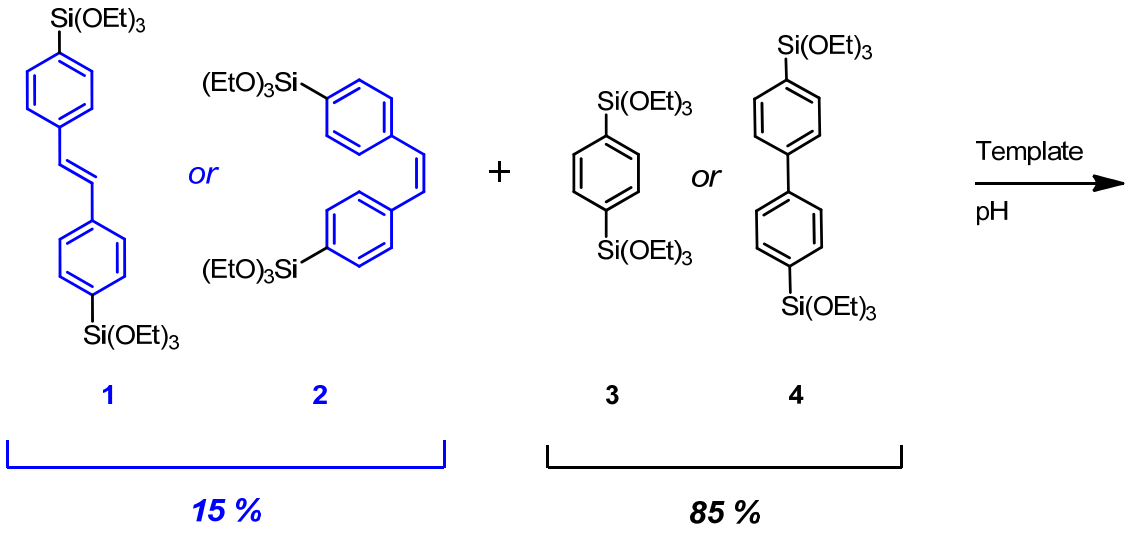

Figure 2.4 PMO synthetic scheme. (**1**) BTETB; (**2**) BTECS; (**3**) BTEB; (**4**) BTEBP

Table 2.1 Synthetic conditions for PMOs using 15 % stilbene functional monomer (**1** or **2**) and 85 % structural monomer (**3** or **4**).

Material	Functional Monomer	Structural Monomer	Template	pH
PMO-1/4^{H+}	**1**	**4**	Brij 76	Acidic
PMO-1/4^{OH-}	**1**	**4**	C_{18}TMACl	Basic
PMO-2/4^{H+}	**2**	**4**	Brij 76	Acidic
PMO-1/3^{H+}	**1**	**3**	P123	Acidic

Molar ratios: **PMO-1/4^{H+}** (BTEBP: BTETS: Brij 76: H_2O: HCl: NaCl) (0.85: 0.15: 0.534: 601: 8.05: 19.0)[11]; **PMO-1/4^{OH-}** (BTEBP: BTETS: C_{18}TAMCl: H_2O: NaOH) (0.85: 0.15: 1.28: 1320: 12100)[12]; **PMO-2/4^{H+}** (BTEBP: BTECS: Brij 76: H_2O: HCl: NaCl) (0.85: 0.15: 0.534: 601: 8.05: 19.0)[11]; **PMO-1/3^{H+}** (BTEB: BTETS: P123: HCl: H_2O) (0.85: 0.15: 0.068: 0.944: 800)[13].

2.2.3 Characterization of textural properties

Following isolation, the textural properties of the functional materials are characterized by nitrogen physisorption. The adsorption and desorption isotherms are shown in Figure 2.5 with textural properties of the materials listed in Table 2.2.

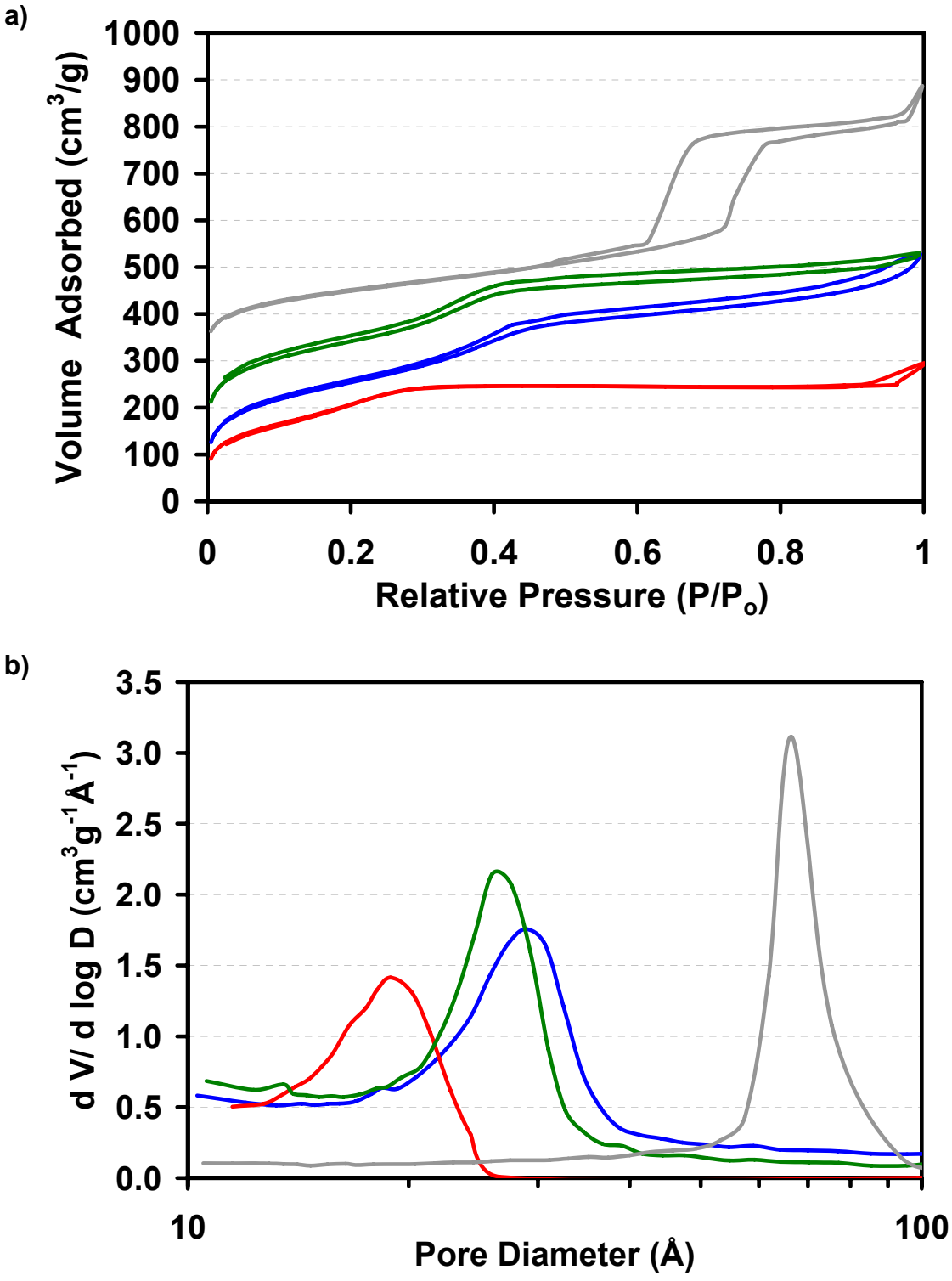

Figure 2.5 (a) N_2 adsorption-desorption isotherms and (b) BJH adsorption pore size distribution curves of PMOs. **PMO-1/4^{H+}**-blue, **PMO-1/4^{OH-}**-red, **PMO-2/4^{H+}**-green, **PMO-1/3^{H+}**-grey. Note: **PMO-2/4^{H+}** -green and **PMO-1/3^{H+}** -grey are raised on the y-axis of a) by 75 and 300 cm^3g^{-1} respectively for clarity.

Table 2.2 Textural properties of prepared PMOs.

Material	Surfactant	BET Surface Area (m^2g^{-1})	Pore Diameter[a] (Å)	Pore Volume[b] (cm^3g^{-1})
PMO-1/4^{H+}	Brij 76	914	28.9	0.75
PMO-1/4^{OH-}	C_{18}TMACl	774	18.9	0.31
PMO-2/4^{H+}	Brij 76	952	26.0	0.65
PMO-1/3^{H+}	P123	553	73.9	0.85

[a] Maximum value of BJH pore diameter distribution (adsorption branch).
[b] BJH cumulative pore volume of pores between 10 and 3000 Å.

As we can see from the data of Table 2.2, the resultant textural properties and pore characteristics of the PMOs are highly dependent on the surfactant and conditions used. **PMO-1/4^{H+}** has high surface area (914 m^2/g) and large pore volume (0.75 cm^3/g), as is commonly observed in PMOs made under these conditions.[14,15] For comparison a PMO made using these conditions with only the biphenyl-bridged structural monomer **4** (**PMO-Brij76-4^{H+}**) had similar properties (BET surface area of 843 m^2/g, pore diameter of 27.3 Å, and pore volume of 0.68 cm^3/g), which indicates that the functional monomer is not greatly affecting the textural properties in this case. Likewise, in **PMO-2/4^{H+}** which uses the *cis* isomer **2** as the functional monomer, the properties are quite similar to those observed for the *trans* isomer with only slightly smaller pore diameters and pore volume. In contrast, **PMO-1/4^{OH-}** with lower surface area and smaller pore diameters resulted from the alkylammonium C_{18}TMACl surfactant under basic conditions. Pore sizes for the alkyl ammonium surfactants are generally smaller than for the Brij surfactants due to a smaller micelle size. Under these conditions, Inagaki's group reported a purely biphenyl-bridged material from **4,** with BET surface area

of 869 m²/g and pore diameters of 35.4 Å,[12] however this was calculated using a density functional theory (DFT) method[16] not the BJH model which is known to underestimate the pore diameter.[17] Our reproduction of this purely biphenyl-bridged material (**PMO-C_{18}TMACl-4^{OH-}**) gave a PMO with BET surface area of 796 m²/g, pore diameters of 20.8 Å and a BJH pore volume of 0.48 cm³/g, which is very much in line with the results for **PMO-1/4^{OH-}** containing 15 % functional *trans*-stilbene monomer. **PMO-1/3^{H+}** uses a phenylene-bridged structural monomer **3** and 15 % **1** with P123 as a surfactant. The main difference in this material is in the larger pore diameter of 73.9 Å. The BET surface area is slightly lower than the other materials and is much lower than a PMO from pure **3** reported by Inagaki (1029 m²/g).[13] Our attempts at a PMO of only structural monomer **3** (**PMO-P123-3^{H+}**) gave a BET surface area of 523 m²/g. It is encouraging that the functional monomer at 15 % incorporation does not appear to be negatively affecting the textural properties of the PMOs to any large degree.

The BET surface areas obtained from the Brij 76 [$C_{18}(EO)_{10}$] and P123 ($EO_{20}PO_{70}EO_{20}$) surfactant can be partly attributed to area within smaller micropores. The microporous surface areas of **PMO-1/4^{H+}** and **PMO-2/4^{H+}** are 100 and 142 m²/g respectively and that of **PMO-1/3^{H+}** is 45 m²/g. It is believed for these types of surfactants, the polyethylene oxide chains can penetrate into the silica walls resulting in mesopores interconnected by micropores.[18,19] This interconnectivity is more abundant at higher synthetic temperatures as the polyethylene oxide chains become dehydrated and thus mix with the hydrophobic

polyethylene chains to a larger extent. As the Brij 76 templated materials are prepared starting at 60 ºC and the P123 material is made with a starting temperature of 0 ºC, this could explain the reason for lower microporous surface areas in **PMO-1/3^{H+}**. Nitrogen physisorption analysis did not reveal any microporous area from **PMO-1/4^{OH-}**.

From these results, it is shown it can be possible to produce functional materials of a desired pore diameter with judicious choice of surfactant (and perhaps co-solvent or swelling agent which was not studied here). For example, mesoporous organosilica can be used as a host for such guest molecules as drugs, thus one will need to choose a surfactant that will produce pores large enough to host these molecules.

2.2.4 TEM

To confirm the presence of the regular porosity, TEM images were taken of the materials as seen in Figure 2.6. The insets of (a) and (b) are close ups, while those of (c) and (d) are electron diffraction patterns. **PMO-1/4^{H+}** (a), and **PMO-1/4^{OH-}** (b), appear to have less ordered, mesoporosity, resembling more of a wormhole type mesostructure. The appearance of regular porosity in **PMO-2/4^{H+}** (c), and **PMO-1/3^{H+}** (d), indicates a successful surfactant template assembly process in these materials.

In agreement with the physisorption results, the pore diameters of d) are larger than the others (estimated at 7 nm from the image) and the most highly ordered. The walls of the pores appear to be between 4 and 5 nm in thickness.

The porous order may also be due in part to the use of the phenylene-bridged precursor **3** as the structural monomer which is known to give well ordered 2D-hexagonal ordered materials under these conditions.[13] Interestingly, it appears that the *cis* isomer **2** gave slightly better ordered materials than the *trans* isomer **1**, under the same conditions (a *versus* c). It should be kept in mind that although representative images were targeted, TEM images represent only small areas of the bulk material. Furthermore, the order can be more quantitatively assessed from the width of diffraction peaks of PXRD patterns.

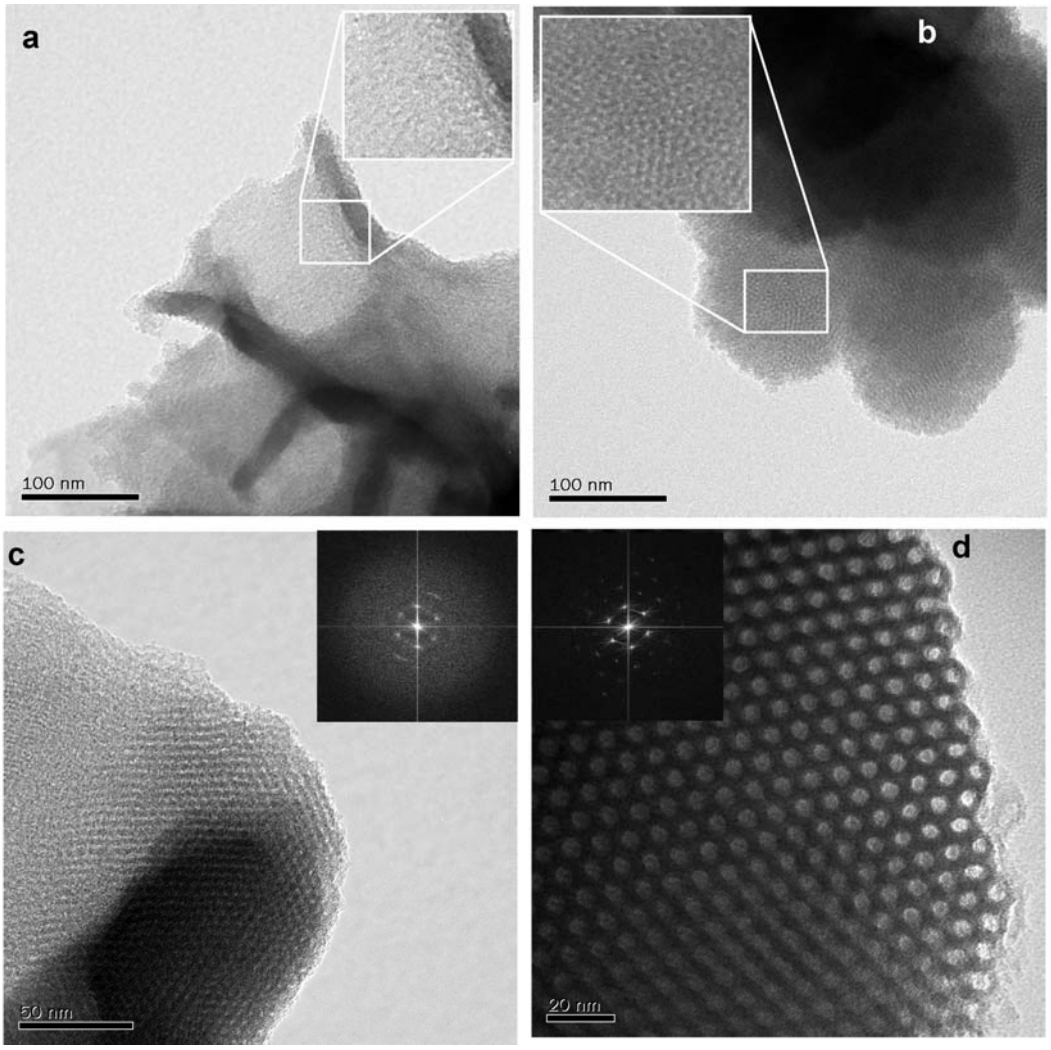

Figure 2.6. TEM images of (a) **PMO-1/4^{H+}** (b) **PMO-1/4^{OH-}** (c) **PMO-2/4^{H+}** (d) **PMO-1/3^{H+}**. Insets of (a) and (b) show close up of pore structure and (c) and (d) are electron diffraction patterns.

2.2.5 Solid state NMR

As each of the above materials were mesoporous, we chose to examine **PMO-1/3^{H+}**, since it had the largest and highest ordered pores as judged by the physisorption analysis and TEM. The isotherm of this material had the most obvious capillary condensation, which could be used later on to gauge the effect of functionalization upon structural order. The following characterizations pertain to **PMO-1/3^{H+}** (unless otherwise noted) and are not generally applicable to the other three materials from Table 2.1.

In order to confirm the presence of both monomers in the material, solid state NMR was acquired. The CP MAS ^{13}C NMR of **PMO-1/3^{H+}** is shown in Figure 2.7. The major peak is of the aromatic carbons of the major phenylene-bridged component at 135 ppm. Unfortunately, given the broadness of the solid state NMR technique, peaks are often overlapping and it is difficult to obtain well-resolved spectra. Fortunately, a peak from the stilbene fragment at 127 ppm is removed enough from the other aromatic peaks so as to indicate the presence of the functional monomer. The asterisks indicate spinning side bands.

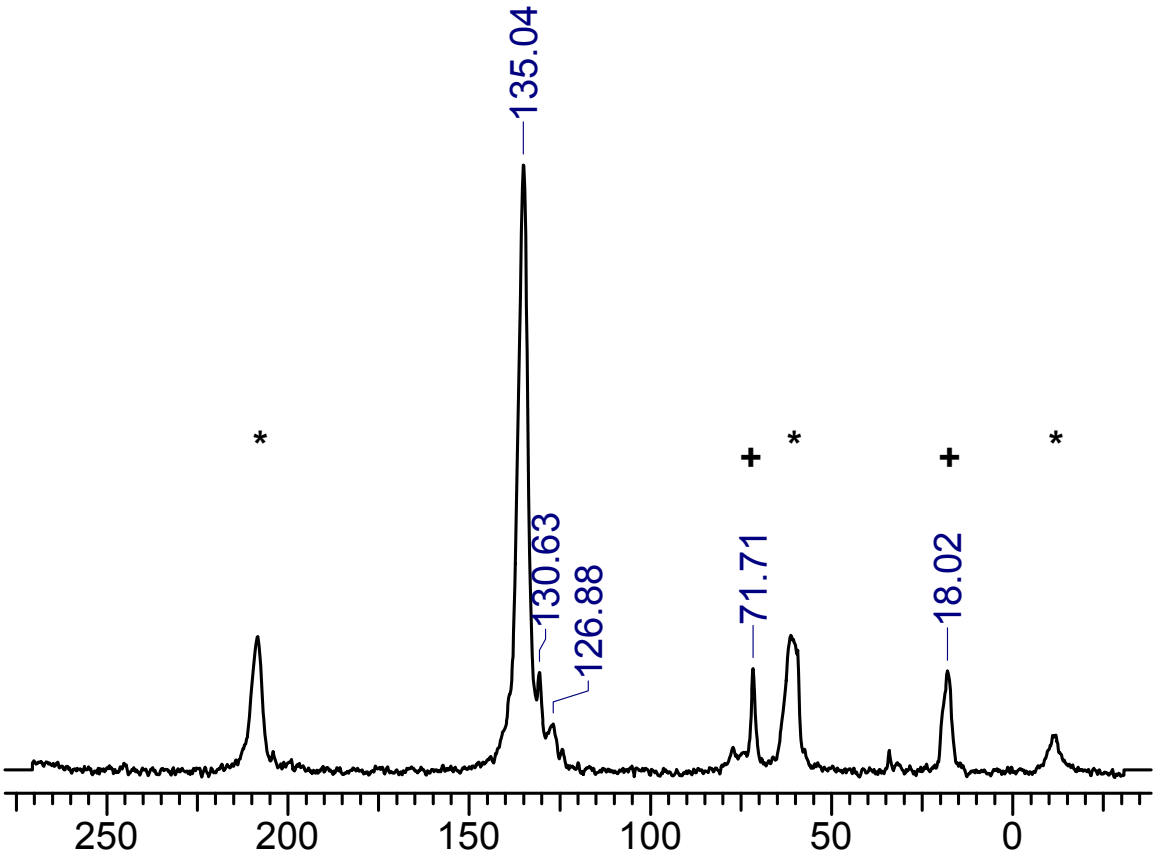

Figure 2.7 CP MAS ^{13}C NMR (11 050 Hz) of **PMO-1/3^{H+}**. The peak from **3** is seen at 135 ppm and the peaks from **1** are seen overlapping with **3** from 127 to 142 ppm. Symbols "*****" and "**+**" denote spinning side bands and residual P123 surfactant respectively.

The ^{21}Si CP MAS NMR holds important information about the condensed material. While cross-polarization (CP) MAS NMR is not quantitative, it has been shown in the case where no protons are in the vicinity of the studied nuclei, that single pulse experiments do not differ significantly from CP MAS experiments with respect to the relative peak intensities of the spectra.[20,21] The extent of hydrolysis and condensation is important to the overall structural strength of the material and can be judged from the relative intensities of the peaks in the ^{29}Si

CP MAS NMR. These peaks are described according to the General Electric Q notation, where monofunctional silicon is designated by M, a difunctional silicon by D, a trifunctional silicon by T and a quadrafunctional silicon by Q, where functionality here refers to the number of reactive, hydrolysable groups.[22] A subscript will further indicate the number of functional groups hydrolyzed to silanols while a superscript will indicate the number of siloxane linkages. Since silanols and siloxy groups cannot be resolved in ^{29}Si CP MAS, the subscript is omitted (Figure 2.8).[23]

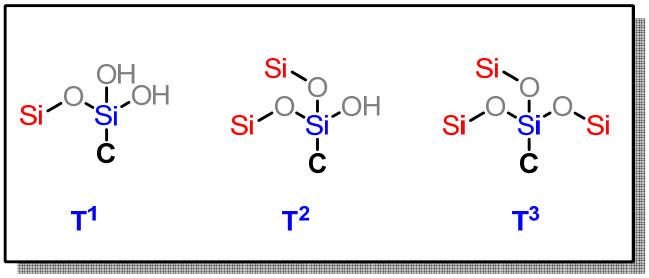

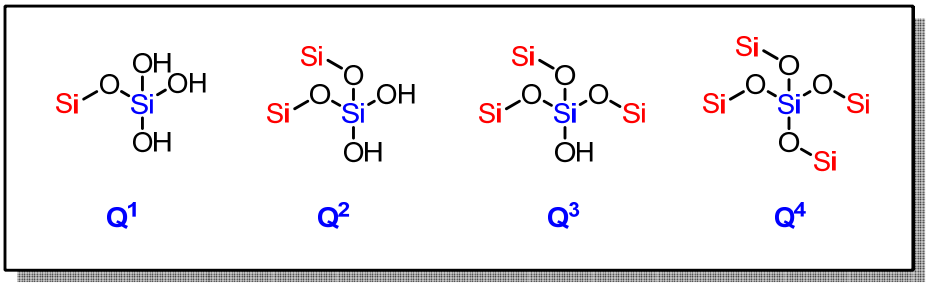

Figure 2.8 ^{29}Si NMR notation for trifunctional (T) and quadrafunctional (Q) sites for silicon NMR. Note that H can also be R.

For the silica sources used here, T peaks are found from approximately -60 to -80 ppm with more siloxane bonds causing an upfield shift. As seen from Figure 2.9, **PMO-1/3^{H+}** contains T^1, T^2 and T^3 silicon sites, with the majority being T^2 type. This confirms the full framework linkage of the organic groups and

means that most silicon atoms have one free hydroxy (or possibly ethoxy) group. This is quite typical of materials prepared under these acidic conditions.[13] What is also very important to note in this spectrum is the lack of Q sites. These Q sites are further upfield (-90 to -100 ppm) than T sites.[24] Since no silica sources of Q type were added, the presence of Q sites would indicate undesired Si-C bond cleavage. The absence of Q sites further supports the intact nature of the organic bridging groups.

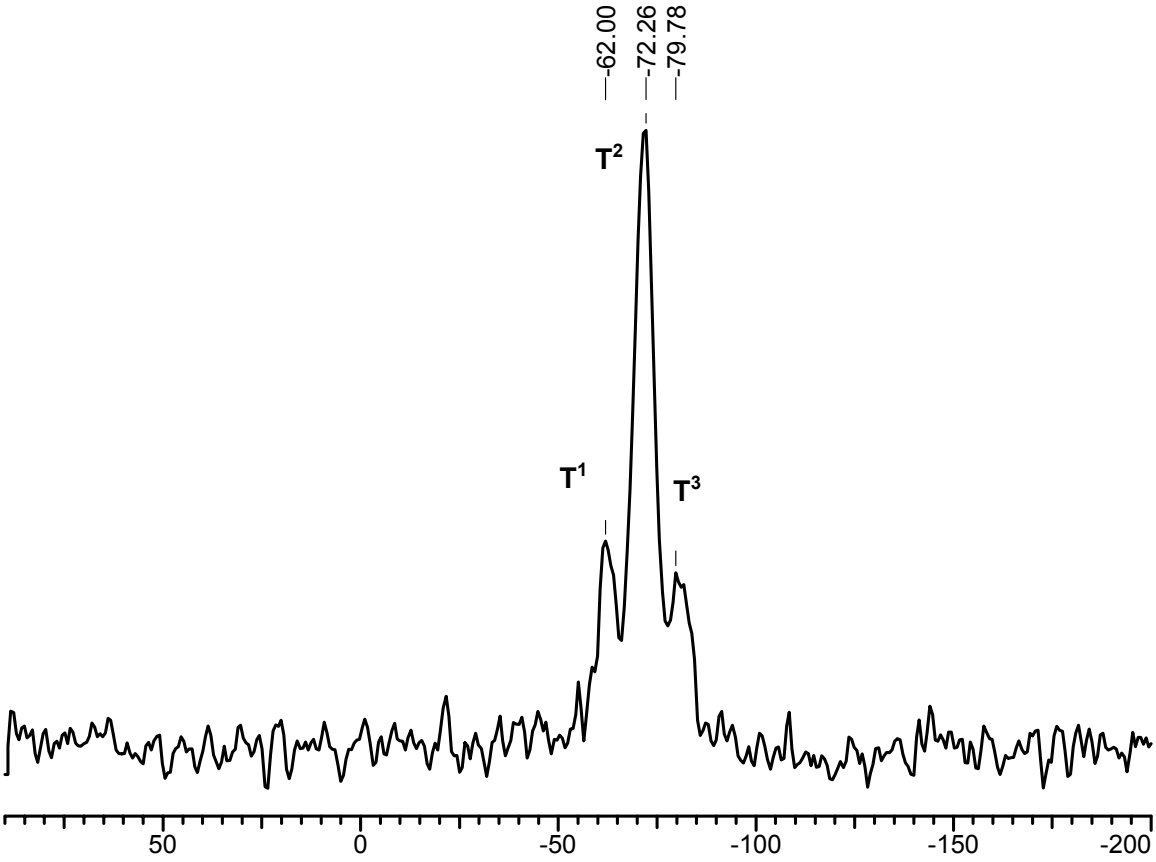

Figure 2.9 CP MAS ^{29}Si NMR of **PMO-1/3^{H+}**.

In contrast to **PMO-1/3^{H+}**, made under acidic conditions, **PMO-1/4^{OH-}**, prepared under basic pH, shows a higher proportion of T^3 linkages in the CP MAS ^{29}Si NMR, indicating a higher degree of condensation and cross linking

(Figure 2.10). This is typical when comparing CP MAS ^{29}Si NMR spectra of PMOs made under these two conditions. Higher pH is known to promote siloxane condensation, while acidic conditions favour hydrolysis of siloxanes. There are also no visible peaks from Q sites in the spectrum of **PMO-1/4^{OH-}**.

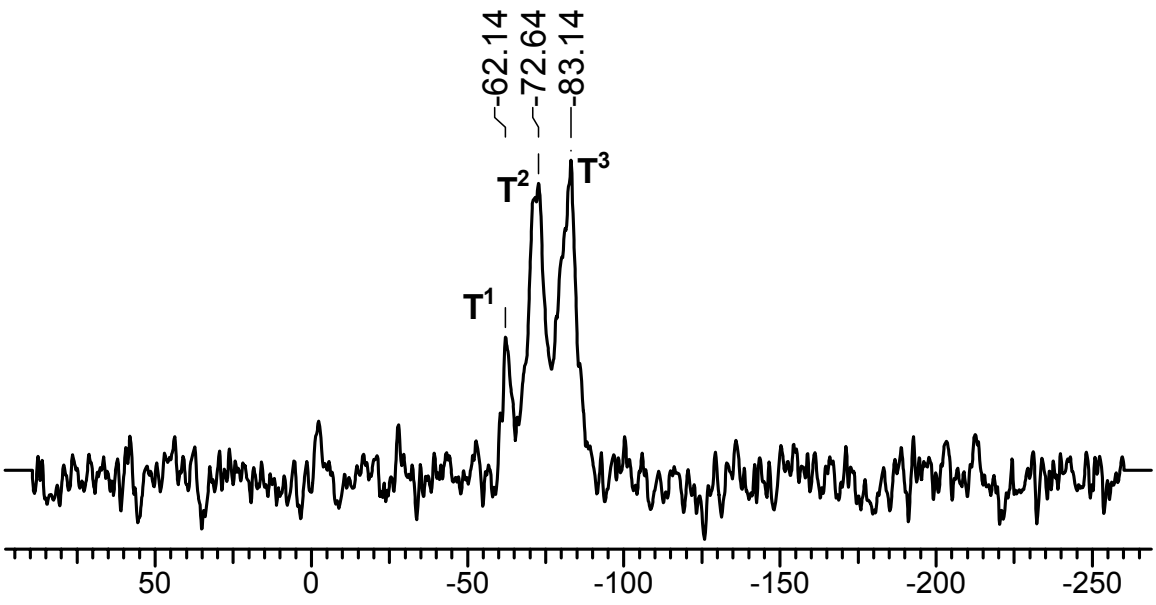

Figure 2.10 CP MAS ^{29}Si NMR of **PMO-1/4^{OH-}**.

2.2.6 SEM-Brij 76 particles

With conventional syntheses of PMOs, amorphous powders are generally obtained with no specific shape and non-uniform size. However, many applications benefit from having a controlled morphology. For example, uniform spheres of about 10 μm in diameter are advantageous for chromatographic applications, whereas a uniform film thickness might be desirable in a coating application.

The few studies on controlled PMO morphology in the literature point at the symmetry of the micellar shape leading to the overall particle shape.[25] Inagaki described well-defined external morphologies of rod-like particles with a hexagonal cross-section for materials of 2D-hexagonal order, and spherical particles of 3D-hexagonal order in his initial study of ethane-bridged PMOs.[26] The particle shapes arise from the micelle shapes defined by the liquid-crystalline phase of the surfactant under the specific synthetic conditions.

Kapoor and Inagaki have also reported spherical organosilica using phenylene-bridged monomer **3** under ammonia solution with alkylammonium surfactants. They observed 0.6-1.0 μm spherical particles with increasing monodispersity as the length of the alkyl chain was reduced from 18 to 12 carbons.[27]

With the novel *cis* and *trans* isomers of the stilbene precursors **1** and **2** now available, we were interested in determining what potential influences each isomer would have on the morphology of the PMO particles. Our initial comparison for this purpose was between the *cis* and *trans* materials prepared under identical conditions, **PMO-1/4^{H+}** and **PMO-2/4^{H+}** which use Brij 76 as a structure directing agent. The powders were gold-coated before being imaged by high resolution field-emission SEM at various magnifications (Figure 2.11 and Figure 2.12).

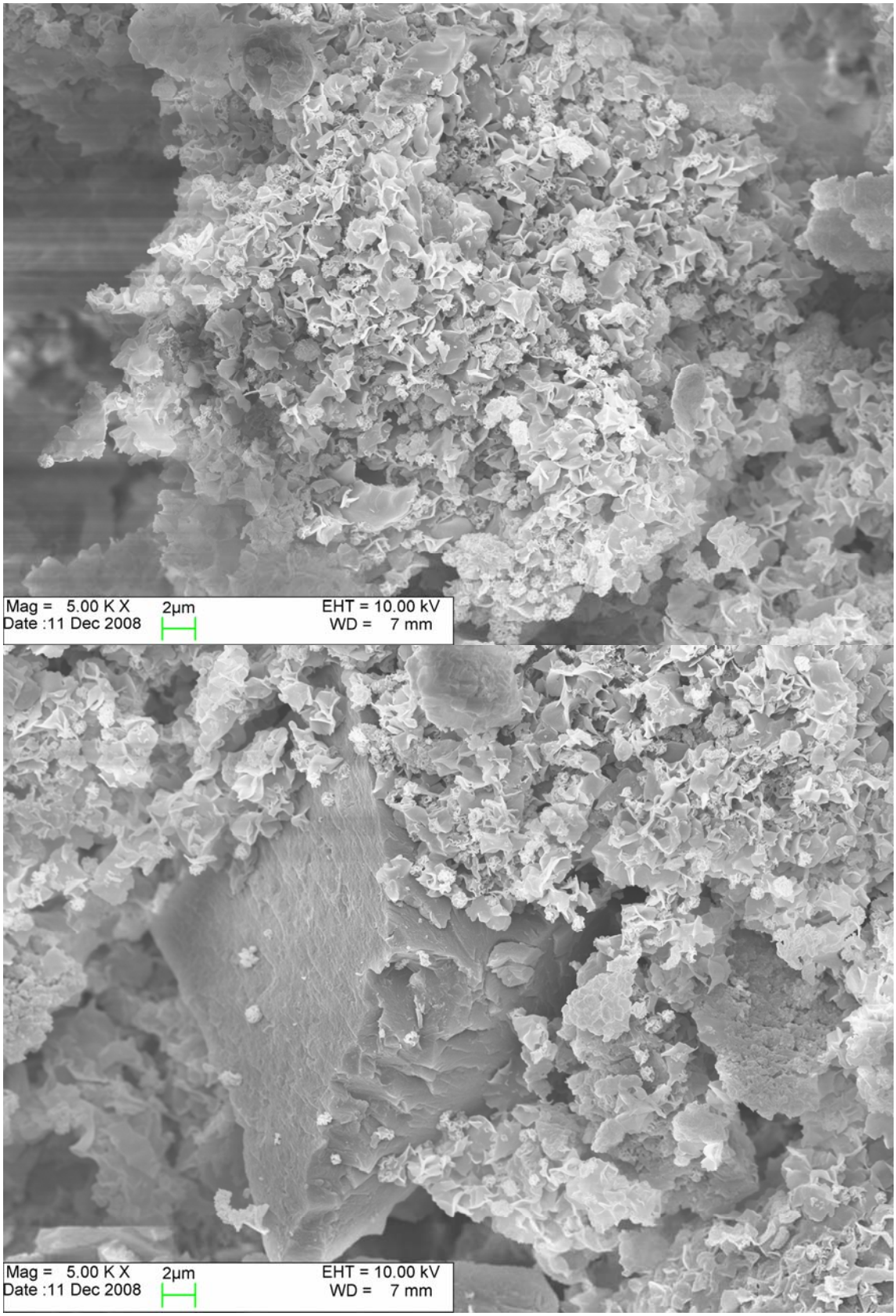

Figure 2.11 HRSEM images of *trans*-stilbene-bridged **PMO-1/4^{H+}**.

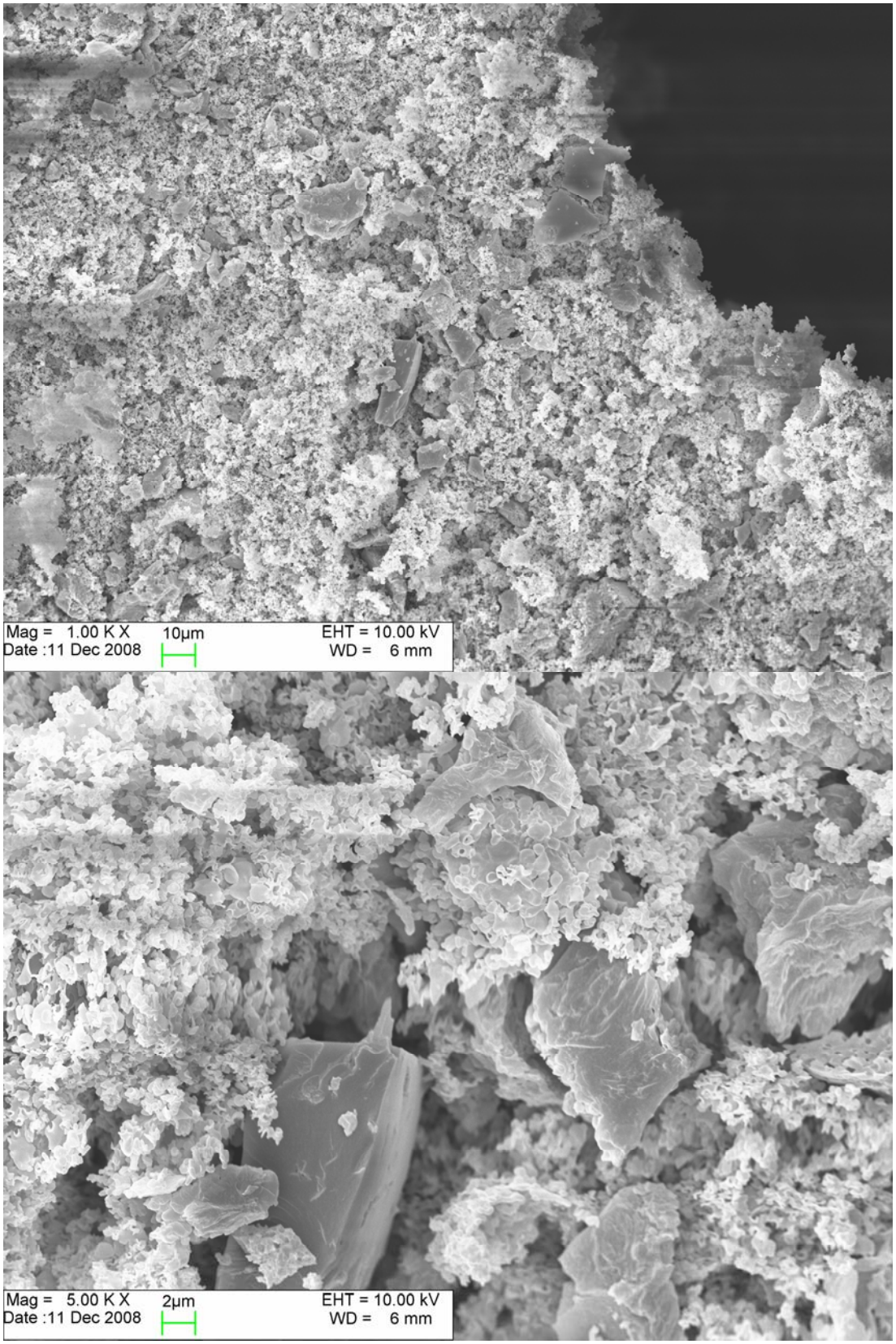

Figure 2.12 HRSEM images of *cis*-stilbene-bridged **PMO-2/4**$^{H+}$.

Unfortunately, there are no obvious differences between the materials made with the *cis* and *trans* precursors based on the SEM images above. Both materials appear to have random particle sizes and shapes. Mixed with the highly curved particles, there are also larger monolithic particles present. It was possible these monolithic particles could represent functional stilbene monomer **1** or **2** that had condensed mostly with itself (homocondensation) however, even in **PMO-Brij76-4^{H+}**, without the presence of any functional monomer, the SEM images still show that monolithic particles are present (arrows, Figure 2.13).

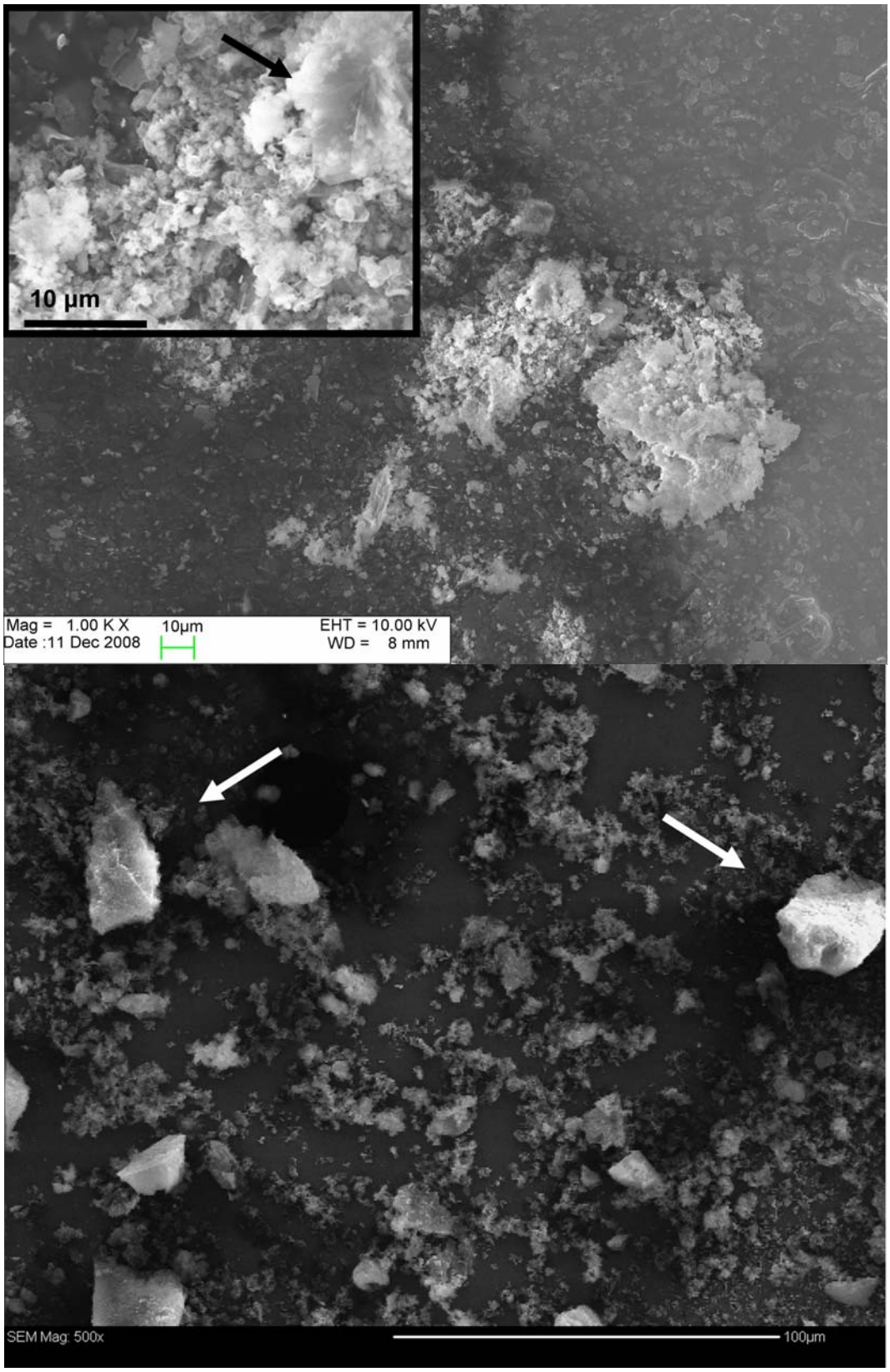

Figure 2.13 (Top) HRSEM and (bottom) SEM images of **PMO-Brij76-4^{H+}**. Arrows are indicating monolithic particles.

Materials were prepared at even higher loadings of **1** and **2**, using the same conditions as the 15 % stilbene-bridged PMOs (Brij 76 surfactant under acidic conditions), to see if a particular morphology would begin to emerge. **PMO-1(20%)/4^{H+}**, and **PMO-1(30%)/4^{H+}** incorporating 20 % and 30 % of *trans* monomer **1** respectively, as well as **PMO-2(30%)/4^{H+}** and **PMO-Brij76-2^{H+}** incorporating 30 % and 100 % of *cis* monomer **2** respectively, were prepared and imaged by SEM (Figure 2.14-Figure 2.17).

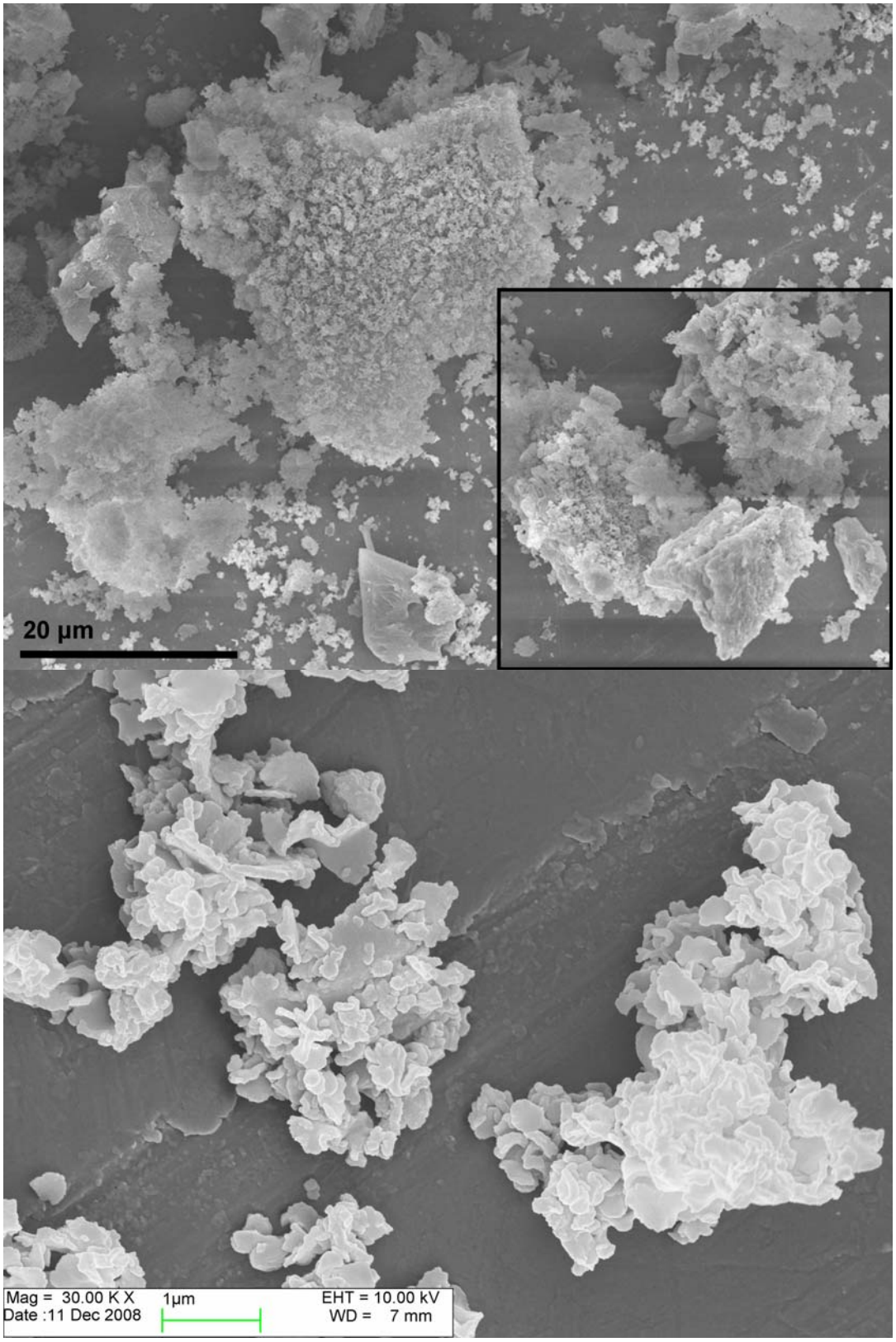

Figure 2.14 HRSEM images of **PMO-1(20%)/4^{H+}**.

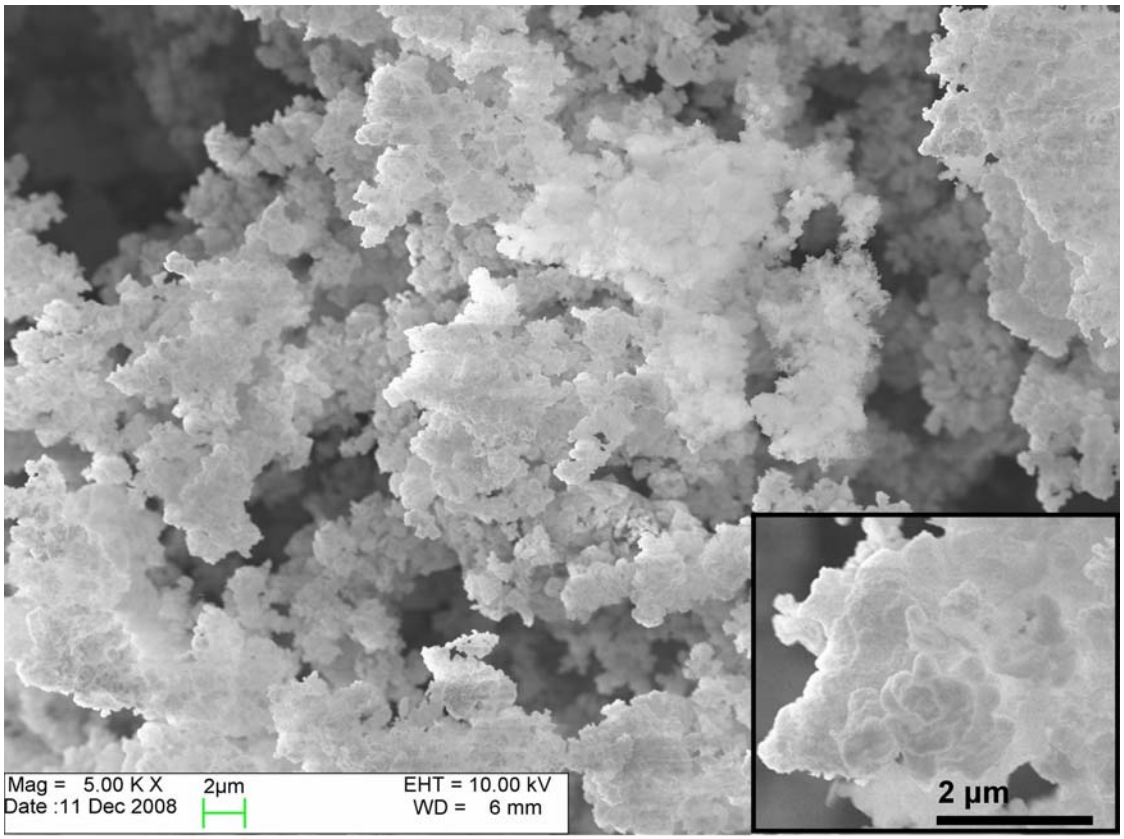

Figure 2.15 HRSEM images of **PMO-1(30%)/4^{H+}**.

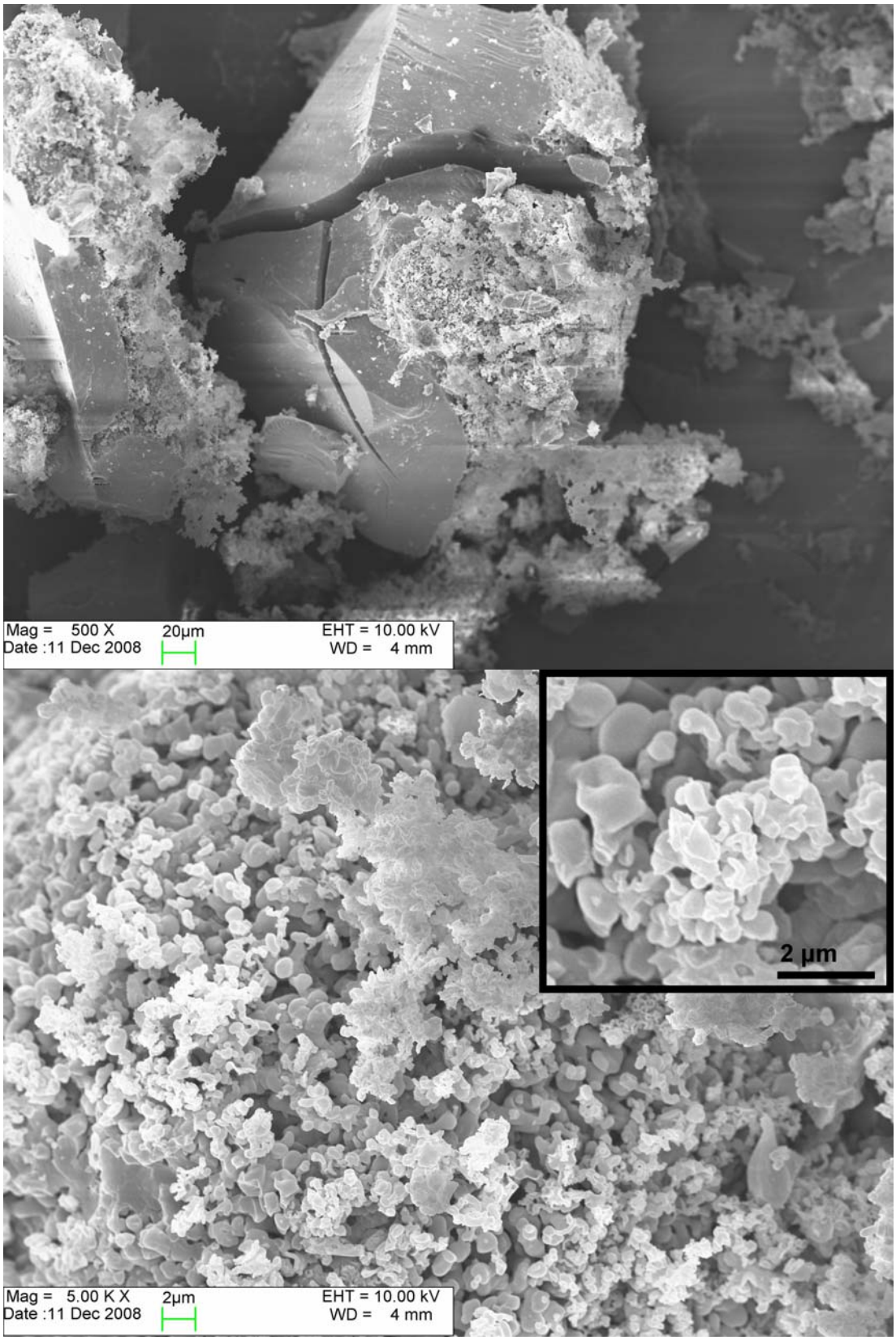

Figure 2.16 HRSEM images of **PMO-2(30%)/4^{H+}**.

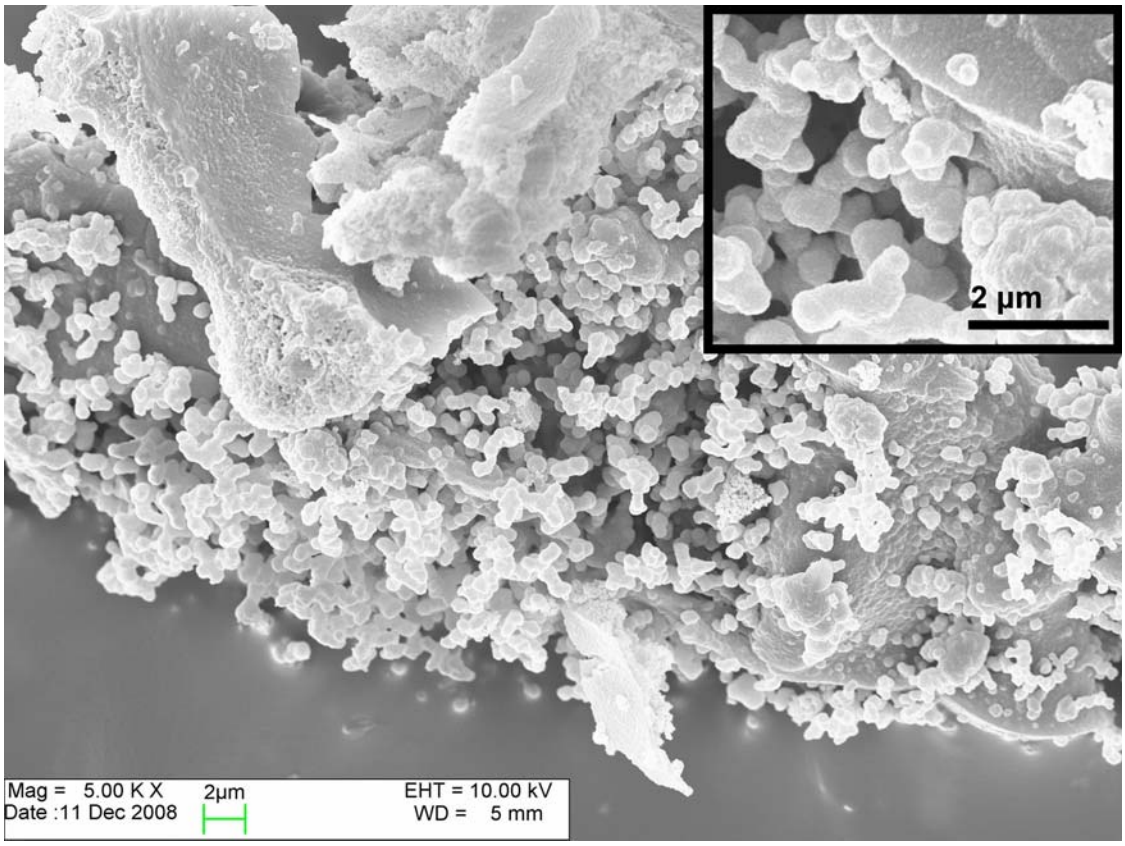

Figure 2.17 HRSEM images of **PMO-Brij76-2^{H+}**.

There were no apparent trends that appeared in the morphology of the materials as the proportion of stilbene monomer was increased. All materials consisted of a mixture of larger, monolithic particles and smaller, agglomerated particles having a rounded, almost spherical shape. Interestingly, **PMO-2(30%)/4^{H+}** displayed a Type IV nitrogen sorption isotherm, indicating the presence of mesopores (pore diameters of 23.3 Å) and had a BET surface area of 880 m²/g at 30 % functional monomer loading. Although the 100 % *cis*-stilbene-bridged functional monomer **PMO-Brij76-2^{H+}** was determined to be microporous by nitrogen sorption porosimetry (the "PMO" notation kept for simplicity), it did exhibit a significant surface area of 583 m²/g.

2.2.7 SEM-C_{18}TMACl particles

We also imaged **PMO-1/4^{OH-}** made from the trialkalkylammonium C_{18}TMACl surfactant using 15 % *trans*-stilbene-bridged monomer **1** and biphenyl-bridged monomer **4**. The particles mostly consisted of small (< 0.5 μm) spherical particles agglomerated together (Figure 2.18). Again, increasing the amount of **1** in the materials to 20 and 30 % (**PMO-1(20%)/4^{OH-}** and **PMO-1(30%)/4^{OH-}** respectively) resulted in PMOs of nearly identical morphology. It should be noted that the *trans*-stilbene monomer **1** was determined to be incorporated into the PMOs at increasing proportions by monitoring the C=C_{ST} of at 1636 cm^{-1} in the Raman spectra (Figure 2.21). Although these spherical particles appear more monodisperse in diameter than those from Brij 76 (above), they are approximately 1 order of magnitude too small to be useful for chromatographic applications.

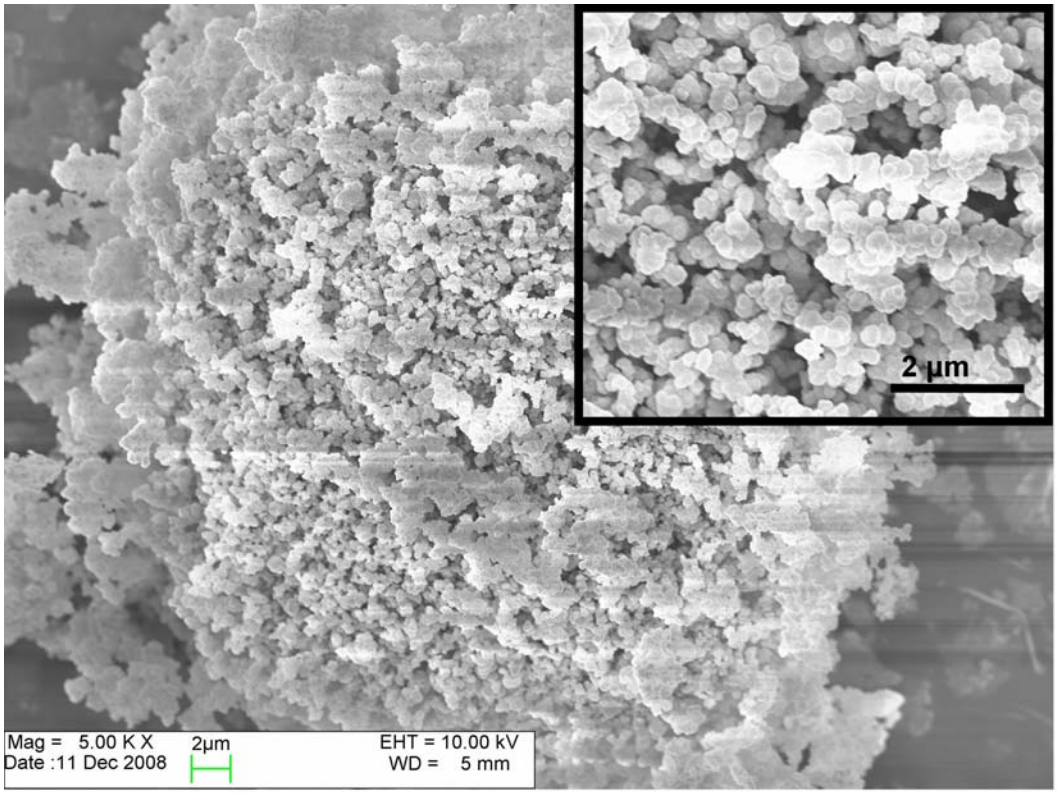

Figure 2.18 HRSEM image of **PMO-1/4^{OH-}**.

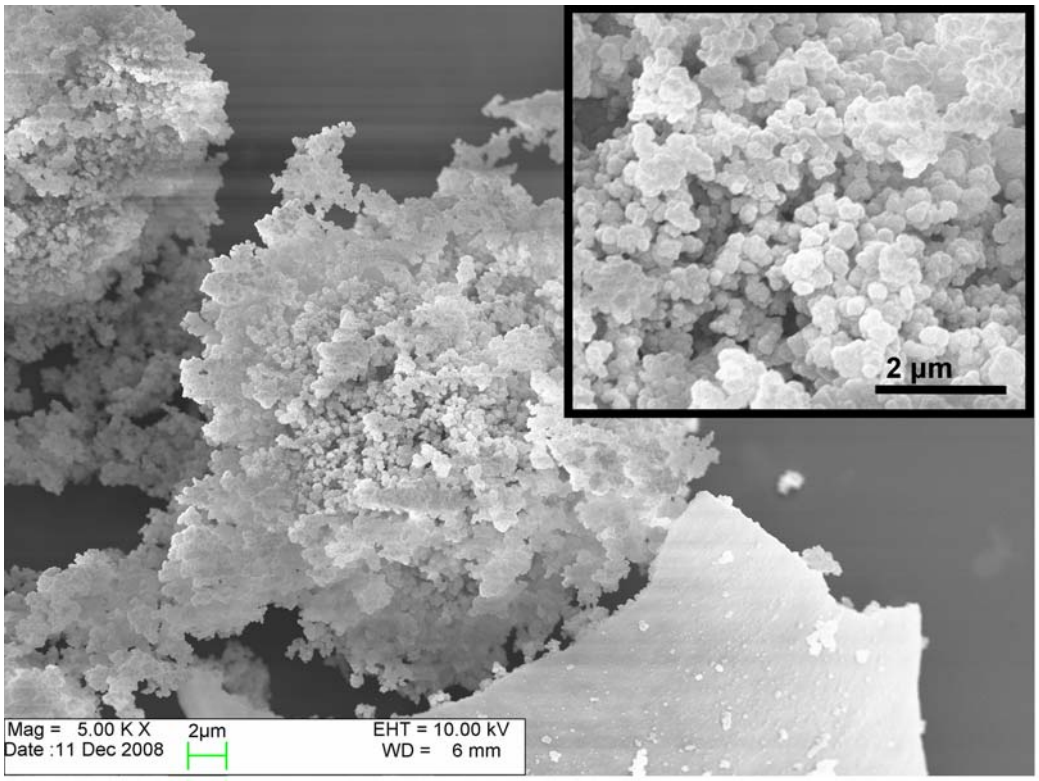

Figure 2.19 HRSEM of **PMO-1(20%)/4^{OH-}**

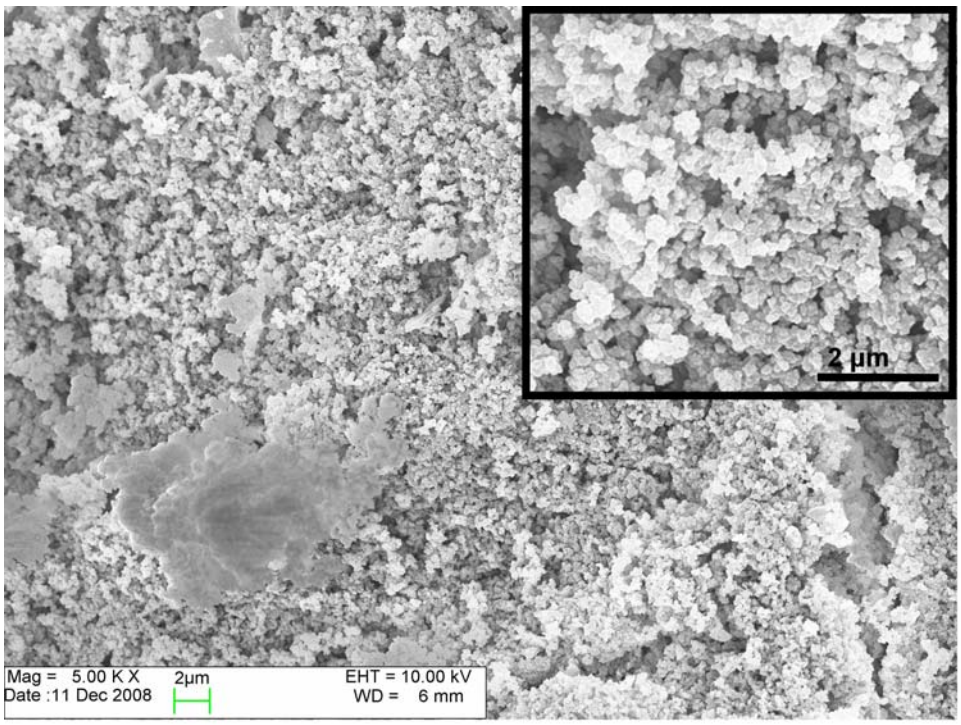

Figure 2.20 HRSEM of **PMO-1(30%)/4^{OH-}**.

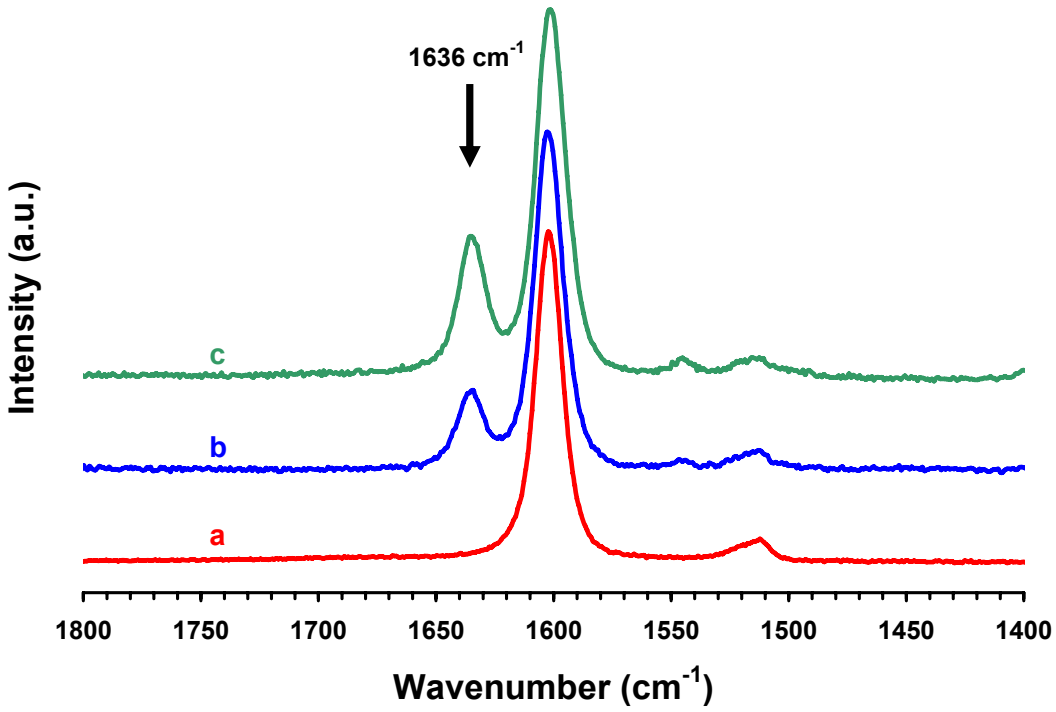

Figure 2.21 Raman spectroscopy of a) **PMO-C$_{18}$TMACl-4^{OH-}** b) **PMO-1(20%)/4^{OH-}** c) **PMO-1(30%)/4^{OH-}** showing increasing incorporation of **1** by growth of C=C$_{st}$ at 1636 cm^{-1}.

The morphology of stilbene-bridged silica particles under acidic conditions, using Brij 76 as surfactant does not appear to differ much between the *cis* and *trans* isomers. The common particle shape of the two isomers may simply reflect a common surfactant micelle shape. Under basic pH conditions, using structural monomer **4** and C_{18}TMACl as surfactant, agglomerations of tiny, spherical particles are visible. Although phenylene-bridged precursor **3** under similar conditions has given plate-like morphologies,[28] this spherical morphology has been observed in other systems involving ammonia[27] as well as some MCM-type preparations.[29] Further studies may benefit from particles imaged at earlier stages of the synthetic process to determine if there are any well-defined morphologies that nucleate, but grow into the spheres as observed by Sayari's group.[30]

2.2.8 Powder X-ray diffraction

The powder X-ray diffraction patterns of the PMOs give insight into the size of the mesopores and the extent of long range order. In addition, this technique has considerable value since it is a bulk technique as compared with microscopy. The peaks in an X-ray diffraction pattern are directly related to the atomic distances of repeating structures. Well ordered crystals give discrete patterns which are treated as a fingerprint of the material and can be matched with the help of a computer and database. Unlike zeolites as mentioned previously, organosilicas are generally characterized by amorphous silica walls. The peaks that are usually observed are at low angles of 2θ and represent the large-distance repeat units of the porous mesophase.

As can be seen from Figure 2.22, all materials have large reflections at low 2θ, indicating long range order is present. Materials (a) **PMO-1/4^{H+}** and (c) **PMO-2/4^{H+}** which are made under similar conditions using Brij 76 as surfactant, have one peak representing mesostructured materials. This single peak in combination with the SEM and TEM images suggest a disordered 'wormhole'[31] mesostructure is present, in agreement with the results of Ozin and coworkers using the same surfactant with 4-phenyl sulfide and 4-phenyl ether bridged monomers (Figure 2.23).[11] The position of the peaks for (a) **PMO-1/4^{H+}** and (c) **PMO-2/4^{H+}** correspond to *d* spacings of approximately 66.5 Å and 53.1 Å respectively. Pattern (d) is diagnostic of a 2D hexagonal pattern since the (100), (110), and (200) peaks indexed at *d* spacings of 100.3, 58.45, 50.87 Å respectively are all observed. The peaks of this pattern are much sharper than the others, representing a much higher ordering of the porous mesostructure. The unit cell dimensions (including pore and wall) of the hexagonal lattice for this material is a_o= 115.8 Å, calculated from $a_0 = \frac{2d_{100}}{\sqrt{3}}$, where d_{100} is the *d* spacing of the 100 plane. With pore sizes measuring 73.9 Å from physisorption analysis, this leaves a wall thickness of 41.9 Å which is in good agreement with the thickness estimated from the TEM image.

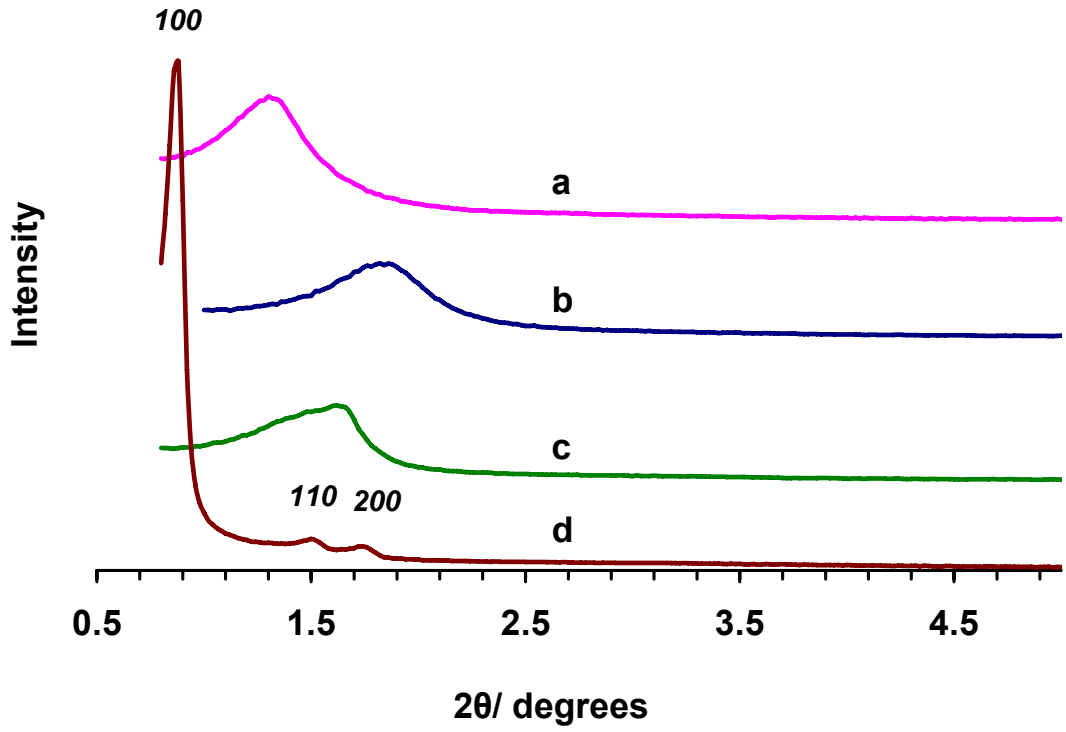

Figure 2.22 PXRD at low angles of (a) **PMO-1/4^{H+}** (b) **PMO-1/4^{OH-}** (c) **PMO-2/4^{H+}** (d) **PMO-1/3^{H+}** with 2D hexagonal reflections marked.

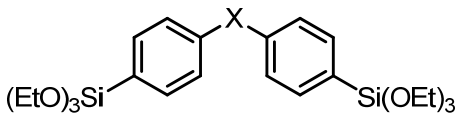

X= O or S

Figure 2.23 4-Phenyl ether and 4-phenyl sulfide-bridged monomers which gave rise to wormhole materials using Brij 76 as surfactant under acidic pH.[11]

Pattern (b) for **PMO-1/4^{OH-}** (Figure 2.24) has a low angle peak with a *d* spacing of 48.0 Å, indicating a mesoscopic order which is in agreement with that observed by Inagaki's group for a PMO from monomer **4**, templated with the same C_{18}TMACl surfactant.[12]

In addition to the low angle peak, the XRD profile also shows five medium angle (6 - 40 º *2θ*) reflections, indicative of molecular scale periodicity. The *d* spacings for these peaks are 11.9, 5.96, 3.96, 2.97 and 2.40 Å and also match closely those reported by Inagaki. This molecular scale ordering has been observed in biphenyl and other aromatic-bridged PMOs but only when prepared with trialkylammonium salts under alkaline pH.[28,32] These conditions are known to promote a more highly condensed siloxane network and can be shown by comparing relative T^3 peak areas in MAS ^{29}Si NMR spectra (compare Figure 2.9 and Figure 2.10). Alternating hydrophilic Si-O groups and hydrophobic biphenyl groups are proposed to arrange in a lamellar fashion within the pore walls as shown in Figure 2.25. The medium angle reflections observed here in pattern (b) are consistent with a spacing of 11.9 Å due to the biphenyl length, and higher order reflections (*n* = 2, 3, 4, and 5 in the Bragg equation).

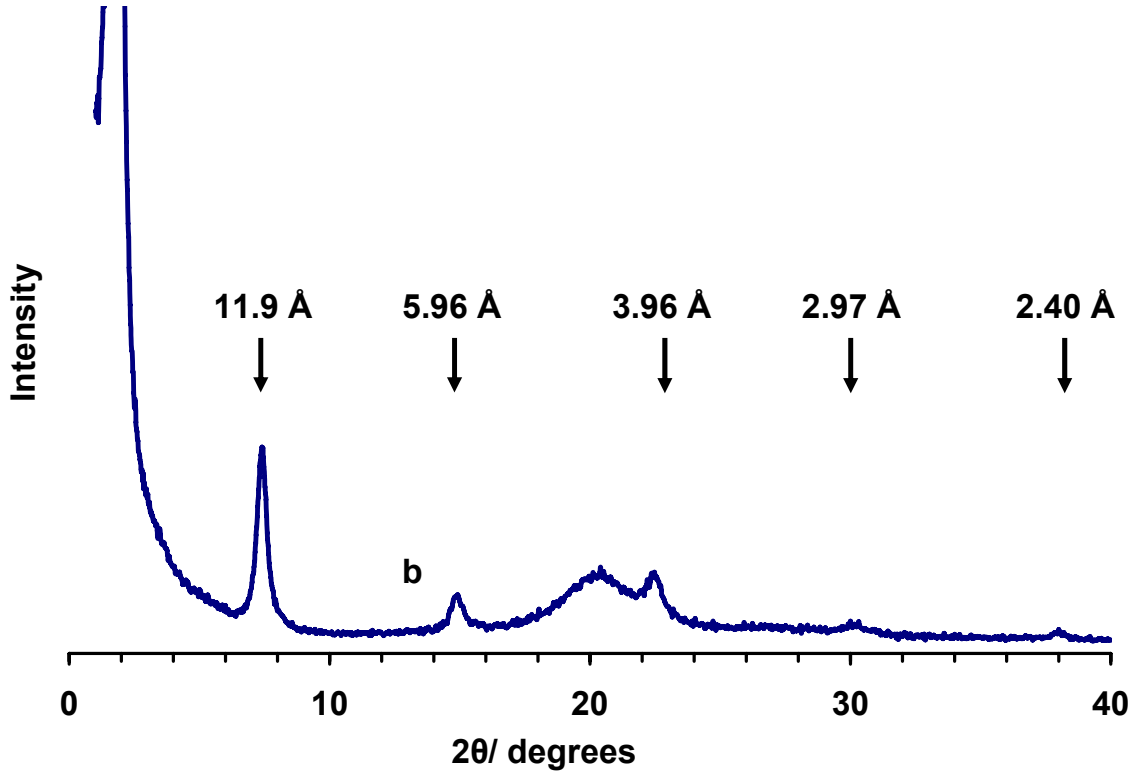

Figure 2.24 PXRD of (b) **PMO-1/4^{OH-}** at higher angles. Broad peak near 20 º *2θ* is amorphous background.

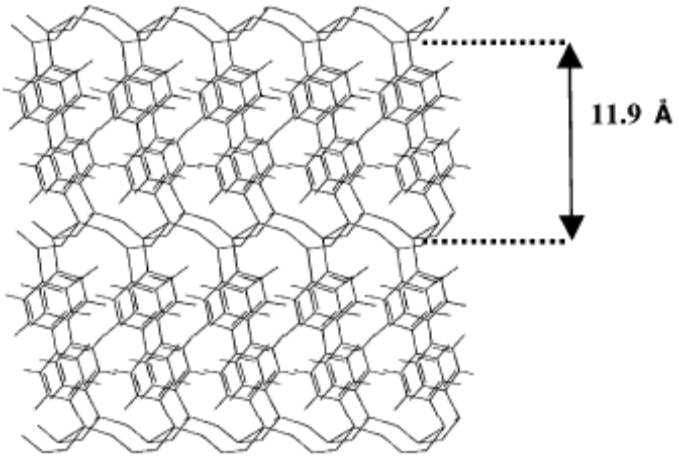

Figure 2.25 Structural model for biphenylene-bridged PMO giving rise to molecular-scale periodicity in **PMO-1/4^{OH-}**. Reproduced from reference [12].

The *trans*-stilbene functional monomer **1** could be considered a good candidate to display crystal-like properties in a PMO, given its flat and rigid

aromatic structure. Under basic conditions, (pattern (b) for **PMO-1/4^{OH-}** above) no diffraction peaks of the stilbene-bridged monomer **1**, were apparent. If the stilbene units were ordering within the pore walls akin to the biphenyl groups, we would expect to see a peak at a slightly larger *d* spacing (~14.2 Å) than that observed for biphenyl (11.9 Å) due to the extra length of the ethenyl bridge. It is possible that at 15 % **1**, the loading was too low to be visible in the XRD profile. However, even in the PMOs prepared at 20 and 30 % **1** (**PMO-1(20%)/4^{OH-}**, **PMO-1(30%)/4^{OH-}**), there were no peaks appearing that could be attributed to the stilbene moiety (Figure 2.26, c and d) despite having confirmed its presence (see Figure 2.21 above). This is strong evidence for a well-dispersed functional monomer **1**, throughout the structural monomer **4** in the PMO. The high dispersion will be confirmed by osmium staining in the next section 2.2.9.

It is also evident that under these conditions, up to 20 % **1** can be incorporated with **4**, while maintaining a well-ordered material, however at 30 % **1** the mesoscale and molecular scale ordering of the PMO begins to suffer considerably as judged by the relative intensities of the peaks (Figure 2.26, profile (a) of **PMO-C$_{18}$TMACl-4^{OH-}** is added for reference). At higher loadings of **1** (50 %), no precipitate was obtained from these preparation conditions and only a gel resulted.

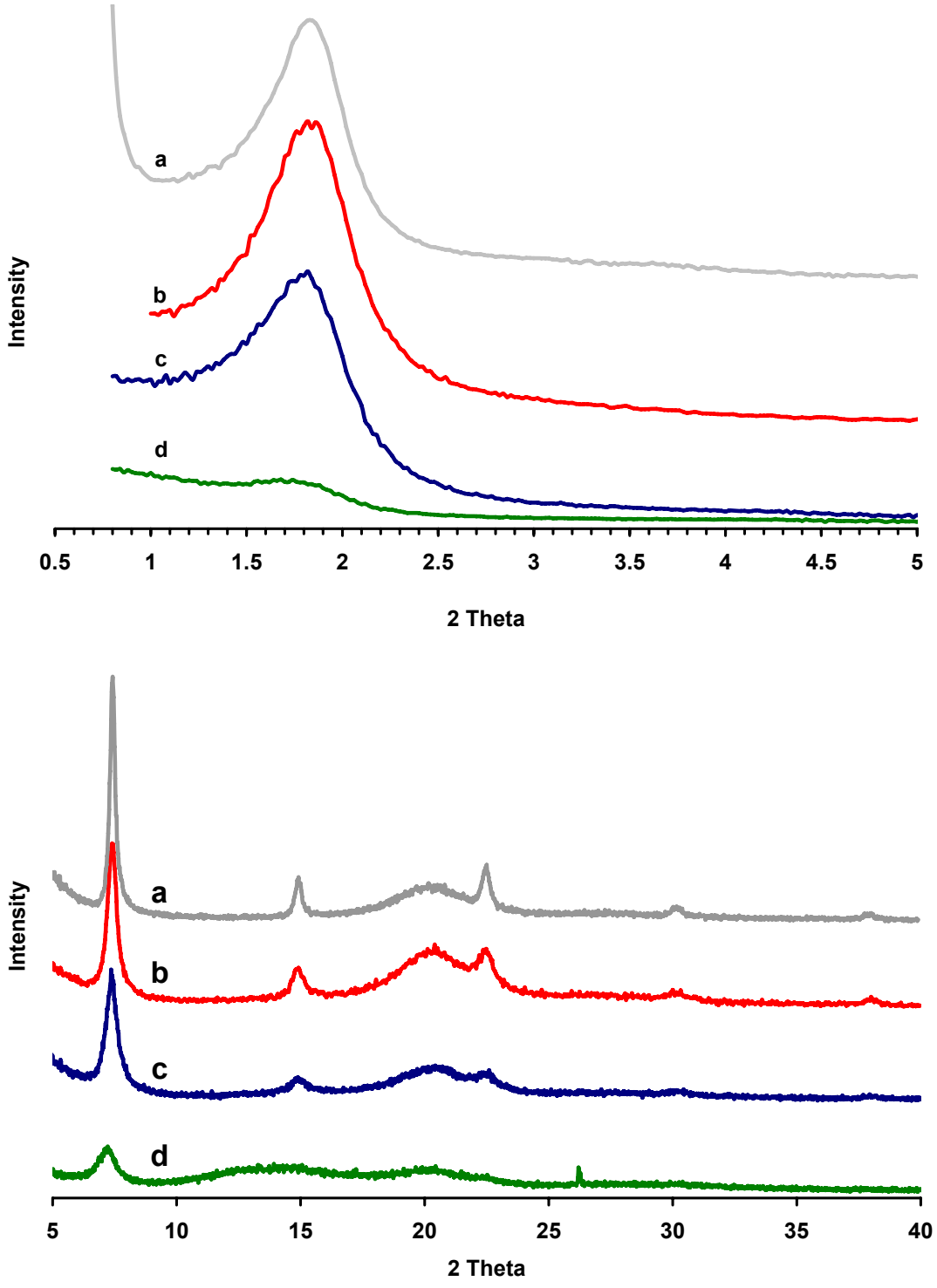

Figure 2.26 (Top) low angle and (bottom) medium angle powder XRD profiles of a) **PMO-C_{18}TMACl-4^{OH-}** b) **PMO-1/4^{OH-}**, c) **PMO-1(20%)/4^{OH-}**, and d) **PMO-1(30%)/4^{OH-}** containing 0, 15, 20 and 30 % **1** respectively.

2.2.9 Determining homogeneity and accessibility of olefin

For most applications, a homogeneous distribution of the two monomers in a composite material would be desired and we therefore needed to consider any phase segregation that could be occurring. Sayari and Yang conducted a study on the co-condensation versus phase segregation in PMOs composed of mixtures of the two aromatic structural monomers **3**, and **4** (see Figure 2.4), templated with C_{18}TMACl under basic conditions.[33] The resulting powder XRD patterns displayed characteristic peaks attributed to the lamellar packing of *each* monomer in the pore walls. These data were consistent with either phase segregation or localized domains (islands) of phase segregated monomers. In our case, the initial powder XRD results did not give any evidence of the *trans*-stilbene-bridged monomer **1**, being phase segregated.

In order to determine whether the olefin functionality was homogeneously distributed throughout the bulk of the material, **PMO-1/3^{H+}** (containing 15 % **1** with phenylene-bridged monomer **3**), was treated with an osmium tetroxide vapour stain at room temperature for four hours.[32] The osmium absorbs or scatters electrons that would otherwise contact the detector thus enhancing contrast in TEM imaging. The accessible monomer reacts with osmium, and forms an osmate ester as shown in Scheme 2.3. After reaction with OsO_4, the PMO was imaged by TEM in bright and dark field modes in conjunction with energy dispersive X-ray spectroscopy (EDX) in order to observe the presence of osmium. Unfortunately, we were unable to distinguish contrast differences within a single sample, even under high-angle annular dark field (HAADF) mode which

is even more sensitive to atomic number than the normal bright field mode. Since this could have indicated an extremely well dispersed sample, we carried out a number of control experiments. Thus materials prepared with and without olefin were treated with OsO_4, and then analyzed by EDX spectroscopy. The control material, with no olefin, did not react with any osmium tetroxide and therefore no peaks were observed for osmium (Figure 2.27), while the olefin-containing material showed a distinct signal arising from the osmium (Figure 2.28). The EDX spectrum of Figure 2.28 shows a clear shoulder near 1.96 keV, overlapping slightly with Si-K lines, which is attributed to Os-M electronic energies. Deconvolution of the peaks confirmed that the ratio of Os-M to Si-K was consistent in all five locations tested. Furthermore, a sample prepared containing both the control material and osmium-stained **PMO-1/3^{H+}-Os** *on the same TEM grid*, shows a significant contrast difference by HAADF (Figure 2.29). This indicates that the stilbene component is extremely well-dispersed within the organosilica material.

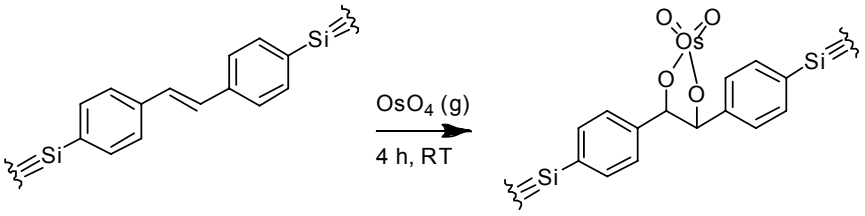

Scheme 2.3 Osmium treatment of **PMO-1/3^{H+}** to **PMO-1/3^{H+}-Os.**

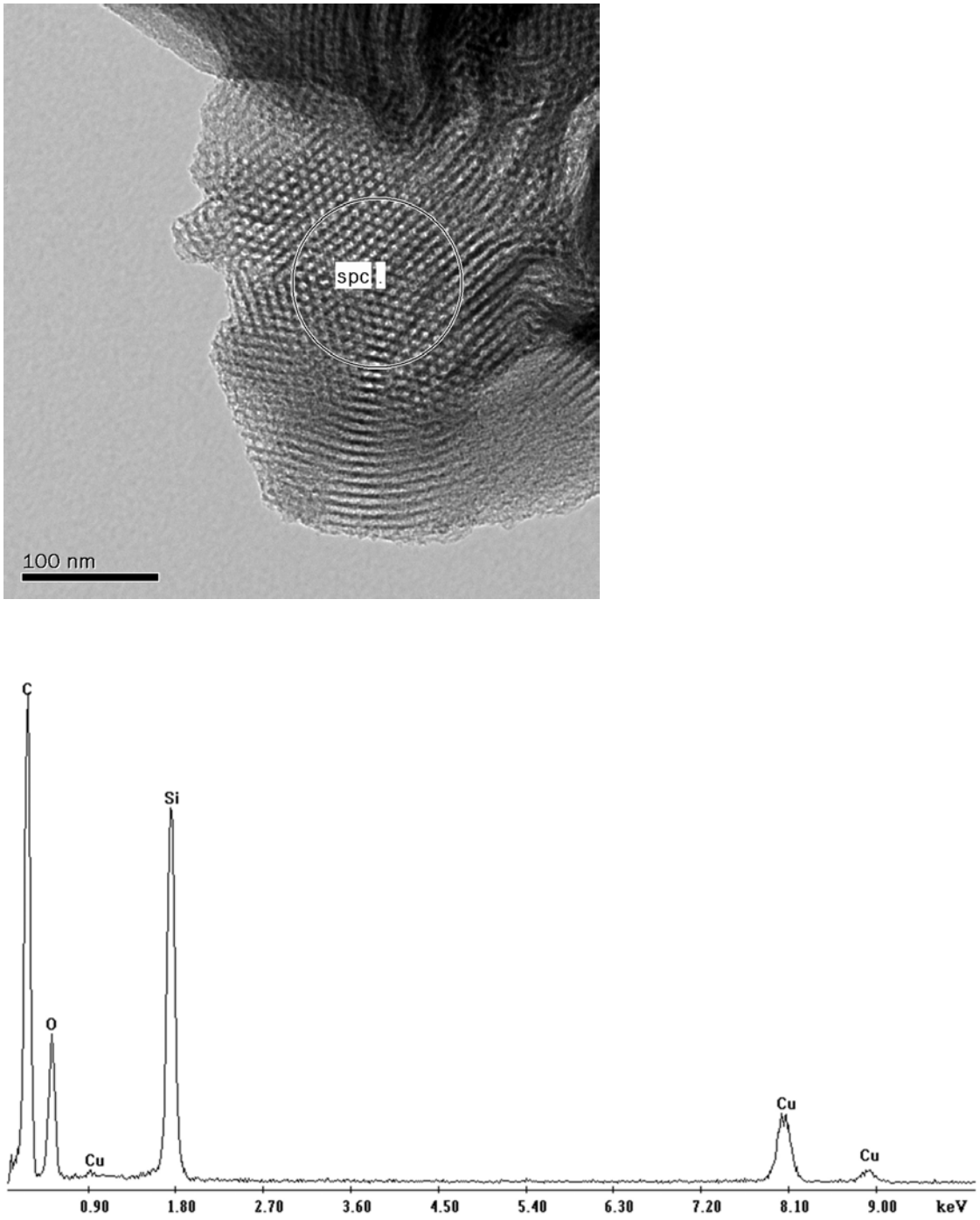

Figure 2.27 Top: TEM image of control material (containing no olefin) with circle indicating EDX sampling area. Bottom: EDX spectrum showing lack of Os.

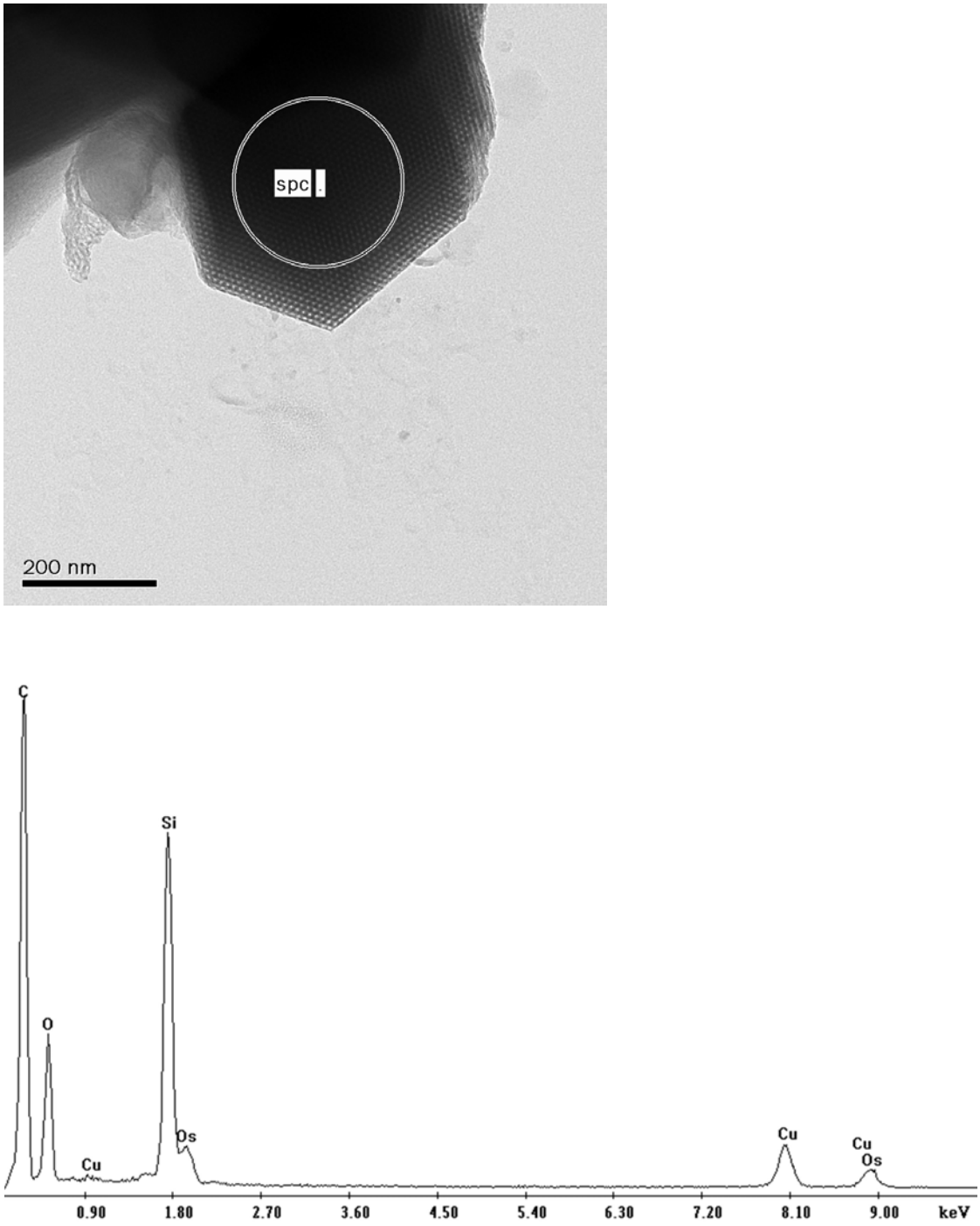

Figure 2.28 Top: TEM image of **PMO-1/3^{H+}-Os** with circle indicating EDX sampling area. Bottom: EDX spectrum showing presence of Os near 1.96 **keV**.

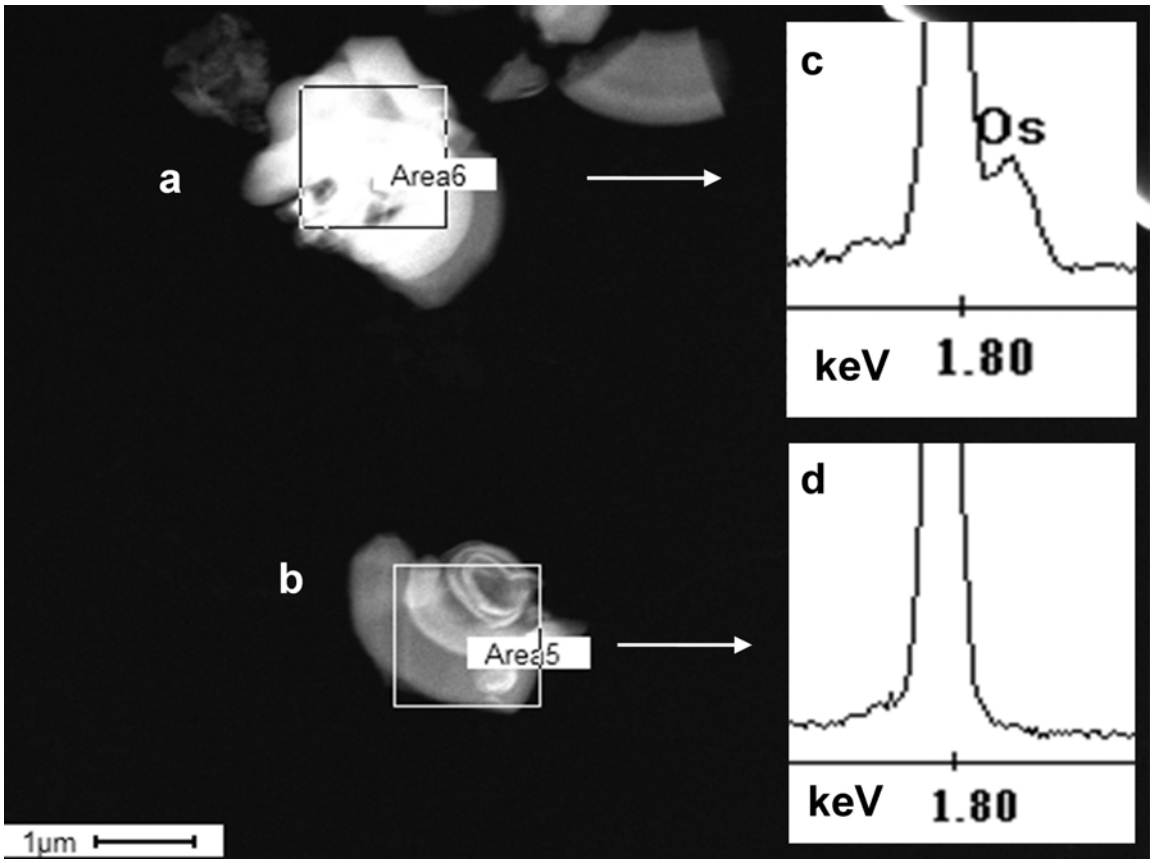

Figure 2.29 High angle annular dark field (HAADF) image of a) **PMO-1/3^{H+}-Os** and b) control material with no olefin showing contrast difference and the respective EDX spectra near Os-M line energy (c and d).

2.2.10 Ozonolysis of *trans*-stilbene PMOs

In order to reveal the functionality within the composite materials, material **PMO-1/3^{H+}** was subjected to ozonolysis at -78 °C, followed by a reductive workup with dimethyl sulfide (Me_2S). This procedure is known to cleave olefins resulting in two aryl aldehydes.[34] The resulting material is labeled **PMO-1/3^{H+}-O_3**. We first performed a Tollen's test (Equation 2.1) on **PMO-1/3^{H+}-O_3** for the presence of aldehydes.

$$(R\text{-}CH{=}O + 2\ Ag^{+} + 2\ OH^{-}(aq) \rightarrow R\text{-}CO_2H + H_2O + 2\ Ag^{o}\downarrow) \qquad \text{(Equation 2.1)}$$

Tollen's reagent was prepared fresh and added to the oxidized **PMO-1/3^{H+}-O$_3$** and a control material, (unoxidized **PMO-1/3^{H+}**). The control material gave no colour change, while **PMO-1/3^{H+}-O$_3$** turned brown immediately with the precipitation of silver indicating the presence of surface-bound aldehydes (Figure 2.30). Infrared spectroscopy supported the effectiveness of this reaction as a new band appeared as a shoulder at 1700 cm^{-1}, which is diagnostic of an aromatic aldehyde (Figure 2.31). Quite remarkably, this treatment appeared to *completely* oxidize the olefin of **PMO-1/3^{H+}** as determined *via* confocal micro-Raman spectroscopy (Figure 2.32). The peaks at 1632 cm^{-1} (C=C$_{ST}$) and 1196 cm^{-1} (C-X$_{ST}$), where X represents *trans*-stilbene, less one phenyl ring[35] attributable to the stilbene moiety are absent after ozonolysis, while a carbonyl stretch at 1700 cm^{-1} appears. This indicates that *all surface and pore olefins* present in the material have been modified. Although CP MAS ^{13}C NMR was not sensitive enough to observe the aldehyde peak at 15 % *trans*-stilbene monomer **1** in **PMO-1/3^{H+}**, a material with 25 % functional monomer **1** does display an aldehyde peak at 197 ppm.

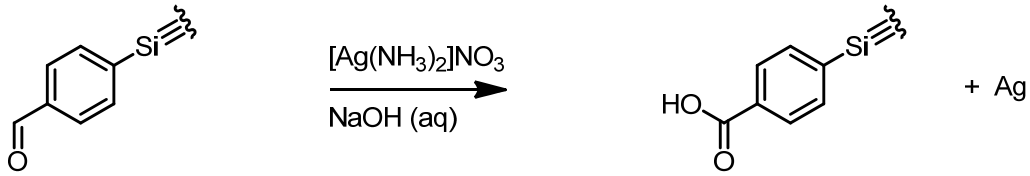

Figure 2.30 Tollen's test with **PMO-1/3^{H+}-O$_3$** (left, brown) and unoxidized **PMO-1/3^{H+}** (control material right, clear) for presence of aldehyde. Scheme for **PMO-1/3^{H+}-O$_3$** is shown below.

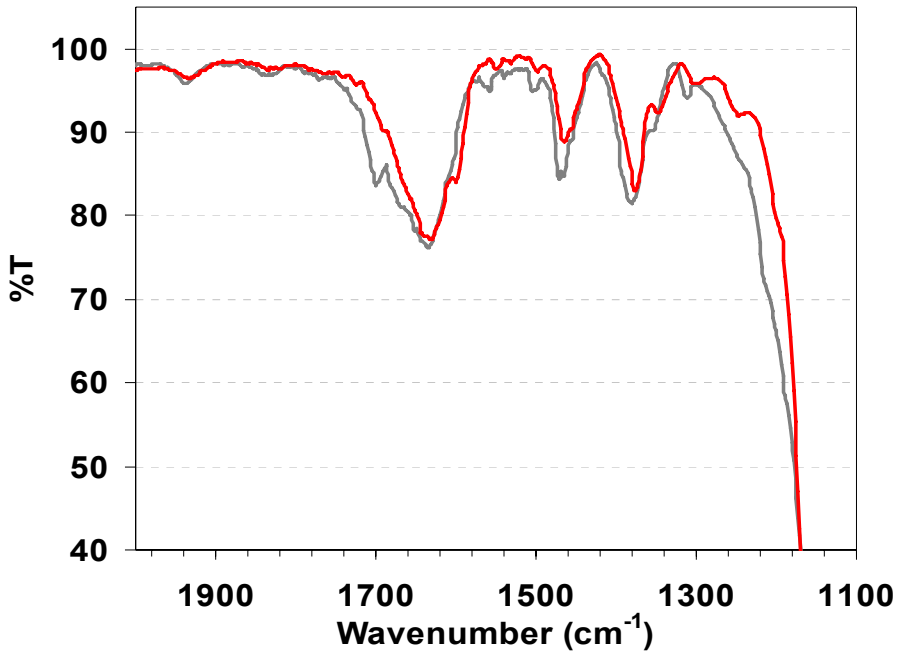

Figure 2.31 Infrared spectra of **PMO-1/3^{H+}** before (red) and after O_3 treatment (**PMO-1/3^{H+}-O$_3$**) (grey) showing the C=O peak for the aryl aldehyde at 1700 cm^{-1}.

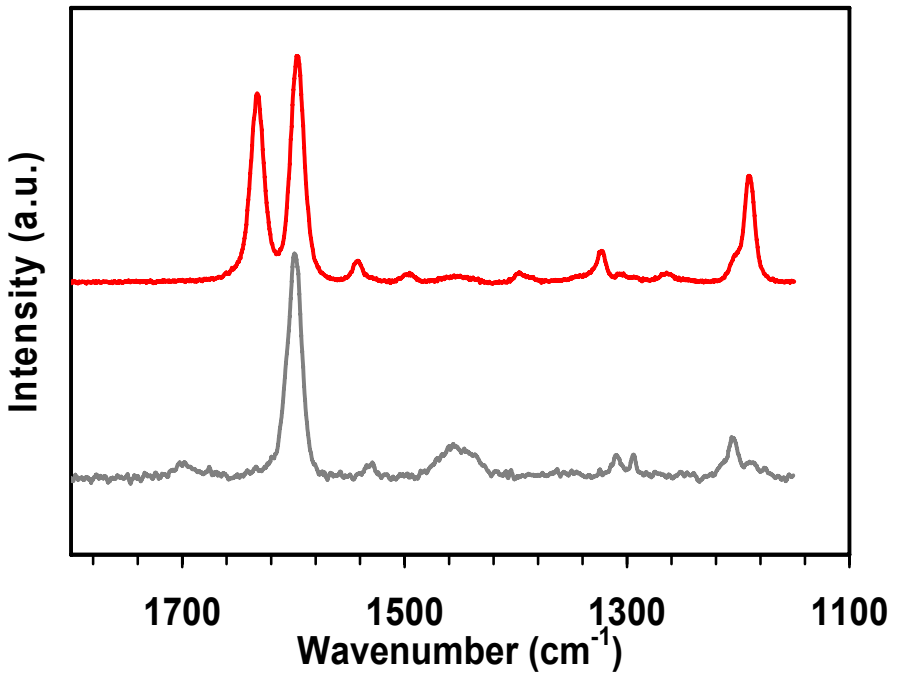

Figure 2.32 Raman spectra of **PMO-1/3^{H+}** (red) and **PMO-1/3^{H+}-O$_3$** (grey) showing loss of C=C peak at 1632 cm^{-1} and a slight C=O peak for the aryl aldehyde at 1700 cm^{-1}.

To ensure that the aromatic rings were not participating in the oxidation, a control reaction was run wherein a PMO with no stilbene component was oxidized. The resulting infrared and Raman spectra were unchanged from that of the original material (Figure 2.33, Figure 2.34).

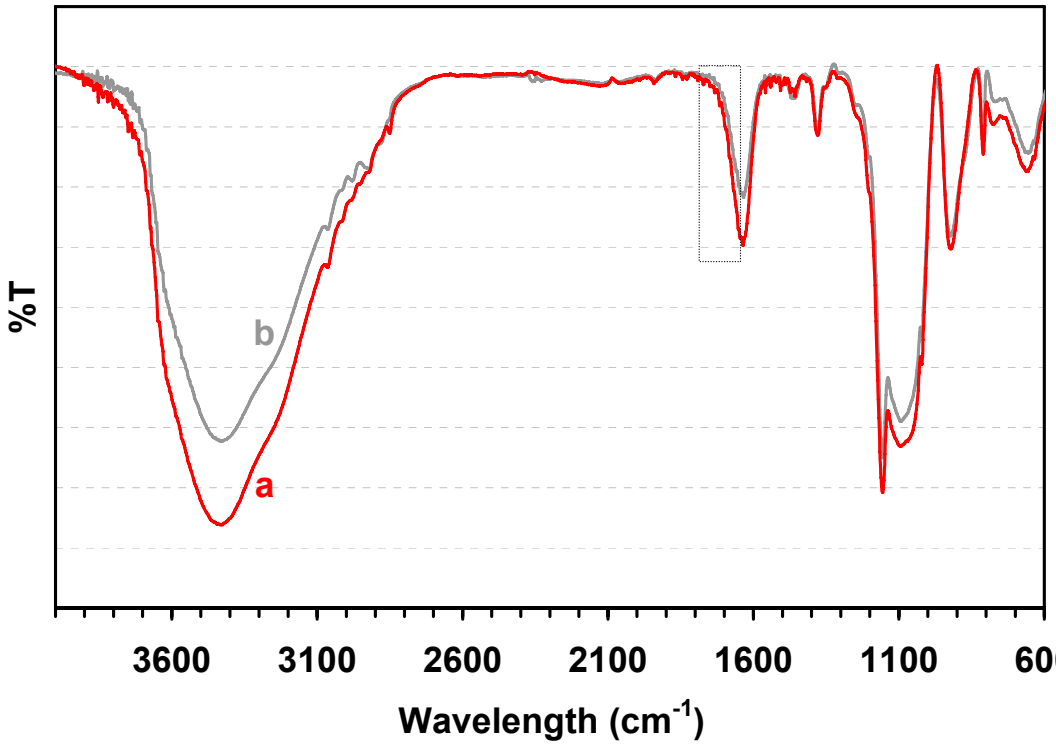

Figure 2.33 Infrared spectra of control material a) pre- and b) post-oxidation with O_3 reaction showing no C=O peak. The box indicates region where carbonyl peaks would occur.

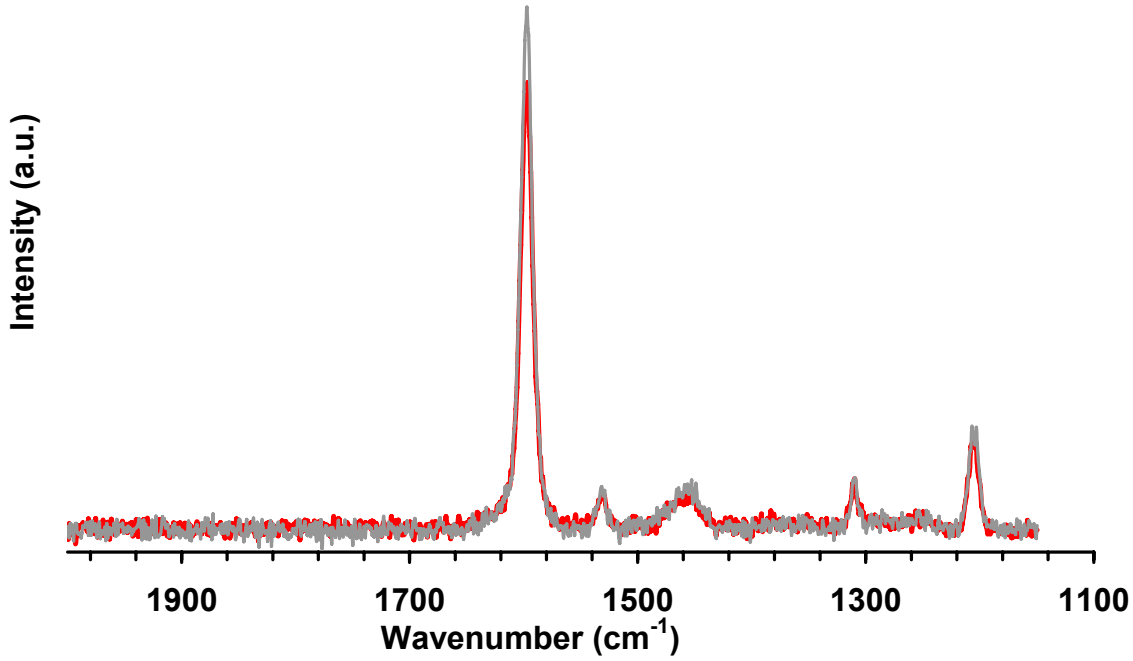

Figure 2.34 Raman spectra of control material pre- (red) and post-oxidation (grey) with O_3 reaction showing no C=O peak.

Importantly, nitrogen adsorption analysis of the material following ozonolysis (**PMO-1/3^{H+}-O_3**) demonstrated that the ordered mesoporous structure was unaffected by this treatment. The BET surface area increased slightly from 282 m^2/g to 345 m²/g, while the pore dimensions were virtually unaltered (Figure 2.35 and Figure 2.36). This verifies that the structural monomer performed its role, which was to support the mesostructure of the material.

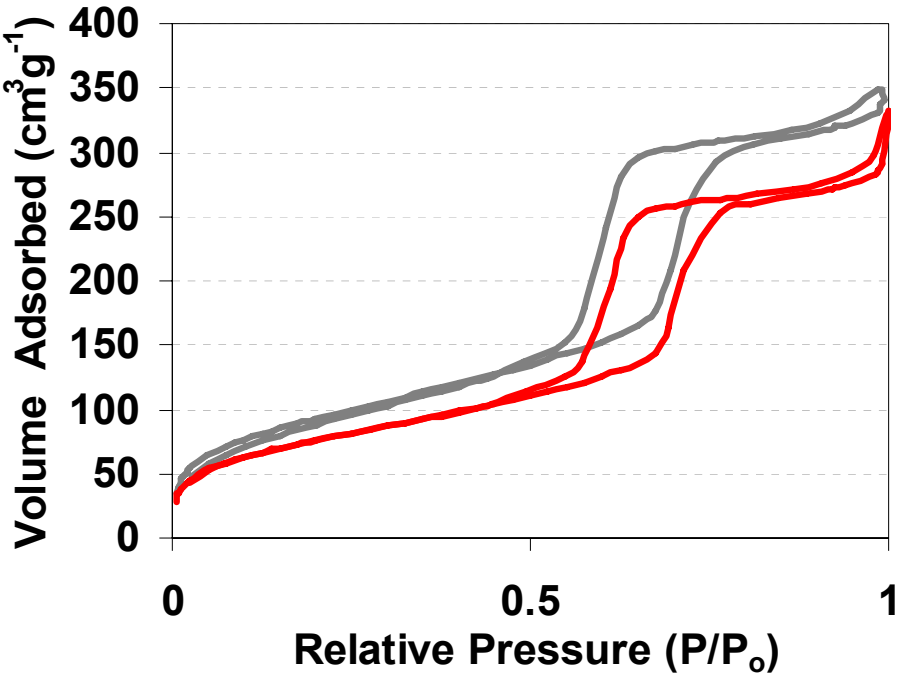

Figure 2.35. Nitrogen isotherms for **PMO-1/3^{H+}** (red) and **PMO-1/3^{H+}-O$_3$** (grey).

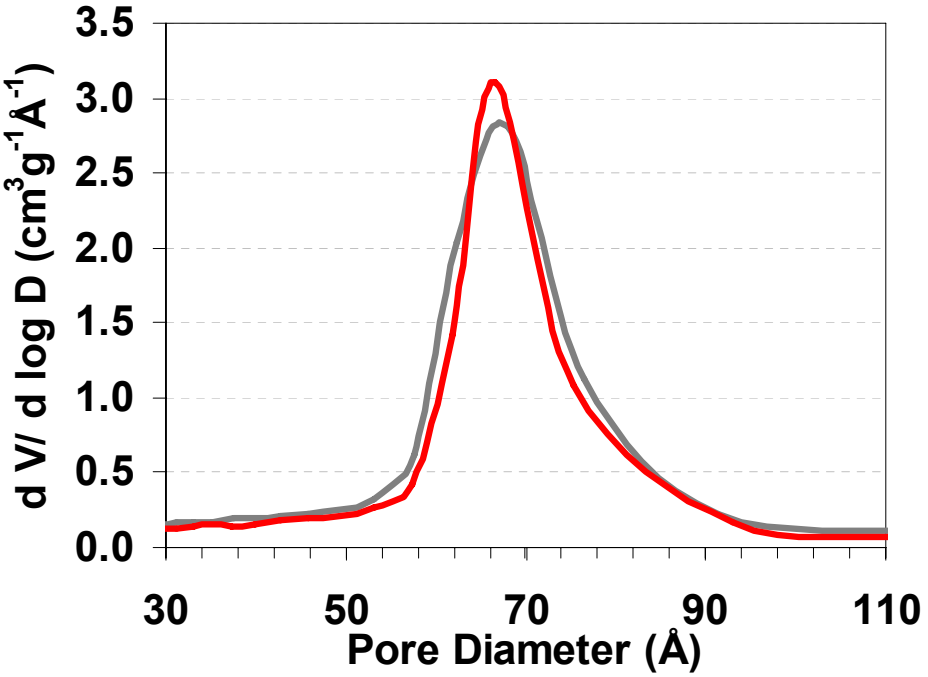

Figure 2.36 BJH pore size distribution plots of **PMO-1/3^{H+}** (red) and **PMO-1/3^{H+}-O$_3$** (grey).

The powder X-ray diffraction patterns of **PMO-1/3^{H+}** before and after ozonolysis are shown in Figure 2.37. The low angle diffraction peaks characteristic of a 2D-hexagonal mesostructure (100, 110, and 200) were still present, if not slightly improved, following ozonolysis. There was a slight reduction in the hexagonal lattice parameter from 116.9 to 112.2 Å, which indicated minor (~ 4 %) shrinkage of the network had occurred, perhaps due to a further condensation of the material.

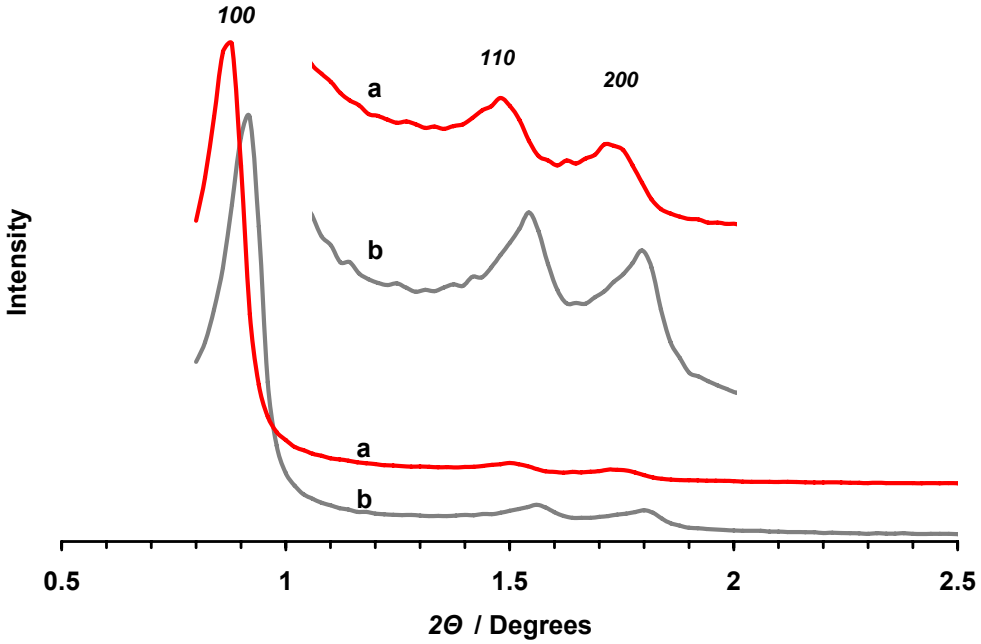

Figure 2.37 Powder X-ray diffraction patterns (low angle) of (a) **PMO-1/3^{H+}** (red) and (b) **PMO-1/3^{H+}-O$_3$** (grey) with 2D-hexagonal index trio marked. The a_0 lattice parameter decreases from 116.9 Å in (a) to 112.2 Å in (b).

Occasionally, weaker, medium angle peaks occurred in the XRD profiles of **PMO-1/3^{H+}** (Figure 2.38 a), the most prominent of which had *d* spacings of 16.0 and 4.48 Å. The peaks however were absent following the oxidation in **PMO-1/3^{H+}-O$_3$** (Figure 2.38 b) indicating they were due to the *trans*-stilbene

groups of **1**. The identity of these peaks is still under investigation, as they could not be indexed by the crystallographer, and are not at the expected interval spacings to be explained by higher order reflections of lamellar stacking, like those seen for other aromatic units.[4,12,28]

With ozonolysis, we have demonstrated a novel method of introducing the versatile aldehyde functionality throughout the porous network, while maintaining the initial mesostructure and dimensions of the pores.

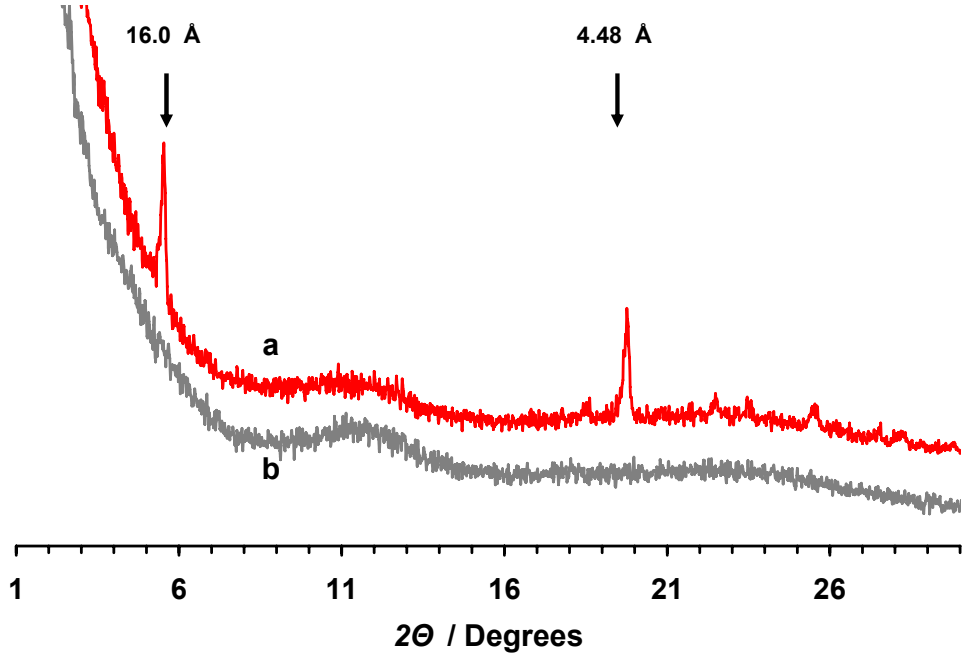

Figure 2.38 Powder X-ray diffraction patterns (medium angle) of (a) **PMO-1/3^{H+}** (red) and (b) **PMO-1/3^{H+}-O$_3$** (grey) showing loss of peaks upon ozonolysis.

2.2.11 Imine formation from C=O functionalized PMO

With the electrophilic carbonyl character of **PMO-1/3^{H+}-O$_3$** present, we could now attempt the addition of desirable organic groups to the PMO framework through the formation of an imine. Important ligand architectures are

known which contain a Schiff base,[36,37] moreover, this typically high-yielding reaction could be employed for binding amino-functionalized biomolecules. Furthermore, the addition of a chiral group to the PMO surface could lead to interesting optical properties. Therefore, as a proof of principle, we sought to react the carbonyl-containing **PMO-1/3^{H+}-O$_3$** with L-alanine methyl ester (Figure 2.39).

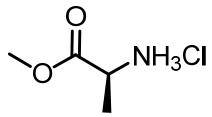

Figure 2.39 L-alanine methyl ester hydrochloride.

The reason for the acid-protection is to avoid as much as possible non-covalent adsorption of the acid onto the organosilica PMO, which would lead to a higher than expected loading. The IR stretch for the carbonyl group of the methyl ester-containing product (~1735 cm^{-1}) is sufficiently removed from the region where the aryl aldehyde starting material occurs (1700 cm^{-1}), thus giving a handle by which we could easily monitor the success of imine formation. With each additional step, the material becomes more precious, so we favoured the use of characterization techniques such as IR and Raman spectroscopy, which require little sample.

The hydrochloride salt of L-alanine methyl ester was prepared according to a literature reference[38] and was first allowed to react in a control experiment with benzaldehyde in dichloromethane and triethylamine at room temperature for 1 h. This resulted in roughly 95 % conversion to the imine product as determined

by ^{1}H NMR. Unfortunately, keeping as close to these conditions as possible (the concentration of aldehyde is low and unknown) did not give any significant reaction with **PMO-1/3^{H+}-O$_3$** as judged by the resulting IR spectrum. Reactivity was optimized by minimizing the presence of water in the reagents and using 4 Å molecular sieves as a desiccant at elevated temperatures (Figure 2.40). The molecular sieves were manually removed from the mixture before centrifugation was used to isolate the small PMO particles from excess soluble ester. The PMO was washed several times and dried under an inert gas stream before being analyzed by infrared spectroscopy.

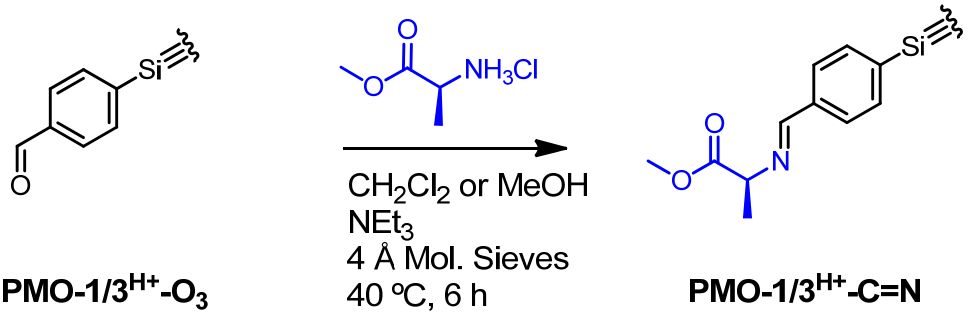

PMO-1/3^{H+}-O$_3$ **PMO-1/3^{H+}-C=N**

Figure 2.40 Imine functionalization of **PMO-1/3^{H+}-O$_3$** to give **PMO-1/3^{H+}-C=N**.

The infrared spectrum shows a small growth in the ester region (1735 cm^{-1}) relative to the aldehyde region (1700 cm^{-1}) (Figure 2.41). Furthermore, the imine C=N stretch was apparent near 1640 cm^{-1}. As evidenced from the control reaction, a desiccant is not necessary for imine formation, in fact, aryl aldehydes typically undergo spontaneous imine formation,[39] however molecular sieves did prove beneficial in our case. It is possible that the surface of the PMO had a strongly adhered hydration layer which was inhibiting reaction with the amino ester.

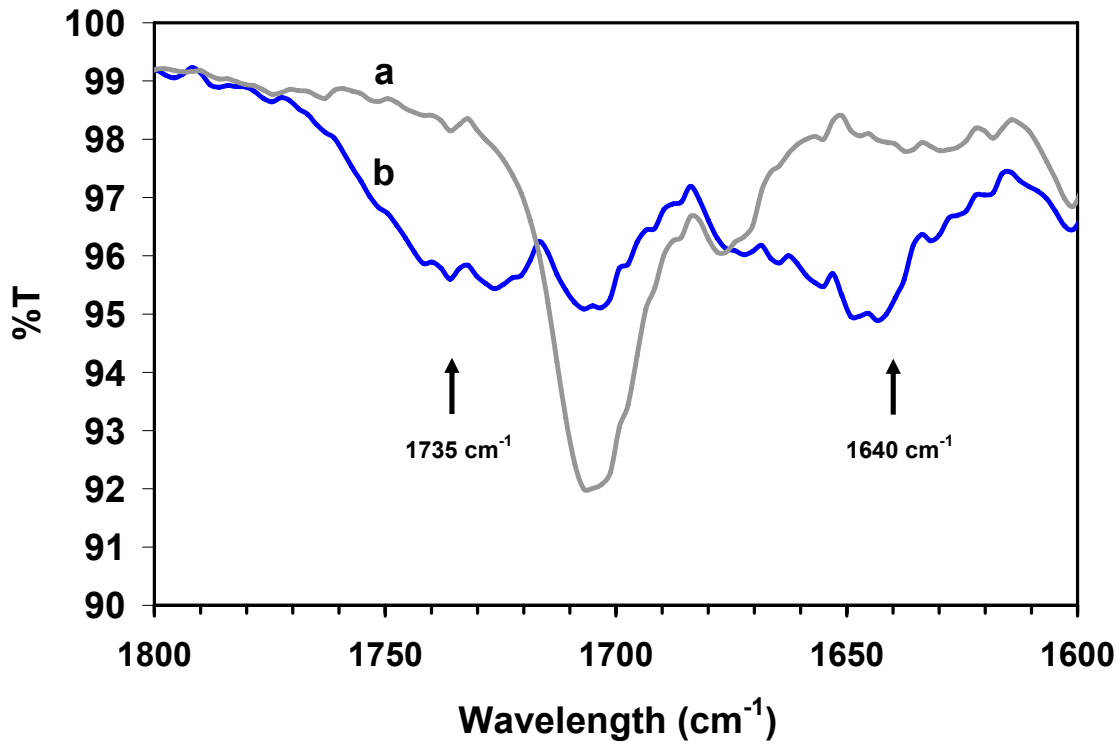

Figure 2.41 Infrared spectrum of a) **PMO-1/3^{H+}-O$_3$** (grey) and the imine-functionalized product b) **PMO-1/3^{H+}-C=N** (blue).

The conversion of the aldehyde did not appear quantitative as was the case in the ozonolysis oxidation of **PMO-1/3^{H+}-O$_3$**. This is perhaps not very surprising as it is well known that the functionalization of porous silica materials in this manner can be plagued by inhomogeneous loadings, which may preferentially block pore openings, and prevent further reactions at the pore interior. Also, a reason for the higher reactivity of ozone may be because it is a gaseous reagent which penetrates deep into the porous network, whereas a larger, highly solvated amino ester, would have difficulty reacting with an aldehyde in the smallest of microporous cavities.

Although full reactivity of the aldehyde-functionalized PMO (**PMO-1/3^{H+}-O$_3$**) was not achieved, we have demonstrated the surface functionalization through imine formation with a chiral amino methyl ester. Further work in this area needs to confirm these preliminary results and improve upon the reactivity of the aldehyde PMO. This may simply come from increasing the temperature or duration of the reaction, screening different solvents. Elemental analysis should prove beneficial in quantifying the loadings and optical activity could be assessed to confirm the presence of a PMO containing a chiral surface.

2.2.12 Metathesis of PMOs

In continuing to explore the potential for these stilbene PMOs to be further functionalized we attempted to use the original, stilbene-bridged PMO (**PMO-1/3^{H+}**) as a partner olefin in an olefin metathesis. As the Grubbs metathesis is a very efficient reaction and tolerant of many functional groups,[6] this could offer a versatile method to prepare a wide variety of functionalized PMOs (Scheme 2.4).

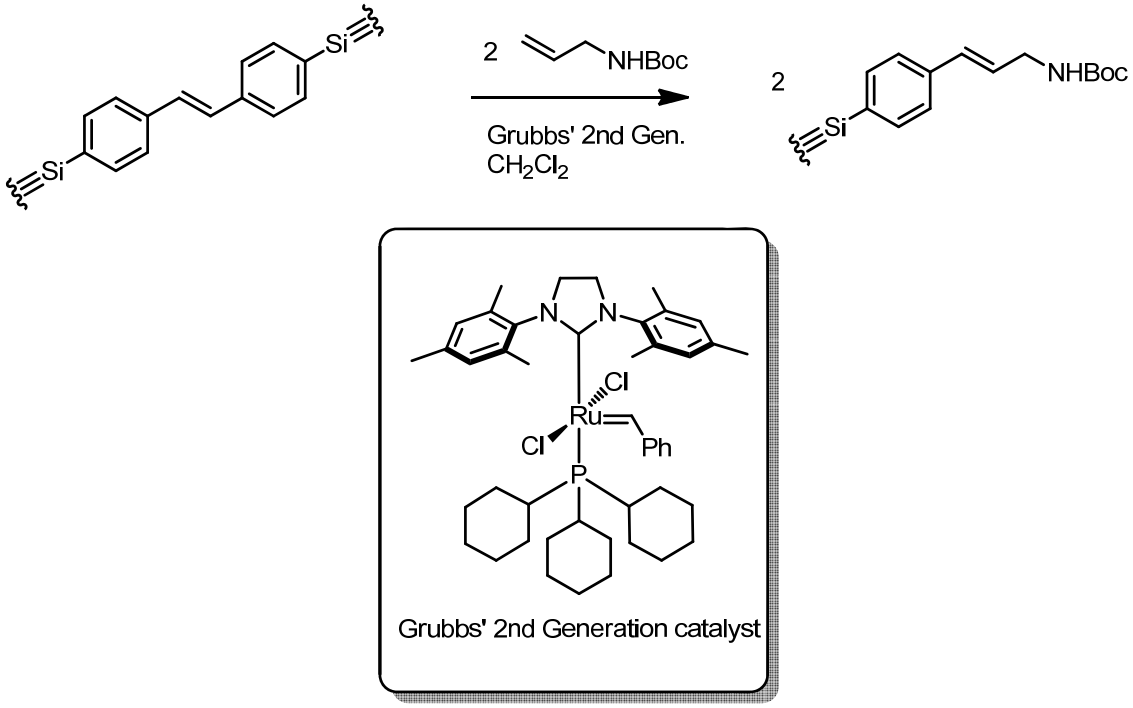

Scheme 2.4 Metathesis scheme for **PMO-1/3^{H+}**.

The coupling partner chosen for the stilbene olefin was a protected *N*-Boc-allylamine. The amino functionality was chosen so as to have a method to determine the extent of functionalization *via* elemental analysis and the protection was performed to avoid catalyst deactivation.

Unfortunately, there was no significant difference by Raman spectroscopy between the product and the starting material **PMO-1/3^{H+}** under the metathesis conditions with *N*-Boc-allylamine olefin. Furthermore, using a material with a higher olefin loading of 25% resulted in the same negative result. Although there are reports of bulky, secondary, amine-protected metathesis reactions with Grubbs' second generation catalyst,[40] there are also reports of this catalyst with less-bulky tertiary, allylamines giving rise to deallylated products as well as

allylamides rearranging to enamides.[41] It is possible that deallylation has occurred here to produce products which deactivate the catalyst. A solution-phase reaction of *trans*-stilbene and *N*-Boc-allylamine would be valuable in determining the potential of this reaction. It is also possible that the catalyst is too large to access and react with olefins in the walls. In this case, only a small amount of surface olefin would react, which may quickly block any further access to the pore channels leaving the loading of the allylamine below the limit of detection for Raman spectroscopy.

2.2.13 Hydrophobic *trans*-stilbene PMO

The above PMO transformations involve reaction at the organic bridging group, however reaction at surface silanols also offers a means for PMO modification. Indeed, this is a more traditional method to organosilica from pure silica phases, and is known as “post-synthetic grafting”.

Here, we were interested in preparing a hydrophobic surface, which could give interesting properties to the PMO such as increased stability or separation capability for chromatography. Hydrophobic materials offer an alternative to the typical PMO surface which under certain synthetic conditions, could contain many silanol groups. We chose hexamethyldisilazane (HMDS) as our hydrophobizing agent, which would cap any reactive silanols with a trimethylsilyl group (Figure 2.42). **PMO-1/3^{H+}** was stirred in neat HMDS to cap the surface silanols before it was centrifuged from sequential washings of fresh EtOH and Et_2O. The recovered product was dried overnight and analyzed by IR spectroscopy and nitrogen adsorption porosimetry.

The successful modification was observed from the IR band at ~1260 cm^{-1} for the Si-CH_3 symmetric deformation and another band was present at 850 cm^{-1} for a Si-CH_3 rocking[42] (Figure 2.43).

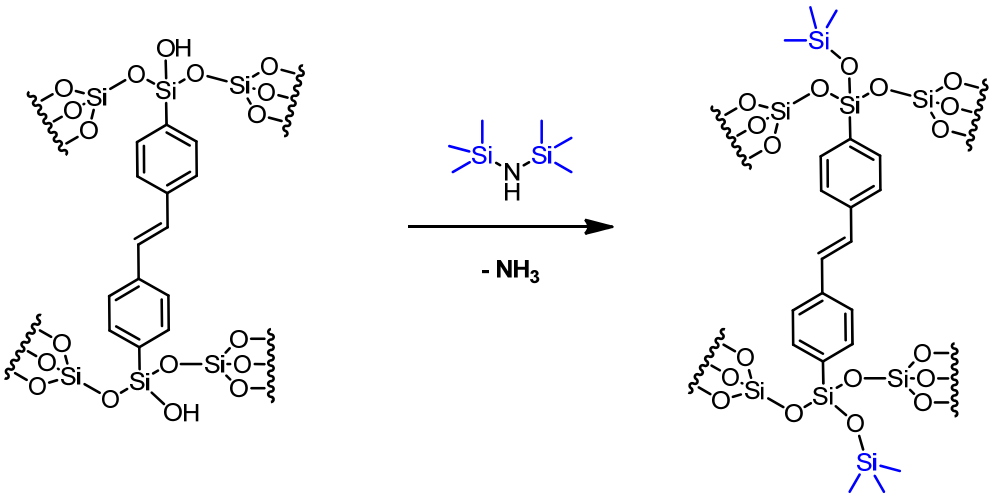

Figure 2.42 Hydrophobic **PMO-1/3^{H+}-SiMe$_3$** from **PMO-1/3^{H+}** and HMDS.

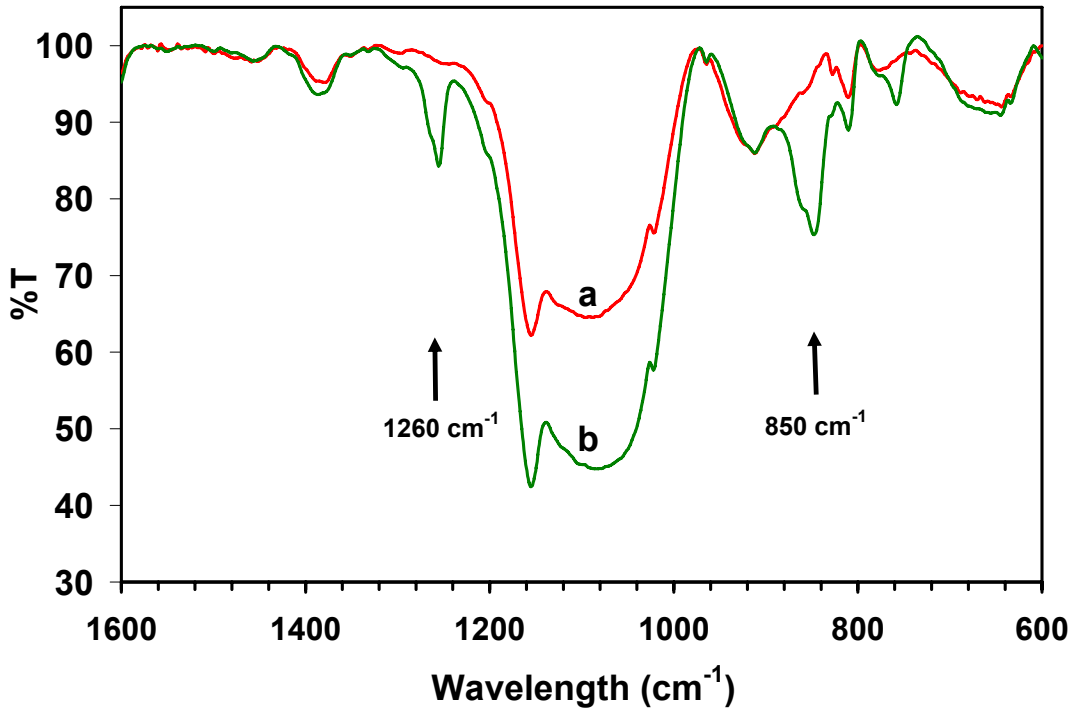

Figure 2.43 Infrared spectra of a) **PMO-1/3^{H+}** (red) and b) **PMO-1/3^{H+}-SiMe$_3$** (green).

As can be seen from Figure 2.44, there is surprisingly little change in the nitrogen isotherm. There appears to be a very slight increase in the surface area from 556 to 614 m^2/g yet the pore dimensions are unaffected. There is also little change in the C value. The C value of the BET isotherm is related to the heat of adsorption of the gas molecules to the surface. In short, a higher C value indicates a higher heat of adsorption translating to a more polar surface, while the C value of a non-polar surface would be much smaller. The C value here upon hydrophobizing with HMDS drops from 101 to 97, which is likely within the error of the measurement. These results may be rationalized by considering that the material was likely quite hydrophobic to begin with, and introducing more silyltrimethyl groups to the material did not result in a large surface polarity change. Although the trimethylsilyl capping of the surface silanols has been achieved, this reaction has not been quantified. Elemental analysis or thermogravimetric-mass spectrometry analysis could prove useful for this purpose.

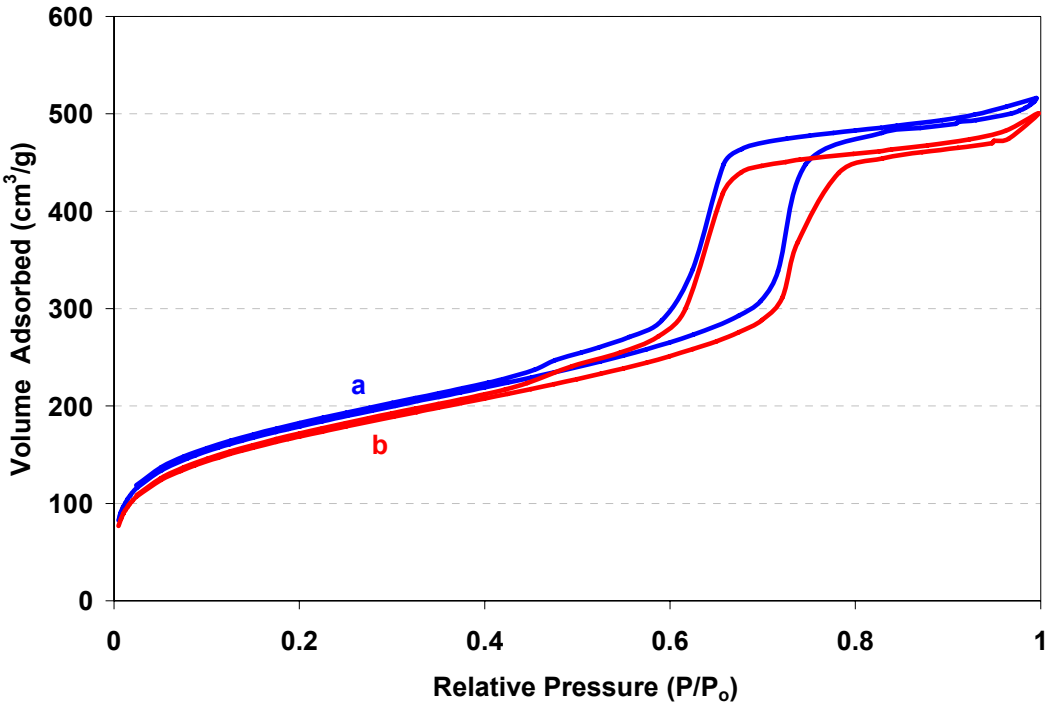

Figure 2.44 Nitrogen physisorption isotherms of a) **PMO-1/3^{H+}** and b) **PMO-1/3^{H+}-SiMe$_3$**.

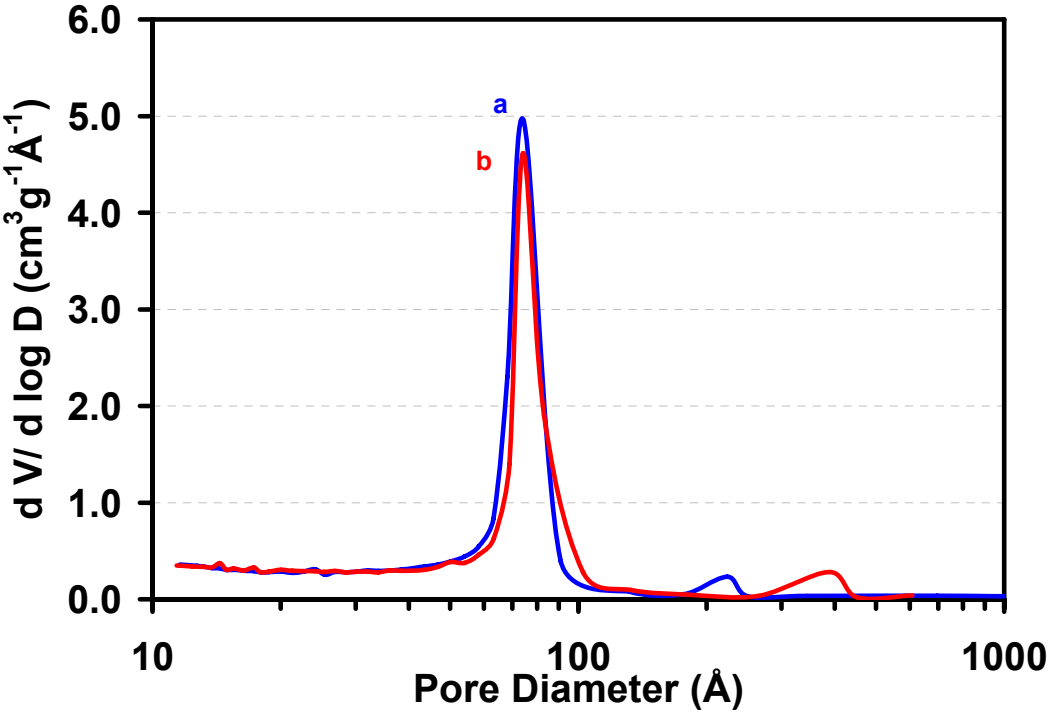

Figure 2.45 BJH pore size distributions of a) **PMO-1/3^{H+}** and b) **PMO-1/3^{H+}-SiMe$_3$**.

2.2.14 Increasing stilbene content in PMOs

Although it was desirable for us to maintain a high degree of structural monomer component to the PMOs, we have also pursued materials where the content of the stilbene was increased. This would lead to materials with greater functional character and increased utility, although perhaps at a cost of the structural order and integrity of the PMOs. As mentioned in the introduction, it is not a trivial matter to alter the synthetic conditions and maintain well-ordered PMOs. Seemingly minor changes may result in drastic property changes of PMOs. As evidence for this fact, it has been well noted that an upper limit for the amount of organosilane that can be incorporated into a purely silica mesophase is roughly 25 % before considerable order of the material is lost.

2.2.15 Basic pH conditions

Under the conditions employed for **PMO-1/4^{OH-}**, which use C_{18}TAMCl as a surfactant template, the proportion of **1** with **4** was increased up to 30 mol %. The textural data of the materials are given in Table 2.3 with the isotherms and pore size distributions shown in Figure 2.46.

Table 2.3 Textural properties of materials prepared using functional monomer **1** and structural monomer **4**, under basic conditions with C_{18}TMACl as surfactant.

Material	% Functional Monomer	BET Surface Area (m^2g^{-1})	Pore Diameter[a] (Å)	Pore Volume[b] (cm^3g^{-1})
PMO-1/4^{OH-}	15%	774	18.9	0.31
PMO-1(20%)/4^{OH-}	20%	806	17.9	0.40
PMO-1(30%)/4^{OH-}	30%	951	18.5	0.79

[a] Maximum value of BJH pore diameter distribution (adsorption branch).
[b] BJH cumulative pore volume of pores between 10 and 3000 Å.

PMO-1/4^{OH-} and **PMO-1(20%)/4^{OH-}** are quite similar to one another in their textural properties, and these numbers are likely within experimental error here. It should be noted that the yield of **PMO-1(30%)/4^{OH-}** was lower as was the available mass for nitrogen analysis. Thus the surface area and pore volume data on such small amounts (< 10 mg) should be understood to have a larger associated error. Under these conditions, at 50 % *trans*-stilbene precursor **1** with **4**, the material unfortunately began to show very slow condensation kinetics and resulted in a gel with no precipitate.

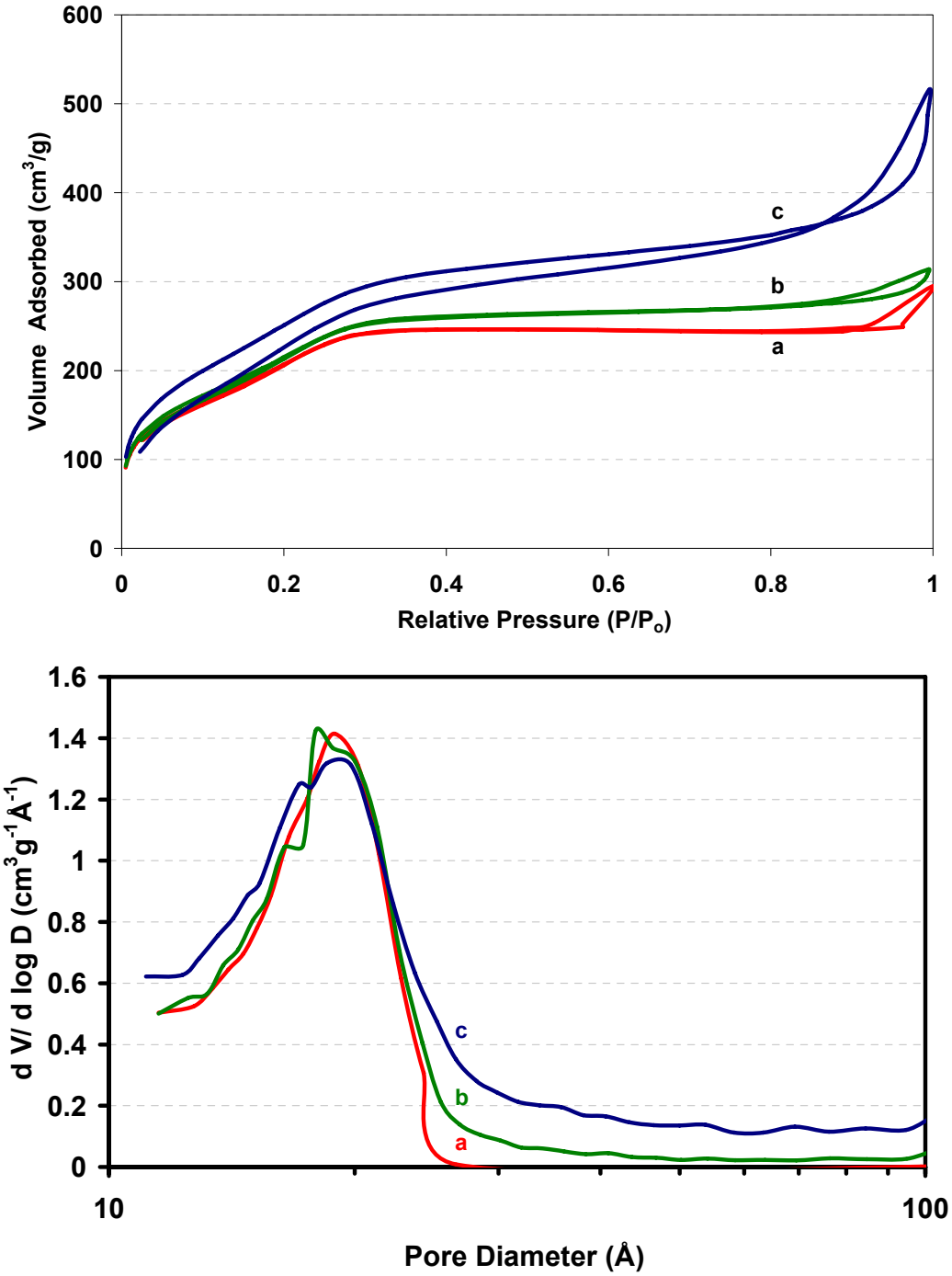

Figure 2.46 Upper: Isotherms and lower: BJH Pore size distributions (adsorption branch) of a) **PMO-1/4^{OH-}** b) **PMO-1(20%)/4^{OH-}** and c) **PMO-1(30%)/4^{OH-}**.

Ozin *et al*. have shown that PMOs prepared using phenylene and thiophene precursors, undergo substantial C-Si cleavage and loss of all organic

moieties under certain strongly basic conditions employed by.[43] Notably, there is no C-Si cleavage under the basic conditions employed here for material increasing the stilbene content from 15 % to and 20 % in **PMO(20)-1/4^{OH-}** (Figure 2.47). However, to confirm that the stilbene was incorporated in this case, Raman spectroscopy proved useful as the stilbene C=C stretch is visible at 1635 cm^{-1} (see Figure 2.21 above).

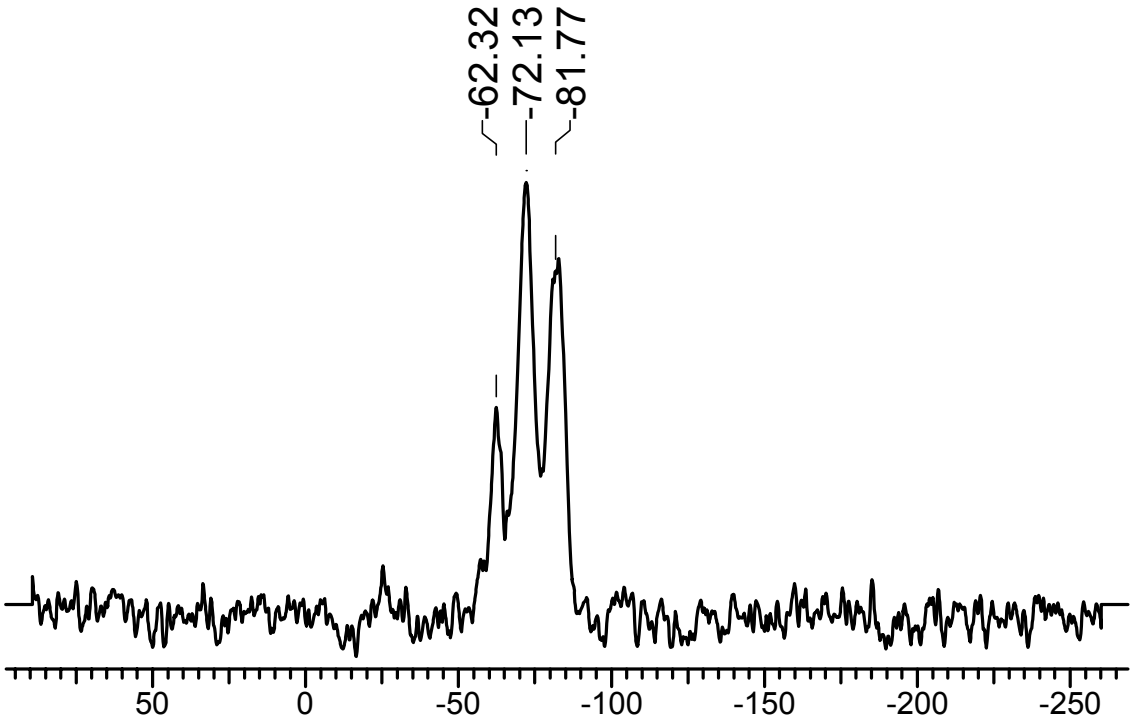

Figure 2.47 CP MAS ^{29}Si NMR of **PMO(20)-1/4^{OH-}** showing no C-Si bond cleavage.

2.2.16 Basic conditions: 100 % *trans*-stilbene materials

Since the *trans*-stilbene precursor is aromatic and rigid like the monomers commonly used to give highly ordered materials, we thought it could potentially offer the structural stability to the materials in place of the phenylene or biphenyl-bridged precursors, while giving a material with exceptionally high functionality.

With this in mind, we explored materials made completely from the stilbene precursor.

Nitrogen adsorption analysis is often a good screening method to determine the porosity of the materials and the periodic long-range order of these pores. This is usually done by comparisons of the BJH pore size distribution plots. The procedure chosen for synthesizing the 100 % *trans*-stilbene-bridged materials was that from Inagaki's group where a biphenylene-bridged PMO was reported under basic conditions, using a quaternary ammonium alkyl surfactant, C_{18}TMACl.[12]

Nitrogen adsorption analysis was used as the method to determine the porosity and surface area of the materials. We attempted to optimize the reported conditions by using additives such as ethanol and adjusting parameters such as the Si:surfactant ratios. The materials obtained in this section are given in Table 2.4, with the detailed procedures given in the experimental section. They are labeled as "**POS-#**" for porous organosilica.

Table 2.4. Materials prepared under basic pH with 100 % BTETS (1) and C_{18}TMACl. [12]

Material	Conditions	BET Surface Area (m^2g^{-1})	Pore Diameter[a] (Å)	Pore Volume[b] (cm^3g^{-1})
POS-1	Standard	762	84	0.82
POS-2	No surfactant	465	77	0.58
POS-3	EtOH (last)	703	94	0.73
POS-4	EtOH (first)	620	190	0.85
POS-5	EtOH (excess)	10.3	-	-
POS-6	1:1 (EtOH:H_2O)	493	-	-
POS-7	¼ NaOH	729	56	0.69
POS-8	½ BTETS	342	-	-

[a] Maximum value of BJH pore diameter distribution (adsorption branch).
[b] BJH cumulative pore volume of pores between 10 and 3000 Å.

Using 100 % functional monomer **1,** under the conditions reported by Inagaki, resulted in a porous material (**POS-1**) with BET specific surface area of 762 m²/g, however a very broad pore size distribution from the adsorption curve was obtained (Figure 2.48).

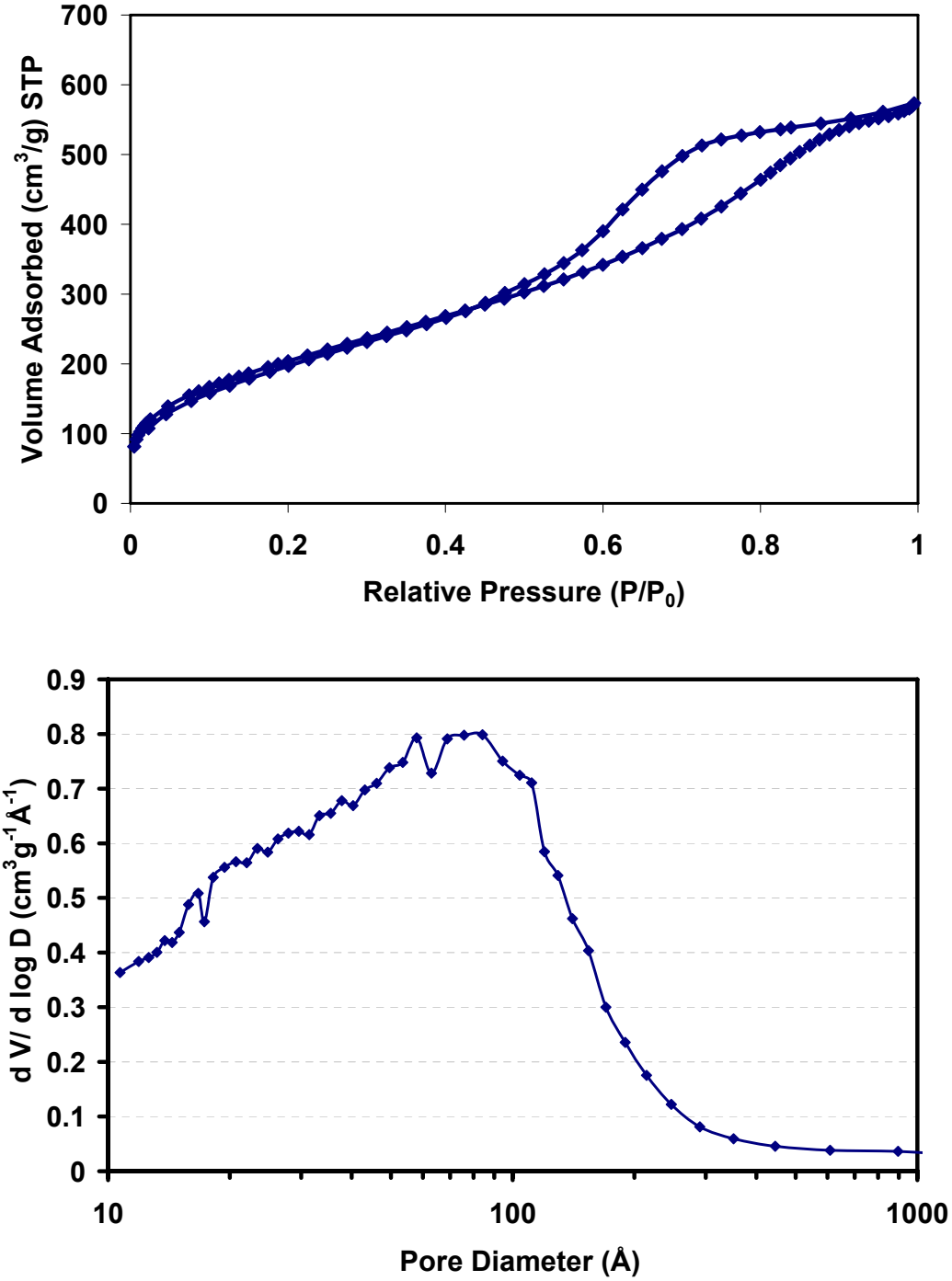

Figure 2.48 Nitrogen physisorption data of **POS-1.** Upper: isotherm; lower: BJH pore size distribution plot of adsorption branch.

The isotherm data of **POS-1** looks somewhat different than that reported by Inagaki. Most notably, it has a broader adsorption branch which suggests a larger pore size distribution and thus a less ordered material than that obtained by Inagaki. This is not altogether surprising, as these conditions have been optimized for the biphenylene-bridged monomer, **4**. Due to a small amount of sample, only a weak CP MAS ^{29}Si NMR spectrum resulted, which could not rule out a minor presence of Q sites, however there were obvious peaks in the T^2 (-74 ppm) and T^3 (-84 ppm) regions to indicate the organic *trans*-stilbene bridge was still intact. This was confirmed by the presence of aromatic peaks in the CP MAS C^{13} NMR (129-141 ppm). It is somewhat surprising that a precipitate was obtained here, while at intermediate concentrations of **1** (50 mol % with **4**), a stable gel resulted. We also prepared a material under the same conditions as **POS-1**, but in the absence of the C_{18}TMACl surfactant. The BET surface area of the resulting material was decreased to 465 m²/g which indicates a beneficial effect from the surfactant template on the textural properties. Although the surface area was lower in **PMO-2**, it is inline with what might be expected for non-templated aromatic organosilica.[44]

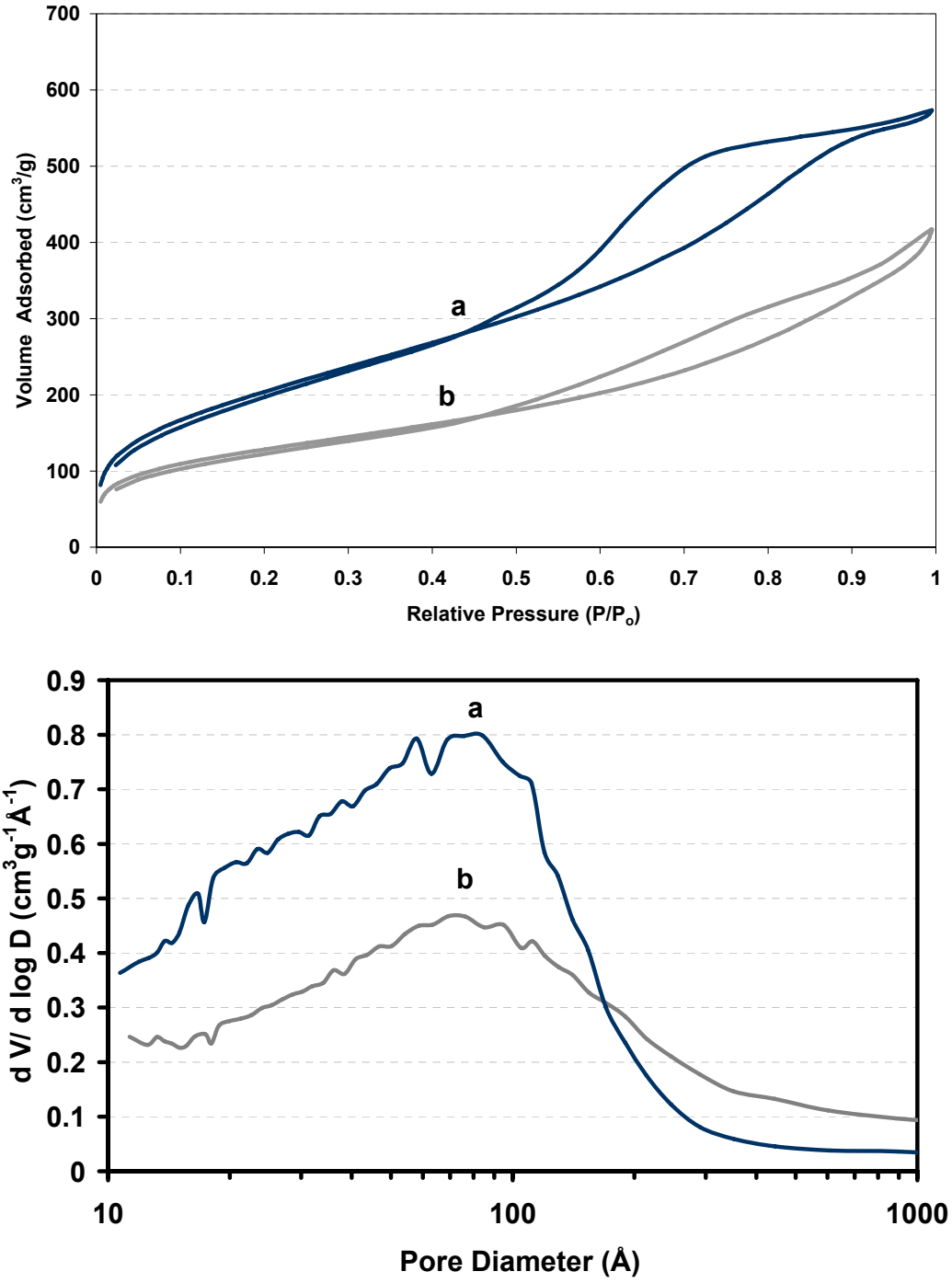

Figure 2.49 Upper: Isotherms and lower: BJH Pore size distributions (adsorption branch) of a) **POS-1** (templated) and b) **POS-2** (non-templated).

Attempts to increase the yield and long range order of the material were then made. It was thought that it could be advantageous to include a minimal

amount of ethanol in the process in order to help dissolve the solid, *trans*-stilbene monomer and enhance the hydrolysis and condensation about the surfactant template. The order of addition proved important here. By adding all the reagents first, followed by ethanol (**POS-3**), the isotherm of the resulting material was very similar to that of **POS-1**, slightly decreased in surface area (703 m^2/g). However when the monomer was first dissolved in ethanol and then added to the surfactant assembly (**POS-4**), the capillary condensation of the isotherm shifted towards larger pore diameters (190 Å) (Figure 2.50, c).

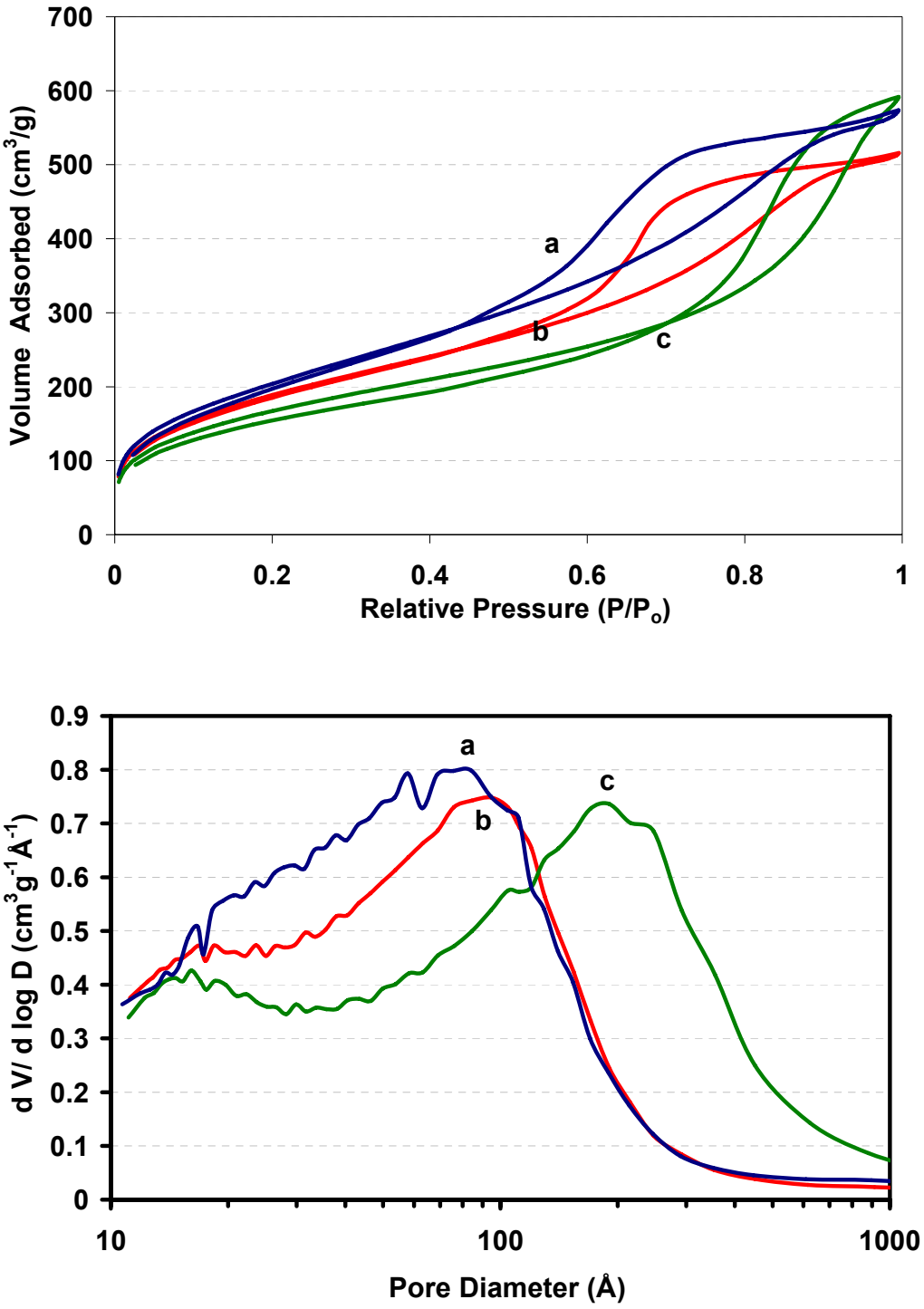

Figure 2.50 Upper: Isotherms and lower: BJH Pore size distributions (adsorption branch) of a) **POS-1** b) **POS-2** and c) **POS-3**.

These results can be explained by considering that ethanol could be acting as a pore-swelling agent. Being somewhat more hydrophobic than water, it is likely there was a preference for the concentration of ethanol to the interior of the micellar assemblies as is often the case with other less polar molecules such as butanol and pentanol.[45,46]

Other conditions were surveyed for the optimization of the material order and porosity. Judging from the isotherms, further increasing the amount of EtOH in the reaction had a detrimental effect on the surface area of the material (Figure 2.51, b). Adjusting the volume ratios of water and ethanol to 1:1 (c), decreasing the amount of base (d), and decreasing the amount of monomer (e) offered no benefit to the surface areas or long range pore order.

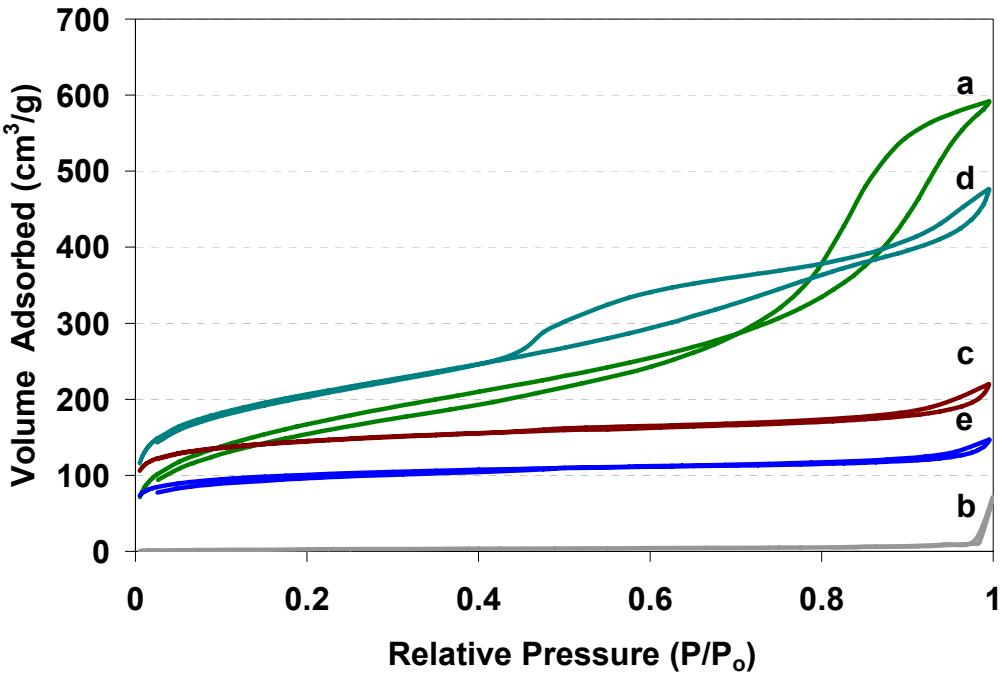

Figure 2.51 Isotherms of a) **POS-4** b) **POS-5** c) **POS-6** d) **POS-7** e) **POS-8**.

Likewise, continuing to adjust the ratios of surfactant to monomer, trying to delay the condensation process by adding the base last, and changing the base from sodium hydroxide to ammonia all resulted in low surface area, microporous materials (isotherms not shown).

It has been found in studies of mesoporous silica that prolonged aging of the material in the presence of the surfactant template at elevated temperatures or under certain pH conditions or with other additives, one can affect the structures of some silicas so that for example, they can have increased condensation of the silica network, an increased pore size or even an increased ordering of the pore structure. The groups of Ozin and Stucky aged MCM-type materials for extended periods (1-10 d) at elevated temperatures (150 ºC), which led to a metamorphosis of the silica phase and an increase in the mesopore sizes.[47,48] As a small investigation into whether the order of these materials could be improved by hydrothermal treatment, we undertook an aging study of the high surface area material **POS-1**. It was found that by aging **POS-1** in water for 3 and 5 days at 95 ºC in the presence of the surfactant, no significant improvement in the long range order of the pores occurred. The pore size distributions remained quite broad and therefore caution should be used when reporting the pore diameter values (Table 2.5). Perhaps higher temperatures or an ammonia treatment to help condense the silica network would result in an improvement in the long range order of the pores.

Table 2.5 Aging study on **POS-1**.

Material	Conditions	BET Surface Area (m^2g^{-1})	Pore Diameter[a] (Å)	Pore Volume[b] (cm^3g^{-1})
POS-1	BTES-t-SB/ C18TMACl/ NaOH	762	84	0.82
POS-1-3d	Aging 3 d	705	69	0.73
POS-1-5d	Age 5 d	692	104	0.79

[a] Maximum value of BJH pore diameter distribution (adsorption branch).
[b] BJH cumulative pore volume of pores between 10 and 3000 Å.

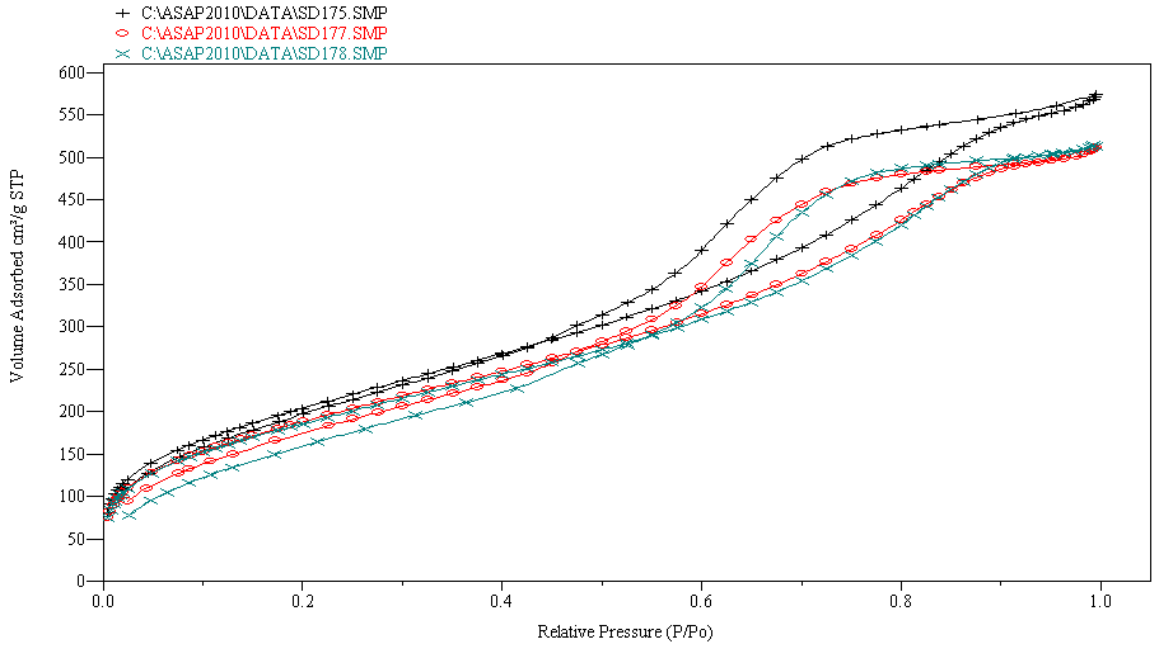

Figure 2.52 Isotherms of materials aged at 95 °C for 1 d (black), 3 d (red) and 5 d (green).

By using a base-catalyzed sol-gel procedure with C_{18}TMACl as surfactant template, we were able to produce porous organosilica materials with using solely *trans*-stilbene-bridged precursor **1**. The surface area in some cases has been observed above 900 m²/g with pores in the range of 100 Å. The long range

order of the organosilica has yet to be determined from PXRD and TEM measurements, however nitrogen porosimetry suggests a low order from the broad adsorption branches of the isotherms. With the addition of a small amount of ethanol to this procedure, we were able to increase the diameter of the pores, and achieve a more consistent and higher yield. A slight broadening of the adsorption isotherm branch occurred with the addition of a small amount of ethanol, while higher amounts, led to complete pore collapse. Although not extensively investigated, variations in the reagent ratios also had a large negative effect on the resulting surface areas and porosity, with the optimal ratios consistent with those reported by Inagaki. Future work will explore the transformation possibilities of these 100 % functional monomer materials and their ability to maintain a porous structure.

2.2.17 Acidic conditions: *trans*-stilbene materials

In contrast to the basic conditions, under acidic conditions, increasing the stilbene content was not quite as successful in creating porous materials. The procedure followed was that of Inagaki[13] *et al*. where they produced a large pore phenylene-bridged PMO using P123 as the surfactant template under acidic conditions. In these PMOs, we added increasing amounts of stilbene precursor **1** (15 %, 30 %, and 100 %) with the phenylene-bridged monomer **3**. The quality of the order of the material was judged by the steepness of the capillary condensation in the isotherms (Figure 2.53). The textural properties are listed in Table 2.6.

Table 2.6 Textural properties of materials prepared using functional monomer **1** and structural monomer **3**, under acidic pH with P123 as surfactant.

Material	% Functional Monomer	BET Surface Area (m^2g^{-1})	Pore Diameter[a] (Å)	Pore Volume[b] (cm^3g^{-1})
POS-9	0%	523	84.0	.58
PMO-1/3^{H+}	15%	553	73.9	.85
POS-10	30%	568	62.8	.78
POS-11	100%	9.4	-	.07

[a] Maximum value of BJH pore diameter distribution (adsorption branch).
[b] BJH cumulative pore volume of pores between 10 and 3000 Å.

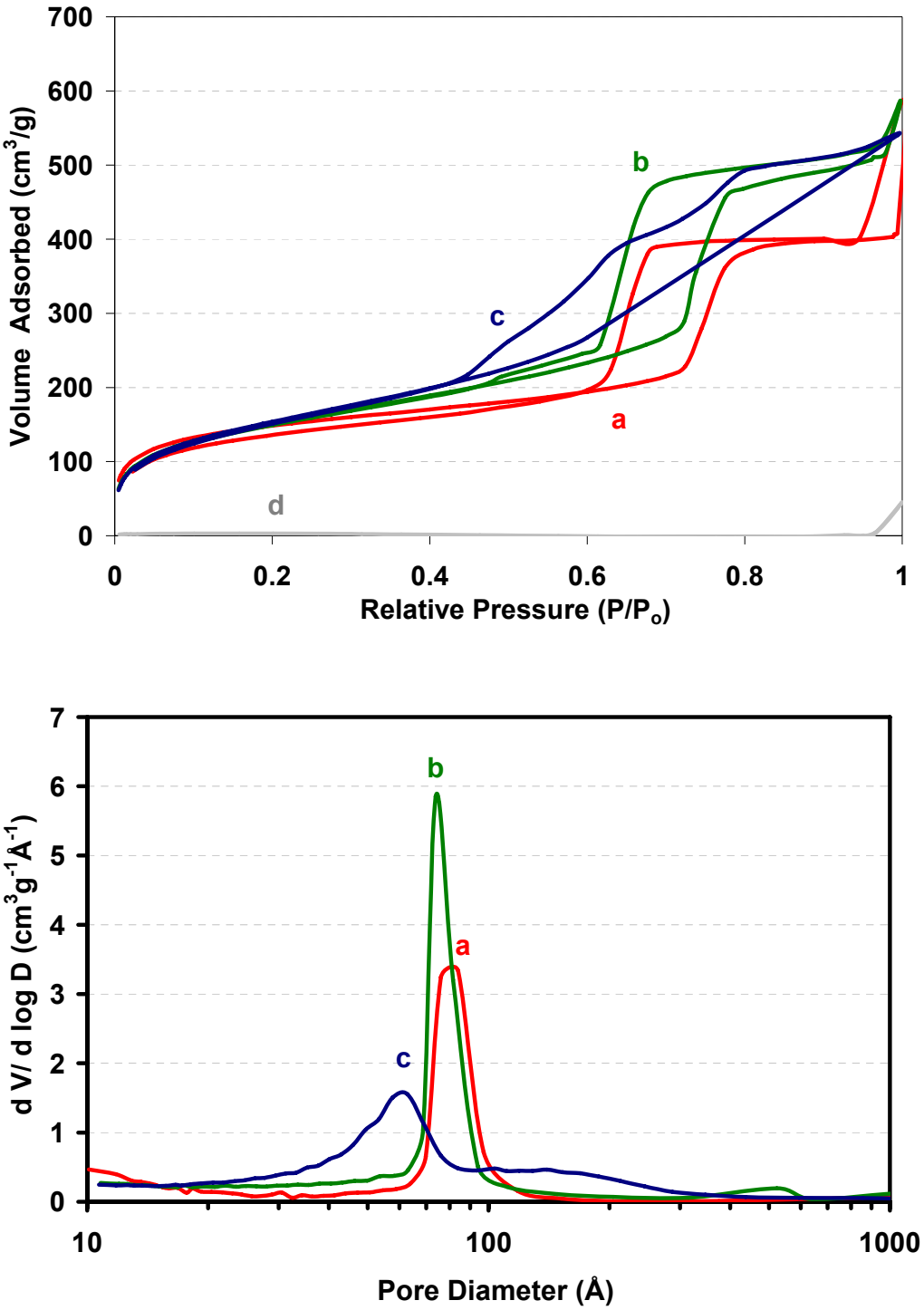

Figure 2.53 Upper: nitrogen isotherms and lower: BJH pore size distributions (adsorption branch) of a) **POS-9**, b) **PMO-1/3**$^{H+}$, c) **POS-10**, and d) **POS-11** (not in lower plot).

While the control material **POS-9** gave a well-ordered mesoporous material as expected with a high BET surface area of 523 m²/g, a BJH pore diameter of 84.0 Å and a pore volume of 0.58 cm³/g the addition of 15 % **1** to the material seemed to improve the mesoporous order. **PMO-1/3^{H+}** had a BET surface area of 553 m²/g, a slightly improved pore size distribution and a higher mesoporous volume of 0.85 cm³/g. At higher concentrations of monomer **1**, the materials suffered from a loss of order and total pore collapse in the 100 % material **POS-11.** This is not surprising as these conditions were optimized for monomer **3**.

Interestingly, as the proportion of functional monomer **1** was increased in the materials, it became apparent from CP MAS ^{29}Si NMR spectroscopy that a new silicon environment was forming. A sharp peak for a -Si(OH)$_3$ at (-55 ppm) was becoming increasingly expressed (Figure 2.54).

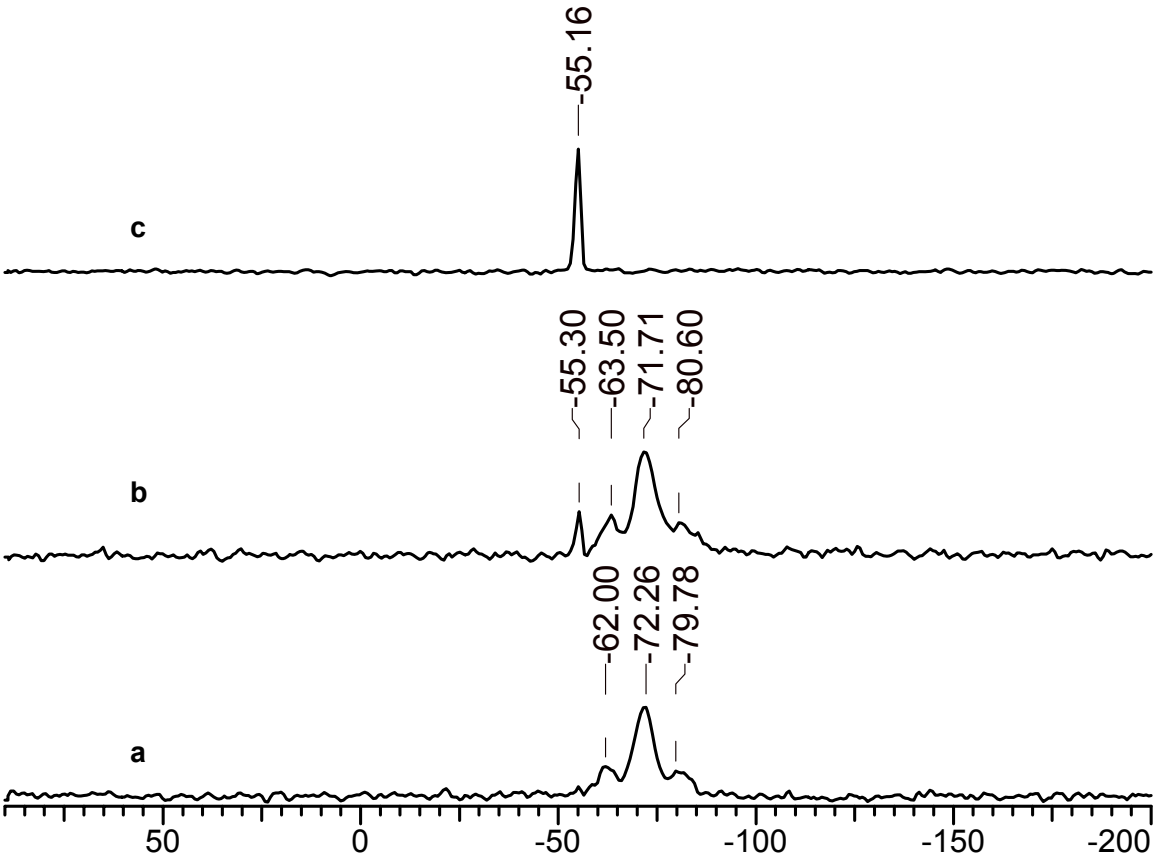

Figure 2.54 CP MAS ^{29}Si NMR of materials containing a) 15 %, b) 30 %, c) 100 % BTETS **1** under acidic pH with P123. Stilbene-bridged bis(silanetriol) **BST** appearing at -55 ppm is not observed at 15 % loading of **1**.

This was postulated to be a result of the formation of a bis(silanetriol), which forms from complete hydrolysis of the ethoxy groups on silicon and crystallization during the preparation. This product was prepared by Corriu *et al.*,[34] where **1** hydrolyzes and crystallizes in a biphasic medium of ether and aqueous acetic acid (Figure 2.55). This is problematic for PMO synthesis where the goal is to have the monomer condense around the surfactant template.

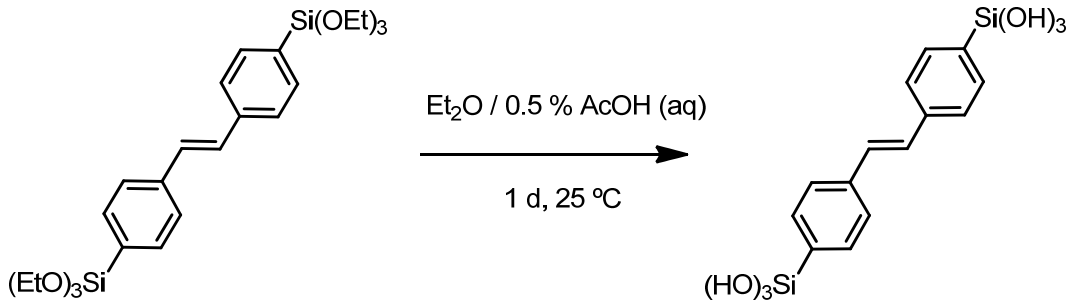

BTETS (1) **BST**

Figure 2.55 Corrius's preparation of stilbene-bridged bis(silanetriol) **BST**. [34]

Judging from the CP MAS ^{29}Si NMR spectra (Figure 2.54 above), at 30 % loading of **1**, **POS-10** was a mixture of condensed precursors (showing T peaks from -62.5 to -80 ppm) and crystallized triol (T^0 peak at -55 ppm). At 100% **1**, the entirety of the monomer had crystallized with a sole T^0 peak at -55 ppm. The material was imaged by TEM and optical microscopy to reveal a transparent, nonporous, plate-like crystal (Figure 2.56).

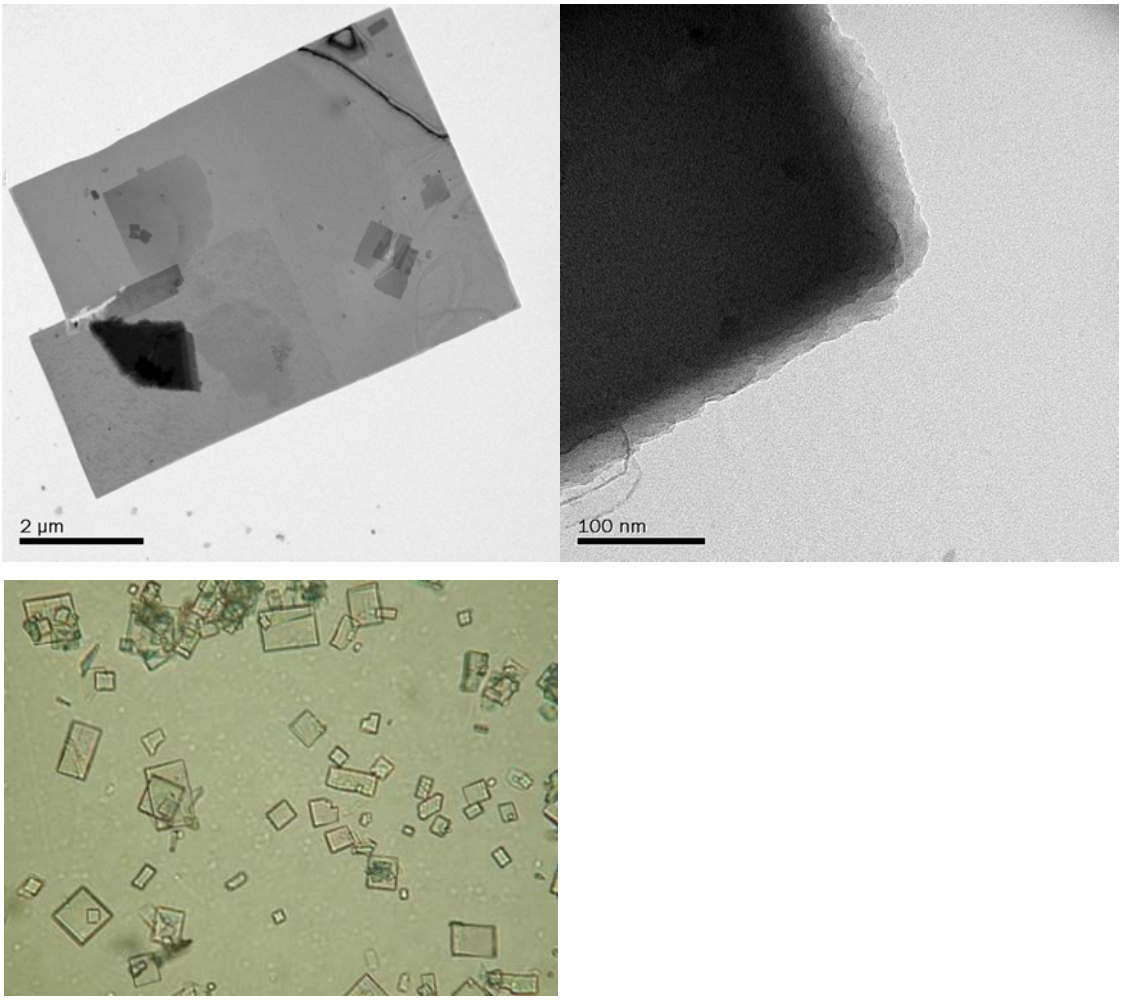

Figure 2.56 Upper: TEM and lower: optical microscope images of materials containing 100 % **1** prepared under acidic conditions, showing nonporous, bis(silanetriol) plate-like crystals.

Interestingly, despite the fact that our conditions were harsher than those of Corriu *et al*., no triol was observed when **PMO-1/3^{H+}** was prepared using 15 % loading of **1** relative to **3**. This indicates that at least 15 % (but less than 30 %) of the functional monomer **1** can be incorporated into a PMO with **3** under acidic conditions before an observable amount of triol is found. Although, there was an upper limit of less than 30 % of the functional monomer being able to be incorporated into the PMOs under acidic conditions, no triol was observed under

basic conditions even at 100% loadings. This observation is likely found as a result of the kinetics of hydrolysis and condensation at the various pH ranges. Under acidic conditions, hydrolysis is fast, while condensation is slow, while under basic conditions, the opposite is true.

2.2.18 Acidic conditions: *cis*-stilbene materials

It is interesting to note that when materials were made with an increased amount of *cis*-stilbene monomer **2**, in combination with the biphenylene-bridged monomer **4**, using Brij 76 as surfactant, the same problems of siloxane hydrolysis and crystallization that occurred with the *trans*-stilbene monomer under acidic conditions with P123 as surfactant did not exist. This is believed to be in part due to an increased solubility of the *cis* versus the *trans* isomer (**2** versus **1**). As shown in the CP MAS NMR spectra (Figure 2.57), even in the 100 % *cis*-stilbene material, there is no C-Si bond confirmed by the lack of Q sites in the Si NMR.

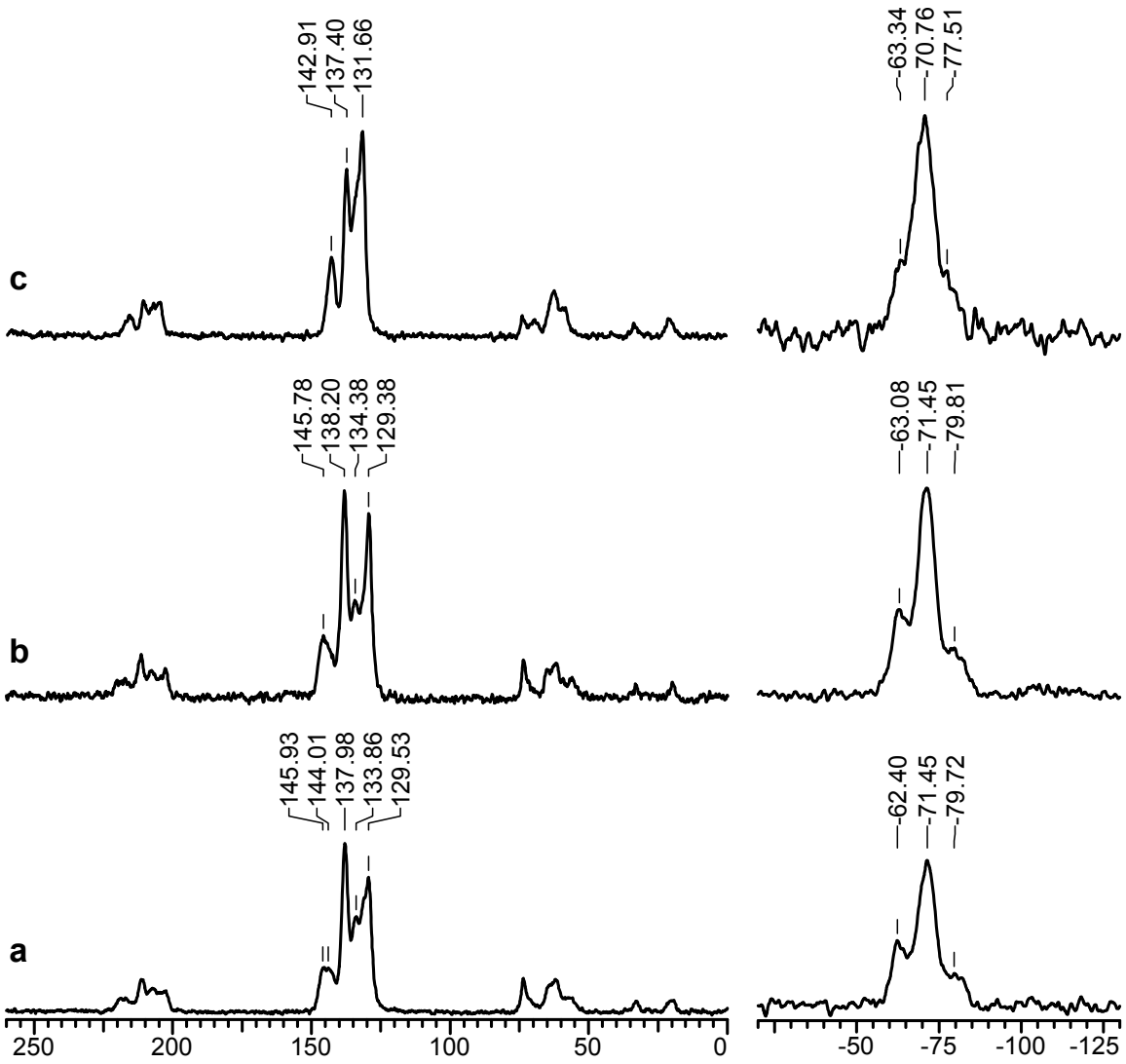

Figure 2.57 CP MAS ^{13}C (left) and CP MAS ^{29}Si NMR (right) of a) **PMO(15)-2/4^{H+}** b) **PMO(30)-2/4^{H+}** and c) 100% *cis*-stilbene material prepared under acidic pH with Brij 76 as surfactant.

Unfortunately, it appeared however that the materials began to lose mesoporous order upon increasing the *cis*-stilbene content based on the nitrogen adsorption isotherms, BJH pore size distribution plots and TEM images. (Figure 2.58- Figure 2.61).

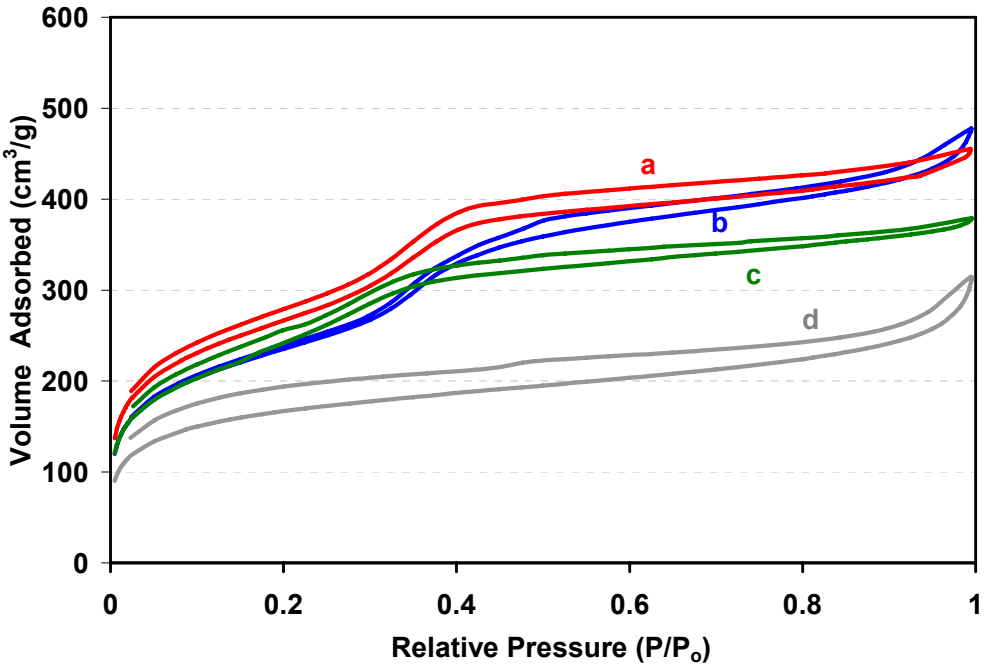

Figure 2.58 Isotherms of materials incorporating a) 0% b) 15% c) 30% and d) 100% *cis*-stilbene precursor with **4** as structural monomer under acidic pH with Brij 76 as surfactant.

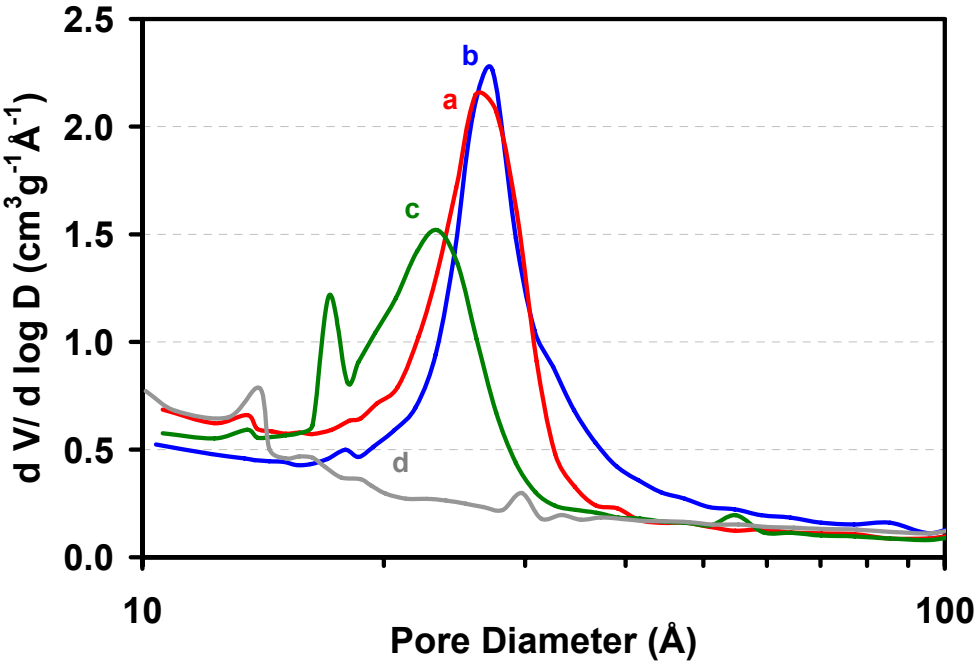

Figure 2.59 BJH adsorption pore size distribution plots of materials incorporating a) 0% b) 15% c) 30% and d) 100% *cis*-stilbene precursor with **4** as structural monomer under acidic pH with Brij 76 as surfactant.

.

Table 2.7 Textural properties of *cis*-stilbene and biphenylene containing PMOs using Brij 76 under acidic conditions.

Material	BET Surface Area (m^2g^{-1})	Pore Diameter[a] (Å)	Pore Volume[a] (cm^3g^{-1})
PMO(15)-2/4^{H+}	952	26	0.65
PMO(30)-2/4 $^{H+}$	880	21	0.54
PMO(100%)-2^{H+}	583	-	-

[a] Maximum value of BJH pore diameter distribution (adsorption branch).
[b] BJH cumulative pore volume of pores between 10 and 3000 Å.

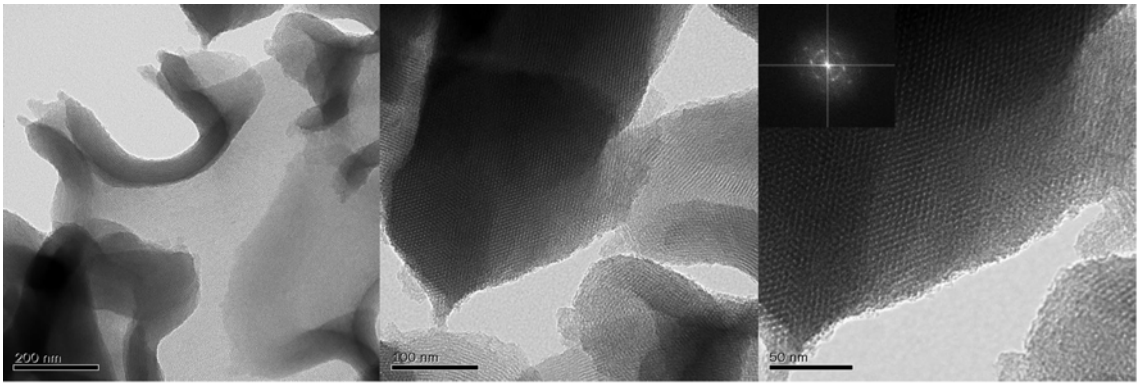

Figure 2.60 TEM images of 30% *cis*-stilbene material showing ordered pore structure. Inset of third image shows electron diffraction pattern.

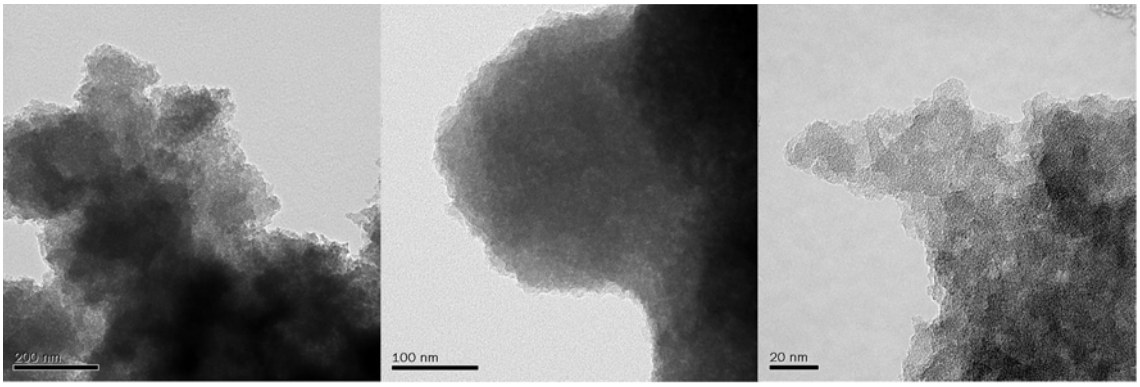

Figure 2.61 TEM images of 100% *cis*-stilbene material showing lack of ordered pores.

As can be seen from the isotherm and TEM images, the material made from 100 % *cis*-stilbene precursor **2** is not well ordered, although it does have a relatively high surface area of 583 m^2/g, despite the lack of an ordered pore structure.

2.3 Conclusions

We have created novel, organosilica based materials, which incorporate functional groups capable of being transformed without negatively affecting the materials properties. The functional olefin of the *trans*- and *cis*-stilbene precursor (**1** and **2**) was synthesized and incorporated with aromatic-bridged structural monomers (phenylene or biphenylene-bridged, **3** or **4**), producing a variety of ordered organosilica materials. The resulting materials were characterized by various techniques including CP MAS ^{13}C and ^{29}Si NMR, nitrogen physisorption analysis, SEM, and powder XRD among others. A large-pore material incorporating 15 % **1** with **3** (**PMO-1/3^{H+}**) was treated with osmium and imaged with TEM coupled with EDX spectroscopy. The results indicated the uniform presence of the olefin about the material.

PMO-1/3^{H+} was assessed for further chemical modifications. A highly successful ozonolysis demonstrated an ability to introduce a uniformly oxidized surface to periodic mesoporous organosilica without considerably affecting the porous nature of the material. Further attempts at increasing the organic complexity of the material through imine formation required optimization but was shown to be effective.

Novel PMOs with increased functional character were also prepared by incorporating more *cis*- and *trans*-stilbene component. Under acidic conditions with P123 as surfactant, at 30 % *trans*-stilbene component and above, the resulting materials were contaminated with the hydrolyzed stilbene-bridged bis(silanetriol), which crystallizes readily from the mixture. Materials of increasing *cis*-stilbene concentrations under acidic conditions using Brij 76 as a templating agent, showed no signs of bis(silanetriol) formation by CP MAS ^{29}Si NMR, however at increasing olefin concentrations, the materials began to lose ordered pore structures as demonstrated by the isotherms and TEMs. Under basic conditions, the resulting materials from the *trans*-stilbene monomer **1** displayed nitrogen isotherms characteristic of high surface area silicas, despite a low long-range order. The use of a small amount of ethanol in the procedure resulted in higher yields of organosilica with slightly larger pore diameters than is normally obtained using a purely aqueous system. Future work will seek to improve the mesoporous order of these functionally-rich materials and explore their transformation potential.

Organosilica materials remain a growing area of interest within the research community. The continued investigation of such materials will lead to contributions to many other related areas such as catalysis, sensing, and chromatography.

2.4 References

(1) Wang, Z.; Sharpless, K. *J. Org. Chem.* **1994**, *59*, 8302-8303.
(2) Shi, Y. *Acc. Chem. Res.* **2004**, *37*, 488-496.
(3) Long, J.; Yuan, Y.; Shi, Y. *J. Am. Chem. Soc.* **2003**, *125*, 13632-13633.
(4) Sayari, A.; Wang, W. *J. Am. Chem. Soc.* **2005**, *127*, 12194-12195.
(5) Ding, X.; Lv, X.; Hui, B.; Chen, Z.; Xiao, M.; Guo, B.; Tang, W. *Tetrahedron Lett.* **2006**, *47*, 2921-2924.
(6) Chatterjee, A. K.; Choi, T.-L.; Sanders, D. P.; Grubbs, R. H. *J. Am. Chem. Soc.* **2003**, *125*, 11360-11370.
(7) Chang, H.-K.; Datta, S.; Das, A.; Odedra, A.; Liu, R.-S. *Angew. Chem., Int. Ed.* **2007**, *46*, 4744-4747.
(8) Murata, M.; Ishikura, M.; Nagata, M.; Watanabe, S.; Masuda, Y. *Org. Lett.* **2002**, *4*, 1843-1845.
(9) Hopf, H.; Hucker, J.; Ernst, L. *Eur. J. Org. Chem.* **2007**, 1891-1904.
(10) Bosanac, T.; Wilcox, C. S. *Org. Lett.* **2004**, *6*, 2321-2324.
(11) Hunks, W. J.; Ozin, G. A. *Chem. Commun.* **2004**, 2426-2427.
(12) Kapoor, M. P.; Yang, Q.; Inagaki, S. *J. Am. Chem. Soc.* **2002**, *124*, 15176-15177.
(13) Goto, Y.; Inagaki, S. *Chem. Commun.* **2002**, 2410-2411.
(14) Wang, W. H.; Xie, S. H.; Zhou, W. Z.; Sayari, A. *Chem. Mater.* **2004**, *16*, 1756-1762.
(15) Burleigh, M. C.; Jayasundera, S.; Thomas, C. W.; Spector, M. S.; Markowitz, M. A.; Gaber, B. P. *Colloid Polym. Sci.* **2004**, *282*, 728-733.
(16) Webb, P. A.; Orr, C. *Analytical methods in fine particle technology*; Micromeritics Norcross, GA, 1997; Vol. 229.
(17) Kruk, M.; Jaroniec, M. *Chem. Mater.* **2001**, *13*, 3169-3183.
(18) Kruk, M.; Jaroniec, M.; Ko, C.; Ryoo, R. *Chem. Mater.* **2000**, *12*, 1961-1968.
(19) Ryoo, R.; Ko, C. H.; Kruk, M.; Antochshuk, V.; Jaroniec, M. *J. Phys. Chem. B* **2000**, *104*, 11465-11471.
(20) Cerveau, G.; Corriu, R.; Lepeytre, C.; Mutin, P. *J. Mater. Chem.* **1998**, *8*, 2707-2713.
(21) Cerveau, G.; Corriu, R.; Framery, E. *Chem. Commun.* **1999**, 2081-2082.
(22) Oviatt Jr, H.; Shea, K.; Small, J. *Chem. Mater.* **1993**, *5*, 943-950.
(23) It should be noted that J. Brinker, in Sol-Gel Science (p. 101), describes the subscript in Q notation as indicating the number of that type of silicon atom in the molecule.
(24) Engelhardt, G.; Jancke, H. *Polym. Bull. (Berlin)* **1981**, *5*, 577-584.
(25) Yang, H.; Coombs, N.; Ozin, G. A. *Nature* **1997**, *386*, 692-695.
(26) Inagaki, S.; Guan, S.; Fukushima, Y.; Ohsuna, T.; Terasaki, O. *J. Am. Chem. Soc.* **1999**, *121*, 9611-9614.
(27) Kapoor, M. P.; Inagaki, S. *Chem. Lett.* **2004**, *33*, 88-89.
(28) Inagaki, S.; Guan, S.; Ohsuna, T.; Terasaki, O. *Nature* **2002**, *416*, 304-307.

(29) Grun, M.; Unger, K. K.; Matsumoto, A.; Tsutsumi, K. *Microporous Mesoporous Mater.* **1999**, *27*, 207-216.
(30) Sayari, A.; Hamoudi, S.; Yang, Y.; Moudrakovski, I. L.; Ripmeester, J. R. *Chem. Mater.* **2000**, *12*, 3857-3863.
(31) A wormhole structure may still contain a narrow pore size distribution but does not have the same degree of long-range ordeing as is seen in 2D hexagonal or other mesophases.
(32) Waki, M.; Mizoshita, N.; Ohsuna, T.; Tani, T.; Inagaki, S. *Chem. Commun.* **2010**, *46*, 8163-8165.
(33) Yang, Y.; Sayari, A. *Chem. Mater.* **2008**, *20*, 2980-2984.
(34) Cerveau, G.; Chappellet, S.; Corriu, R. J. P.; Dabiens, B.; Le Bideau, J. *Organometallics* **2002**, *21*, 1560-1564.
(35) Arenas, J.; Tocon, I.; Otero, J.; Marcos, J. *J. Phys. Chem.* **1995**, *99*, 11392-11398.
(36) Degrado, S. J.; Mizutani, H.; Hoveyda, A. H. *J. Am. Chem. Soc.* **2002**, *124*, 13362-13363.
(37) Vachal, P.; Jacobsen, E. N. *J. Am. Chem. Soc.* **2002**, *124*, 10012-10014.
(38) Rengasamy, R.; Curtis-Long, M. J.; Seo, W. D.; Jeong, S. H.; Jeong, I.-Y.; Park, K. H. *J. Org. Chem.* **2008**, *73*, 2898-2901.
(39) March, J.; NetLibrary, I. *Advanced organic chemistry: reactions, mechanisms, and structure*; McGraw-Hill New York, 1968.
(40) Toste, F.; Chatterjee, A.; Grubbs, R. *Pure Appl. Chem.* **2002**, *74*, 7-10.
(41) Alcaide, B.; Almendros, P.; Alonso, J.; Aly, M. *Org. Lett* **2001**, *3*, 3781-3784.
(42) Lambert, J. B.; Shurvell, H. F.; Lightner, D. A.; Cooks, G. R. *Organic structural spectroscopy*; Prentice Hall, 1998.
(43) Yoshina-Ishii, C.; Asefa, T.; Coombs, N.; MacLachlan, M. J.; Ozin, G. A. *Chem. Commun.* **1999**, 2539-2540.
(44) Shea, K. J.; Loy, D. A. *Chem. Mater.* **2001**, *13*, 3306-3319.
(45) Feng, P. Y.; Bu, X. H.; Pine, D. J. *Langmuir* **2000**, *16*, 5304-5310.
(46) Kleitz, F.; Solovyov, L. A.; Anilkumar, G. M.; Choi, S. H.; Ryoo, R. *Chem. Commun.* **2004**, 1536-1537.
(47) Khushalani, D.; Kuperman, A.; Ozin, G. A.; Tanaka, K.; Coombs, N.; Olken, M. M.; Garcés, J. *Adv. Mater.* **1995**, *7*, 842-846.
(48) Huo, Q. S.; Margolese, D. I.; Stucky, G. D. *Chem. Mater.* **1996**, *8*, 1147-1160.

Chapter 3

Chiral periodic mesoporous organosilica

3.1 Introduction

Chirality or “handedness” is an important property of many natural and synthetic materials. The applications of such materials are found in areas of chemistry, physics and biology. Origins of the near homochirality of most natural molecules such as amino acids and sugars is also a topic of interest for many researchers.[1] The chirality of inorganic materials such as quartz is often discussed as one potential mechanism for the preparation of enantiomerically enriched organic molecules, either by selective adsorption of one enantiomer, selective destruction or promotion of some other reaction by absorption to this chiral surface. Thus preparing solid state materials that possess chirality is an important step in understanding any processes by which chirality may be transmitted in in the solid state and in understanding chirality transfer in general.

Periodic mesoporous organosilicas (PMOs) are hybrid organic/inorganic materials offering high surface areas and excellent meso-scale order.[2-4] Control over the properties of such materials is possible because of the variety of organic groups tolerated in the synthetic precursors.[5,6] It has been shown by Inagaki and others that in addition to ordered pore structures, exceptional molecular-scale ordering in the pore-walls can be obtained from aromatic monomers under appropriate synthetic conditions.[7-11,12] The synthesis of these materials with crystal-like pore walls with molecular scale order was a significant advancement

in the development of mesoporous hybrid materials, with potential for producing, for example, conducting materials.

One precursor which exhibited this molecular scale ordering was 4,4'-bis(triethoxysilyl)biphenyl, or BTEBP (Figure 3.1).[8] It is interesting to note that biphenyl itself adopts a chiral conformation in the ground state, with a 40 ° dihedral angle about the central C-C bond.[13] A solid state analog of this species, 4,4'-di(*t*-butyl)biphenyl, has a very similar structure, with its two most stable polymorphs displaying a dihedral angle close to 40 °.[14]

Our group has reported the synthesis of both enantiomers of a chiral, tetra-substituted biaryl precursor,[15] (Figure 3.1) which has recently been used as a chiral dopant to impart enantiomeric conformational preferences to BTEBP in the solid state of an ordered PMO.[16]

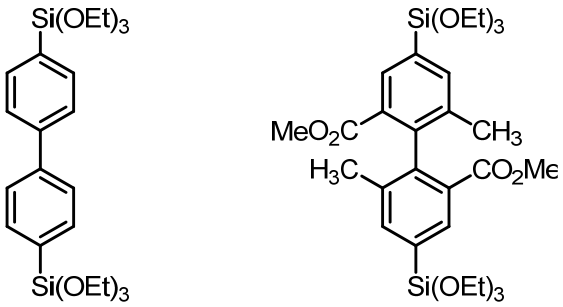

BTEB

tetra-substituted biaryl synthesized by Crudden et al.

Figure 3.1 4,4'-bis(triethoxysilyl)biphenyl, BTEBP and a chiral tetra-substituted biaryl synthesized by Crudden et al.[16]

In this work, we demonstrate the synthesis of ordered PMOs possessing an optically active solid-state arrangement of biphenylene-bridging groups. The

optical activity is most likely a result of a stable, non-zero dihedral angle between the planes of the rings in the biphenylene precursor, caused by incorporations of small amounts of the novel chiral monomer (**CM**) synthesized here for the first time. It is also likely that the highly ordered, crystalline nature of the materials under basic pH is aiding in the propagation of this asymmetric biphenylene arrangement.

3.2 Results and discussion

3.2.1 Monomer Synthesis

The chiral templating monomer **CM** was synthesized as shown in Scheme 5. A dimerization of 4-bromostyrene using Grubbs' 2nd generation metathesis catalyst with the loss of ethane results in near-quantitative yield of the desired 4,4'-dibromostilbene.[17] Both enantiomers of the *vic*-diol were obtained from the high-yielding, Sharpless asymmetric dihydroxylation protocol.[18] Subsequent ketalization and bromo-iodo halogen exchange were carried out prior to incorporating the triethoxysilyl groups *via* a C-Si coupling reaction to yield monomer **CM**.[19] Attempts at performing this C-Si coupling from the dibromo precursor resulted in a large amount of the mono-silylated by-product (Figure 3.2), which ultimately was difficult to separate from the desired bis-silylated product, however by converting to iodo substituents, we were able to get higher yields and isolate a product free of any impurities as confirmed by ^{1}H and ^{13}C NMR. The enantioselectivity of the dihydroxylation transformation was

determined to be > 99%, two steps later at the di-iodo intermediate by supercritical fluid chromatography (SFC).

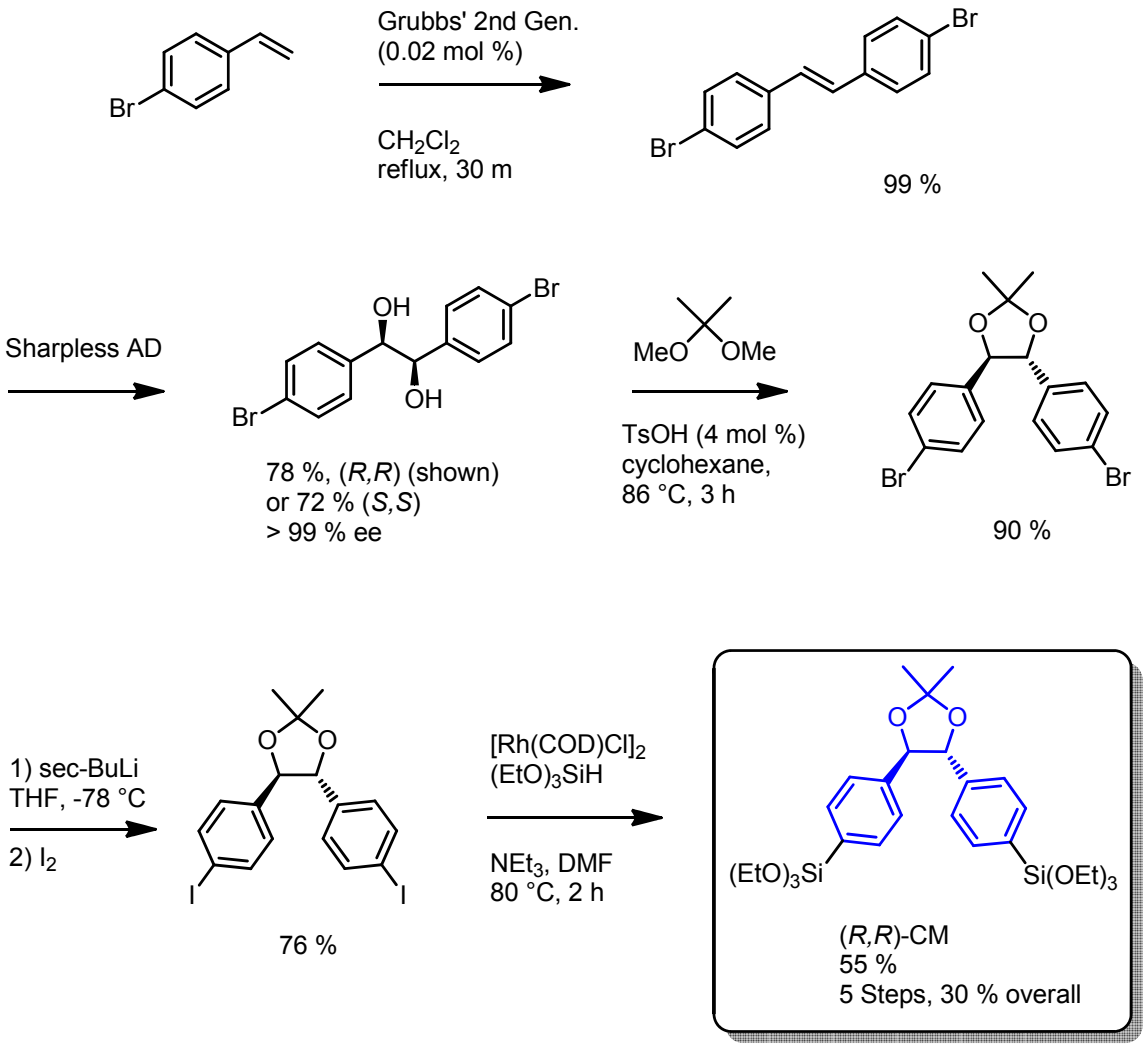

Scheme 5. Synthesis of chiral templating monomer **CM**.

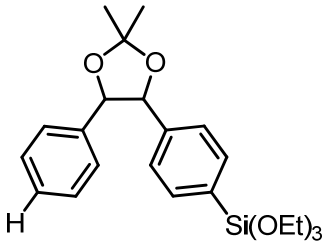

Figure 3.2 Byproduct of C-Si coupling reaction **H/Si-CM**.

The motivation for the use of this templating monomer comes from the high stereoselectivity that can be obtained in the asymmetric dihydroxylation reaction as well as the presence of the aromatic rings that should be able to interact with the aromatic rings of the BTES-biphenyl (**BP**) precursor (Figure 3.3).

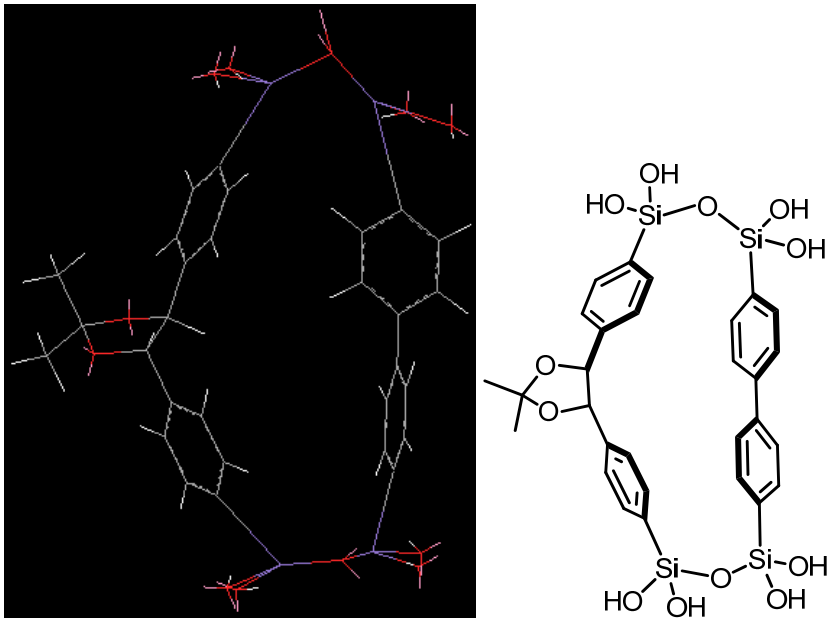

Figure 3.3 Possible chiral templating interactions of **CM** with biphenylene precursor (**BP**).

3.2.2 Material preparation

Periodic mesoporous organosilica with chiral templating monomer (**CM**) was prepared using an ionic templating procedure at high pH, previously employed by Inagaki's group[8] which afforded materials with molecular scale periodicity. The effect of incorporating variable amounts of enantiopure **CM** was evaluated. The materials were extracted with acid-free ethanol to avoid ketal deprotection.

It was initially envisioned that the chiral monomer **CM** would be covalently incorporated into the material and the resulting properties of such PMOs would be examined, however, during the course of the study, it became apparent that **CM** was not being incorporated to the extent expected. In Figure 3.4, the ^{13}C NMR of **CM** has the diagnostic methyl and quaternary carbon peaks of the ketal at 27 and 110 ppm respectively distinct from those of **BP**. As well, the benzylic carbons of **CM** at 85 ppm are evident. Unfortunately, none of these resonances were apparent at a 15 % loading in **BR15**. Furthermore, after increasing the proportion of **CM** to 30 % total monomer concentration in **BR30**, the expected peaks were still not visible.

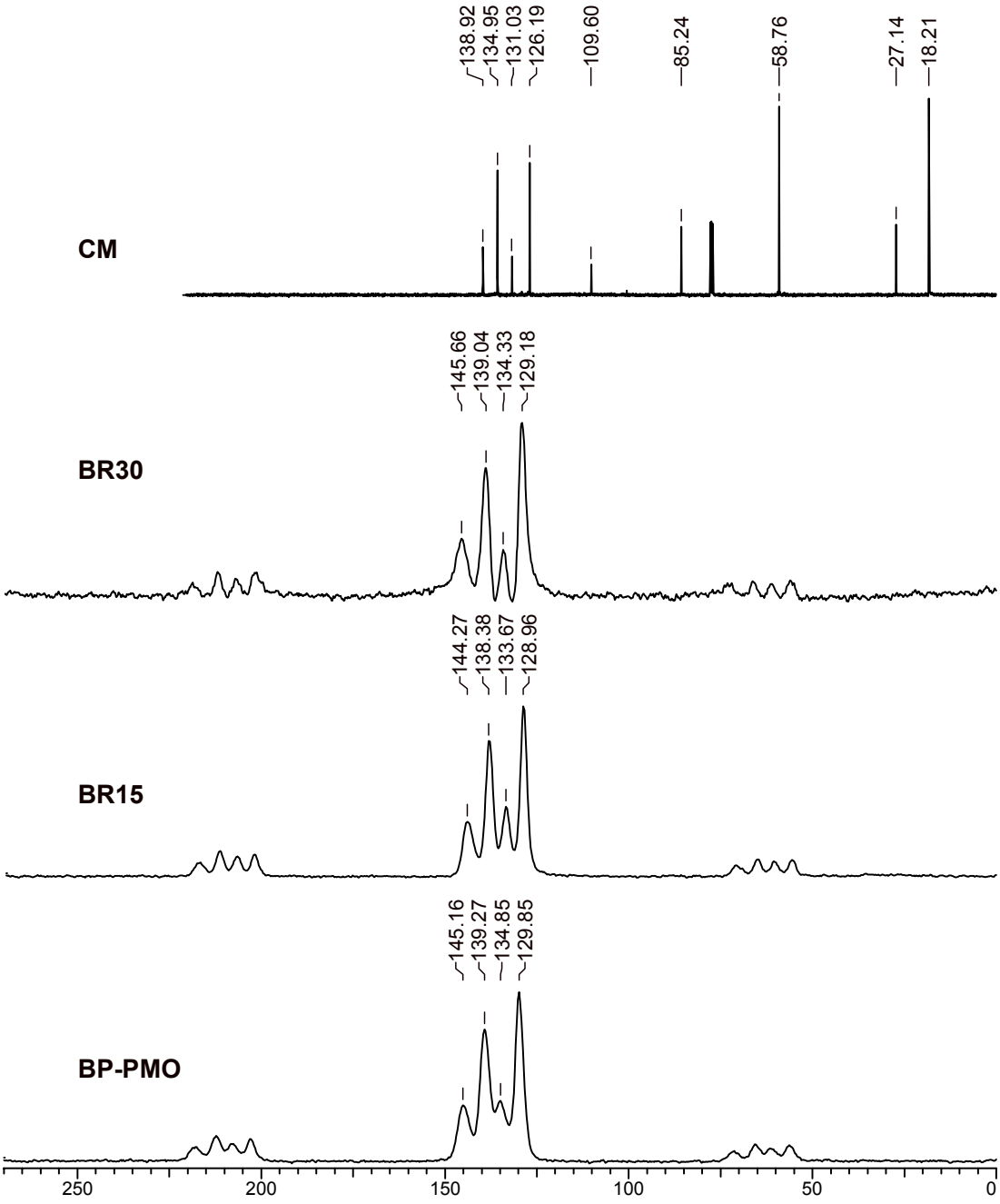

Figure 3.4 ^{13}C NMR of precursor (**CM**) and ^{13}C CP MAS NMR of PMOs **BR30**, **BR15**, **BP-PMO**.

To confirm the absence of **CM** in the materials, confocal micro-Raman spectroscopy was performed. The instrument used for the analysis was able to interrogate a volume of ~1 μm^3 of material. This is roughly two orders of

magnitude greater than the lattice dimensions of the porous mesophase and should be fairly representative of the structural composition. An acid-catalyzed material using Brij 76 as surfactant and 100 % ***R*-CM** as precursor, (**AR100**), was used as a control spectrum for **CM** in the condensed state. The strongest peaks occurred at 1130, 856, and 633 cm^{-1}. Although most peaks of **AR100** were overlapping with those of **BP**, the most intense peaks of **CM**, were not increasingly observed in **BS15**, **BS20** or **BS30** (Figure 3.5). It should be noted that weak peaks at 2870-2950 cm^{-1} in the region for C-H alkyl stretching were present, however these cannot be confidently assigned to **CM** due to the likelihood of a small amount of surfactant remaining in the material.

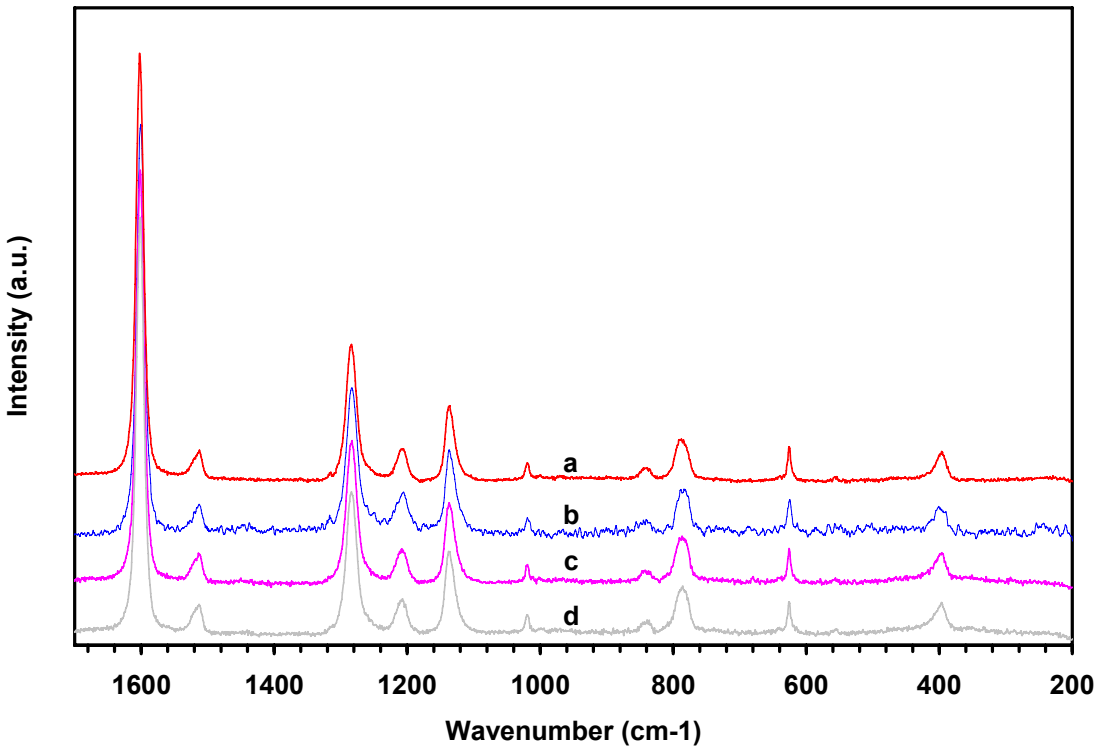

Figure 3.5 Raman spectra of a) **BP-PMO** (0 % *S*-**CM**) b) **BS15** c) **BS20** and d) **BS30** showing a lack of any signals from ***S*-CM**.

Despite the absence of **CM**, the TEM images of the materials showed a successful mesophase templating process had occurred with the presence of a porous structure (Figure 3.6-Figure **3.11**).

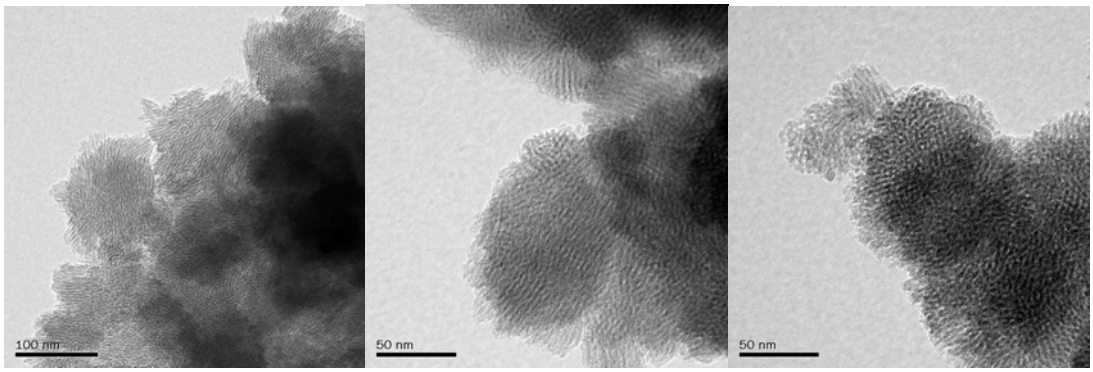

Figure 3.6 TEM image of **BS15**.

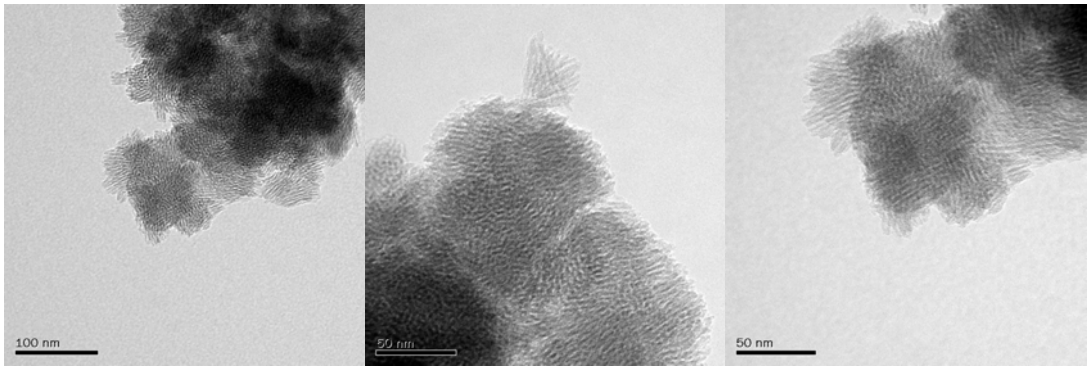

Figure 3.7 TEM images of **BS20.**

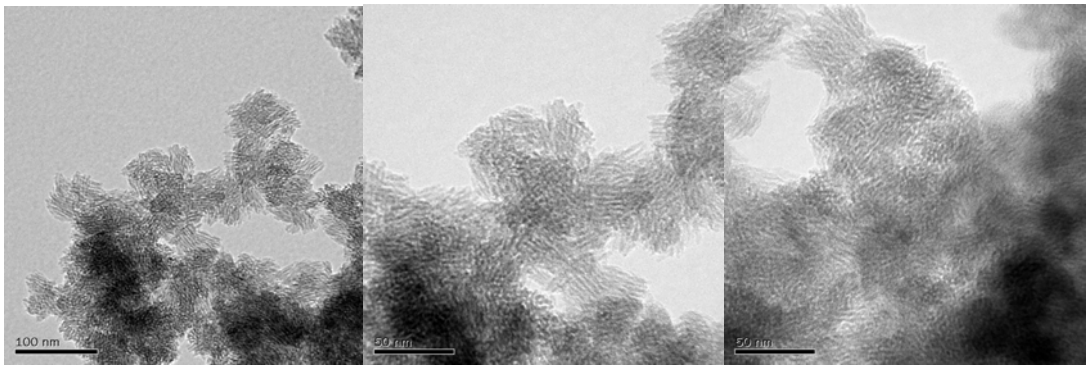

Figure 3.8 TEM images of **BS30**.

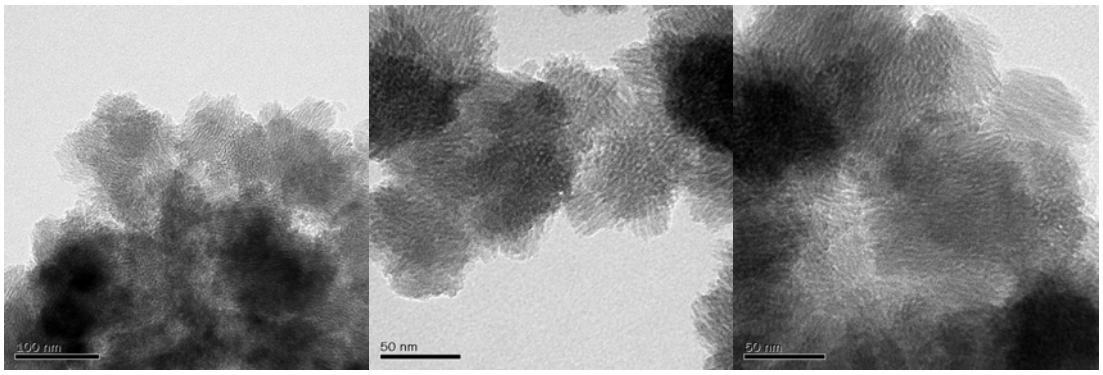

Figure 3.9 TEM images of **BR15**.

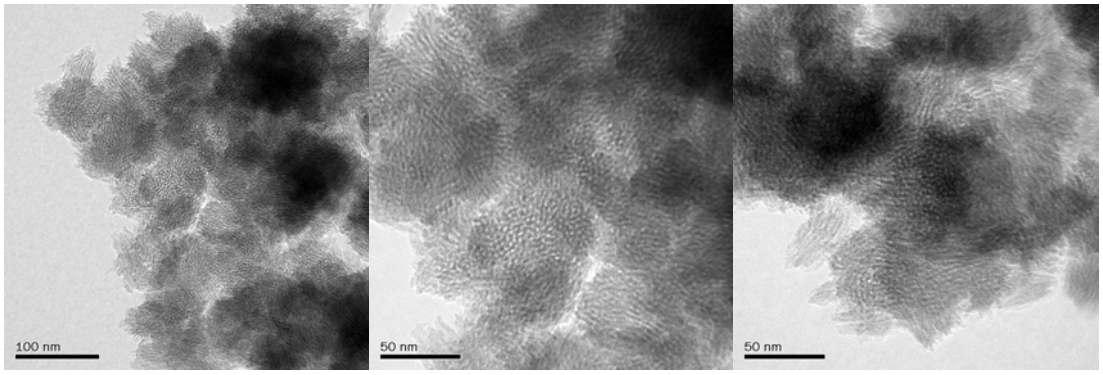

Figure 3.10. TEM imagesof **BR20.**

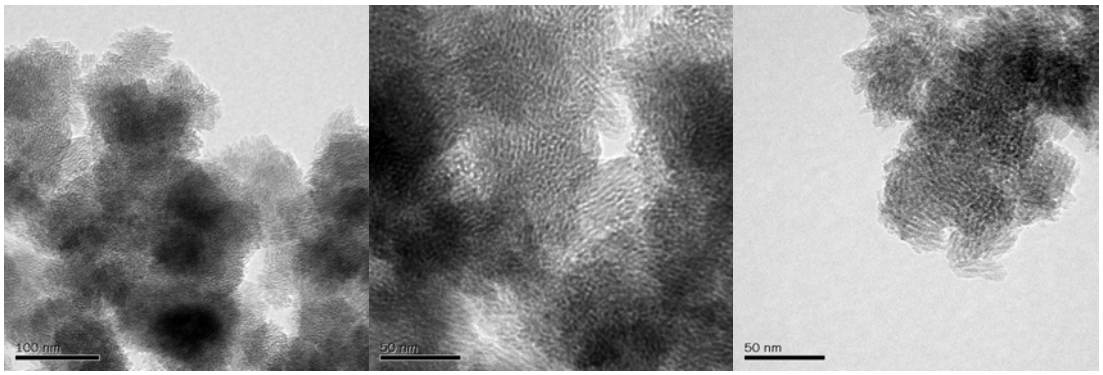

Figure 3.11 TEM images of **BR30**.

The difficulties in incorporating higher amounts of ‘dopant’ monomers into biphenylene-bridged PMOs has been observed in our lab under these same high

pH conditions, for example, with the tetra-substituted biaryl from Figure 3.1. The reasons for the lack of incorporation of **CM** into the materials are likely related to a combination of the low solubility of the monomer, a significant difference in condensation kinetics between **CM** and the biphenylene precursor or due to poor **CM**-surfactant interactions, which is known to slow condensation.

3.2.3 Morphology

The overall morphology of the materials did not appear to differ very much from a PMO made entirely of biphenylene-bridged monomer (**BP-PMO**). Even at 30 % chiral templating monomer, the particles still appeared to be somewhat spherical, and very small (most < 500 nm in diameter), much like the **BP-PMO**.

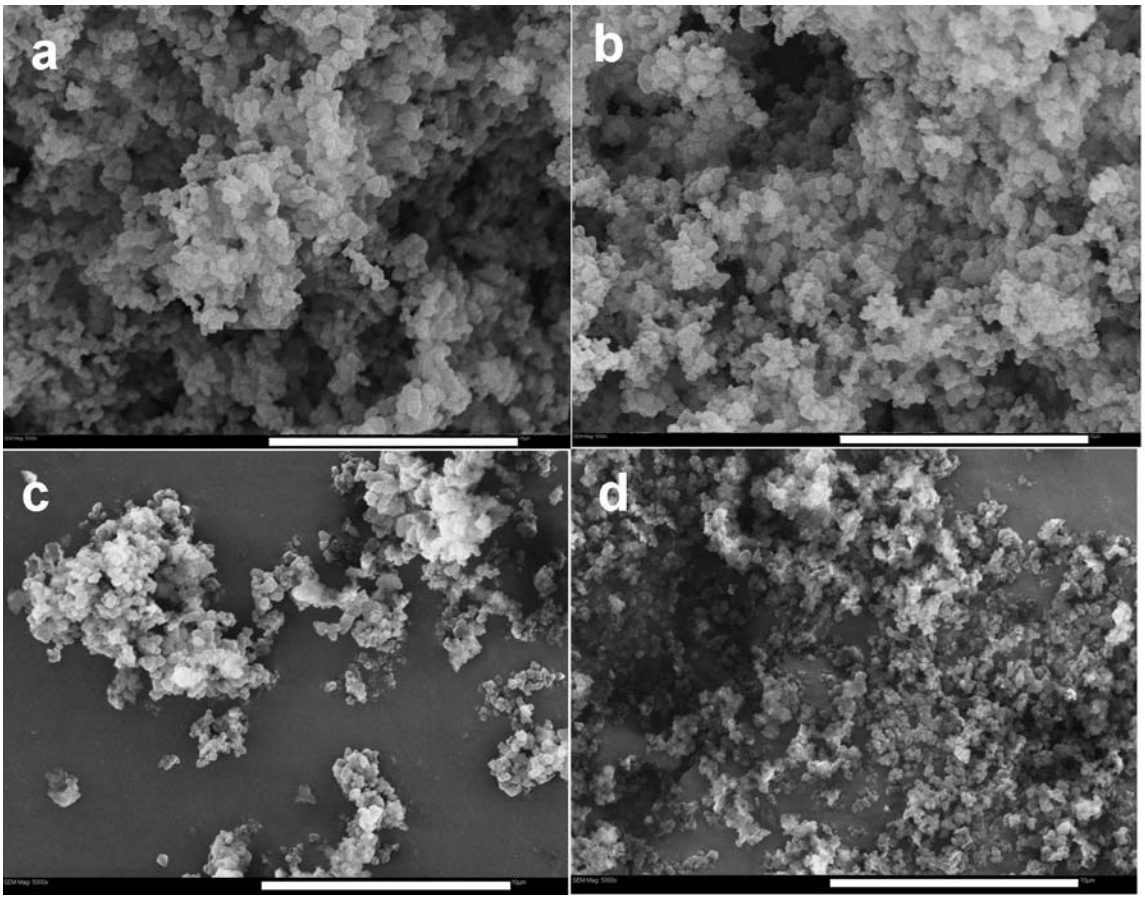

Figure 3.12 SEM images of a) **BP-PMO** b) **BR15** c) **BR20** and d) **BR30** (scale bar = 10 μm)

3.2.4 Circular dichroism

Despite the lack of incorporation of **CM** into the PMOs as determined from CP MAS ^{13}C NMR and Raman spectroscopy, it was the presence of a distinct circular dichroism spectrum that was most surprising (Figure **3.13**). The CD spectrum of alcohol-soluble **CM** was taken in ethanol while those of the PMOs were recorded as dilute suspensions in distilled water. It should be noted that identical CD spectra were obtained when using water or ethanol for several PMO suspensions, but water was chosen as the suspending liquid as it has a lower UV

cutoff (205 nm) than ethanol (210 nm). Due to the heterogeneous system and the associated difficulties in determining concentrations of suspended species,[20] we only wished to use the CD measurements in a qualitative or semi-quantitative sense at best. It was imperative to avoid over-concentrated suspensions which scattered or blocked the light and led to high absorbance readings with no CD signal. A concentration of approximately 0.05 mg/mL was used for the suspensions. Pelletized potassium bromide was examined as a matrix for CD measurements, however problems arose including pellet opacity which led to high absorbance and irreproducible spectra at varying analyte concentrations which were not difficulties under the liquid suspension conditions.

The chiral ***S*-CM** monomer has a negative peak at 228 nm (Figure **3.13**, a). The PMOs templated with 15 % ***S*** or ***R*-CM** gave mirror-like Cotton effects (Figure **3.13**, b and c respectively) with peaks at 248 nm and 300 nm. Here it is important to note the UV absorbance λ_{max} of **CM** and **BP** are 225 nm and 260 nm respectively (Figure 3.13 e, f). The CD spectrum of the control material, **BP-PMO** (100 % biphenylene) has no optical activity (not shown). Both enantiomeric forms of chiral biphenylene materials are produced in the presence of the respective chiral templating monomer. It should be noted that the optical activity was determined to be present in the solid PMOs by filtering the optically active suspensions through a 0.45 um syringe filter to yield an optically *inactive* filtrate.

In order to determine the origins of the CD peaks, an MCM-type material[21] (**MCM-*S*-CM**) with silica as the main constituent was made without the biphenylene precursor, but still containing 15 % chiral monomer, ***S*-CM**. Unlike

the previous PMOs, in this material, the monomer *was* identified to be present from Raman spectroscopy, having aromatic C-H stretching at 3057 cm^{-1} as well as C=C stretching at 1607 cm^{-1}. This material produced a 7 nm red-shifted negative CD peak from the uncondensed, solution-phase monomer at 228 nm to 235 nm as seen from spectrum d in Figure **3.13.** This slight peak shifting is commonly encountered upon altering the chemical environment of the corresponding chromophore, for example with solvent or conformational changes, however the peak remains near λ_{max} of **CM** (225 nm). Notably missing are peaks at longer wavelengths (248 nm - 300 nm). This supports the hypothesis that the peaks from spectra b and c at 248 nm and 300 nm are attributed at least in part to the biphenylene precursor. These peaks are also in the region of λ_{max} of **BP** (260 nm).

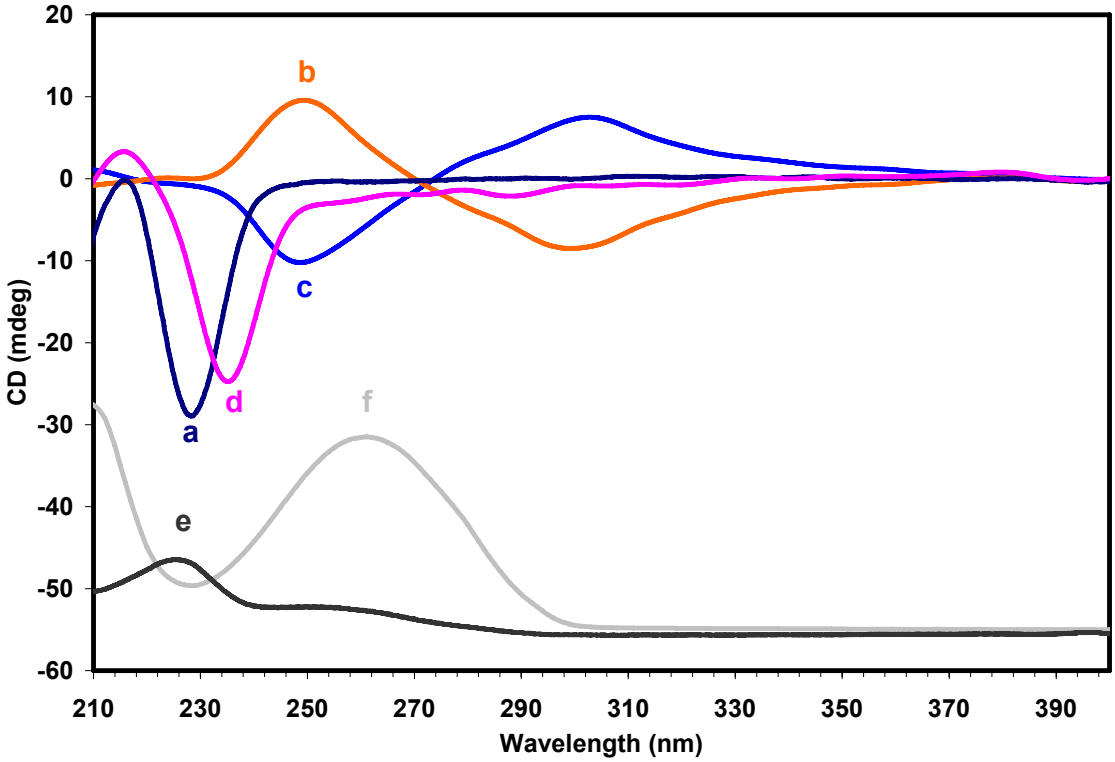

Figure 3.13 **Upper:** CD spectra of a)***S*-CM**, b) **BS15**, c) **BR15** and d) **MCM-*S*-CM**. Lower: UV spectra of e) **CM** and f) **BP**.

Interestingly, a set of materials made from *phenylene*-bridged monomer (BTEB)[7] in place of the biphenylene units incorporating 15, 20, and 30 % of the same ***S*-CM** monomer resulted in a *lack* of any strong CD peaks, despite the Raman spectra which confirmed the presence of the chiral monomer when compared to a material made under acidic conditions using 100% ***S*-CM**, **AS100** (Figure 3.14). Here, there are no chiral conformations of BTEB available from rotation of the phenylene bridge between two Si-C bonds. The reason for the CD peak occurring in **MCM-*S*-CM** and yet being absent in the phenylene-bridged materials is not entirely clear. A working hypothesis is given as follows: although the UV absorbance of **CM** is relatively weak, it is visible in **MCM-*S*-CM** because

this MCM-type material is composed mostly of pure silica, which is largely transparent to ultraviolet light. On the other hand, the phenylene-bridged precursors have a much higher UV absorbance than **CM** in the region where the CD peak of **CM** is observed (~225 nm) and therefore the absorbance is dominated by the achiral phenylene-bridged monomer. This may have the effect of under-representing the presence of the chiral monomer in the CD spectrum.

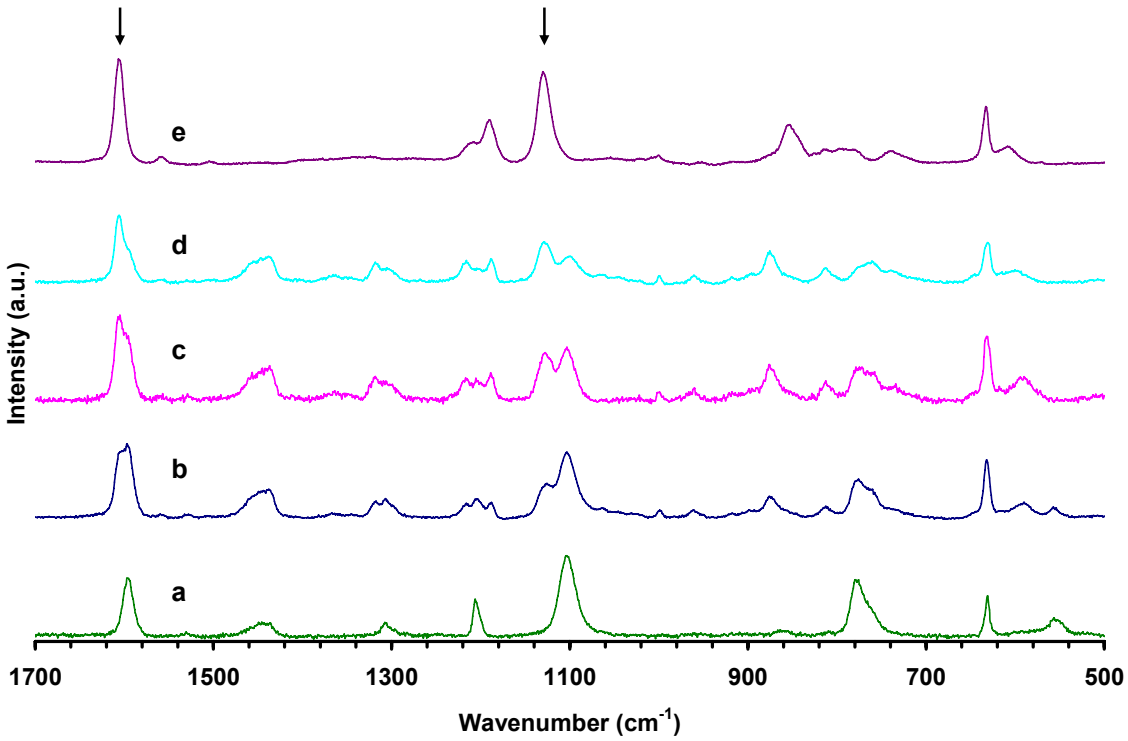

Figure 3.14 Raman spectra of materials prepared under basic conditions with phenylene-bridged monomer and a) 0 % b) 15 % c) 20 % d) 30 % *S*-**CM**. Spectrum e) is included for reference: **AS100** (100 % ***S*-CM** under acidic conditions).

As a final experiment to support the notion that the peaks at 248 nm - 300 nm are not directly attributed to the presence of the chiral monomer **CM**, a 100 % ***S*-CM** material was prepared (**BAS100**). Although this particular sol resulted

initially in a gel, rather than a solid precipitate, upon acidification of the sol to induce hydrolysis, a precipitate was obtained. The acid-sensitive ketal appeared to be largely intact in this material by CP MAS ^{13}C NMR with resonances for the methyl and ketal carbons observed at 29.7 and 113 ppm respectively. The benzylic C's of any deprotected diol are predicted to appear slightly upfield from the corresponding protected ketal (89 ppm) and thus are likely overlapped from the ketal and spinning side band at 84 ppm (Figure 3.15). The CP MAS ^{29}Si NMR confirmed no C-Si cleavage (Figure 3.16). Interestingly, the CD spectrum of this material, composed *entirely of the chiral monomer*, was lacking any strong signal. The reason for this is still under consideration, however it is possible that in the case of the MCM particles above, TEOS may allow **CM** to adopt a chiral conformation with a higher absorption coefficient than that which is obtained in the TEOS-free material.

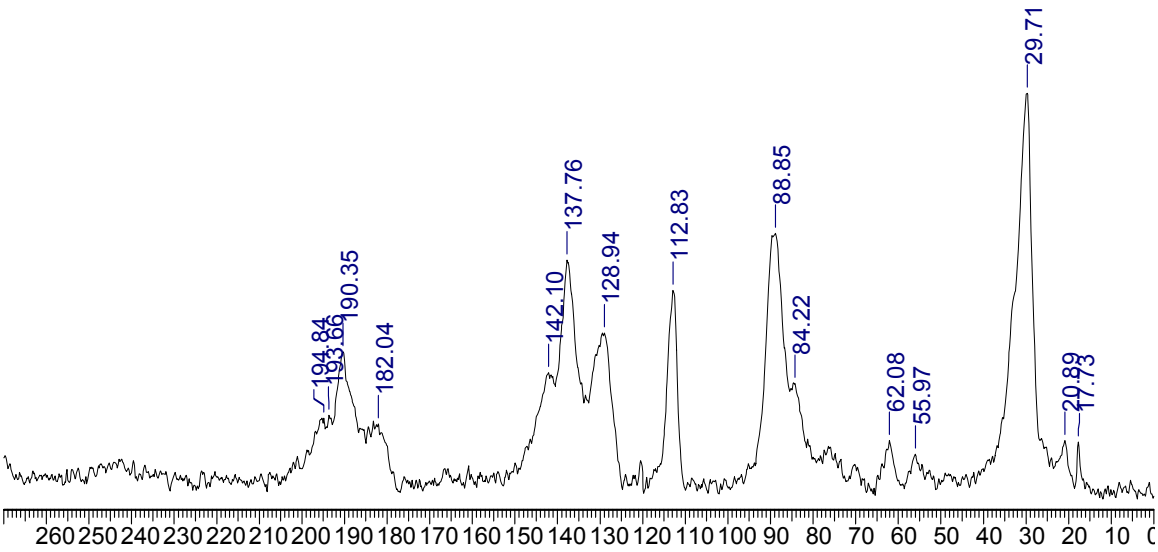

Figure 3.15 ^{13}C CP MAS NMR of **BAS100** showing ketal carbon at 112 ppm and methyl carbons at 30 ppm.

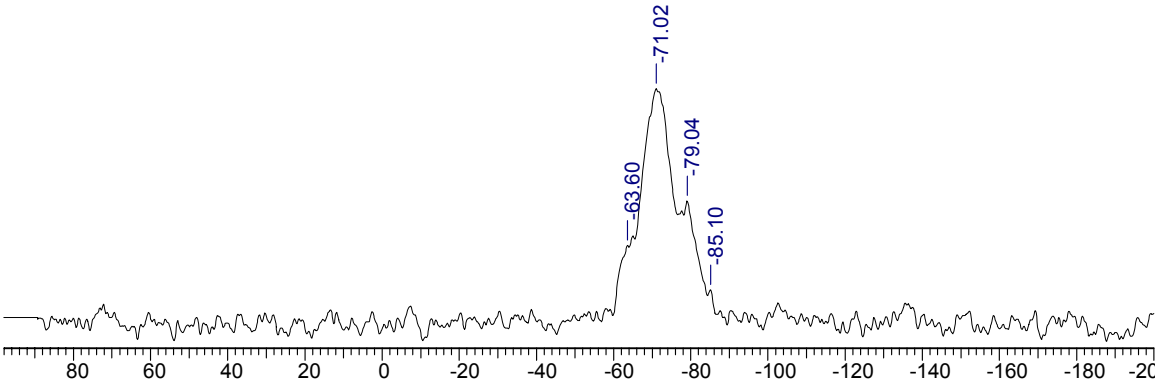

Figure 3.16 ^{29}Si CP MAS NMR of **BAS100** showing no C-Si cleavage.

3.2.5 Effect of increasing CM concentration on circular dichroism

Upon increasing the concentration of the chiral template **CM** in the PMOs, the CD spectra appeared to have less intense signals (Figure 3.17). In order to get comparable data, the CD spectra were divided by their absorbance spectra (Figure 3.18), which results in absorbance-normalized CD spectra (Figure 3.19). Although there is little qualitative change in the normalized spectra, the advantage of this data treatment is that it clearly shows there is a decrease in the ellipticity of the materials upon increasing the **CM** content. If the ellipticity was due only to the presence of the chiral monomer **CM**, we would expect an increase in the CD signal with an increasing percentage, but as the template is not incorporated to any observable extent as shown from Raman spectroscopy, the signal is most likely due to the biphenylene precursor.

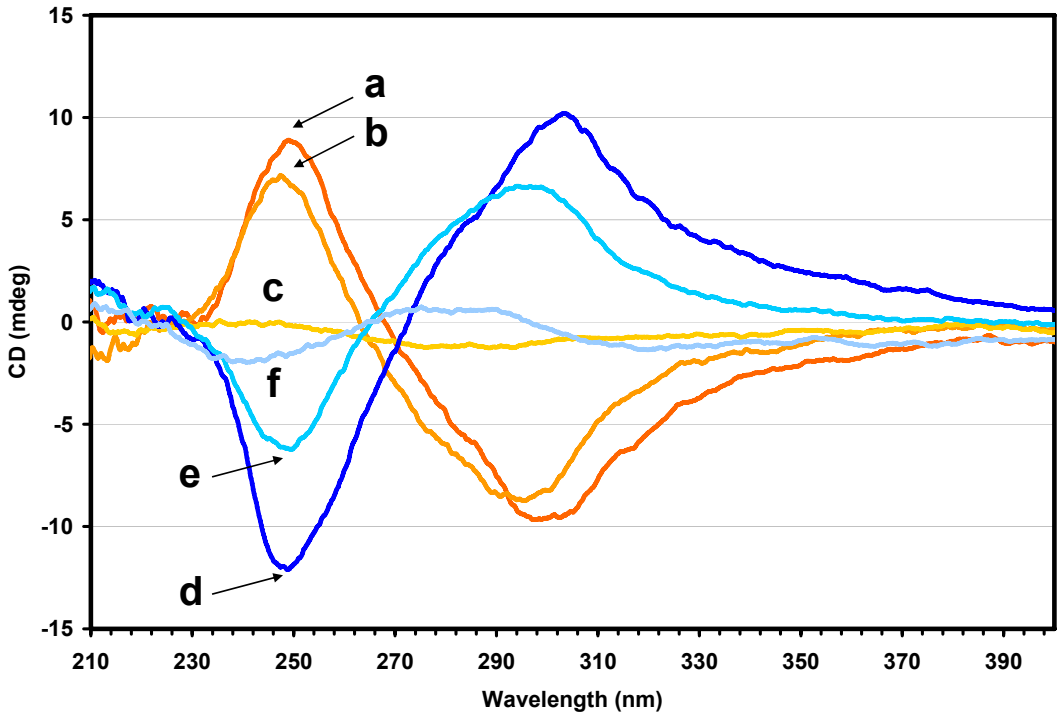

Figure 3.17 CD spectra of materials containing enantiomeric forms of **CM** with **BP**. a) **BR15**, b) **BR20**, c) **BR30**, d) **BS15**, e) **BS20**, and f) **BS30**.
Note: all spectra have been background corrected with distilled H_2O.

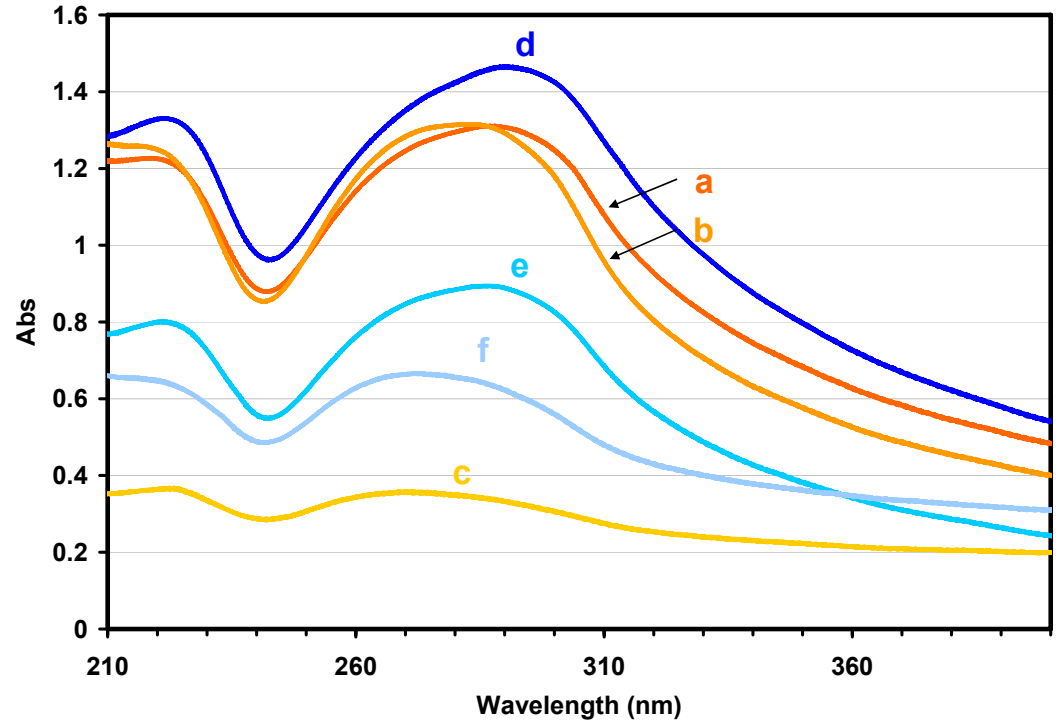

Figure 3.18 Corresponding absorbance spectra of Figure 3.17.

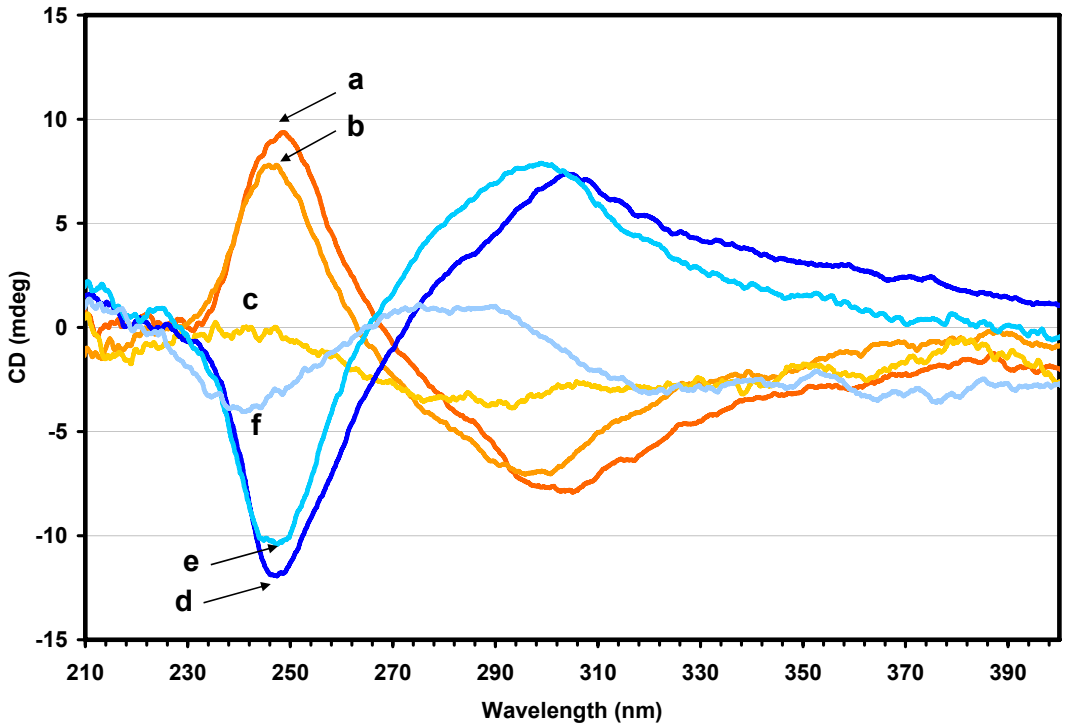

Figure 3.19 Absorbance normalized CD spectra of a) **BR15**, b) **BR20**, c) **BR30**, d) **BS15**, e) **BS20**, and f) **BS30**.

To further probe this strange phenomenon, PMOs of lower ***S*-CM** concentrations (10 %, 5 % and 1 %) were prepared to see if the trend of increasing circular dichroism intensity continued. The trend did not continue as the lowest concentration of chiral monomer (1 % ***S*-CM**) with **BP** gave the weakest CD signal (Figure 3.20). This same result was observed in the absorbance normalized plot (not shown). Moreover, under what were believed to be the same experimental conditions, the general shape of the CD spectra changed to display a negative peak at 255 nm and a shoulder appearing at ~290 nm (Figure 3.20). Furthermore, the shape of the absorbance spectrum was quite different as well, not displaying the same peaks at 220 -230 nm and 290 - 300 nm (Figure 3.21). Due to the significant differences in the CD and UV

spectra between these two batches of PMOs, it is clear that although the procedures were repeated as closely as possible, materials with very different optical properties resulted.

The reason for the different spectral shapes has not been identified, but it could be related to a number of issues including a change in particle morphology, a different conformational packing of the biaryl units, aggregated species or the purity of the monomer. As CD spectroscopy is a very sensitive technique, like UV-vis spectroscopy, it usually requires analyte concentrations in the range of 10^{-5} to 10^{-6} M and it will require little chiral impurity to produce a change in the spectra. Although the **CM** monomers are deemed pure by ^{1}H and ^{13}C NMR before use, **CM** monomer was purified by column chromatography, thus the most likely candidate for a chiral impurity is that of the mono-silylated form, **H/Si-CM** (Figure 3.2), which elutes on silica gel very close to that of the product. A very small amount of this byproduct could result in a spectral change. It also cannot be ruled out that perhaps there are a number of different chiral conformations that the biphenylene units may adopt, which could have varying optical properties. This would be closely related to the phenomenon of polymorphism which is the ability to exist in more than one crystal modification. Because polymorphs have different structures, they may differ greatly in density, solubility and optical or electrical properties. Dunitz and Bernstein[22] have reviewed this topic and acknowledge the difficulty at times, in reproducing properties of some crystals due to the existence of polymorphs.

One important point to note is the occurrence of Rayleigh scattering occurring here. Rayleigh scattering is due to the elastic scattering of the radiation photons. This type of scattering intensity varies with respect to the sixth power of the particle size and varies inversely with the fourth power of the wavelength.[23] Since we didn't analyze all of our samples for particle size distributions, it is possible that a slight increase in particle diameter could lead to high intensity scatterings explaining the different absorbance spectra in Figure 3.21.

Since mirror images of both shapes of CD traces have been obtained, this work needs to be repeated with highly purified reagents before a conclusion on the proper CD spectrum is warranted.

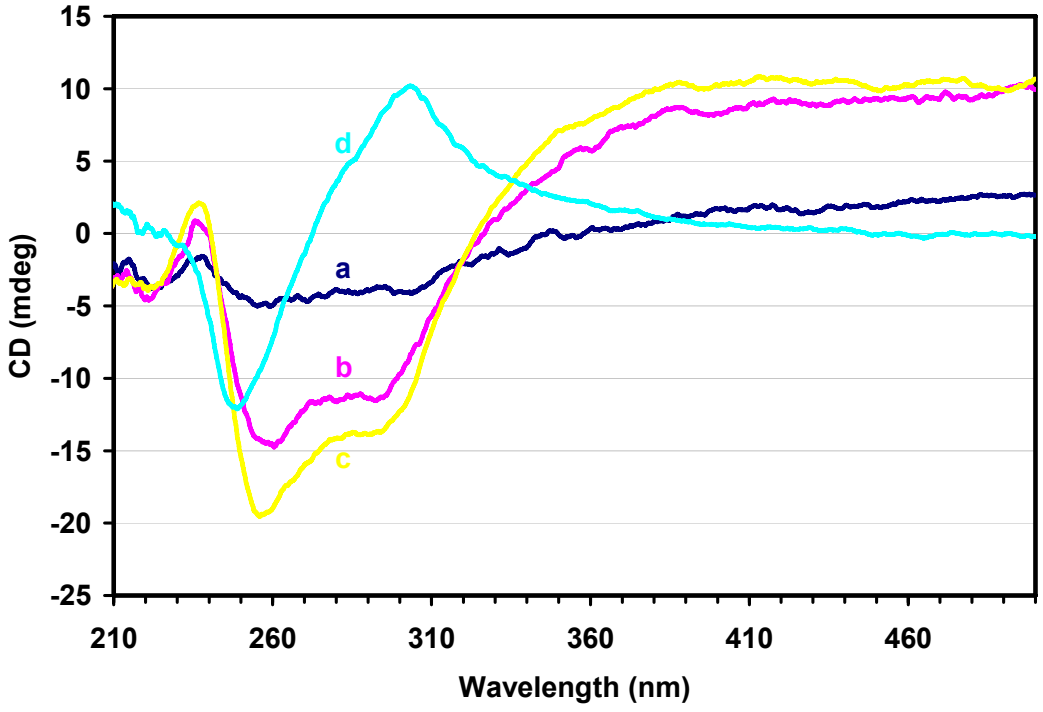

Figure 3.20 CD spectra of lower concentrations of ***S*-CM** with **BP**. a) **BS1**, b) **BS5**, c) **BS10** and d) **BS15** for comparison.

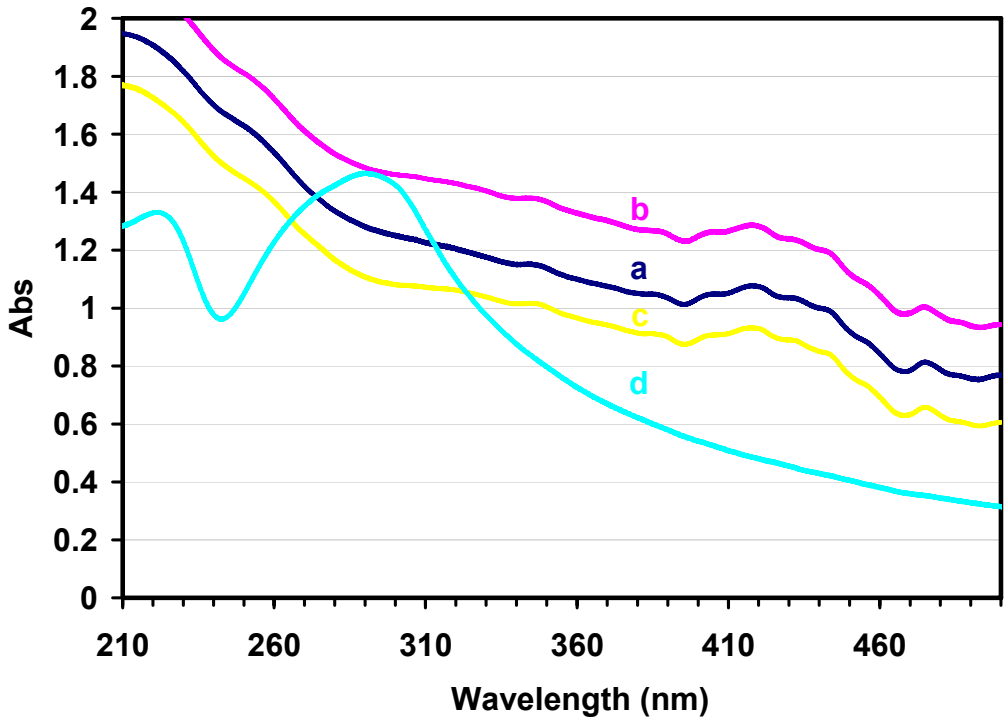

Figure 3.21 UV absorbance spectra of lower concentrations of ***S*-CM** with **BP**. a) **BS1**, b) **BS5**, c) **BS10** and d) **BS15** for comparison.

As mentioned, a similar structure which could be considered a model to our 4,4'-disubstituted biphenyl, 4,4'-di(*tert*-butyl)biphenyl (Figure 3.22), does indeed exhibit polymorphism.[14] In fact, it is trimorphic with three different crystal forms, the least stable form of which has been acknowledged by researchers, as not always easy to reproduce. They also noted that two separate bottles purchased from Fluka were two distinct polymorphs.

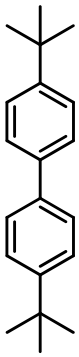

Figure 3.22 Structure of 4,4'-di(*tert*-butyl)biphenyl.

It is not entirely clear as to whether there are different condensed-phase forms of the prepared PMOs, but it is possible that molecular conformations, or other aggregation phenomena in the condensed phase can vary, giving rise to materials of differing optical properties.

3.2.6 Powder X-ray diffraction

With powder X-ray diffraction measurements, one can qualitatively relate the relative intensities of the peaks in the patterns to the crystalline order of the materials and draw comparisons between a series of samples (ensuring the same scanning rates were used). Upon increasing the concentration of chiral monomer **CM**, the mesoporous order of the materials began to erode. This was seen from the loss of the peak intensity at 1.8 º *2θ*, from 20 % **CM** (**BS20**), to 30 % **CM** (**BS30**) (Figure 3.23). This peak represents the mesoscale order of the materials having a *d*-spacing of 48.6 Å. Coexisting with a loss of *mesoscale* order was a loss of *molecular* scale order as indicated by the loss of peak intensity in the medium angle reflections. Most noticeable was a decrease in the peak at 7.5 º *2θ*, corresponding to a *d*-spacing of 11.9 Å (Figure 3.24). This peak is the

first and strongest of 5 higher order reflections which result from the lamellar structure of the biphenylene units within the pore walls with a repeating distance of 11.9 Å (Figure 2.25).[8] It is more difficult to see the decreased order from the TEM images of these materials presented above, as each material appear to be well-ordered. However PXRD is a bulk analysis technique and gives a more representative analysis than TEM, where only small, selected areas are imaged.

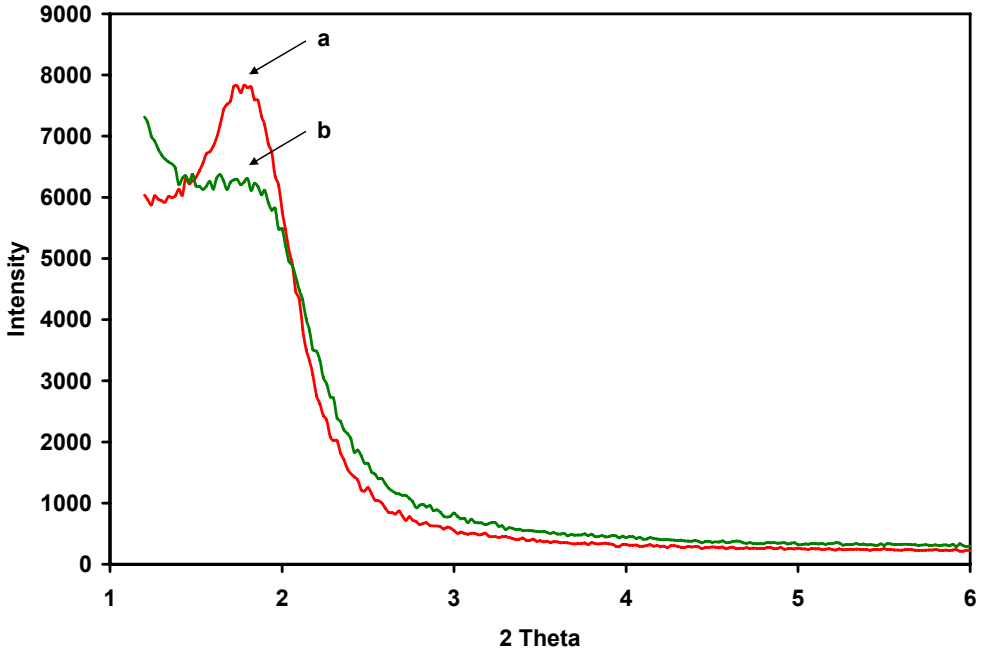

Figure 3.23 Low angle PXRD data of a) **BS20** and b) **BS30** showing a loss of the mesoscale ordering with increasing **CM**.

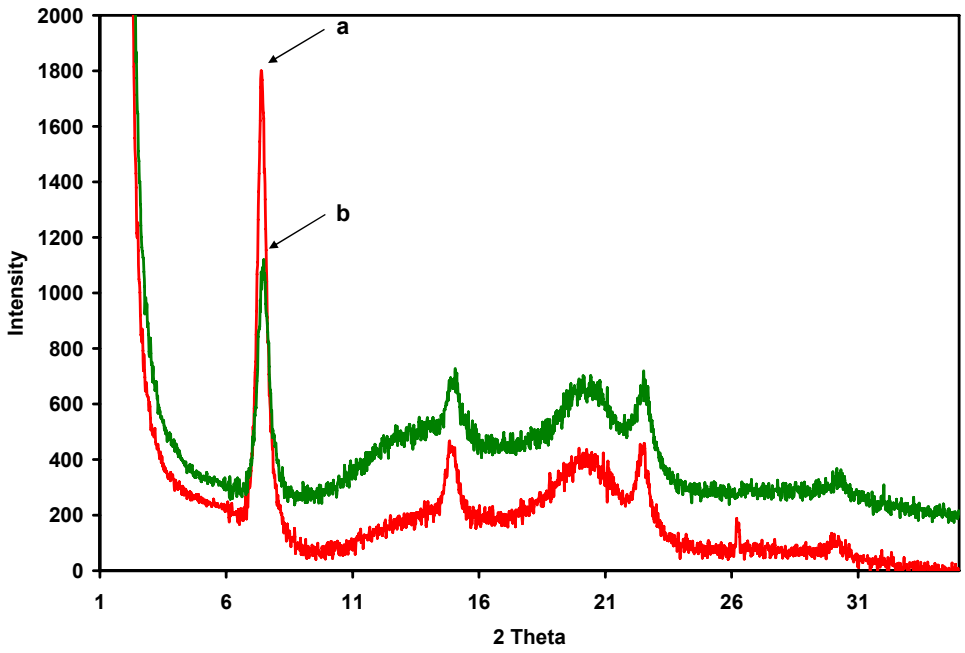

Figure 3.24 Medium angle PXRD data of a) **BS20** and b) **BS30** showing peaks for molecular scale ordering, which are weaker with increased proportion of **CM**.

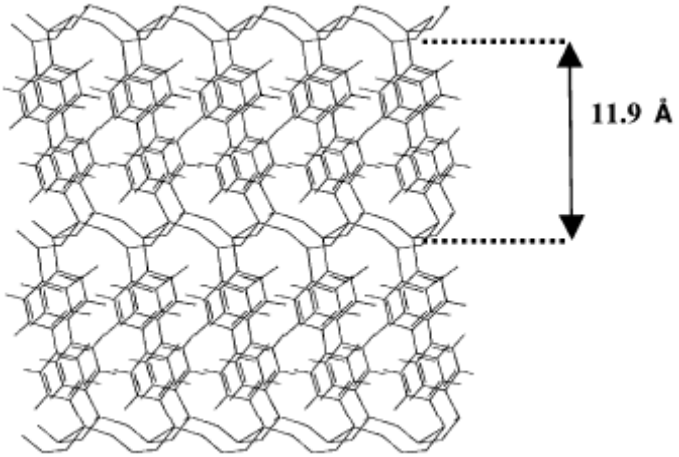

Figure 3.25 Structural model for biphenylene-bridged PMO giving rise to molecular-scale periodicity in **BS15**, **BS20** and **BS30**. Reproduced from Inagaki *et al*. [8]

It is likely that the decreased intensity in the circular dichroism of materials containing increased **CM**, is related to the decreased long-range order observed from the powder XRD measurements. A loss of mesoporous order is commonly observed upon incorporating a less compatible precursor to a PMO preparation.

It has also been noted by Morell *et al.*[24] that mesoscale and molecular scale ordering may be closely related in their formation mechanisms, therefore the concurrent loss of molecular scale with the mesoscale ordering is not surprising. It is proposed that this molecular scale layering, leading to a tightly packed crystal-like wall, is the mechanism by which the chiral biphenylene conformation is able to propagate to adjacent biphenylene groups. This proposal is discussed further below.

3.2.7 Templating discussion

It is certain that under basic pH conditions, **CM** is not incorporated in the PMOs to the expected degree which would be visible by CP MAS ^{13}C NMR at 30 mol %. It is possible that **CM** is acting transiently in a noncovalent manner and never becoming incorporated into the PMOs, however it is more likely that there is a very small amount which is covalently incorporated but below our limits of detection.

It is proposed that at 15 % **CM**, the interaction of **CM** with **BP** is biasing the rotation of the biphenylene axis such that one enantiomeric rotamer is present in excess. It is this chiral templating effect which is likely propagating to local domains or throughout the backbone of the material, promoted by the close-packed, crystal-like walls of the biphenylene system and resulting in larger CD signals. This crystal-like wall is confirmed by the molecular scale periodicity of the powder X-ray diffraction patterns (Figure 3.24). With higher percentages of **CM** in the material (20% and 30 %), it is likely that **CM** begins to interfere with the surfactant self-assembly process and mesophase formation as is often observed

with organosilica co-condensing procedures. Furthermore, the molecular scale periodicity is also negatively affected. At higher **CM** loadings, the degree of crystallinity in the material wall is lessened and the mechanism to propagate any biphenylene chirality is diminished, thus resulting in decreased CD signals. The powder X-ray diffraction patterns support this hypothesis of a decreasing molecular and mesoscale order upon increasing **CM** concentration. This is also in accordance with the work by Morell *et al.* who have previously shown that the formation of the mesophase serves to induce the crystallinity in the walls as a cooperative process.[24]

3.2.8 Acid-catalyzed PMOs with CM

For comparison purposes, materials were prepared under acidic pH conditions with Brij 76 as surfactant using the same biphenylene precursor **BP** with **CM**. These PMOs were analyzed by nitrogen physisorption with the textural data given in Table 2.4. It should be noted that under these acidic conditions, the ketal of **CM** becomes deprotected to yield the corresponding chiral 1,2-diol. These materials all exhibit high BET surface areas at 900 m^2/g and above, pore diameters from 25-27 Å and pore volumes from 0.60 – 0.77 cm^3/g.

Table 3.1. Textural data of acid catalyzed PMOs prepared from **BP** and **CM** using Brij 76 as surfactant from nitrogen porosimetry.

Material	% CM	BET Surface Area (m^2g^{-1})	Pore Diameter[a] (Å)	Pore Volume[b] (cm^3g^{-1})
BP-PMO	0	889	27.7	0.69
AR15	15	1009	27.1	0.77
AR20	20	996	27.1	0.66
AR30	30	977	25.2	0.60

[a] Maximum value of BJH pore diameter distribution (adsorption branch).
[b] BJH cumulative pore volume of pores between 10 and 3000 Å.

In materials prepared with increasing amount of **CM**, from CP MAS ^{13}C NMR, it was shown that the monomer *was incorporated* at increasing amounts by observing the growth of the deprotected benzylic C peaks appearing at 80-85 ppm (Figure 3.26). The CP MAS ^{29}Si NMR spectra confirmed that the organic bridges were intact from the T^1- T^3 peaks at -63 to -80 ppm and even at 30 % **CM** there is very little C-Si cleavage occurring (101 ppm).

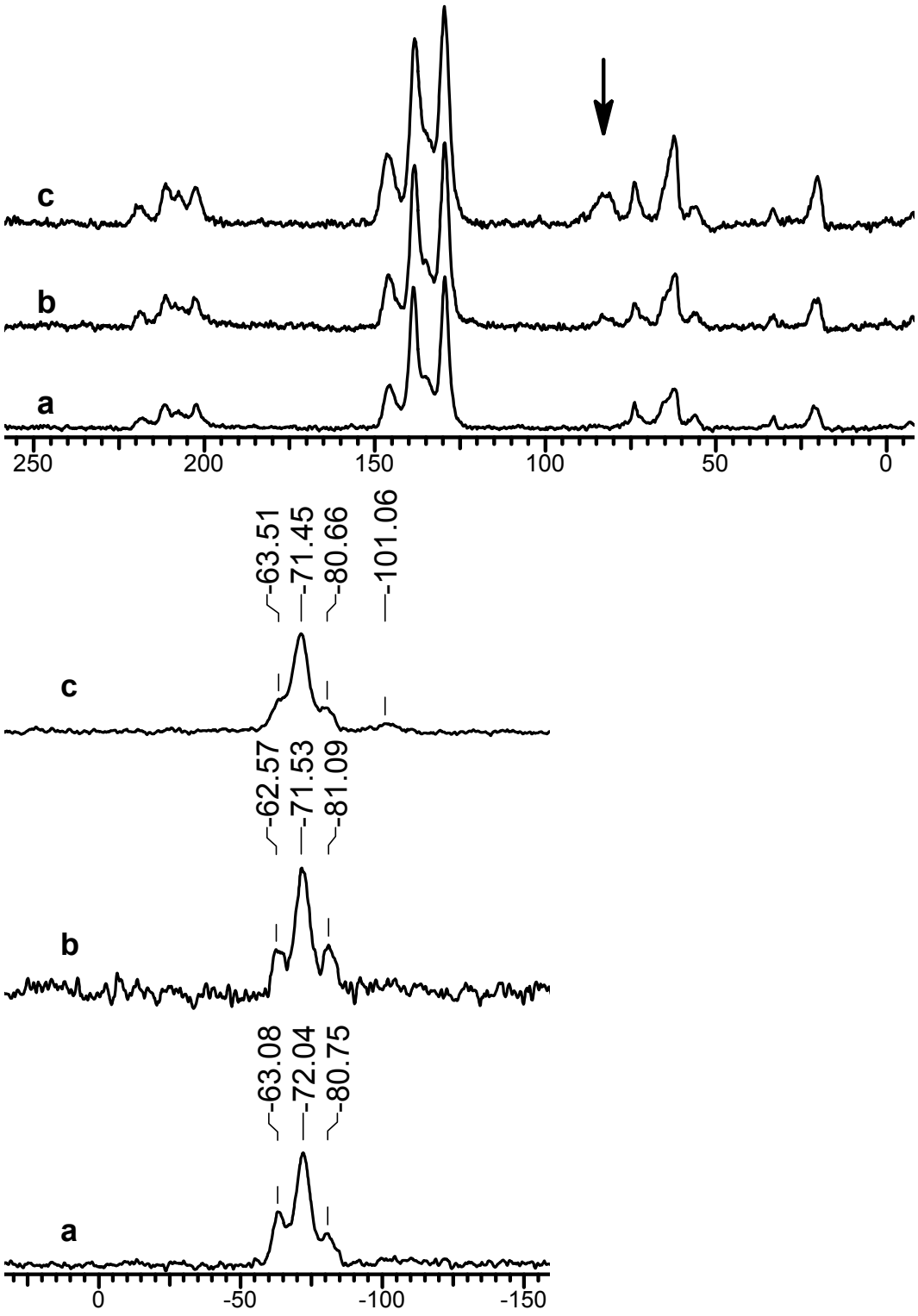

Figure 3.26 Upper: CP MAS ^{13}C NMR of PMOs a) **BP-PMO** b) **AR15** and c) **AR30** showing increased peak intensity at 80-85 ppm for benzylic carbon of deprotected **CM**. Lower: corresponding CP MAS ^{29}Si NMR.

TEM images of the materials provided evidence of a well ordered mesoporous structure, even up to 30 mol % **CM** with the biphenylene precursor under acidic conditions templated with Brij 76 surfactant.

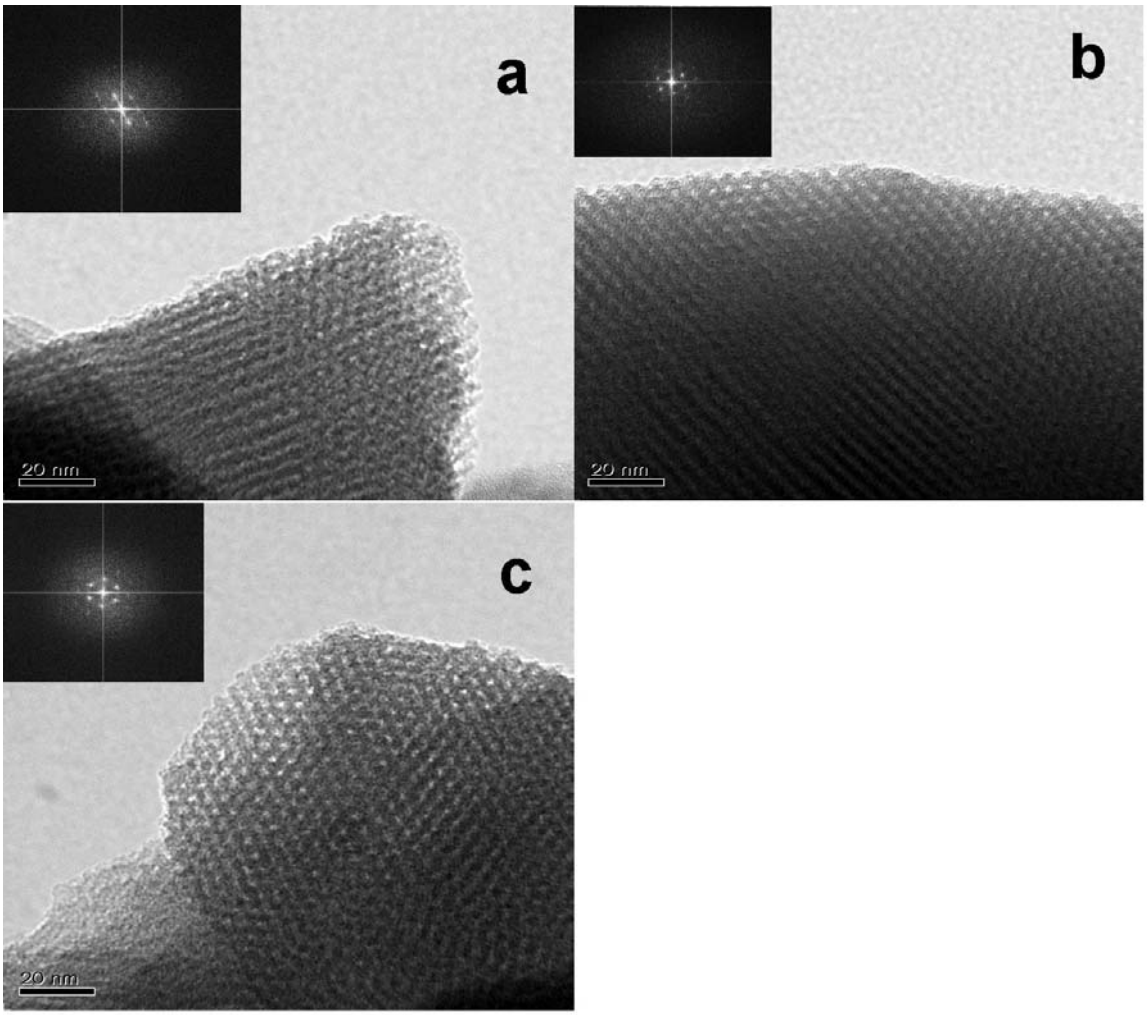

Figure 3.27 TEM images with electron diffraction patterns inset of a) **AR15** b) **AR20** c) **AR30**.

The powder X-Ray diffraction patterns of these materials under acidic conditions, each exhibit 1 peak at low 2θ which indicates an ordered mesoporous structure with *d*-spacings of 68.8, 57.4, 55.2 and 51.9 Å for **BP-PMO**, **AR15**, **AR20** and **AR30** respectively. It is noted that the *d*-spacings decrease with

increasing **CM** component, which could be due to the **CM** monomer preferring a smaller pore structure in the PMO, or we could be observing gradual pore collapse of the material from templating interference.

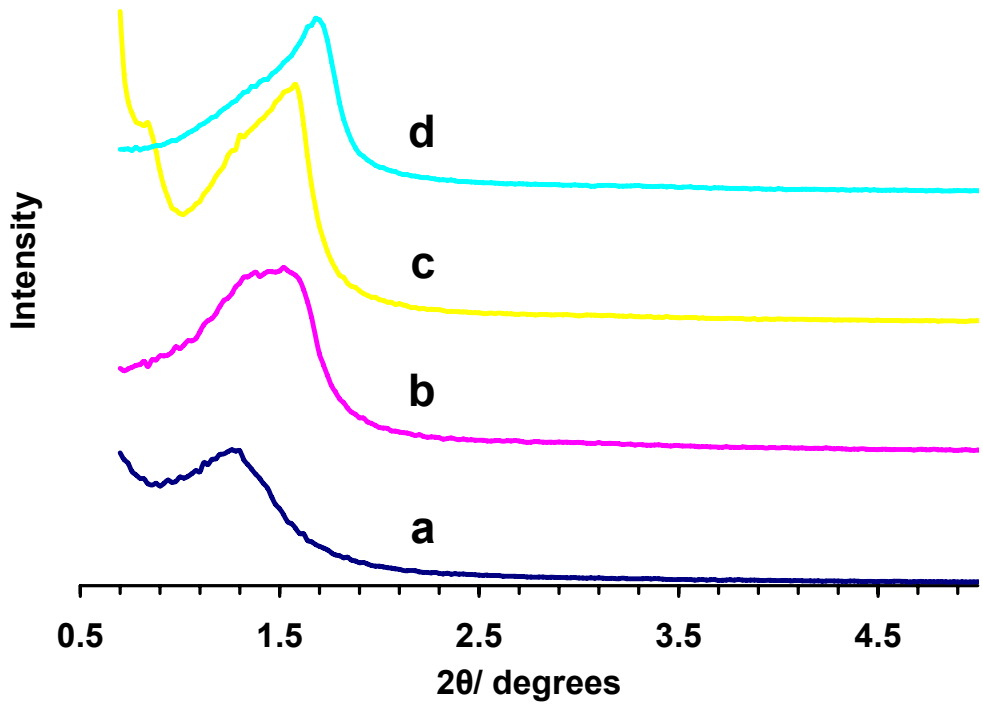

Figure 3.28 PXRD patterns of a) **BP-PMO**, b) **AR15** c) **AR20** and d) **AR30**.

What is important to note is that there are no reflections occurring in the PXRD patterns at medium angles in contrast to the materials prepared under basic pH with **CM** and **BP**. This result confirms the lack of a close-packed biphenylene layer in the walls of the acid catalyzed materials.

In contrast again to the materials prepared with the biphenylene-bridged precursor under basic pH conditions, these PMOs under acidic conditions exhibited no distinct CD spectra. Even in materials prepared with 100 % loadings

of **CM**, the CD signals were too weak to be observed which is in agreement with the phenylene-bridged materials and **BAS100** (presented above) under basic pH where no CD signal was observed.

These results, suggest a well-ordered and tightly packed layered structure of biphenylene-bridged precursors are required for effective chiral transfer from **CM** throughout the biphenylene-bridged backbone of the material. It is likely that the base-catalyzed conditions promote this type of structure because of a higher degree of condensation than is afforded under acidic conditions.

3.2.9 Chiral PMOs as stationary phase

One potential application of organosilica materials is as chromatographic stationary phases. In collaboration with the Oleschuk lab, at Queen's University, we examined these chiral materials as stationary phases in nanofluidic HPLC. Unfortunately, for ideal chromatographic separation, there are very stringent particle dimensions which are desired and the basic pH conditions which gave chiral materials did not give the optimum morphology. In fact, the small particle morphology that was obtained led to high back pressures in the packed columns. Large (5-10 μm) spherical particles are indeed superior for this technique and thus we sought to control the morphology of the chiral materials. Rather than create 100% spherical particles from our materials, we thought it was much more efficient to start with commercially available, chromatographic silica spheres of appropriate size, and grow a shell of the chiral material on the surface. Indeed, there was a report by Deng, et al. who grew a porous 'corona' or shell around a metal nanoparticle. A TEM image of the resulting particle is shown in Figure 3.29.

We adapted this procedure to produce our own mesoporous shells around silica spheres (Figure 3.30).

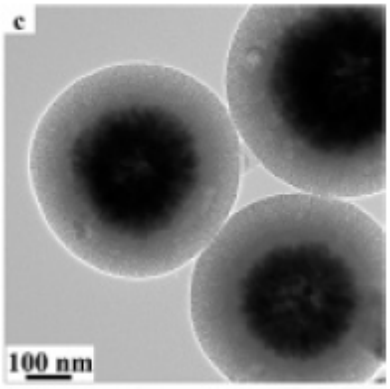

Figure 3.29 Corona or core-shell particle. Image reproduced from Deng *et al.* [25]

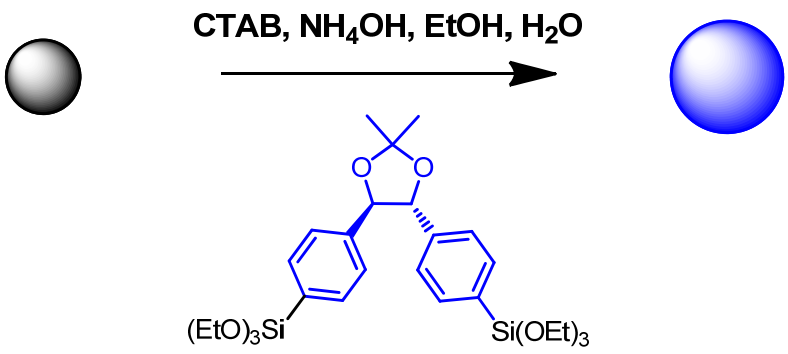

Figure 3.30 Scheme representing our procedure to produce porous shell-silica particles.

We started with 5 µm silica beads and treated them under the desired conditions with a CTAB, NH_4OH, EtOH and ***S*-CM** solution at a pH of ~ 8 - 8.5. The beads were stirred for 24 h at room temperature as the chiral monomer was allowed to condense on the surface of the silica bead. Following extraction of the template and drying of the particles, the beads were imaged on an optical microscope (Figure 3.31). Unfortunately, the commercial silica was not monodisperse enough to determine film thickness of the particles by difference

measurements of particle sizes before and after the growth of the shell. However, it was obvious that the spherical nature of the silica beads remained, while Raman spectroscopy confirmed the presence of the organic chiral monomer with aromatic C-H stretching at 3060 cm^{-1} as well as C=C stretching at 1607 cm^{-1} (Figure 3.32).

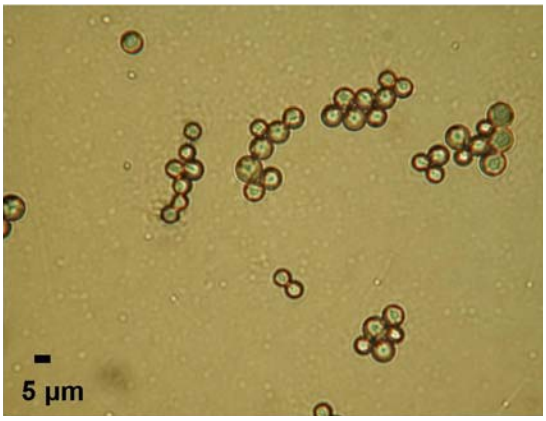

Figure 3.31 Optical microscope image of coated 5 µm silica spheres.

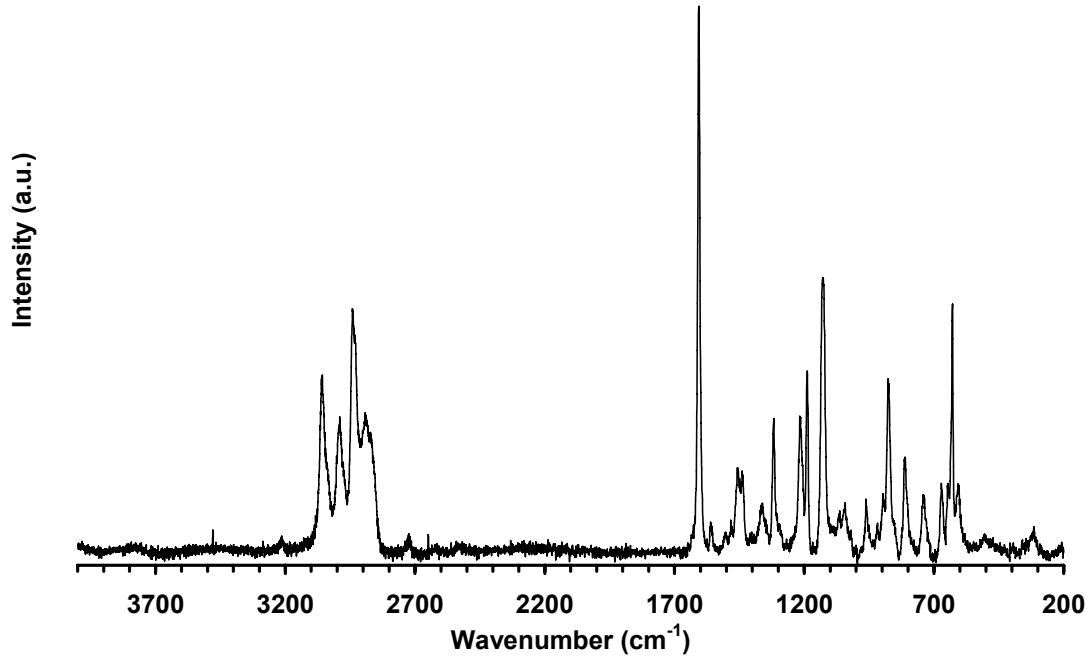

Figure 3.32 Raman spectroscopy of silica beads coated with ***S*-CM**.

A slurry of the materials was prepared in acetonitrile (~5-8 mg/mL in acetonitrile) followed by ultrasonication for 5 min to decrease particle aggregation and increase the wetting of the particles. The slurry was packed into a fritted 75 μm inner diameter capillary column (Figure 3.33) using an HPLC pump at pressures of 500 to 1500 psi to obtain a 10 cm long column (see experimental for details). The column was flushed with the mobile phase (50 % water/acetonitrile) overnight to equilibrate the column. A gradient elution from 99 % water to 30 % water in acetonitrile was used to determine appropriate isocratic solvent strength conditions for the elution. Then the isocratic conditions were used for both enantiomers and a racemic mixture of the analytes. Column efficiencies were then determined.

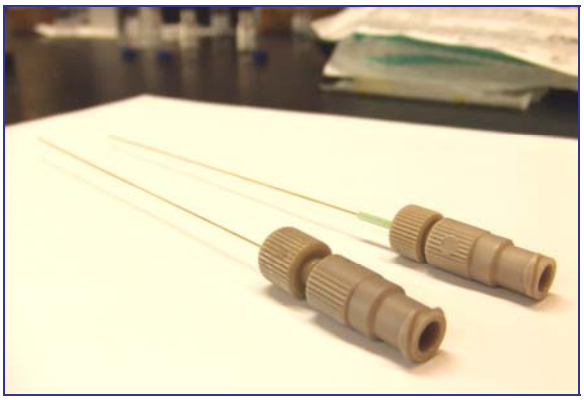

Figure 3.33 Nano-HPLC capillary columns with connectors.

The first analyte we chose to separate was the di-iodo precursor to **CM**, since we had both enantiomers available in high enantiopurity as determined from supercritical fluid chromatography with a chiral OD column. As can be seen from the chromatograms below, there is a difference of about 0.5 min between the ***R*-CM** and ***S*-CM**. This is a statistically significant difference, as the retention

time reproducibility of a repeated analysis is usually less than 1 % of the retention times, which here, is 0.1 min. However, when the racemic mixture of the enantiomers was analyzed, they co-eluted, resulting in one broadened peak. The column efficiency was calculated to be 2000 plates/m from the peak width at half height. Attempts at separation of other chiral molecules were made, however none gave a better enantiomeric resolution that the diiodo intermediates of Scheme 5.

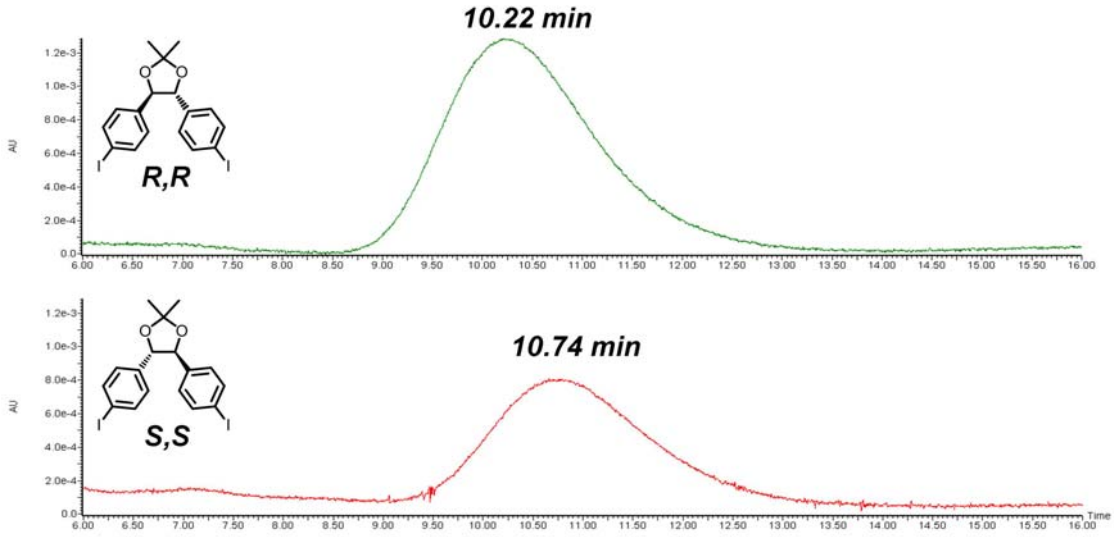

Figure 3.34 Chromatograms showing 0.5 min separation of diiodo analytes from Scheme 5.

In order to improve upon the current separation one must be aware of the factors affecting the chromatographic efficiency. Column efficiency is related to the number of pathways in the column, axial and longitudinal diffusion, partition coefficients between the mobile and stationary phases and the flow rate. The column efficiency or plate count is determined from Equation 3.1, where *N* is the

efficiency or number of theoretical plates (reported per metre), t_r is the retention time of the analyte peak, and $W_{1/2}$ is the peak width at half height.

$$N = 8\ln(2) \cdot \left(\frac{t_r}{W_{1/2}} \right)^2 \qquad \text{(Equation 3.1)}$$

The next logical step in improving the column efficiency is to improve the monodispersity of the silica spheres. This should lead to a more uniform packing of the silica beads, fewer paths available for the analyte molecules to travel and thus minimize diffusion. Work is already underway with monolithic silica columns, which is a promising alternate form for the stationary phase.

3.3 Conclusions

We have shown for the first time that optically active biphenylene-bridged PMOs can be produced under basic pH conditions in the presence of chiral monomer **CM**, which imparts an asymmetric conformational preference to the biphenylene rings. Under these conditions the template monomer **CM** is not observed to be incorporated into the final PMOs, by ^{13}C CP MAS NMR or by micro-Raman spectroscopy, however, mirror-like CD spectra clearly support the presence of chiral species in both enantiomeric forms. Thus it is likely that this monomer is present in quantities below the detection limit of the techniques used to probe the material.

Since a decrease in powder X-ray diffraction pattern intensity is concurrent with a loss of ellipticity of the PMOs, the chiral nature of the PMOs is believed to be strongly dependent on the crystallinity of the biphenylene groups in the

materials. Under acidic conditions, there is no circular dichroism of the PMOs containing **CM** observed. Since these PMOs also lack crystallinity in the pore walls, these results support our hypothesis. Further investigation into the circular dichroism of these materials is needed to identify other important properties affecting the circular dichroism of the PMOs.

3.4 References

(1) Kawasaki, T.; Nakaoda, M.; Kaito, N.; Sasagawa, T.; Soai, K. *Origins of Life and Evolution of Biospheres* **2010**, *40*, 65-78.
(2) Inagaki, S.; Guan, S.; Fukushima, Y.; Ohsuna, T.; Terasaki, O. *J. Am. Chem. Soc.* **1999**, *121*, 9611-9614.
(3) Melde, B. J.; Holland, B. T.; Blanford, C. F.; Stein, A. *Chem. Mater.* **1999**, *11*, 3302-3308.
(4) Asefa, T.; MacLachlan, M. J.; Coombs, N.; Ozin, G. A. *Nature* **1999**, *402*, 867-871.
(5) Dickson, S. E.; Crudden, C. M. *Chem. Commun.* **2010**, *46*, 2100-2102.
(6) Fujita, S.; Inagaki, S. *Chem. Mater.* **2008**, *20*, 891-908.
(7) Inagaki, S.; Guan, S.; Ohsuna, T.; Terasaki, O. *Nature* **2002**, *416*, 304-307.
(8) Kapoor, M. P.; Yang, Q.; Inagaki, S. *J. Am. Chem. Soc.* **2002**, *124*, 15176-15177.
(9) Bion, N.; Ferreira, P.; Valente, A.; Goncalves, I. S.; Rocha, J. *J. Mater. Chem.* **2003**, *13*, 1910-1913.
(10) Goto, Y.; Okamoto, K.; Inagaki, S. *Bull. Chem. Soc. Jpn.* **2005**, *78*, 932-936.
(11) Xia, Y. D.; Wang, W. X.; Mokaya, R. *J. Am. Chem. Soc.* **2005**, *127*, 790-798.
(12) Cornelius, M.; Hoffmann, F.; Froba, M. *Chem. Mater.* **2005**, *17*, 6674-6678.
(13) Almenningen, A.; Bastiansen, O.; Fernholt, L.; Cyvin, B. N.; Cyvin, S. J.; Samdal, S. *J. Mol. Struct.* **1985**, *128*, 59-76.
(14) Näther, C.; Jeß, I.; Havlas, Z.; Bolte, M.; Nagel, N.; Nick, S. *Solid State Sci.* **2002**, *4*, 859-871.
(15) Montoya-Pelaez, P. J.; Uh, Y.-S.; Lata, C.; Thompson, M. P.; Lemieux, R. P.; Crudden, C. M. *J. Org. Chem.* **2006**, *71*, 5921-5929.
(16) MacQuarrie, S.; Thompson, M. P.; Blanc, A.; Mosey, N. J.; Lemieux, R. P.; Crudden, C. M. *J. Am. Chem. Soc.* **2008**, *130*, 14099-14101.
(17) Ding, X.; Lv, X.; Hui, B.; Chen, Z.; Xiao, M.; Guo, B.; Tang, W. *Tetrahedron Lett.* **2006**, *47*, 2921-2924.
(18) Wang, Z.; Sharpless, K. *J. Org. Chem.* **1994**, *59*, 8302-8303.
(19) Murata, M.; Ishikura, M.; Nagata, M.; Watanabe, S.; Masuda, Y. *Org. Lett.* **2002**, *4*, 1843-1845.
(20) Ide, A.; Voss, R.; Scholz, G.; Ozin, G. A.; Antonietti, M.; Thomas, A. *Chem. Mater.* **2007**, *19*, 2649-2657.
(21) Grun, M.; Unger, K. K.; Matsumoto, A.; Tsutsumi, K. *Microporous Mesoporous Mater.* **1999**, *27*, 207-216.
(22) Dunitz, J. D.; Bernstein, J. *Acc. Chem. Res.* **1995**, *28*, 193-200.
(23) *Physical Chemistry*; Seventh ed.; Atkins, P.; Paula, J. d., Eds.; W. H. Freeman and Company: New York, 2002.

(24) Morell, J.; Teixeira, C. V.; Cornelius, M.; Rebbin, V.; Tiemann, M.; Amenitsch, H.; Froba, M.; Linden, M. *Chem. Mater.* **2004**, *16*, 5564-5566.
(25) Deng, Y.; Qi, D.; Deng, C.; Zhang, X.; Zhao, D. *J. Am. Chem. Soc.* **2008**, *130*, 28-29.

Chapter 4
Thin films of periodic mesoporous organosilica

4.1 Introduction

As environmental pollutants become an ever-increasing concern for governmental agencies and the general public alike, it is becoming essential to have fast, accurate and inexpensive methods of monitoring the quality of essential resources such as drinking water. For the purposes of this study we are interested in the detection of heavy metals such as mercury.

Mercury is known to be highly toxic to human health, with a particular threat to the development of a child *in utero* as recognized by the World Health Organization (WHO).[1] It occurs naturally in many forms (organic, inorganic and elemental) and is a hazardous waste from many industrial processes such as coal-burning power plants, and the electrolytic production of chlorine. Airborne mercury ultimately settles in the sediments of riverbeds, lakes and bays where it is then able to enter the food chain starting with phytoplankton, zooplankton, and fish and eventually being concentrated in larger species like swordfish, shark and tuna. Although methylation of inorganic mercury can occur in water, almost all mercury in uncontaminated drinking water is believed to be in Hg^{2+} form.[2] The WHO currently sets a drinking water limit to 0.006 mg/L for inorganic mercury. Fibre optic cables with embedded sensors are one type of instrumentation that could potentially offer an inexpensive and rapid detection method for inorganic heavy metals such as mercury.

4.1.1 Fibre optic cables and long period gratings (LPGs)

As reviewed by James and Tatam,[3] the development of fibre gratings has had a large impact on the research and development in areas of telecommunications and fibre optic sensing. These gratings are devices that allow control over the properties of light propagating within a fibre and it is the sensitivity of these properties to perturbations of the fibre surroundings which has led to the use of these devices as sensors. Fibre gratings consist of a periodic perturbation of the properties of the fibre which is generally a modulation of the refractive index (*n*) of the core. When the modulation of the core refractive index has a period in the range of 100 μm to 1 mm, this is typically called a long-period grating (LPG) (Figure 4.1) which is in contrast to shorter period gratings called fibre Bragg gratings (FBGs), that typically act as mirrors. The LPG promotes coupling between the propagating core mode and the co-propagating cladding modes. Since the cladding modes have a high attenuation, the resulting transmission spectrum contains a series of attenuation bands resulting from the coupling to different cladding modes. An example of the transmission spectrum of an LPG is shown in Figure 4.2. As can be seen, there are at least two attenuation bands, the larger being near 1550 nm, however the exact form of this spectrum is dependent on several factors including the period and length of the LPG as well as the local environment including strain, temperature and the refractive index of the surrounding medium. Changes in these parameters ultimately modify the phase matching conditions for coupling to the cladding modes, which leads to a change in the central wavelength of the attenuation band.[3]

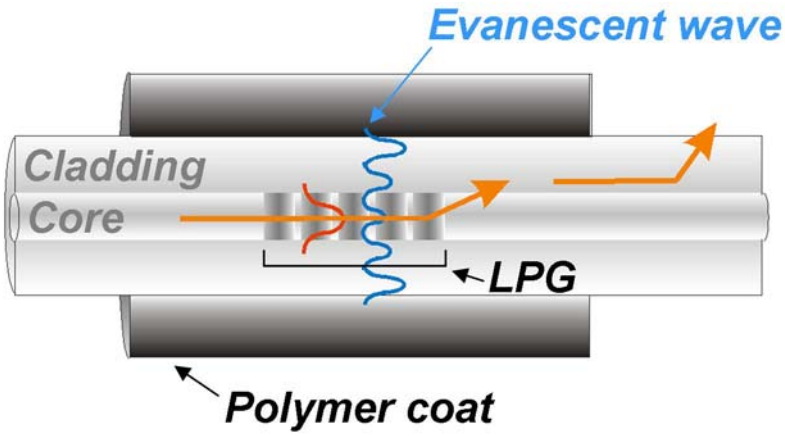

Figure 4.1 Fibre optic cable with LPG. The red curve represents light of a propagating core mode and the blue is a co-propagating cladding mode. Image adapted from reference [4].

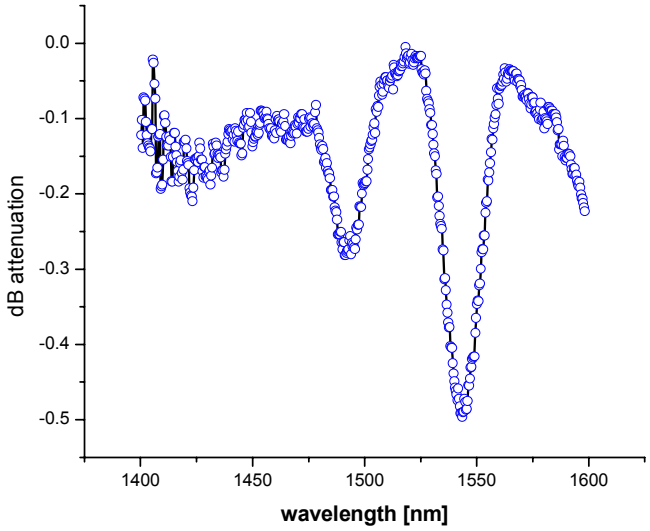

Figure 4.2 Typical LPG attenuation spectrum. Image adapted from reference [4].

As mentioned, the fibre consists of two waveguide structures- one being a high-index core, surrounded by a low-index cladding and the other is the cladding

surrounded by air (or another medium).[3] At resonant wavelengths (λ_f), phase-matching of the core mode and a cladding mode is achieved and losses in the attenuation spectrum are where is satisfied.[5,6]

$$\lambda_f = \Lambda[n_{core}(\lambda) - n^i_{clad}(\lambda)] \qquad \text{(Equation 4.1)}$$

Here, Λ is the period of the LPG, and n_{core} and n^i_{clad} are the effective refractive indices of the core and the i^{th} cladding mode respectively, at a given wavelength. In addition to the order of the cladding mode, the surrounding ambient environment will influence the effective refractive index to some degree. This is because the evanescent wave (a standing wave at the boundary interface) penetrates to a small extent (with an exponential decay) into the surrounding medium (see Figure 4.1). As the refractive index of the cladding surroundings increase (e.g. upon analyte adsorption), so too does the cladding effective refractive index (n^i_{clad}) and as a result the resonant wavelength (λ_f) shifts to shorter wavelengths according to Equation 4.1.

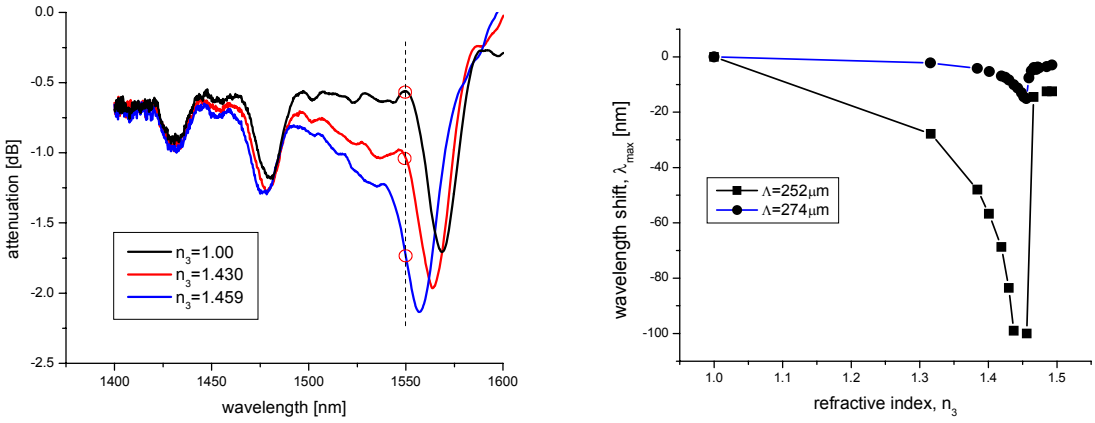

(a) **(b)**

Figure 4.3 (a) Changes in LPG attenuation spectra with change in ambient refractive index (n_3) from 1.00 (black), to 1.430 (red) and 1.459 (blue). (b) The magnitude of the resonant wavelength shift with respect to the ambient refractive index of two different LPG periodicities (Λ). Image adapted from reference [4].

As is evident from Figure 4.3 (a), the LPG attenuation spectra are blue-shifting in response to increasing ambient refractive indices ($n_3 > n_2 > n_1$). Figure 4.3 (b) demonstrates that the sensitivity (the magnitudes of the resonant wavelength shift) of the LPG is greatest at $n \approx 1.45$. This is because at $n_3 = 1.45$, there is better coupling of light from the cladding mode ($n_{clad} \approx 1.45$) to the ambient and therefore deeper penetration of the evanescent wave to the surrounding medium.[7]

There have been a number of reports of using bare LPGs as a detector for example for hydrocarbons[8] and aqueous solutions of salts[9] or sugars.[10] Others have used overlays on the cladding surface of the LPGs to impart chemical selectivity to the sensing region.[11-13] The overlays we wished to explore for use with LPGs are organosilica films.

4.1.2 Organosilica films

One of the more interesting features of mesoporous silica and sol-gel chemistry is the ability to process the materials into many different forms or morphologies.[14,15] These morphologies can range from non-uniform, irregular particles to highly monodisperse spheres, nanotubes, polyhedra, etc. Apart from the particle morphology, the sol-gel process allows for the formation of monoliths which will adopt the shape of the container or the casting of a sol to produce films of silica onto desired substrates.[16] A variety of applications can benefit from the development of organosilica in the thin film morphology (in this text arbitrarily referring to films of less than ~ 1000 nm in thickness). For example, many sensing applications where one needs to coat an electronic device, or to create chemically selective membranes or even more recent attempts in organic photovoltaic devices are often using thin film morphologies.

As with the particle morphology, incorporating organic functionality into thin silica films can lead to hybrid materials with tunable physicochemical properties, which are suitable for desired applications. The same methodologies for incorporating organic functionality into particles of silica exist for films as well, namely post-synthetic grafting, co-condensation and using siloxane-bridged precursors to make PMO films.

Ozin *et al*. were the first to report the preparation of periodic mesoporous organosilica films[17] with organic groups in the pore walls. Later, Inagaki *et al.* reported the fluorescence properties of aromatic PMO films, showing some films can have enhanced quantum yields over their precursors.[18]

It should be noted that the film morphology also tends to be a much more challenging and technologically demanding area of chemistry to work in than the uncontrolled particles discussed previously. With thin films, the actual masses of silica produced from these castings are often low and therefore characterization can be difficult.

4.1.3 Hybrid materials for mercury

There are many reports on the use of hybrid materials for the removal of heavy metal pollutants.[19] As thiol-modified silica has been shown to be an excellent adsorbent for mercury solutions,[20,21] we envisioned employing an organosilica film containing a thiol ligand as a component in an LPG sensing apparatus.

The film will function as an overlay on a fiber optic cable waveguide incorporating a LPG. As the film selectively adsorbs the metal from solution, a change in the optical properties (refractive index) of the film surrounding the LPG results, and thus a response in the transmission spectrum is observed. While work with thiol-functionalized mesoporous powders has shown great selectivity of the materials towards Hg^{2+} ions, there are few reports of thiol-functionalized mesoporous silicate films.[22]

In order to achieve maximum sensitivity from this spectroscopic technique, the film overlay needs to adhere to rather strict parameters. For instance, the refractive index of the film should be very close to that of the waveguide (n = ~1.45), the thickness of the film should be roughly 1.5 microns and the porous film should have interconnected pores to allow for maximum diffusion rates.

Calculations[23] have suggested that high sensitivity can also be achieved if the overlay has a high refractive index (~1.58) with a smaller thickness (~ 400 nm).

4.1.4 Sensor setup

To further increase the sensitivity of such a device, the envisioned fibre waveguide would be integrated into a phase-shift fibre-loop ring-down spectrometer (PS-FLRDS) (Figure 4.4).[24] Under this setup, analogous to phase-shift cavity ring-down spectroscopy (PS-CRDS),[25] intensity-modulated light is introduced into the loop which will then make several passes through the sensor region (LPG and chemically sensitive overlay) which serves to increase the effective optical pathlength and increase the signal-to-noise ratio. Here, a shift in the resonant wavelength is not measured, but a phase-shift (Φ) from light entering and exiting the loop is monitored. The advantage with measuring phase-shifts is that a fluctuation in laser or detector performance from one experiment to the next does not affect the results as a difference in signals is what is measured rather than absolute values. Other advantages of this setup include the ability to integrate the system components into a single board with a computer interface and the speed, low cost and sensitivity of the technique.

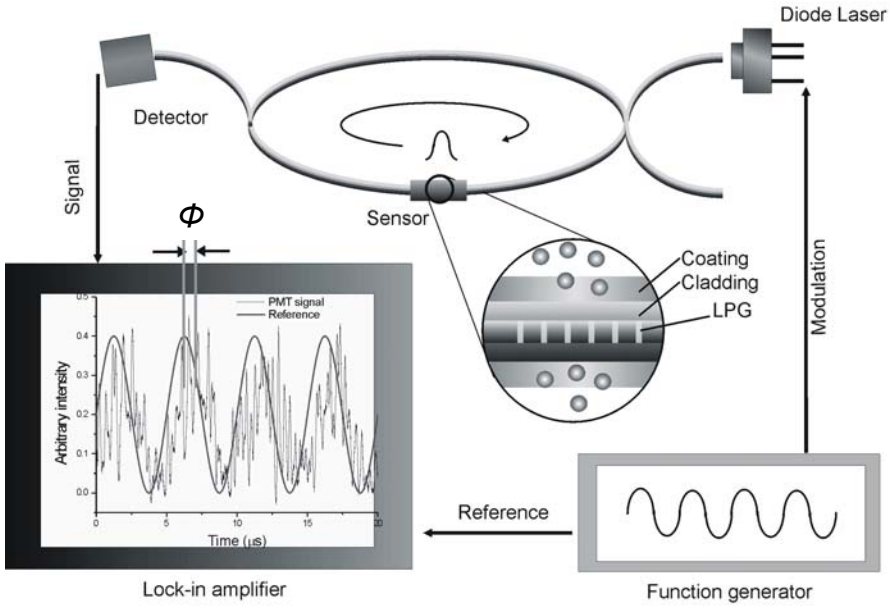

Figure 4.4 Schematic of PS-FLRDS setup integrating the LPG component. Φ is the phase-shift detected by the binding of an analyte to the chemically selective coating with reference to the generated signal. Image reproduced from reference [26].

With the concern for mercury contamination in the environment and a desire for fast, inexpensive yet sensitive determinations, the focus of this research project was to develop a chemically selective film which can be applied to the LPG. The challenges clearly lie in the need to satisfy the optical and mechanical requirements for such a film, for which organosilica films seemed to hold much promise.

4.2 Results and discussion

4.2.1 Determining refractive index and thickness of non-mesoporous silica films

One of the key features of our bottom-up approach to the functionalized film which will coat the LPG sensor unit was that we could control and modify if necessary any one of the many processing parameters to tune the resulting films

to the target properties. One important factor identified was the refractive index (*n*) of the film. As mentioned, the film overlay would be most sensitive if it were to match the refractive index of the cladding of the LPG section.[7] This was one of the benefits of using silicate films for this project, since this would essentially be a glass cladding with a glass overlay having very similar refractive indices. We initially envisioned adjusting the thiol content to increase the refractive index of the resulting material (if necessary) as the thiol is highly polarizable and therefore has a higher RI than that of glass.

Our initial attempts at film preparation were to simplify the process by avoiding the use of a surfactant and concentrate on the optical properties of the films. An early procedure was adapted from a report by Plawsky *et al.* where a thick (> 1 μm), highly porous (> 70 %) SiO_2 xerogel film from TEOS and a 2-step, acidic hydrolysis, basic condensation procedure with a solvent saturated atmosphere during drying.[27] We incorporated 25 % of (3-mercaptopropyl)triethoxysilane (MPTES) into the film preparation as the organothiol ligand for selective mercury adsorption.

Figure 4.5 (3-mercaptopropyl)triethoxysilane, MPTES

Unfortunately, it appeared through reflectometry measurements that our initial attempts at film preparation gave films of refractive index measured at *n* = 2.28. This was clearly too high of a RI to be useful for this purpose. In order to decrease the RI of the material, we deemed it necessary to incorporate porosity,

which should effectively lower the index of the film, depending on the amount of void space.

It should also be noted that an early technique which we used for film characterization was spectroscopic ellipsometry. This technique is non-destructive and very powerful for determining film properties such as dielectric constants and film thickness. Ellipsometry measures the change in polarization of the incident light upon reflection. One drawback of ellipsometry is that an accurate model of the complete film under analysis (including the optical constants of multilayers) is required in order to obtain the necessary data. Although a number of measurements were made, ultimately we abandoned this technique for lack of a sufficient model which gave rise to uncertain results.

4.2.2 Films incorporating mesoporosity

In order to determine an appropriate recipe for our purposes, an initial goal was to identify one which gave a well-ordered mesoporosity. Our studies in this area relied heavily on the nitrogen adsorption-desorption isotherms of condensed materials. A well-ordered mesoporous material would display a typical type IV isotherm with a sharp capillary condensation (see Figure 1.6). One of the first recipes we targeted for film preparation was a modified film of Ozin *et al.* where the silica source used was BTEE (Figure 4.6).[28] The organic-bridged silica monomers, were chosen as they offer the potential for increased flexibility and specific organic functionality within the silica backbone of the film.

We incorporated 5 % of the sulfur ligand (MPTMS) in an evaporation induced self assembly (EISA) approach using CTAB as the surfactant for

porosity. The sol was spun onto various wafers and any remaining sol was set to cure in a glass petri dish to obtain a bulk amount of the material. The as-synthesized film (organosilica material containing surfactant) was scraped from the petri dish and extracted using a MeOH/ HCl solution. The extracted film material (**F-BTEE-SH**) was subjected to N_2 physisorption analysis to determine the textural properties along with a control material (**F-BTEE**) with no thiol (Figure 4.7, a and b). By incorporating 5 % of the thiol ligand, the resulting isotherm changed from a type IV to an intermediate isotherm of type I and IV. Also, surface area decreased from 994 to 567 m^2/g, while the pore size distribution maximum dropped from roughly 2.2 to 2.0 nm. These observations can be rationalized by recalling the loss of mesoporosity that is often observed on the addition of organosilica precursors during the co-condensation process.[29] The surfactant templating process is disturbed and as a result there is a loss of porosity and surface area in the mesophase.

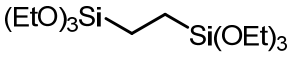

Figure 4.6 1,2-Bis(triethoxysilyl)ethane, BTEE.

By exposing these films to a saturated atmosphere of NH_3 vapour at room temperature for several hours, a dramatic improvement in the order of the mesoporous silica films was observed, as indicated by the increased steepness of the capillary condensation in the nitrogen isotherm of **F-BTEE-SH-NH_3** (Figure 4.7, c). Here, the strongly basic environment was clearly aiding in the condensation of the silica network to allow for a less destructive extraction of the

surfactant, largely maintaining the templated mesophase. Other common post-treatments, such as exposure to water at 100 ºC for 36 h, were not beneficial as these resulted in a large loss in the mesoporous order.

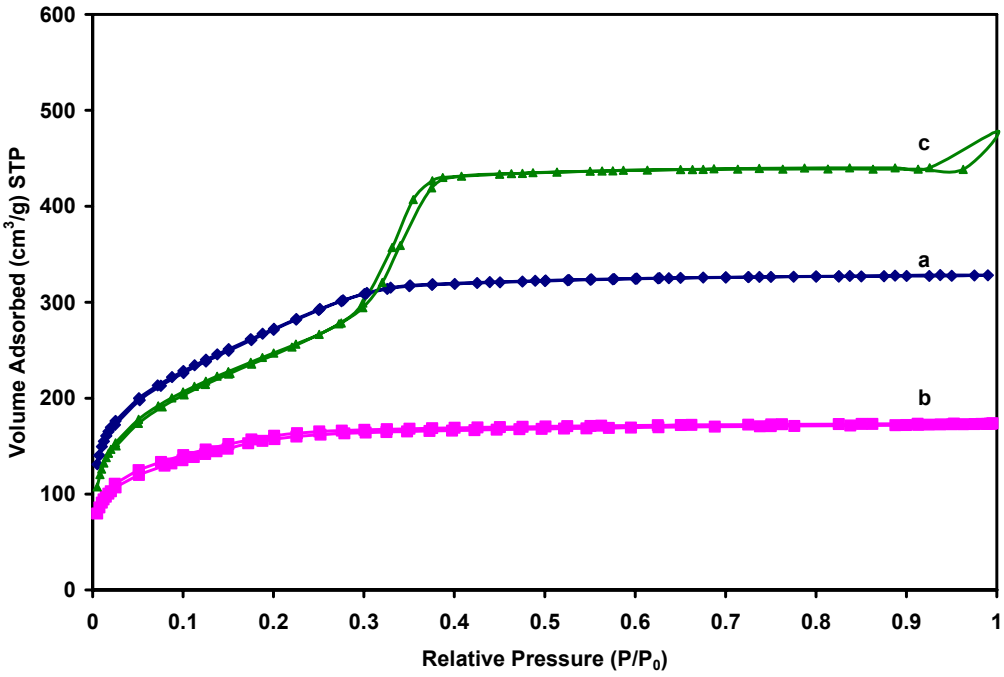

Figure 4.7 Nitrogen physisorption isotherms of film materials a) **F-BTEE**, b) **F-BTEE-SH** and c) **F-BTEE-SH-NH_3.**

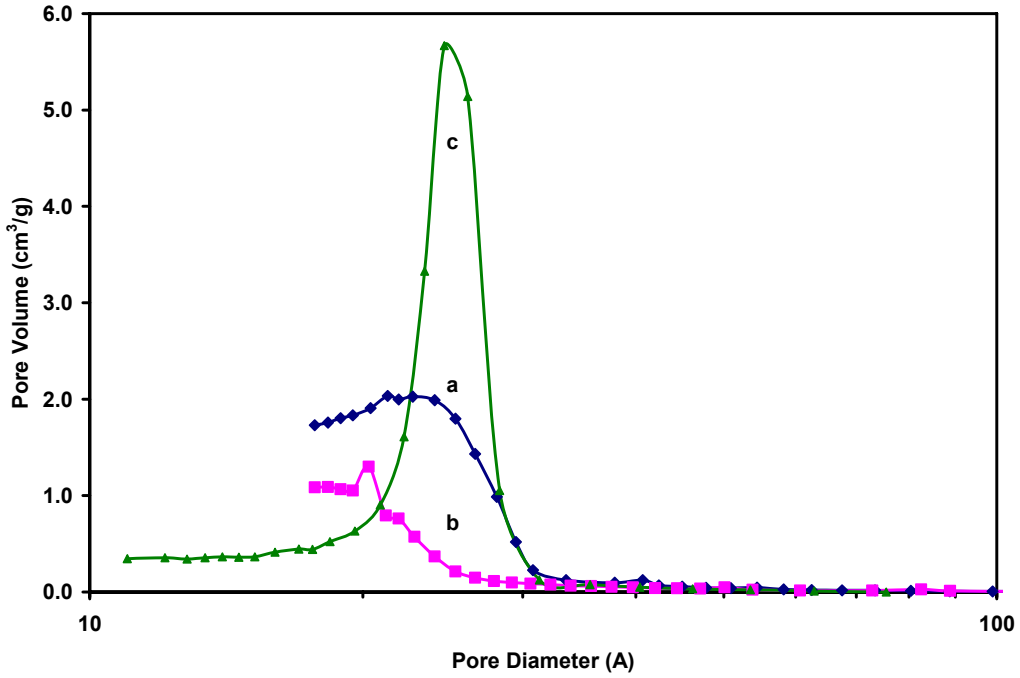

Figure 4.8 BJH Pore size distribution of film materials a) **F-BTEE**, b) **F-BTEE-SH** and c) **F-BTEE-SH-NH_3**.

4.2.3 Microprofilometry

With encouraging results from other lab members obtained from a different surfactant, Pluronic F127, (Figure 4.9), known to produce a more open, cubic network, we decided to pursue a study on the resulting film thickness following the coating of substrate. In addition, we were seeking to understand the properties of the films upon spin-coating a substrate, such as thickness and resistance to cracking.

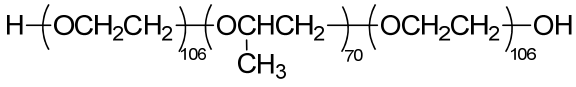

Figure 4.9 Structure of Pluronic F127 surfactant.

We found a more successful technique than ellipsometry for obtaining film thickness was micro-profilometry, which uses a stylus to measure height differences in the films. Here, a stylus is moved across a film coated on a silicon wafer, recording the valleys and peaks of the surface (Figure 4.10).

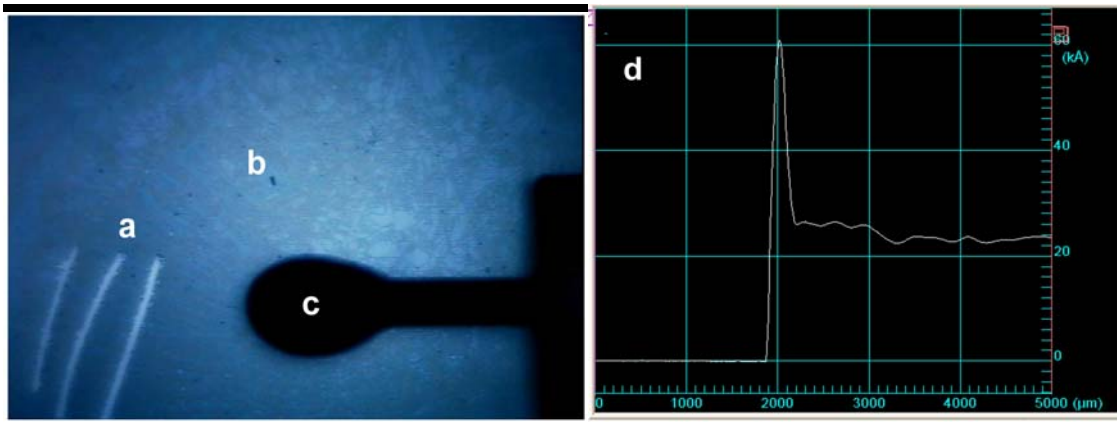

Figure 4.10 CCD camera image from microprofiler. a) scratches in film b) film c) profiler stylus d) Typical screen shot of a 2-D film profile.

Using this technique, we were able to successfully measure the thickness of a number of films from two different sol compositions. This enabled us to compare the differences in the film thickness for a TEOS based film, versus an organic-bridged, BTEE-based film. Films were coated at 24 h intervals and spun at 4 different speeds using a spin-coater (1000, 2000, 3000 and 4000 rpm). The resulting films were measured by micro-profilometry (Figure 4.11).

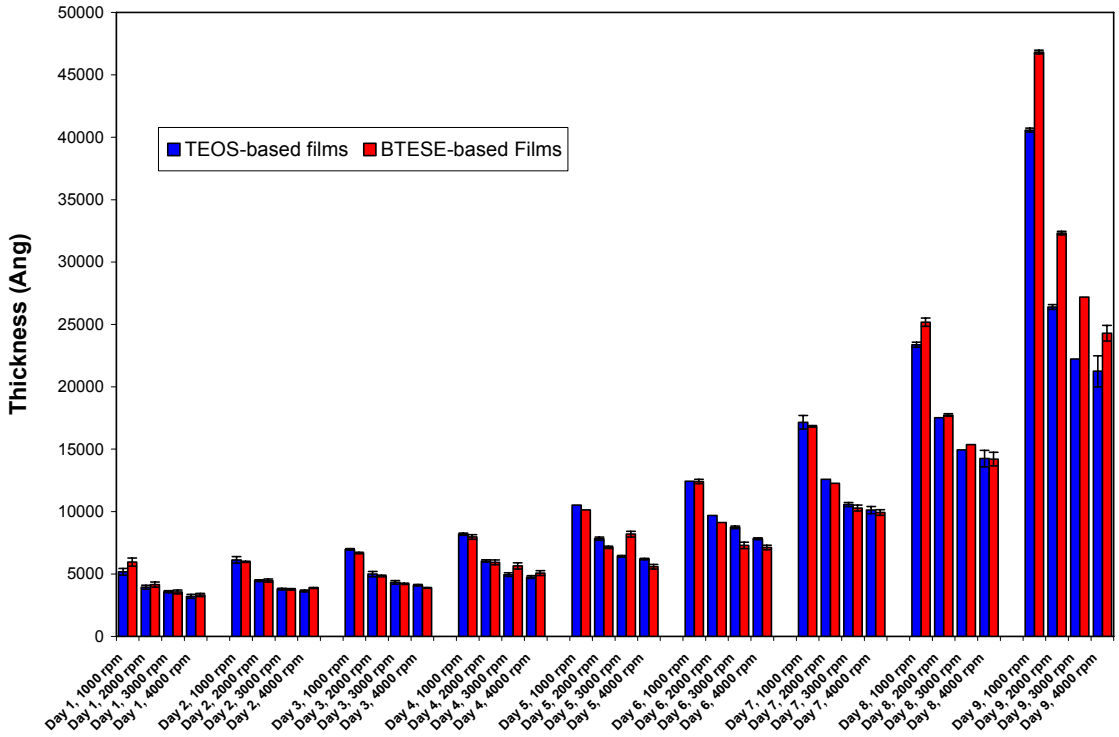

Figure 4.11 Organosilica film thicknesses measured by micro-profilometry. Films were prepared from TEOS or BTEE as a silica source, with 5 % MPTMS, and F127 as surfactant.

As can be seen from Figure 4.11, the films become increasingly thinner with a faster spin rate and the thickness increases by roughly 3 times over the first week. However, upon nearing the gelation stage, the resulting films become drastically thicker. This is related to the viscosity of the sol. As the sol ages over time, solvent evaporates and more cross-linking of the monomers occurs, resulting in a more viscous film being spun. Other points to note are that there is not much difference in thickness between the entirely inorganic silica films made from TEOS and those made from the BTEE. As we were initially targeting 1.5 μm

thick films, it soon became apparent that waiting 7 or 8 days for a sol to age was not very practical.

An interesting observation which was made during the profilometry of one set of films, was the intriguing cracking patterns that were apparent from the CCD camera images (Figure 4.12). Over time, as the silica network becomes more condensed and excludes water and other imbibed solvent molecules, shrinkage of the film may occur. It is fairly common for thicker silicate films to crack such that it is notoriously difficult to prepare crack-free films thicker than approximately 1 μm.[30] There has been at least one report on the cracking patterns from xerogel films but it does not touch on the patterns observed here.[31] Ozin *et al.* have also remarked on the origins of channel and surface patterns.[32] These particular films are non-templated, which discounts the regularities being caused as a result of surfactant micelle assemblies. The patterns are currently unexplained but are likely related to a semi-regular crystallization of the silica precursors.

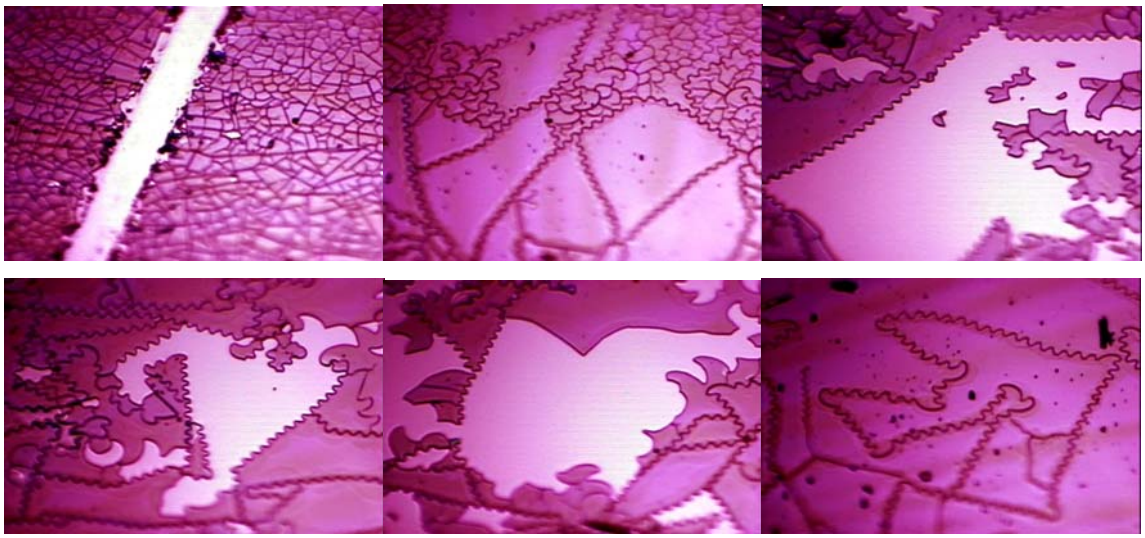

Figure 4.12 Cracked BTEE-film images. Field of view is roughly 2 mm.

4.2.4 Fibre-dip coating

As the goal of our work was to coat a fibre-optic cable, we needed to determine how the films would be processed on this substrate, rather than flat silicon wafers. In order to coat the fibre, we moved from the spin-coating to the dip-coating technique. Brinker *et al.* have reviewed the fundamentals of sol-gel dip-coating.[33]

Dip coating is somewhat counter-intuitive for most, in that the faster the substrate is removed from the sol, the thicker the resulting film is. When the substrate speed and liquid viscosity are low, as is normally the case in sol-gel film deposition, the thickness of the entrained liquid on the substrate upon removal from the sol, is determined by the effect of different forces including viscous force, capillary force and gravity on its flow.[34] It has been shown that the thickness is proportional to approximately ½ the power of the withdrawal rate.[35]

One of the major challenges here was to measure the film thickness on fibre-optic cables. The first method we tried which would have proven very efficient and non-destructive was that of profilometry once again. Although attempts were put forth into determining whether the technique would be able to determine a reliable film thickness, it was eventually decided that the profiler was not giving consistent enough data due to the cylindrical nature of the substrate.

Also, optical microscopy was surveyed for its potential in measuring film thickness, however this too had the drawback of poor depth of field imaging and difficulties in determining the rounded fibre-edges of the transparent glass. Therefore, it appeared SEM, although more expensive, destructive and time-consuming, was our best solution to the current issue.

For our optimization, fibre-optic cables, not containing an LPG segment, were dip-coated by submerging a section (~ 5 cm) at the end of the fiber into a tall container holding the sol. The fibre was withdrawn at various speeds by a home-made dip coater to determine this effect on the resulting thickness of the film, much like the experiments on the spin-coated silicon wafers. After the fibres were left to dry and cure, they were prepared for imaging by SEM. In order to determine a proper film thickness it was important to have a clean cross-section of the fibre and film. To achieve this, we used a fibre cleaving device which scores the film and fibre with a diamond wheel before snapping it cleanly into two pieces. The fibre was then mounted onto an SEM stub, and lightly gold-coated, to produce a conductive surface. The contrast between the glass fibre and the organosilica film was enough to take careful measurements from the FE-SEM

images and to determine the optimal withdrawal speed of the fibre (Figure 4.13 and Figure 4.14).

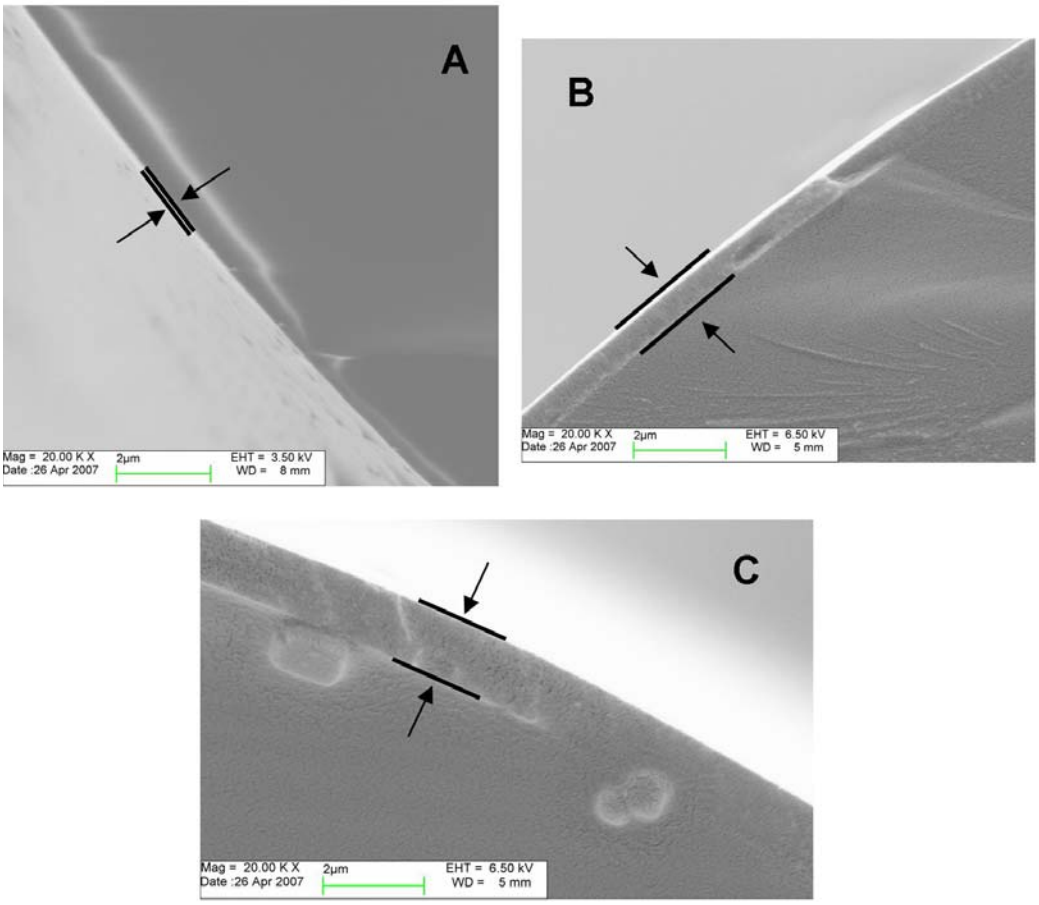

Figure 4.13 HRSEM images of fibres coated with a sol composition including BTEE, 5 % MPTMS, HCl, CTAB, H_2O, and EtOH. Organosilica film thickness measurements were recorded for withdrawal rates of a) 10 mm/s b) 15 mm/s and c) 20 mm/s.

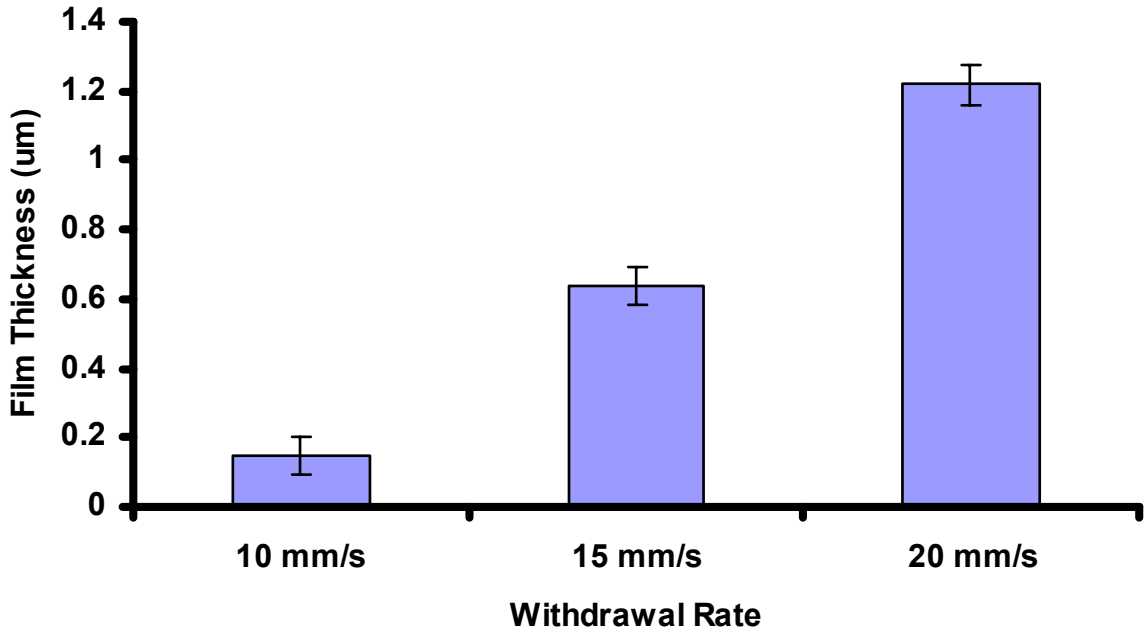

Figure 4.14 Organosilica film thickness on fibres from Figure 4.13. Sol composition included BTEE, 5 % MPTMS, HCl, CTAB, H_2O, and EtOH.

It can be seen from Figure 4.13 and Figure 4.14 that increasing the constant withdrawal speed from 10 to 20 mm/s produces a thicker film as expected from dip-coating theory. From these results, it is desirable to maintain roughly a 15 to 20 mm/s withdrawal rate in order to achieve at least a 1 μm thick film. The thickness of this particular type of film was targeted for less than 1.5 μm in light of communicated results which suggested sensitive film coatings could be obtained from thinner films of higher refractive index.[23]

4.2.5 Calibrating LPGs

As previously mentioned, the refractive index of the medium in which the LPG operates is of critical importance to the sensitivity of the technique. In order

to determine the optimal refractive index region to perform adsorption experiments in, we needed to calibrate the LPG to find the most sensitive region. This was accomplished by connecting the LPG-containing fibre to an optical spectrum analyzer. The optical spectrum analyzer is an instrument that displays the difference spectrum of light (from 1420-1620 nm) that results from comparing a reference fibre with that of the LPG in use. When the LPG couples light to the cladding, a negative peak is observed in the spectrum. This peak will then shift with the changes in the refractive index of the surrounding environment. Thus, when the surrounding environment is an organosilica film, which is coordinating to very polarizable Hg^{2+} ions, there should be an increase in the refractive index, and a shift in the spectrum.

The sensing region of the LPG was suspended taut over a Teflon container. The LPG is also sensitive to temperature and stress fluctuations so it was imperative to keep the fibre relatively untouched once it was ready for calibration. For the calibration, a transmission spectrum was taken in surroundings of various refractive indices, the first one being air (n= 1.00). The Teflon well was then sequentially filled with solutions of increasing refractive index. For this, we used increasing concentrations of DMSO in water to give solutions of n = 1.32 to 1.46 at 1550 nm. As the LPG equilibrated in the presence of the surrounding solution, the spectrum, which displayed a peak of resonant wavelength, shifted towards shorter wavelengths (hypsochromic or blue-shift) and stabilized. The wavelength of this peak was recorded. The shift of this peak is the change in the spectrum that we are interested in. When the calibration was

completed (Figure 4.15 and Figure 4.16) with the desired range of standard RI solutions, a calibration curve was prepared, the sensitive region was noted and the LPG was coated with the organosilica sol.

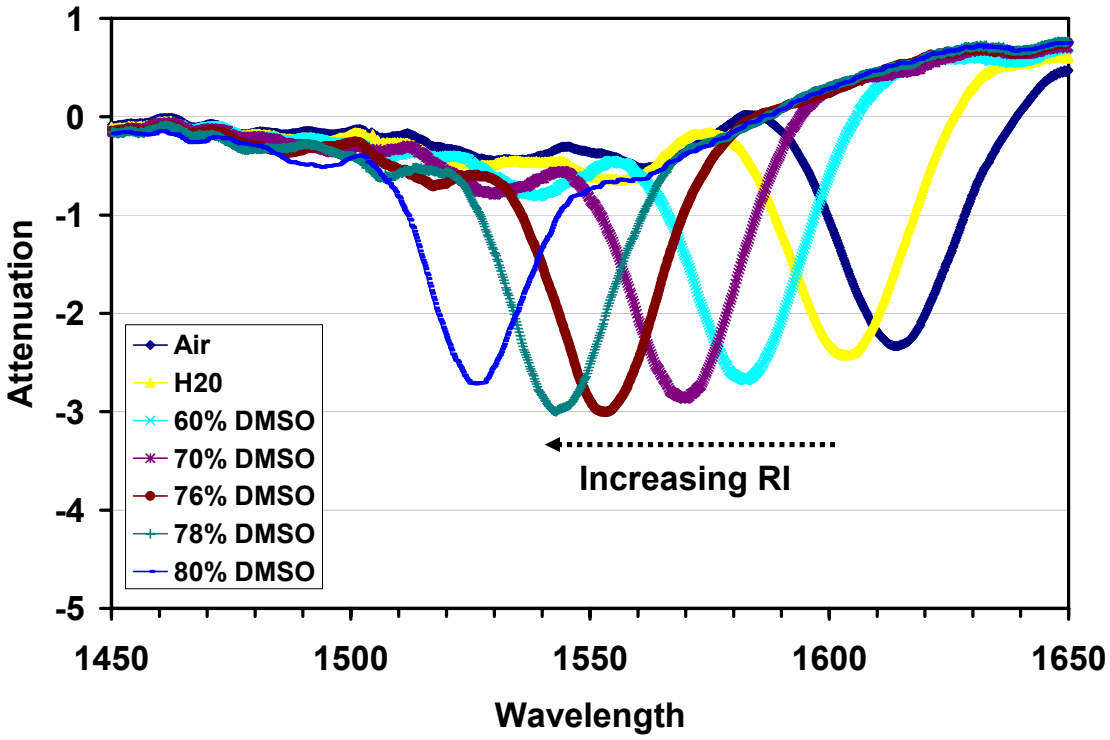

Figure 4.15 LPG calibration with surrounding medium of air (n = 1.00) to 80 % (v/v) DMSO in water (n = 1.43).

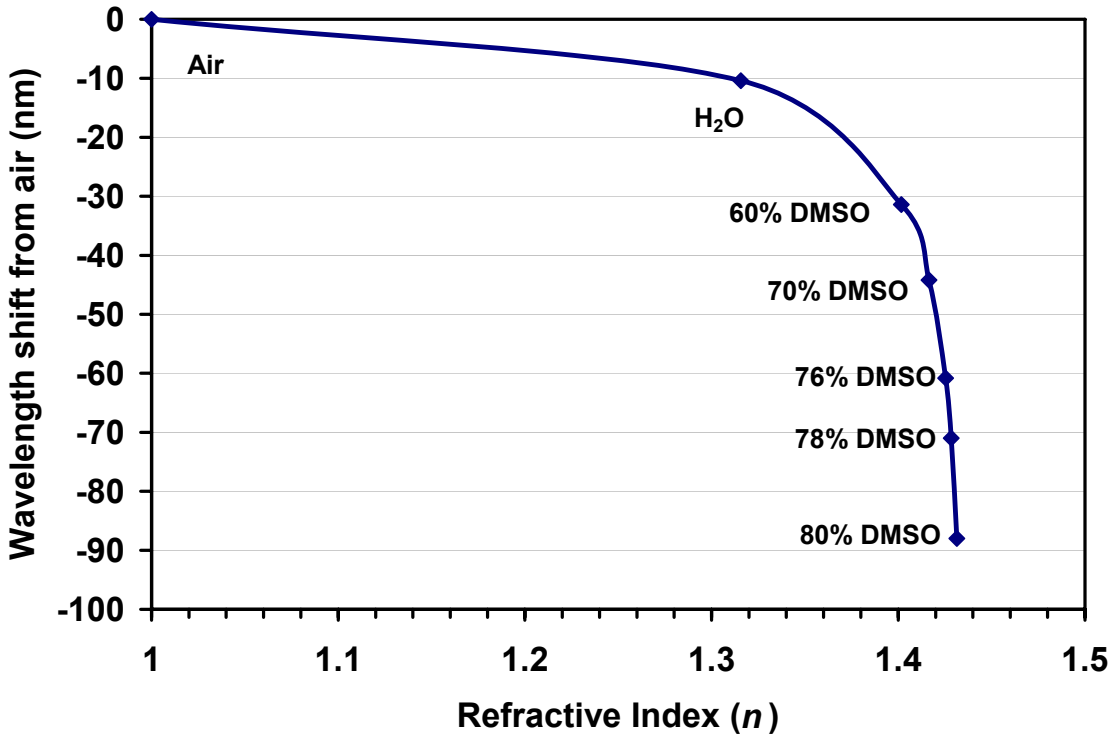

Figure 4.16 LPG refractive index calibration curve using DMSO/water mixtures. The resonant wavelength shift from air (n = 1.00) from Figure 4.15 with DMSO volume percentages marked.

4.2.6 Coating the LPG

With a successful dip-coating technique in hand, we attempted coating the pre-calibrated fibre containing the LPG unit. The same sol composition containing BTEE and 5 % MPTMS which was used for dip-coating the test fibres above, was used here for coating the LPG. After aging the sol to an appropriate viscosity, a fibre containing an LPG section was dip-coated to give the desired thickness of film. The film was air-dried overnight and in the morning, the fibre was treated with NH_3 for 15 min to help condense the film as this had been shown previously to help the mesostructural order. The surfactant was extracted

from the film by carefully placing the fibre in a large 3-neck round bottom flask with 200 mL MeOH/ 12 mL concentrated HCl solution. Once the surfactant was removed from the functional overlay, optical connectors were reattached to the ends of the fibre before it could be reconnected to an optical spectrum analyzer.

4.2.7 Recalibration

At this point, we 'recalibrated' the film to ensure that it was sensitive to changes in refractive index. Indeed, as seen from Figure 4.17, the LPG is still sensitive to changes in RI, however, the sensitive region had been pushed towards lower refractive indices. This is because the film overlay now has a higher refractive index than the bare fibre cladding and is thus contributing to the ambient index the LPG is sensing. With the steepest slope of the coated calibration curve near n =1.3724 which corresponded to a 40 % DMSO/H_2O (v/v) solution, we prepared standard mercury(II) nitrate solutions in 40 % DMSO/ H_2O solution to test for Hg^{2+} detection.

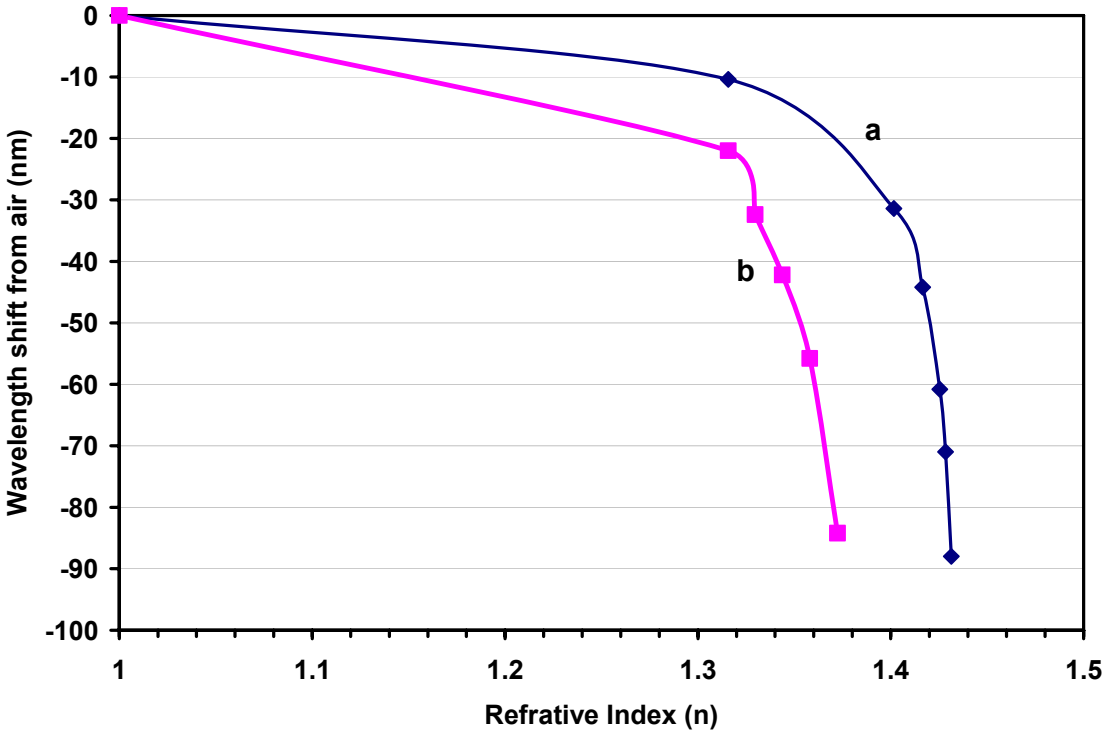

Figure 4.17 LPG refractive index calibration curve using DMSO/water mixtures for a) the uncoated LPG b) the LPG coated with BTEE/ 5% MPTMS film.

The LPG was exposed sequentially to increasingly concentrated mercury solutions. The spectrum was allowed to stabilize for 3 min, before the peak of the resonant wavelength was recorded. Although these were only very early attempts at mercury detection, there appeared to be some promise to the results. The small wavelength shifts at the lower concentrations are likely within error of each other, however, the 5 nm shift overall from air to 10 000 ppm mercury solution can be considered detection of mercury. As the limit of this detection was clearly not optimized, future work sought to improve on this.

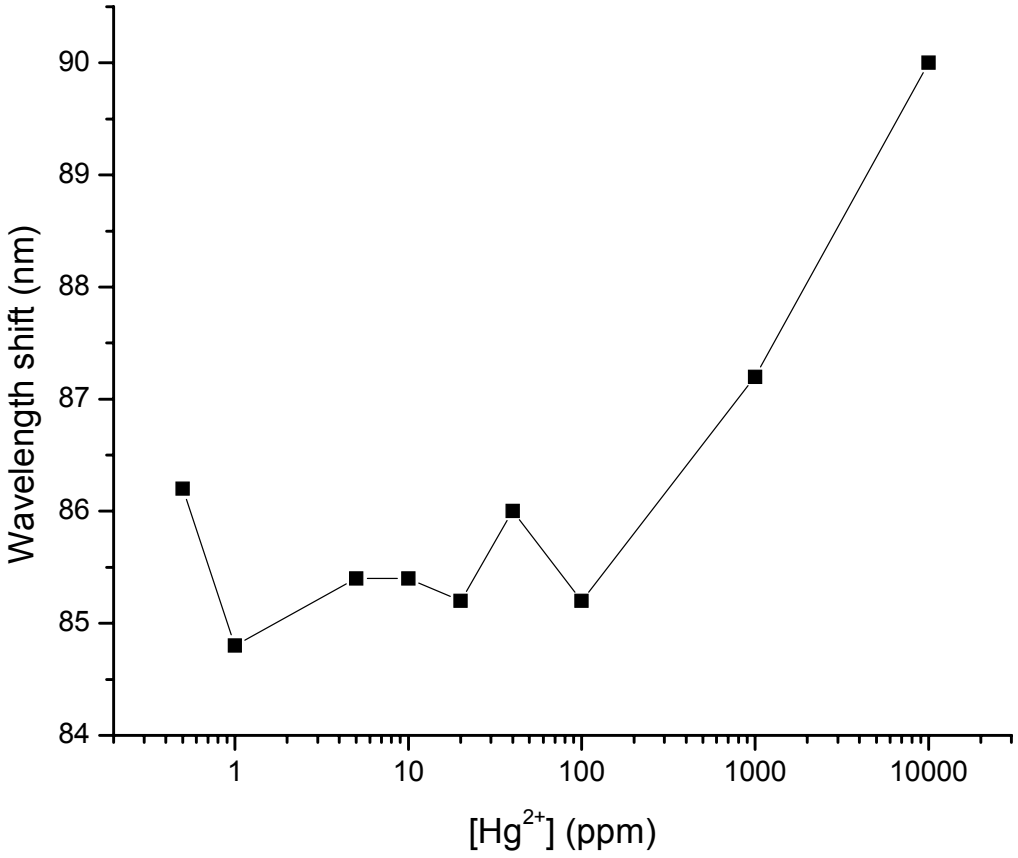

Figure 4.18 Response of LPG to 40% DMSO/H_2O solutions containing $Hg(NO_3)_2$.

In conjunction with others in the lab, the sensitivity of this technique was eventually improved. One important step in the project was the pursuit of lead as an analyte rather than mercury. Although Pb(II) has a much lower distribution coefficient than Hg(II), (913 versus ~10^8),[36] it also has a much higher polarizability volume than Hg(II), (5 $Å^3$ versus 1.25 $Å^3$). Thus, it should have a much higher refractive index and cause larger shifts in the LPG attenuation spectrum. Ultimately our group was able to detect low ppb levels of lead, by

using an organosilica film containing TEOS and bis[3-triethoxysilyl)propyl]tetrasulfide (Figure 4.19) as a metal ligand.[4]

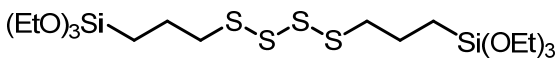

Figure 4.19 bis[3-triethoxysilyl)propyl]tetrasulfide

4.3 Conclusions

The detection of toxic heavy metals has become an issue of ever-increasing importance due to the concern over current and future clean water reserves. Fibre optic cables featuring LPG devices offer a potential opportunity to perform efficient, low-limit detection which could be useful for monitoring remote sites or areas surrounding toxic holding grounds in case of leaks.

Periodic mesoporous organosilica (PMO) thin films have been shown to be useful components of LPGs, as they offer high surface areas and chemical selectivity for analytes which are concentrated for detection. We have shown that by coating the outer surface of the LPG with a functional PMO film containing a sulfur ligand, MPTMS, the refractive index in the vicinity of the LPG changes in the presence of mercury solutions, causing a shift in the LPG transmission spectrum. By calibrating the shift in the resonant wavelength of the spectrum, with the concentration of mercury in solution, we were able to determine the presence of mercury in a DMSO/water solution despite having poor detection limits. Modifications of the organosilica film were successful in producing a sensor for the sub-ppm detection of Pb(II).

4.4 References

(1) Exposure To Mercury: A Major Public Health Concern, World Health Organization, 2007. (http://www.who.int/phe/news/Mercury-flyer.pdf)

(2) Guidelines for Drinking-water Quality, Third Edition Incorporating the First and Second Addenda, Volume 1, Recommendations, World Health Organization, 2008. (http://www.who.int/water_sanitation_health/dwq/fulltext.pdf)

(3) James, S. W.; Tatam, R. P. *Meas. Sci. Technol.* **2003**, *14*, R49.

(4) Du, J.; Cipot-Wechsler, J.; Lobez, J. M.; Loock, H.-P.; Crudden, C. M. *Small* **2010**, *6*, 1168-1172.

(5) Vengsarkar, A. M.; Lemaire, P. J.; Judkins, J. B.; Bhatia, V.; Erdogan, T.; Sipe, J. E. *J. Lightwave Technol.* **1996**, *14*, 58-65.

(6) Bhatia, V.; Campbell, D. K.; Sherr, D.; Dalberto, T. G.; Zabaronick, N. A.; Ten Eyck, G. A.; Murphy, K. A.; Claus, R. O. *Optical Engineering* **1997**, *36*, 1872-1876.

(7) Marazuela, M.; Moreno-Bondi, M. *Anal. Bioanal. Chem.* **2002**, *372*, 664-682.

(8) Klemba, F.; Rosado, R. H. G.; Kamikawachi, R. C.; Muller, M.; Fabris, J. L. *XXIX Encontro Nacional de Física da Matéria Condensada, 2006, São Lourenço-Brazil. Optics Technical Digest* **2006**, ID 559.

(9) Falciai, R.; Mignani, A. G.; Vannini, A. In *European Workshop on Optical Fibre Sensors*; 1 ed.; SPIE: Peebles, Scotland, United Kingdom, 1998; Vol. 3483, p 95-98.

(10) Tang, J. L.; Cheng, S. F.; Hsu, W. T.; Chiang, T. Y.; Chau, L. K. *Sensors and Actuators B-Chemical* **2006**, *119*, 105-109.

(11) Rees, N. D.; James, S. W.; Tatam, R. P.; Ashwell, G. J. *Opt. Lett.* **2002**, *27*, 686-688.

(12) Cusano, A.; Iadicicco, A.; Pilla, P.; Contessa, L.; Campopiano, S.; Cutolo, A.; Giordano, M.; Guerra, G. *J. Lightwave Technol.* **2006**, *24*, 1776.

(13) Cusano, A.; Iadicicco, A.; Pilla, P.; Contessa, L.; Campopiano, S.; Cutolo, A.; Giordano, M. *Opt. Express* **2006**, *14*, 19-34.

(14) Slowing, I. I.; Vivero-Escoto, J. L.; Trewyn, B. G.; Lin, V. S. Y. *J. Mater. Chem.* **2010**, *20*, 7924-7937.

(15) Sanchez, C.; Rozes, L.; Ribot, F.; Laberty-Robert, C.; Grosso, D.; Sassoye, C.; Boissiere, C.; Nicole, L. *C. R. Chimie* **2010**, *13*, 3-39.

(16) Grosso, D.; Cagnol, F.; Soler-Illia, G.; Crepaldi, E. L.; Amenitsch, H.; Brunet-Bruneau, A.; Bourgeois, A.; Sanchez, C. *Adv. Funct. Mater.* **2004**, *14*, 309-322.

(17) Dag, O.; Yoshina-Ishii, C.; Asefa, T.; MacLachlan, M. J.; Grondey, H.; Coombs, N.; Ozin, G. A. *Adv. Funct. Mater.* **2001**, *11*, 213-217.

(18) Goto, Y.; Mizoshita, N.; Ohtani, O.; Okada, T.; Shimada, T.; Tani, T.; Inagaki, S. *Chem. Mater.* **2008**, *20*, 4495-4498.

(19) Walcarius, A.; Mercier, L. *J. Mater. Chem.* **2010**, *20*, 4478-4511.

(20) Feng, X.; Fryxell, G. E.; Wang, L. Q.; Kim, A. Y.; Liu, J.; Kemner, K. M. *Science* **1997**, *276*, 923-926.

(21) Brown, J.; Mercier, L.; Pinnavaia, T. J. *Chem. Commun.* **1999**, 69-70.
(22) Petkov, N.; Mintova, S.; Jean, B.; Metzger, T.; Bein, T. *Mater. Sci. Eng., C* **2003**, *23*, 827-831.
(23) Hochreiner, H. Modelling of long-period fibre gratings in chemical sensing applications. Ph.D. Thesis, Dalhousie University, Halifax, NS, 2008.
(24) Tong, Z. G.; Wright, A.; McCormick, T.; Li, R. K.; Oleschuk, R. D.; Loock, H. P. *Anal. Chem.* **2004**, *76*, 6594-6599.
(25) Engeln, R.; von Helden, G.; Berden, G.; Meijer, G. *Chem. Phys. Lett.* **1996**, *262*, 105-109.
(26) Barnes, J.; Dreher, M.; Plett, K.; Brown, R. S.; Crudden, C. M.; Loock, H. P. *Analyst* **2008**, *133*, 1541-1549.
(27) Nitta, S. V.; Pisupatti, V.; Jain, A.; Wayner Jr, P. C.; Gill, W. N.; Plawsky, J. L. *J. Vac. Sci. Technol., B* **1999**, *17*, 205.
(28) Hatton, B. D.; Landskron, K.; Whitnall, W.; Perovic, D. D.; Ozin, G. A. *Adv. Funct. Mater.* **2005**, *15*, 823-829.
(29) Lim, M.; Blanford, C.; Stein, A. *Chem. Mater.* **1998**, *10*, 467-470.
(30) Brinker, C. J.; Scherer, G. W. *Sol-gel science: the physics and chemistry of sol-gel processing*; Academic Press, 1990.
(31) Chow, L. A.; Xu, Y. H.; Dunn, B.; Tu, K. N.; Chiang, C. *Appl. Phys. Lett.* **1998**, *73*, 2944-2946.
(32) Yang, H.; Coombs, N.; Dag, O.; Sokolov, I.; Ozin, G. A. *J. Mater. Chem.* **1997**, *7*, 1755-1761.
(33) Brinker, C. J.; Frye, G. C.; Hurd, A. J.; Ashley, C. S. *Thin Solid Films* **1991**, *201*, 97-108.
(34) Guglielmi, M.; Zenezini, S. *J. Non-Cryst. Solids* **1990**, *121*, 303-309.
(35) Strawbridge, I.; James, P. *J. Non-Cryst. Solids* **1986**, *86*, 381-393.
(36) Feng, X.; Liu, J.; Fryxell, G. E.; Gong, M.; Wang, L.-Q.; Chen, X.; Kurath, D. E.; Ghormley, C. S.; Klasson, K. T.; Kemner, K. M. Self-Assembled Mercaptan on Mesoporous Silica (SAMMS) technology of mercury removal and stabilization, Pacific Northwest Lab., Richland, WA (United States), 1997.

Chapter 5

Experimental procedures

5.1 General Procedures

Reagents

All reagents unless otherwise noted were purchased and used as received from Sigma-Aldrich. 4-Bromostyrene and Grubbs' 2nd Generation Catalyst were purchased from Aldrich and used without further purification. Triethoxysilane was purchased from TCI America. CH_2Cl_2 was obtained dry from a solvent purification system fitted with alumina columns. THF was freshly distilled from sodium/benzophenone ketyl. Triethylamine was purchased from Aldrich and distilled fresh from CaH_2 prior to use. *N,N*-Dimethylformamide (DMF) was purchased dry from EMD and used without any further treatment. n-BuLi was freshly titrated before use with *N*-benzylbenzamide in dry THF at -78ºC.

Instrumentation

Solution NMR analysis was performed on Bruker (300, 400, 500 and 600 MHz) spectrometers. Solid-state CP MAS ^{13}C and ^{29}Si NMR measurements were recorded on a Bruker Avance 600 spectrometer operating at 150.9 and 119.2 MHz for ^{13}C and ^{29}Si, respectively, and using a Bruker 5 mm CP MAS probe. A typical spinning rate for CP MAS experiments is 11 kHz. A 2 ms cross polarization contact time was used to acquire ^{29}Si and ^{13}C CP MAS spectra with a repetition delay of 2 s. The number of scans was in excess of 600 and 2400 for

^{13}C and ^{29}Si respectively to obtain sufficient signal. ^{13}C and ^{29}Si MAS spectra were referenced to tetramethylsilane. Automated flash chromatography was performed on a Biotage Horizon chromatography system. Gas sorption experiments were performed using a Micromeritics ASAP 2010 physisorption analyzer with nitrogen gas as the adsorbate at 77 K. Samples were degassed at 80 °C for at least 8 hours and until 10^{-3} mm Hg pressure was maintained. Infrared spectroscopy was performed on a BOMEM MB-series or Varian 1000 FT-IR spectrometer. Circular dichroism spectra were obtained on a Jasco J-715 spectropolarimeter. A small amount of the solid PMO was added to a 1 dram vial with a small amount of water (or other solvent) and sonicated at room temperature for 10 s to break up the silica particles. The mixture was then transferred to a 1 cm cuvette and the circular dichroism spectrum was acquired. The concentration was then adjusted so that an appropriate absorbance or a consistent CD spectrum was obtained. The wavelengths scanned were typically 550-190 nm, with a data resolution of 0.2 nm, a band width of 5.0 nm, a response time of 0.5 s and a scanning speed of 1000 nm/min. The number of accumulations was adjusted (1 to 20) in order to obtain acceptable signal to noise ratios. The data collected is expressed as the ellipticity, (one mdeg = 0.001 deg), where molar circular dichroism ($\Delta\varepsilon$) and molar ellipticity ([θ]) are interconverted by the equation: $[\theta] = 3298.2\ \Delta\varepsilon$.[1]

TEM images were obtained using a 200keV JEOL 2010 STEM operated in both transmission and STEM modes. In STEM mode a Gatan High Angle Annular Dark Field Detector was used to image the sample. Elemental maps and

spectra were generated using an EDAX (Genesis) Energy Dispersive X-ray system. The sample was prepared by placing a small amount of powder in ethanol and sonicating for 5 minutes. 20 μL of the solution was pipetted onto a carbon coated, 200 mesh copper grid. Raman spectra were acquired with a Jobin-Yvon/Horiba (Edison, NJ) microRaman Spectrometer (Model: LabRam) with a spectrum resolution capability of 2-3 cm^{-1}, equipped with a 632 nm He/Ne laser source, 1800 1/nm grating and an Olympus BX41 microscope system. Collection of the spectra was performed in backscattered mode at room temperature under the following conditions: x100 microscope objective, 1100 μm pinhole size, 300 μm slit width, and 60 s exposure time. Each spectrum represents the average of two measurements. Powder X-ray diffraction measurements were run on an automated Siemens/Bruker AXS D5000 diffractometer. The system is equipped with a high power line focus Cu-kα source operating at 50 kV/35mA. A solid-state Si/Li Kevex detector was used for removal of k-beta lines. The diffraction patterns were collected on a theta /2-theta Bragg-Brentano reflection geometry with fixed slits. The slits were set up appropriately for both low-and wide angle ranges in order to ensure the optimal quality of the diffraction patterns. A step scan mode was used for data acquisition with step size of 0.02° 2-theta and counting time of 3.0 s per step for low-theta scans and 1.0 s per step for the wide range scans.

5.2 Experimental procedures from Chapter 2

5.2.1 Precursor syntheses

4,4'-dibromo-*trans*-stilbene

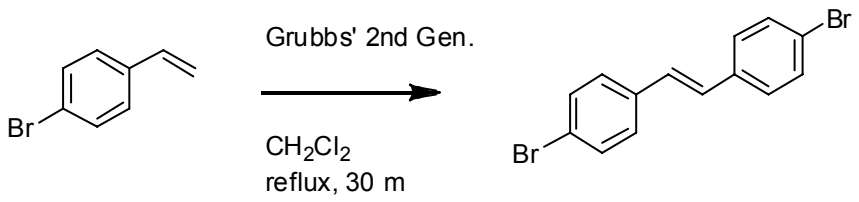

To a flame-dried 250 mL round bottom flask, containing a stirbar, was added *p*-bromostyrene (25 g, 137 mmol). The flask was flushed with Ar and dry CH_2Cl_2 (150 mL) was cannulated in to dissolve the aryl bromide. Finally, Grubbs' 2nd Generation catalyst (23.8 mg, 0.02 mol %) was weighed into a vial in a nitrogen atmosphere glovebox, capped, removed from the glovebox and transferred quickly to the solution under an argon flow. A reflux condenser was fitted to the flask and the solution was refluxed for 17 h. The resulting white precipitate was vacuum filtered using a Buchner funnel and washed with cold CH_2Cl_2 until colourless (~50 mL). Colourless flakes (22.85 g, 99 %) were obtained and used subsequently without further purification. The ^{1}H and ^{13}C spectra obtained matched that of the literature.[2]

4,4'-diiodo-*trans*-stilbene

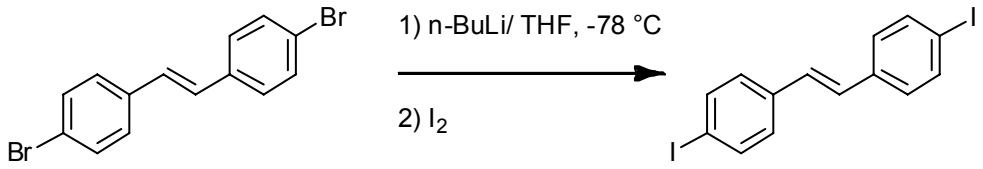

Procedure has been adapted from Chang *et al.*[3] In a 500 mL flame-dried round bottom flask containing a stirbar was added 4,4'-dibromo-*trans*-stilbene (15.6 g, 37.8 mmol) and dry THF (250 mL). The solid was allowed to dissolve and cool in a dry ice/ ^{i}ProH bath to -78 °C before n-BuLi (2.3 eq, 87.0 mmol), was added dropwise over 20 min. The mixture was allowed to stir cold for 30 min before solid I_2 chips (24.1 g, 95.0 mmol) were added. The mixture was then warmed to room temperature and stirred overnight. Saturated Na_2SO_3 solution was added and the mixture was transferred to a separatory funnel. The aqueous layer was extracted with Et_2O (3 x 50 mL) and the organic layers combined, dried over $MgSO_4$, filtered and concentrated to an impure solid. The crude product was dissolved in MeOH and kept cold overnight. An equal volume of H_2O was added to yield precipitate which was vacuum filtered to an off-white solid (14.6 g, 76 %). The ^{1}H and ^{13}C spectra obtained matched that of the literature.[3]

4,4'-Bis(triethoxysilyl)*trans*-stilbene BTETS or
(*E*)-1,2-bis(4-(triethoxysilyl)phenyl)ethene (**1**)

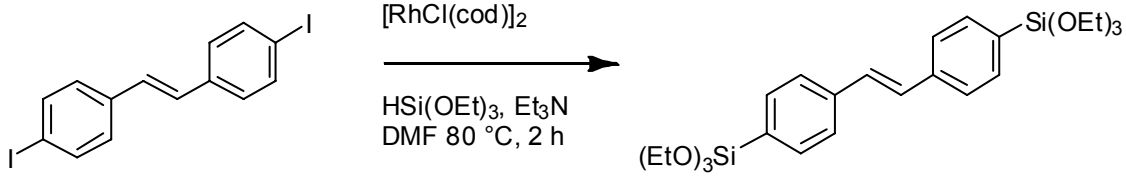

Procedure has been adapted from that of Masuda *et al.*[4] To a flame-dried 100 mL round bottom flask containing a stirbar, was added (*E*)-1,2-bis(4-

iodophenyl)ethane (859 mg, 1.99 mmol) and $[RhCl(cod)]_2$ (29.2 mg, 0.0592 mmol, 6 mol %). The solids were briefly flushed with Ar and DMF (15.8 mL) was added. Et_3N (1.65 mL, 11.8 mmol) and triethoxysilane (1.46 mL, 7.90 mmol) were added via dry needle and syringe and the mixture was stirred for 2 h at 80 °C. The mixture was concentrated *in vacuo* at 50-60 °C under high vacuum. The black residue was filtered through a short plug of silica, using 5:1 Hex:EtOAc, concentrated to a yellow oil and purified by column chromatography using a Biotage Flash chromatograph, with an elution of 2 % EtOAc in hexanes increasing to 20 % EtOAc over 1 L total volume. Collected R_f 0.24 (10: 1 Hex: EtoAc) and concentrated to obtain 557 mg, 55 % yield of white solid.

^1H NMR (CD_2Cl_2) (500 MHz) δ 1.33 (t, *J*= 7.0 Hz, 18H), 3.96 (q, *J*= 7.0 Hz, 12H) 7.28 (s, 2H) 7.64 (d, *J*= 8.0 Hz, 4H) 7.76 (d, *J*= 8.0 Hz, 4H); ^{13}C NMR (CD_2Cl_2) (125 MHz) δ 18.5, 59.1, 126.4, 129.7, 131.3, 135.6, 139.4; ^{29}Si NMR (99.3 MHz) -57.95 ppm. Exact mass calculated for $C_{26}H_{40}O_6Si_2$ m/z = 504.2363, found m/z = 504.2368.

(4-Bromobenzyl)-triphenylphosphonium bromide

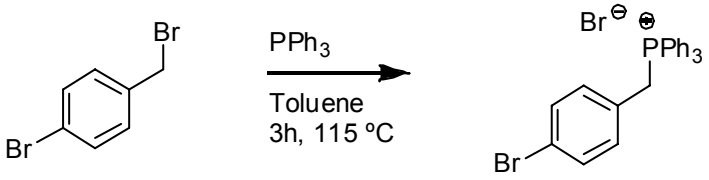

Material was prepared as previously reported by Hopf *et al.*[5] To a solution of 4-bromobenzyl bromide (12.0 g, 48.0 mmol) and triphenylphosphine (14.0 g, 53.4 mmol) in toluene (320 mL) was heated to a gentle reflux (115 ºC) with stirring for 3 h. After cooling to room temperature, the solid was filtered and

washed with cyclohexane (200 mL) and allowed to air dry overnight for a 78 % yield (19.23 g, 37.5 mmol). The ^{1}H and ^{13}C spectra obtained matched that of the literature.[5]

4,4'-dibromo-*cis*-stilbene

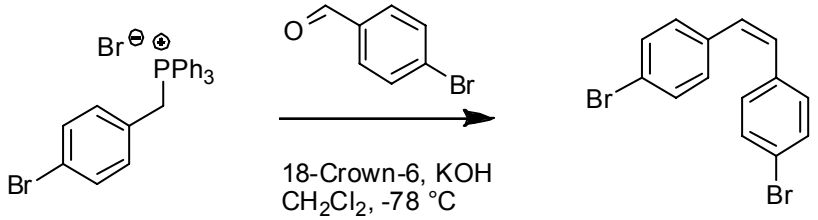

Material was prepared as previously reported by Wilcox *et al.*[6] A solution of 4-bromobenzaldehyde, (4-bromobenzyl)-triphenylphosphonium bromide and 18-crown-6 in CH_2Cl_2 was prepared in a 200 mL round bottom flask and cooled to -78 ºC in an acetone/ dry ice bath. Freshly powdered potassium hydroxide was added and stirred 1.5 h cold. The bath was removed, and the mixture was warmed to room temperature and stirred for 4.5 h. The mixture was then filtered and the filtrate washed with saturated NH_4Cl, dried over $MgSO_4$, filtered and concentrated. The solid was extracted with hexanes and filtered again before being concentrated to a yellow solid. ^{1}H NMR of the crude product shows ~ 80:20 *cis:trans* product ratio. The crude product was purified by column chromatography using hexanes as eluting solvent. Fractions with R_f = 0.26 (hexanes) collected for pure *cis* isomer (6.91 g, 72 %). The ^{1}H and ^{13}C spectra obtained matched that of the literature.[6]

4,4'-diiodo-*cis*-stilbene

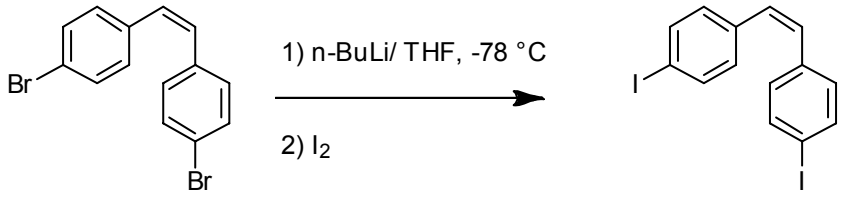

A similar procedure to that reported for the synthesis of 4,4'-diiodo-*trans*-stilbene above was used.

4,4'-Bis(triethoxysilyl)*cis*-stilbene, BTECS
or(*Z*)-1,2-bis(4-(triethoxysilyl)phenyl)ethene (**2**)

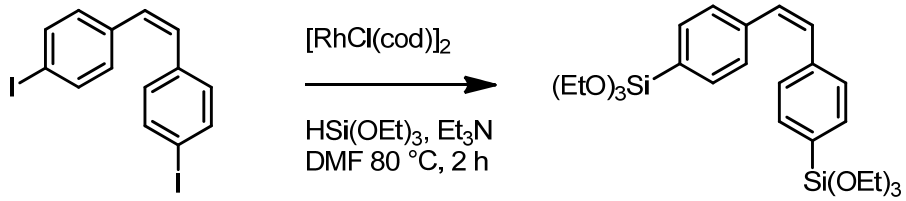

To a flame-dried 100 mL round bottom flask containing a stirbar, was added (*Z*)-1,2-bis(4-iodophenyl)ethane (859 mg, 1.99 mmol) and $[RhCl(cod)]_2$ (29.2 mg, 0.0592 mmol, 6 mol %). The mixture was briefly flushed with Ar and DMF (15.8 mL) was added. Et_3N (1.65 mL, 11.8 mmol) and triethoxysilane (1.46 mL, 7.90 mmol) were added and the mixture was stirred for 2 h at 80 °C under Ar. The mixture was concentrated *in vacuo* at 50 - 60 °C under high vacuum. The black residue was filtered through a short plug of silica, using 5:1 Hex:EtOAc, concentrated to a yellow oil and purified by column chromatography using a Biotage Flash chromatograph, with an elution of 2 % EtOAc in hexanes

increasing to 20 % EtOAc over 1 L total volume. Collected R_f 0.27 (10:1 Hex: EtoAc) and concentrated to clear oil to obtain 448 mg, 45 % yield.

^{1}H NMR ($CDCl_3$) (400 MHz) δ 1.27 (t, *J*= 6.9 Hz, 18H), 3.99 (q, *J*= 6.9 Hz, 12H) 6.63 (s, 2H) 7.28 (d, *J*= 7.9 Hz, 4H) 7.55 (d, *J*= 7.9 Hz, 4H); ^{13}C NMR ($CDCl_3$) (100 MHz) δ 18.2, 58.8, 128.3, 129.8, 130.7, 134.7, 139.1. Exact mass calculated for $C_{26}H_{40}O_6Si_2$ m/z = 504.2363, found m/z = 504.2383.

5.2.2 Material preparation

PMO-1/4^{H+}

Molar Ratios : (BTEBP: BTETS **(1)**: Brij 76: H_2O: HCl: NaCl)

(0.85: 0.15: 0.534: 600: 8.05: 19.0)

This procedure is based on that of Ozin *et al.*[7] In a typical procedure, 0.199 g of Brij 76, 5.67 g distiled H_2O and 0.428 g concentrated HCl (36 wt %) were combined in a capped 30 ml polypropylene Nalgene bottle with stirbar and allowed to stir to homogeneity at 60 °C for 1 hr at which point 0.582 g of NaCl was added and recapped to stir at 60 °C for 3 more hours. BTEBP (0.213 g) and BTETS **(1)** (0.040g) were added and the mixture was stirred for 20 h at 60 °C. The stirbar was removed and the white precipitate was allowed to age statically at 80 °C for 24 h. The bottle was removed from the oil bath, cooled to room temperature and filtered. The powder was washed with 200 mL distilled H_2O and allowed to air dry. The template was extracted by stirring in an acidic ethanol solution (0.45 g c. HCl, 30 mL EtOH, 95 %) for 6 h at 60 °C. The mesoporous material was filtered, washed with 250 mL EtOH and air dried.

PMO-1/4^{OH-}

Molar Ratios : (BTEBP: BTETS **(1)**: C_{18}TAMCl: H_2O: NaOH)

(0.85: 0.15: 1.28: 1320: 12100)

This procedure is based on that of Inagaki *et al.*[8] In a typical procedure, octadecyltrimethylammonium chloride (C_{18}TMACl) (0.186 g), 6 N NaOH (0.85 mL) and distilled H_2O (9.93 g) were combined in a 4 dram glass vial with stirbar. The mixture was stirred until homogeneous. BTEBP (0.170 g) and BTETS **(1)** (0.032 g), were then added with vigorous stirring and allowed to stir at room temperature for 20 h. The vials were then heated without stirring at 95 °C for 22 h. After heating, the precipitate was cooled, filtered and washed with 100 mL of distilled H_2O. The template was extracted by stirring the solid with 40 mL of acidic EtOH solution (500 mL EtOH, 10.3 g 2 M HCl), filtered and washed with fresh EtOH before air drying.

PMO-2/4^{H+}

Molar Ratios : (BTEBP: BTECS **(2)**: Brij 76: H_2O: HCl: NaCl)

(0.85: 0.15: 0.534: 600: 8.05: 19.0)

This material was prepared as **PMO-1/4^{H+}** above using BTECS (**2**) in place of BTETS (**1**).

PMO-1/3^{H+}

Molar Ratios : (BTEB: BTETS **(1)**: P123: c. HCl: H_2O)

(0.85: 0.15: 0.068: 0.944: 800)

This procedure was based on that of Inagaki *et al.*[9] In a typical procedure, 0.625 g of P123, 22.7 mL of distilled water, and 126 µL of hydrochloric acid (36 wt %) were added to a capped 60 mL polypropylene bottle with stirbar. The mixture was stirred until homogeneous and cooled to 0 °C. BTEB (0.542 g) and BTETS **(1)** (0.120 g) were added and the mixture was stirred for 1 h cold. After stirring for 20 h at 39 °C, the white material was filtered, washed with distilled water, and then heated statically in a closed polypropylene bottle containing fresh water at 100 °C for 3 d to improve mesoscale order. The white precipitate was then filtered, and the template was extracted with ethanol at 60 °C for 16 h with stirring.

5.2.3 Osmium staining of PMOs

In a closed, glass chamber containing osmium tetroxide ***(DANGER-Use only in fumehood with proper protection!),*** 2-3 mg of PMOs were placed in separate vials and were exposed to the saturated vapour in the closed vessel for 4 h at room temperature. The PMOs were then placed under an Ar flow overnight to remove any physisorbed Os. The resulting materials were then characterized by TEM and other methods.

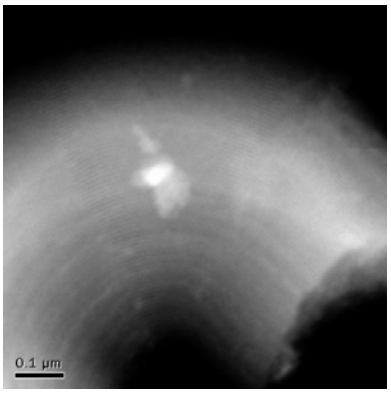

Figure 5.1 HAADF TEM image of **PMO-1/3^{H+}-Os** showing bright contrast for Os.

5.2.4 Ozonolysis of PMO-1/3^{H+} (PMO-1/3^{H+}-O_3)

In a typical procedure, **PMO-1/3^{H+}** (34 mg), was added to a 50 mL glass tube with ground joint and stirbar. Solvent was added (1 mL MeOH: 1 mL CH_2Cl_2) and the mixture was cooled to -78 °C in an isopropanol/dry ice bath. The ozonator outlet line was fitted to a glass adapter with a stopcock to moderate the gas flow and fitted to the glass tube. The gas flow was carried below the solvent level by a pipette which was fitted to the adapter enabling a slow ozone flow, bubbling through the solvent. The O_2 pressure gauge was set to 9 PSI and the voltage to 0.9 V to initiate the O_3 production. After 20 min, the O_3 flow was terminated and the ozonide was quenched with anhydrous dimethylsulfide (0.2 mL). The mixture was allowed to warm up to room temperature over 1.5 h and the fine white powder was collected by centrifugation and subsequently re-suspended (three times in EtOH and once in Et_2O) to remove any soluble reagents. The solvent was removed from the **PMO-1/3^{H+}-O_3** (28 mg) in a vial under an Ar flow.

5.2.5 Synthesis of L-alanine methyl ester

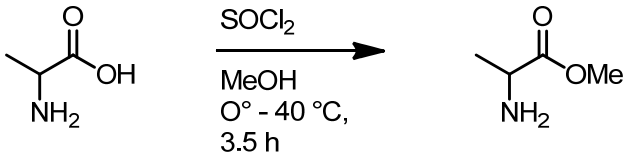

L-alanine methyl ester was prepared according to Rengasamy *et al.*[10] In a 20 mL round bottom flask with stirbar, a suspension of L-alanine (500 mg, 5.61 mmol) was prepared in MeOH (8.3 mL) and cooled to 0 °C in an ice bath with stirring. $SOCl_2$ (0.9 mL, 12.3 mmol) was added dropwise before the mixture was warmed to 40 °C, and stirred for 3.5 h. The flask was cooled to room temperature and evaporated under vacuum to dryness. The ^1H NMR matched that of the reported product and was deemed pure enough for our purposes.

5.2.6 General procedure for imine formation (PMO-1/3-$^{H+}$-C=N)

A capped 1 dram vial containing L-alanine-methylester hydrochloride (8.4 mg) (pre-dried under vacuum in presence of P_2O_5 overnight), triethylamine (9.8 µL) 0.5 mL of MeOH and ten 4 Å molecular sieves (pre-activated in oven at 140 ºC overnight) were allowed to sit statically for 30 min. A small amount of PMO (1.8 mg) was then added and allowed to react in the mixture for 1.5 h at room temperature, followed by heating in an oil bath at 40 ºC for a further 6 h. The molecular sieves were then removed by tweezers following reaction and the PMO was washed by a series of centrifugations with fresh solvent (3 x 10 mL EtOH, 1 x 10 mL EtOH) before being dried under a stream of argon. Infrared and Raman spectroscopy were then performed.

N-Boc allylamine

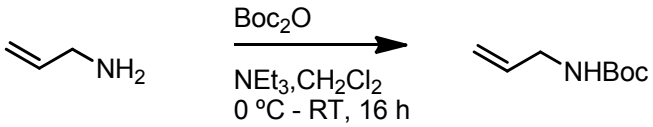

Material was prepared as previously reported by McMills *et al.*[11] To a solution of allylamine (1.0 g, 17.5 mmol), and freshly distilled triethylamine (5.36 mL, 38.6 mmol) in anhydrous CH_2Cl_2 (20 mL) at 0 ºC was added Boc_2O (4.22 g, 19.3 mmol). The reaction was allowed to warm to room temperature overnight. The solvent was removed under reduced pressure and the crude product matching the reported ^1H NMR data was pure enough for our use.

5.2.7 General procedure for metathesis reaction

Grubbs' 2nd Generation catalyst (1.0 mg, 0.11 mmol) was weighed into a 1 dram vial in the glovebox, removed, and quickly fitted with a rubber septum. The septum was briefly removed while the PMO (6.10 mg) was added and the solids were briefly flushed with argon. Dry CH_2Cl_2 (0.4 mL) and *N*-Boc-allylamine (0.05 mL) were then injected before heating the mixture to just below reflux temperature (40 ºC) for 5.5 h. The mixture turned brown and the PMO was washed by a series of centrifugations with fresh solvent (3 x 10 mL EtOH, 1 x 10 mL EtOH) before being dried under a stream of argon. Infrared and Raman spectroscopy were then performed.

5.2.8 Hydrophobic *trans*-stilbene PMO (PMO-1/3^{H+}-SiMe$_3$)

Hexamethyldisilazane (1.6 mL, 7.63 mmol) was added to a 4 dram vial containing **PMO-1/3^{H+}** (79.4 mg) and allowed to react at room temperature for

1.5 h. The PMO was washed by a series of centrifugations with fresh solvent (3 x 10 mL EtOH, 1 x 10 mL EtOH) before being dried under a stream of argon. The hydrophobic material **PMO-1/3^{H+}-SiMe$_3$** (66 mg, 83 %) was recovered. Nitrogen physisorption analysis, and infrared spectroscopy were performed.

5.2.9 Procedure for PMOs with increased stilbene content

Basic conditions- Materials were prepared in the same manner as that of **PMO-1/4^{OH-}** above. For materials with increased BTETS (1) concentration, including POS-1, the molar ratios of BTETS (1) : BTEBP were adjusted as required to keep the total moles of Si constant. For the non-templated material (POS-2), all reagents amounts remained the same, but C_{18}TMACl was removed, for POS-3, all reagents were added, followed by addition of ethanol (3 mL). For POS-4, BTETS (1) was pre-dissolved in 3 mL of anhydrous ethanol (with slight < 60 ºC), and then transferred to the surfactant assembly mixture. For POS-5, a large excess of ethanol was used (EtOH : H_2O = 12.21 g : 3.0 g). For POS-6 a 3 : 2 mass ratio of ethanol to water was used. For POS-7 the amount of 6 N NaOH solution used was ¼ that of the general procedure, for POS-8, a 3:2 mass ratio of ethanol to water was used as well as ½ the amount of monomer from the general procedure was used.

Acidic conditions- (*trans*-stilbene-bridged materials) Materials were prepared in the same manner as that of **PMO-1/3^{H+}** above.[9] For materials with increased BTETS (1) concentration, the molar ratios of BTETS (1) : BTEB were adjusted as required to keep the total moles of Si constant.

Acidic conditions- (*cis*-stilbene-bridged materials) materials were prepared in the same manner as that of **PMO-2/4^{H+}** above.[7] For materials with increased BTECS (2) concentration, the molar ratios of BTECS (2) : BTEBP were adjusted as required to keep the total moles of Si constant.

5.3 Experimental procedures from Chapter 3

5.3.1 Precursor synthesis

4,4'-dibromo-*trans*-stilbene

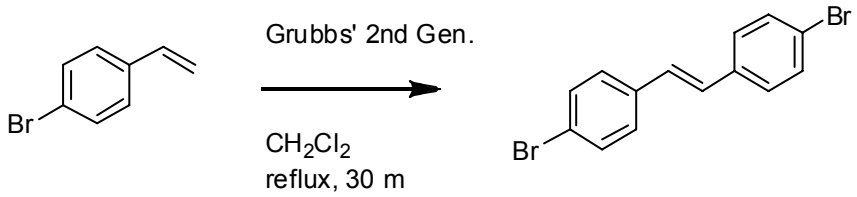

This procedure was reported in the previous chapter.

(*R,R*)- (+)-1,2-bis(4-bromophenyl)-1,2-ethanediol

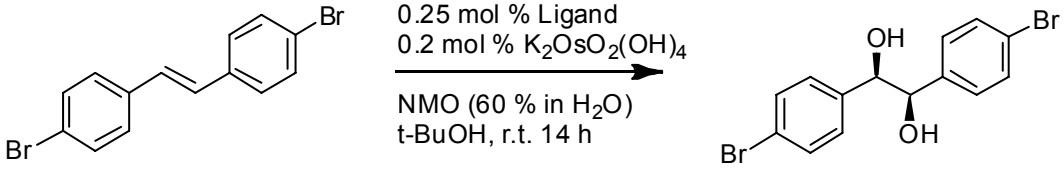

Ligand

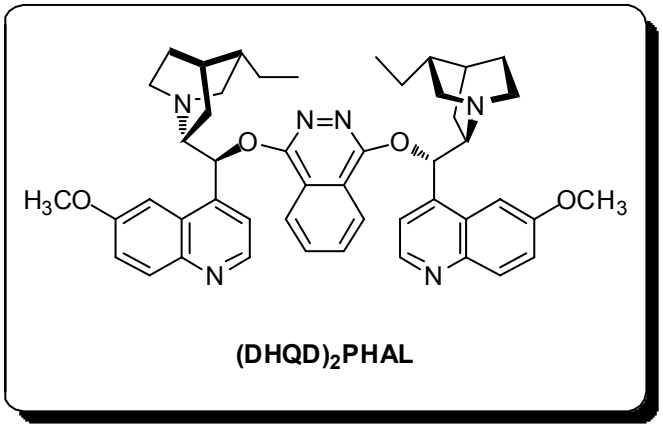

$(DHQD)_2PHAL$

This 1,2-diol was made according to an adapted procedure of Sharpless *et al.* which uses *trans*-stilbene as the olefin substrate.[12] A 100 mL round bottom

flask with stirbar was charged with 4,4'-dibromo-*trans*-stilbene (17.0 g, 50.3 mmol), $(DHQD)_2PHAL$ (97.8 mg, 0.25 mol %), *N*-methylmorpholine *N*-Oxide (NMO) (50 % aqueous, 15.1 mL), and *tert*-butanol (24.2 mL). Potassium osmate dihydrate ($K_2OsO_4 \cdot 2H_2O$) (37.0 mg, 0.20 mol %), was added last and the mixture was let to stir overnight at room temperature in the fume hood. 4,5-dihydroxy-1,3-benzenedisulfonic acid disodium salt, monohydrate (Tiron, Aldrich) (89.8 mg) was added to sequester the osmium, while stirring for 3 h at room temperature. Distilled H_2O (27.0 mL) was added and stirred for another 4 h. The crude product was filtered and washed with 250 mL cold d. H_2O to remove any colour. The solid was dried overnight on the filter paper to give 14.7 g of yellowish powder (78 %). The product was used without further purification as less than 3 % of the diketone byproduct was observed by ^1H NMR analysis.

^1H NMR ($CDCl_3$) (400 MHz) δ 2.97 (s, 2H, OH), 4.59 (s, 2H, ArC*H*), 6.96 (d, *J*= 8.4 Hz, 4H, Ar), 7.37 (d, *J*= 8.4 Hz, 4H, Ar); ^{13}C NMR ($CDCl_3$) (100 MHz) δ 78.51, 122.08, 128.68, 131.37, 138.46.

(*S,S*)-(-)-1,2-bis(4-bromophenyl)-1,2-ethanediol

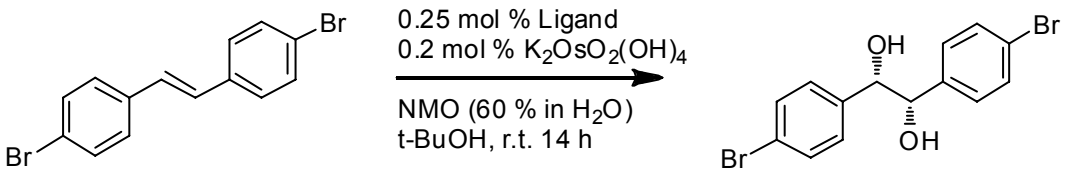

Ligand

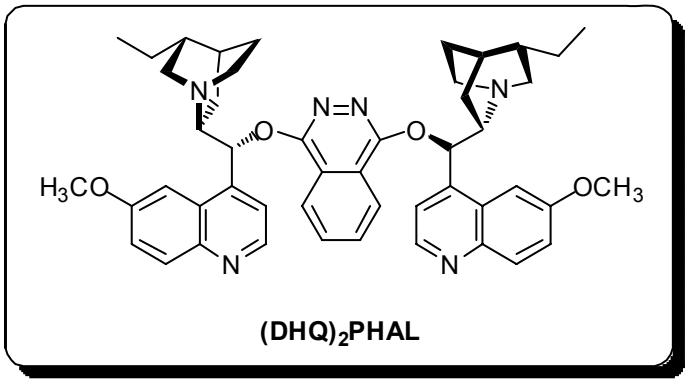

$(DHQ)_2PHAL$

Diol was prepared as (*R,R*) enantiomer previous but using the pseudoenantiomeric ligand $(DHQ)_2PHAL$ instead of $(DHQD)_2PHAL$. A 72 % yield was obtained, spectral data matched that of the enantiomeric (*R,R*) product and it was used without further purification.

The following procedures were repeated for both enantiomeric forms of the starting materials.

4,5-bis-(4-bromophenyl)-2,2-dimethyl-[1,3]dioxolane

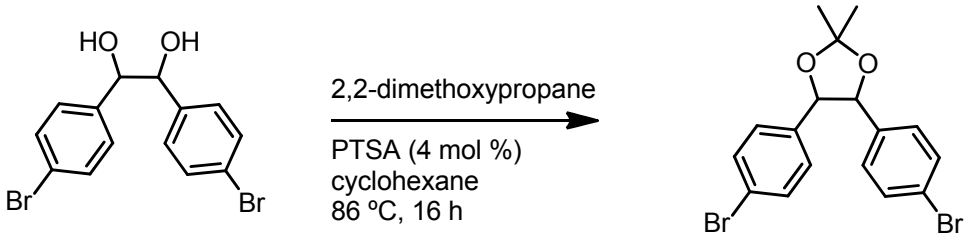

Ketalization was performed according to the procedure reported by Jeong *et al.*[13] (*R,R*)-1,2-bis(4-bromophenyl)-1,2-ethanediol (14.6 g, 39.3 mmol), para-toluene sulfonic acid monohydrate (PTSA·H_2O) (299 mg, 4 mol %), 2,2-dimethoxypropane (7.20 mL, 59.0 mmol) and cyclohexane (500 mL) were combined in a 1 L round bottom flask, fitted with a Dean-Stark trap, and set to reflux at 86 ºC overnight. Cyclohexane was removed at reduced pressure, to give a dark powder. Crude (*R,R*) product was purified by column chromatography using a dry loading (15 g crude, 50 g SiO_2 gel) and 5:1 hexanes: ethyl acetate as elutant. Fractions of R_f = 0.5 (5:1 hexanes: ethyl acetate) were collected and concentrated to give a yellow solid (13.3 g, 82 %). Crude (*S,S*) product was used without purification (93 %). ^{1}H NMR and ^{13}C NMR data matched that of the published literature.

^{1}H NMR ($CDCl_3$) (400 MHz) δ 1.58 (s, 6H, -CH_3), 4.54 (s, 2H, ArC*H*), 7.00 (d, *J*= 8.4 Hz, 4H, Ar), 7.38 (d, *J*= 8.4 Hz, 4H, Ar); ^{13}C NMR ($CDCl_3$) (100 MHz) δ 27.11, 84.83, 109.82, 122.39, 128.30, 131.69, 135.51.

Attempted C-Si coupling from 4,5-bis-(4-bromophenyl)-2,2-dimethyl-[1,3]dioxolane

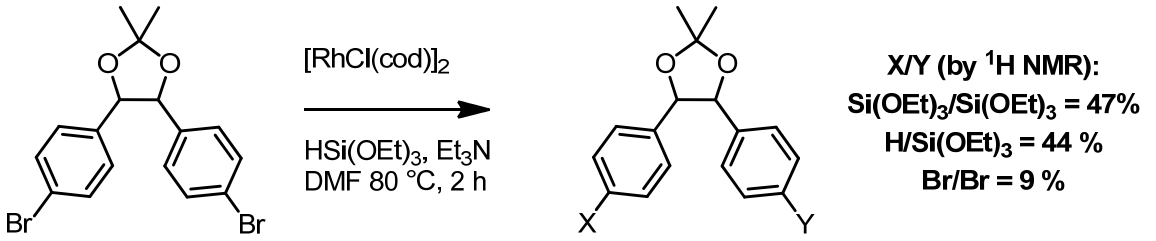

Procedure performed as per the previous chapter[4] using 4,4'-diiodo-*trans*-stilbene, with the addition of Bu_4NI (1.0 eq). From crude ^1H NMR analysis, an approximate conversion to 47 % desired product (X=Y = $Si(OEt)_3$) and 44 % mono-reduced byproduct (X/Y = H/$Si(OEt)_3$) with 9 % unreacted starting material was calculated. Reaction was not optimized.

4,5-bis(4-iodophenyl)-2,2-dimethyl-1,3-dioxolane

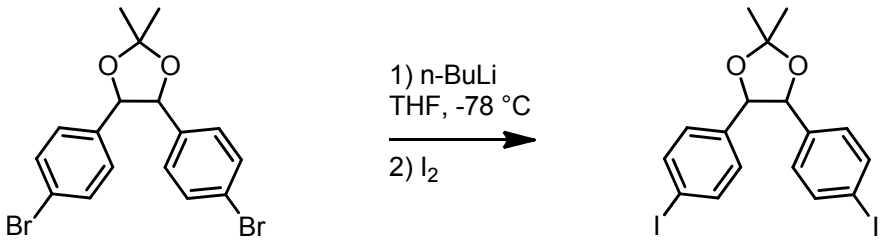

Procedure performed on (*R,R*) and (*S,S*) starting materials as reported in the previous chapter for 4,4'-diiodo-*trans*-stilbene.[3]

The products were purified by recrystallization. (*R,R*): Following workup, dissolution in Et_2O, failed to precipitate crystals. The crude material was dissolved in EtOAc, left in fridge for 1 d, and orange crystals were filtered and washed with cold EtOAc. The mother liquor was concentrated to a dark orange/brown solid and washed with cold Et_2O to give an off-white powder. Both

batches were clean enough by ^{1}H NMR for our use and combined (56 % yield). (*S,S*): A number of other solvent systems were examined here for purification by recrystallization, including CH_2Cl_2/hexanes, acetone, Et_2O, and H_2O. MeOH was chosen as the most effective solvent. Approximately 100 mL of boiling MeOH was used to dissolve each gram of crude material. An equal volume of water was added to the MeOH until cloudiness persisted. The mixture was placed on ice to precipitate off-white crystals. The solid was collected by filtration and let to air dry for a 76 % yield.

^{1}H NMR ($CDCl_3$) (500 MHz) δ 1.69 (s, 6H, -CH_3), 4.63 (s, 2H, ArC*H*), 6.97 (d, *J*= 8.4 Hz, 4H, Ar), 7.69 (d, *J*= 8.4 Hz, 4H, Ar). ^{13}C NMR ($CDCl_3$) (125 MHz) δ 27.52, 85.27, 94.48, 110.23, 128.92, 136.64, 138.04. Exact mass calculated for $C_{17}H_{16}O_2I_2$ m/z = 505.9240, found m/z = 505.9257.

(4-[(4R,5R)-2,2-dimethyl-5-[4-(triethoxysilyl)phenyl]-1,3-dioxolan-4-yl]phenyl)(triethoxy)silane, **CM**

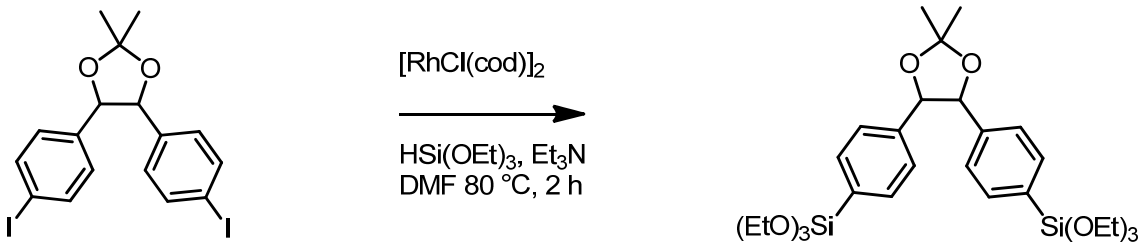

(R,R) or (S,S) **(R,R) or (S,S)**

Rhodium catalyzed C-Si coupling was performed using the same procedures as previously reported for 4,4'-bis(triethoxysilyl)*trans*-stilbene BTETS (1) above. Following a typical workup, the crude material was purified by

automated column chromatography using ethyl acetate (EA) and hexanes (hex). The elution program was as follows: 120 mL @ 2 % EA/ Hex, 1200 mL @ 2 - 10 % EA/ Hex, 1320 mL @ 10 % - 18 % EA/ Hex. Fractions having R_f = 0.20 - 23 (5:1 hex: EA) were collected and concentrated to a clear oil. Yields generally ranged from 45 - 55 % with 10 - 20% mono-reduced byproduct and a small amount of bis-reduction byproduct.

^{1}H NMR ($CDCl_3$) (400 MHz) δ 1.26 (t, J= 6.8 Hz, 18H, -OCH_2CH_3), 1.69 (s, 6H, -CCH_3), 3.89 (q, J= 6.8 Hz, 12H, -OCH_2CH_3), 4.77 (s, 2H, Ar*CH*), 7.26 (d, *J*= 8.4 Hz, 4H, Ar), 7.65 (d, *J*= 8.4 Hz, 4H, Ar). ^{13}C NMR ($CDCl_3$) (125 MHz) δ 18.22, 27.14, 58.77, 85.24, 109.60, 126.20, 131.04, 134.96, 138.93. Exact mass calculated for $C_{29}H_{46}O_8Si_2$ m/z = 578.2731, not found. Exact mass calculated for $[M\text{-}CH_3]^+$ m/z = 563.2497, found m/z = 563.2505.

5.3.2 Chiral material syntheses

BS1, **BS5**, **BS10**, **BS15**, **BS20**, **BS30** and **BR15**, **BR20**, and **BR30** were prepared according to the same procedure as **PMO-1/4-OH**$^-$ above,[8] using ***R***- or ***S*-CM** as a dopant with BTEBP.

Molar Ratios : (BTEBP: **CM** : C_{18}TAMCl: H_2O: NaOH)

(BTEBP: **CM**: 1.28: 1320: 12100); where (BTEBP + **CM**) always equals 1, but is adjusted based on the desired **CM** concentration. It is usually greater than (70:30) for well-ordered materials. In a typical procedure, octadecyltrimethylammonium chloride (C_{18}TMACl) (0.186 g), 6 N NaOH (0.85 mL) and distilled H_2O (9.93 g) were combined in a 4 dram glass vial with stirbar. The mixture was stirred until homogeneous. BTEBP (0.170 g) and **CM** (0.0363

g), were then added with vigorous stirring and allowed to stir at room temperature for 20 h. The vials were then heated without stirring at 95 °C for 22 h. After heating, the precipitate was cooled, filtered and washed with 100 mL of distilled H_2O. To maintain the presence of the ketal protecting group the template was extracted by stirring the solid with 40 mL of ethanol, otherwise a deprotection can occur with the use of acidic EtOH solution (500 mL EtOH, 10.3 g 2 M HCl). The surfactant-free product was filtered and washed with fresh EtOH before air drying

MCM-*S*-CM

This procedure was adapted from Grun *et al*.,[14] using **CM** in a 15 % molar ratio with TEOS as a silica source. Cetyltrimethylammonium bromide (CTAB) (120.3 mg) was combined in a 4 dram vial with NH_4OH (0.528 mL) and distilled H_2O (6.0 mL) before being capped and stirred at room temperature for 3 h. Used a slight amount of heat from heat gun to fully dissolve surfactant, and allowed to return to room temperature. In a separate vial, TEOS (0.425 mL) and ***S*-CM** (194 mg) were quickly combined and transferred to the surfactant vial under vigorous stirring. The mixture was allowed to condense over night before being filtered and washed with d. H_2O (120 mL) and air dried. The surfactant template was removed by stirring in ethanol (20 mL) for 12.5 h, filtered, washed with ethanol (60 mL) and allowed to air dry. Spectroscopic analysis was then performed such as Raman and circular dichroism measurements.

5.3.3 Preparation of AS100

This material was prepared under acidic conditions according to the same procedure as **PMO-1/3-H$^+$** above,[8] using ***S*-CM** as the only silica source.

5.3.4 Preparation of phenylene-bridged PMOs

Materials were prepared according to the report by Inagaki *et al*.[15] as an alternate procedure by this group did not yield precipitates for this bridging unit.[8] In a typical procedure, cetyltrimethylammonium chloride (C_{18}TMACl) (167 mg), 6 N NaOH aqueous solution (400 mg) and distilled H_2O (5.0 g) were combined in a 4 dram vial, stirred at room temperature for a few minutes and gently heated until the surfactant was completely dissolved. BTEB and **CM** were combined in a separated vial and quickly transferred to the stirring surfactant solution resulting in an emulsion. The capped vials were allowed to stir for 20 h at room temperature followed by static heating in an oven at 95 ºC for 20 h. The vials were removed from the oven, cooled to room temperature, and the gelly product was scraped from the vials. The gel was filtered and washed with H_2O (100 mL) and let to air dry. The surfactant was removed by stirring the jelly mass with EtOH (20 mL) at 70 ºC for 8 h. Circular dichroism, Raman spectroscopy and nitrogen porosimetry were performed on the resulting materials.

5.3.5 Circular dichroism of PMOs

The PMO samples for CD were prepared as reported in the general experimental section. CD spectra for monomers were taken in 95 % EtOH. Any

noise reduction of data was performed in *J-700 for Windows Standard Analysis* software, version 1.50.01. Settings were as follows: Top position 20, Bottom position 40, Horizontal gain X 1, Vertical gain X 1, and 1024 Data points. Absorbance normalized spectra were obtained by dividing CD by absorbance values. Potassium bromide was also tested as a matrix for the spectroscopic studies of the PMOs. In this case, the PMO and KBr (dry) were massed to obtain roughly a 0.25 – 1.0 % PMO in KBr mixture. Pellets with higher transparency result from not grinding the KBr, but PMO dispersion then becomes a concern. The mixture is pressed in a die set to give the PMO/KBr pellet which can be positioned in front of the CD detector for analysis. These pellets did not always give reproducible CD data.

5.4 Experimental procedures from Chapter 4

5.4.1 Profilometry

To a 60 mL glass jar with stirbar was added Pluronic F127 (1.00 g) and EtOH (20 mL) and stirred for 20 min to homogenize. To a separate 1 dram vial was added MPTMS (0.098 g) and TEOS (1.979 g) to give a cloudy mixture before being transferred into the jar. 1 M HCl (1 mL) was then added and let to stir for 30 min followed by sitting for 30 min. 0.5 mL was then taken up into a 1 mL syringe. A 0.2 um Nalgene syringe filter was added to the syringe tip and 4 drops (~0.1 mL) of the sol were dropped onto the silicon wafer substrate. The

wafer was spun at 1000, 2000, 3000 and 4000 rpm for 10 s. The wafers were then let to dry overnight before being profiled.

5.4.2 FE-SEM fibre measurements

10^{-3} M HCl (0.714 g), CTAB (0.260 g), deionized H_2O (0.691 g) and anhydrous EtOH (1.151 g) were weighed into a 4 dram, (~16 mL) glass vial containing a stirbar and let to stir until homogeneous. To a separate vial was added BTEE (0.842 g) and MPTMS (0.025 g) and this was transferred to the 1st vial after mixing. The vial was left to stir at room temperature while capped for 8.5 h. At this point, the fibre was fed through a small hole in the bottom of a Teflon container (volume of 0.4 mL) and the sol was added (Figure 5.2). The fibre was withdrawn by a homemade motorized dip-coater which was controlled at varying withdrawal speeds (10, 15, 20 mm/s). After the fibres were dried for 10 h, they were cured in an oven at 70 °C for 7 h. They were then slowly cooled to room temperature to avoid cracking of the films and cleaved using a fibre-cleaving device to produce a clean edge. These small pieces were propped up vertically on an SEM stub before being gold-coated and submitted for FE-SEM imaging. The thickness of the organosilica film was measured directly from the image scale bar.

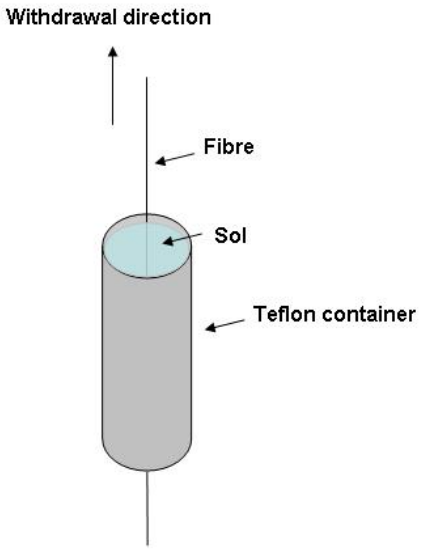

Figure 5.2 Dip-coating setup.

5.5 References

(1) JASCO Model J-715 Instruction Manual, JASCO Corporation 1995, Tokyo, Japan.
(2) Ding, X.; Lv, X.; Hui, B.; Chen, Z.; Xiao, M.; Guo, B.; Tang, W. *Tetrahedron Lett.* **2006**, *47*, 2921-2924.
(3) Chang, H.-K.; Datta, S.; Das, A.; Odedra, A.; Liu, R.-S. *Angew. Chem., Int. Ed.* **2007**, *46*, 4744-4747.
(4) Murata, M.; Ishikura, M.; Nagata, M.; Watanabe, S.; Masuda, Y. *Org. Lett.* **2002**, *4*, 1843-1845.
(5) Hopf, H.; Hucker, J.; Ernst, L. *Eur. J. Org. Chem.* **2007**, 1891-1904.
(6) Bosanac, T.; Wilcox, C. S. *Org. Lett.* **2004**, *6*, 2321-2324.
(7) Hunks, W. J.; Ozin, G. A. *Chem. Commun.* **2004**, 2426-2427.
(8) Kapoor, M. P.; Yang, Q.; Inagaki, S. *J. Am. Chem. Soc.* **2002**, *124*, 15176-15177.
(9) Goto, Y.; Inagaki, S. *Chem. Commun.* **2002**, 2410-2411.
(10) Rengasamy, R.; Curtis-Long, M. J.; Seo, W. D.; Jeong, S. H.; Jeong, I.-Y.; Park, K. H. *J. Org. Chem.* **2008**, *73*, 2898-2901.
(11) Pavlyuk, O.; Teller, H.; McMills, M. *Tetrahedron Lett.* **2009**, *50*, 2716-2718.
(12) Wang, Z.; Sharpless, K. *J. Org. Chem.* **1994**, *59*, 8302-8303.
(13) Jeong, K. S.; Kim, S. Y.; Shin, U.-S.; Kogej, M.; Hai, N. T. M.; Broekmann, P.; Jeong, N.; Kirchner, B.; Reiher, M.; Schalley, C. A. *J. Am. Chem. Soc.* **2005**, *127*, 17672-17685.
(14) Grun, M.; Unger, K. K.; Matsumoto, A.; Tsutsumi, K. *Microporous Mesoporous Mater.* **1999**, *27*, 207-216.
(15) Inagaki, S.; Guan, S.; Ohsuna, T.; Terasaki, O. *Nature* **2002**, *416*, 304-307.